

AUGUST 2023

AJNR

VOLUME 44 • PP 879-998

AJNR

AMERICAN JOURNAL OF NEURORADIOLOGY

Official Journal ASNR • ASFNR • ASHNR • ASPNR • ASSR

AUGUST 2023 | VOLUME 44 | NUMBER 8 | WWW.AJNR.ORG

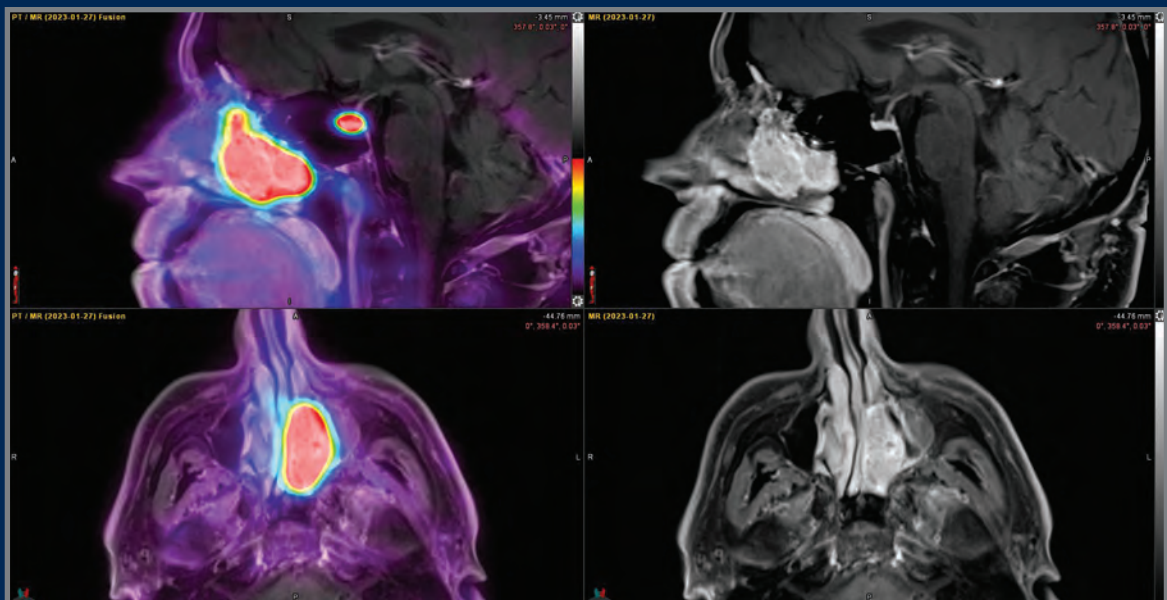
THE JOURNAL OF DIAGNOSTIC AND INTERVENTIONAL NEURORADIOLOGY

MRI of carotid artery atherosclerosis

ASL to differentiate venous-predominant AVM from DVA

Somatostatin receptor-PET of head and neck neuroendocrine tumors

QSM kurtosis biomarker to identify epileptogenic tubers in tuberous sclerosis complex



FRED™ X™

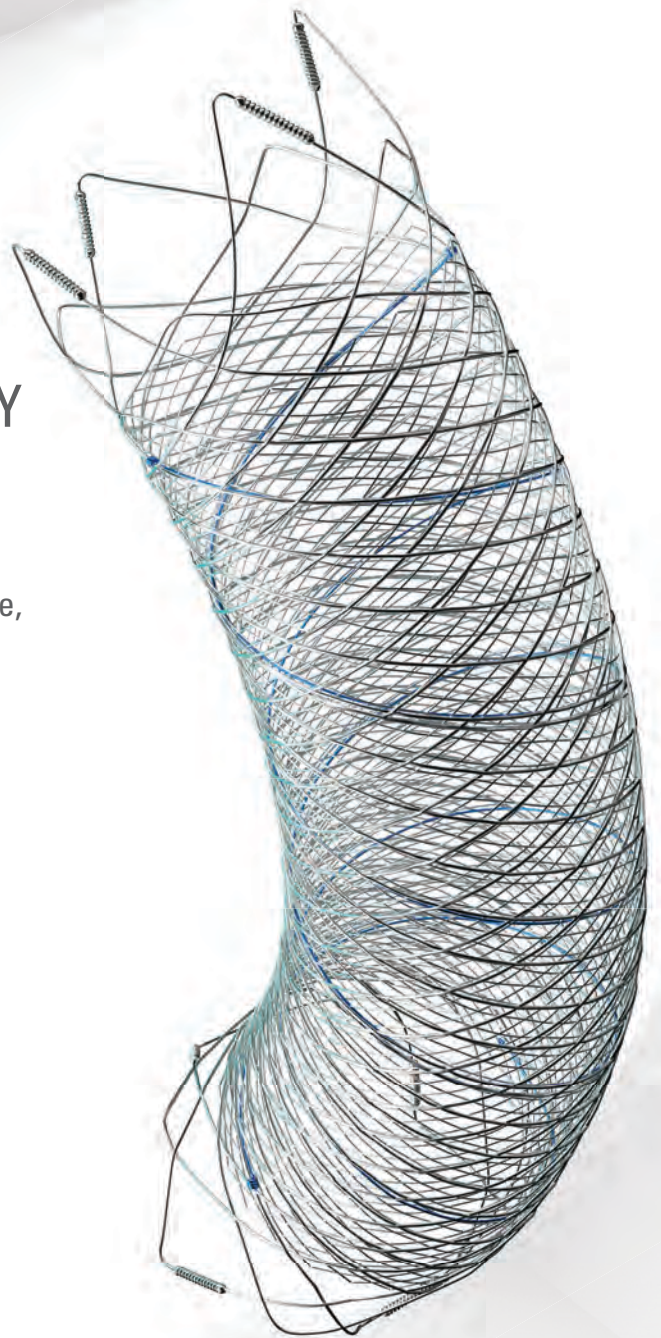
Flow Diverter Stent

THE NEXT ADVANCEMENT IN FLOW DIVERSION TECHNOLOGY

The FRED™ X Flow Diverter features the same precise placement and immediate opening of the FRED™ Device, now with X Technology. X Technology is a covalently bonded, nanoscale surface treatment, designed to:

- **REDUCE MATERIAL THROMBOGENICITY¹**
- **MAINTAIN NATURAL VESSEL HEALING RESPONSE^{2,3,4}**
- **IMPROVE DEVICE DELIVERABILITY AND RESHEATHING¹**

The only FDA PMA approved portfolio with a 0.021" delivery system for smaller device sizes, and no distal lead wire.



For more information, contact your local MicroVention sales representative or visit our website. www.microvention.com



¹ Data is derived from in vivo and ex vitro testing and may not be representative of clinical performance.

¹ Data on file

² Tanaka M et al. Design of biocompatible and biodegradable polymers based on intermediate water concept. Polymer Journal. 2015;47:114-121.

³ Tanaka M et al. Blood compatible aspects of poly(2-methoxyethylacrylate) (PMEA) – relationship between protein adsorption and platelet adhesion on PMEAs surface. Biomaterials. 2000;21:1471-1481.

⁴ Schiel L et al. X Coating™: A new biopassive polymer coating. Canadian Perfusion Canadienne. June 2001;11(2):9.

Indications for Use: The FRED X System is indicated for use in the internal carotid artery from the petrous segment to the terminus for the endovascular treatment of adult patients (22 years of age or older) with wide-necked (neck width 4 mm or dome-to-neck ratio < 2) saccular or fusiform intracranial aneurysms arising from a parent vessel with a diameter 2.0 mm and 5.0 mm.

Rx Only: Federal (United States) law restricts this device to sale by or on the order of a physician. For Healthcare professionals intended use only.

MICROVENTION, FRED and HEADWAY are registered trademarks of MicroVention, Inc. in the United States and other jurisdictions. Stylized X is a trademark of MicroVention, Inc. © 2022 MicroVention, Inc. MM1222 US 03/22

WEB™ 17

Aneurysm Embolization System

LOWER PROFILE



NEW SIZES



MORE ACCESS OPTIONS



INDICATIONS FOR USE:

The WEB Aneurysm Embolization System is intended for the endovascular embolization of ruptured and unruptured intracranial aneurysms and other neurovascular abnormalities such as arteriovenous fistulae (AVF). The WEB Aneurysm Embolization System is also intended for vascular occlusion of blood vessels within the neurovascular system to permanently obstruct blood flow to an aneurysm or other vascular malformation.

POTENTIAL COMPLICATIONS:

Potential complications include but are not limited to the following: hematoma at the site of entry, aneurysm rupture, emboli, vessel perforation, parent artery occlusion, hemorrhage, ischemia, vasospasm, clot formation, device migration or misplacement, premature or difficult device detachment, non-detachment, incomplete aneurysm filling, revascularization, post-embolization syndrome, and neurological deficits including stroke and death. For complete indications, potential complications, warnings, precautions, and instructions, see instructions for use (IFU provided with the device).

VIA 21, 27, 33 - The VIA Microcatheter is intended for the introduction of interventional devices (such as the WEB device/stents/flow diverters) and infusion of diagnostic agents (such as contrast media) into the neuro, peripheral, and coronary vasculature.

VIA 17,17 Preshaped - The VIA Microcatheter is intended for the introduction of interventional devices (such as the WEB device/stents/flow diverters) and infusion of diagnostic agents (such as contrast media) into the neuro, peripheral, and coronary vasculature.

The VIA Microcatheter is contraindicated for use with liquid embolic materials, such as n-butyl 2-cyanoacrylate or ethylene vinyl alcohol & DMSO (dimethyl sulfoxide).

The device should only be used by physicians who have undergone training in all aspects of the WEB Aneurysm Embolization System procedure as prescribed by the manufacturer.

RX Only: Federal law restricts this device to sale by or on the order of a physician.

For healthcare professional intended use only.



MicroVention Worldwide
Innovation Center PH +1.714.247.8000

35 Enterprise
Aliso Viejo, CA 92656 USA
MicroVention UK Limited PH +44 (0) 191 258 6777
MicroVention Europe, S.A.R.L. PH +33 (1) 39 21 77 46
MicroVention Deutschland GmbH PH +49 211 210 798-0
Website microvention.com



WEB™ and VIA™ are registered trademarks
of Sequent Medical, Inc. in the United States.

©2021 MicroVention, Inc. MM1184 WW 11/2021

LIFE IS FULL OF COMPROMISES.
IT'S TIME TO TAKE A STAND.

NO COMPROMISE

HIGH RELAXIVITY, HIGH STABILITY:^{1,2}
I CHOOSE BOTH.

The individual who appears is for illustrative purposes. The person depicted is a model and not a real healthcare professional. Please see Brief Summary of Prescribing Information including Boxed Warning on adjacent page.

VUEWAY™ (gadopiclenol) solution for injection

Indications

VUEWAY injection is indicated in adults and children aged 2 years and older for use with magnetic resonance imaging (MRI) to detect and visualize lesions with abnormal vascularity in:

- the central nervous system (brain, spine and surrounding tissues),
- the body (head and neck, thorax, abdomen, pelvis, and musculoskeletal system).

IMPORTANT SAFETY INFORMATION

WARNING: NEPHROGENIC SYSTEMIC FIBROSIS (NSF)

Gadolinium-based contrast agents (GBCAs) increase the risk for NSF among patients with impaired elimination of the drugs. Avoid use of GBCAs in these patients unless the diagnostic information is essential and not available with non-contrast MRI or other modalities. NSF may result in fatal or debilitating fibrosis affecting the skin, muscle and internal organs.

- The risk for NSF appears highest among patients with:
 - Chronic, severe kidney disease (GFR < 30 mL/min/1.73 m²), or
 - Acute kidney injury.
- Screen patients for acute kidney injury and other conditions that may reduce renal function. For patients at risk for chronically reduced renal function (e.g. age > 60 years,

hypertension, diabetes), estimate the glomerular filtration rate (GFR) through laboratory testing.

- For patients at highest risk for NSF, do not exceed the recommended VUEWAY dose and allow a sufficient period of time for elimination of the drug from the body prior to any re-administration.

Contraindications

VUEWAY injection is contraindicated in patients with history of hypersensitivity reactions to VUEWAY.

Warnings

Risk of **nephrogenic systemic fibrosis** is increased in patients using GBCA agents that have impaired elimination of the drugs, with the highest risk in patients chronic, severe kidney disease as well as patients with acute kidney injury. Avoid use of GBCAs among these patients unless the diagnostic information is essential and not available with non-contrast MRI or other modalities.


Hypersensitivity reactions, including serious hypersensitivity reactions, could occur during use or shortly following VUEWAY administration. Assess all patients for any history of a reaction to contrast media, bronchial asthma and/or allergic disorders, administer VUEWAY only in situations where trained personnel and therapies are promptly available for the treatment of hypersensitivity reactions, and observe patients for signs and symptoms of hypersensitivity reactions after administration.



MR Suite

IN MRI

INTRODUCING


Vueway™
(gadopiclenol) injection
485.1 mg/mL

HALF THE GADOLINIUM DOSE COMPARED TO OTHER
MACROCYCLIC GBCAs IN APPROVED INDICATIONS.^{1,3-6}
FROM BRACCO, YOUR TRUSTED PARTNER IN MRI.



LIFE FROM INSIDE

Gadolinium retention can be for months or years in several organs after administration. The highest concentrations (nanomoles per gram of tissue) have been identified in the bone, followed by other organs (brain, skin, kidney, liver and spleen). Minimize repetitive GBCA imaging studies, particularly closely spaced studies, when possible.

Acute kidney injury requiring dialysis has occurred with the use of GBCAs in patients with chronically reduced renal function. The risk of acute kidney injury may increase with increasing dose of the contrast agent.

Ensure catheter and venous patency before injecting as **extravasation** may occur, and cause tissue irritation.

VUEWAY may **impair the visualization of lesions** seen on non-contrast MRI. Therefore, caution should be exercised when Vueway MRI scans are interpreted without a companion non-contrast MRI scan.

The most common adverse reactions (incidence \geq 0.5%) are injection site pain (0.7%), and headache (0.7%).

You are encouraged to report negative side effects of prescription drugs to the FDA. Visit www.fda.gov/medwatch or call 1-800-FDA-1088.

Please see BRIEF SUMMARY of Prescribing Information for VUEWAY, including BOXED WARNING on Nephrogenic Systemic Fibrosis.

Manufactured for Bracco Diagnostics Inc. by Liebel-Flarsheim Company LLC - Raleigh, NC, USA 27616.

VUEWAY is a trademark of Bracco Imaging S.p.A.

References: 1. Vueway™ (gadopiclenol) Injection Full Prescribing Information. Monroe Twp., NJ: Bracco Diagnostics Inc.; September 2022. 2. Robic C, Port M, Rousseaux O, et al. Physicochemical and Pharmacokinetic Profiles of Gadopiclenol: A New Macrocytic Gadolinium Chelate With High T1 Relaxivity. *Invest Radiol.* 2019 Aug;54: 475–484. 3. GADAVIST® (gadobutrol) Injection. Full Prescribing Information. Bayer HealthCare Pharmaceuticals Inc. Whippany, NJ; April 2022. 4. DOTAREM® (gadoterate meglumine) Injection. Full Prescribing Information. Guerbet LLC. Princeton, NJ; April 2022. 5. CLARISCAN™ (gadoterate meglumine) injection for intravenous use. Full Prescribing Information. GE Healthcare. Marlborough, MA; February 2020. 6. ProHance® (Gadoteridol) Injection. Full Prescribing Information and Patient Medication Guide. Monroe Twp., NJ: Bracco Diagnostics Inc.; December 2020.

Bracco Diagnostics Inc.
259 Prospect Plains Road, Building H
Monroe Township, NJ 08831 USA
Phone: 609-514-2200
Toll Free: 1-877-272-2269 (U.S. only)
Fax: 609-514-2446
© 2022 Bracco Diagnostics Inc.
All Rights Reserved. US-VW-2200012 10/22

VISIT
VUEWAY.COM
FOR MORE
INFORMATION



Vueway™

(gadopiclenol) injection, for intravenous use

BRIEF SUMMARY: Please see package insert of full prescribing information.

WARNING: NEPHROGENIC SYSTEMIC FIBROSIS (NSF)
Gadolinium-based contrast agents (GBCAs) increase the risk for NSF among patients with impaired elimination of the drugs. Avoid use of GBCAs in these patients unless the diagnostic information is essential and not available with non-contrast MRI or other modalities. NSF may result in fatal or debilitating fibrosis affecting the skin, muscle and internal organs.

- The risk for NSF appears highest among patients with:
 - Chronic, severe kidney disease (GFR <30 mL/min/1.73 m²), or
 - Acute kidney injury.
- Screen patients for acute kidney injury and other conditions that may reduce renal function. For patients at risk for chronically reduced renal function (e.g. age >60 years, hypertension, diabetes), estimate the glomerular filtration rate (GFR) through laboratory testing.
- For patients at highest risk for NSF, do not exceed the recommended Vueway dose and allow a sufficient period of time for elimination of the drug from the body prior to any re-administration [see Warnings and Precautions (5.1) in the full Prescribing Information].

INDICATIONS AND USAGE

Vueway™ (gadopiclenol) is a gadolinium-based contrast agent indicated in adult and pediatric patients aged 2 years and older for use with magnetic resonance imaging (MRI) to detect and visualize lesions with abnormal vascularity in:

- the central nervous system (brain, spine, and associated tissues),
- the body (head and neck, thorax, abdomen, pelvis, and musculoskeletal system).

CONTRAINDICATIONS

Vueway is contraindicated in patients with history of hypersensitivity reactions to gadopiclenol.

WARNINGS AND PRECAUTIONS

Nephrogenic Systemic Fibrosis Gadolinium-based contrast agents (GBCAs) increase the risk for nephrogenic systemic fibrosis (NSF) among patients with impaired elimination of the drugs. Avoid use of GBCAs among these patients unless the diagnostic information is essential and not available with non-contrast MRI or other modalities. The GBCA-associated NSF risk appears highest for patients with chronic, severe kidney disease (GFR <30 mL/min/1.73 m²) as well as patients with acute kidney injury. The risk appears lower for patients with chronic, moderate kidney disease (GFR 30-59 mL/min/1.73 m²) and little, if any, for patients with chronic, mild kidney disease (GFR 60-89 mL/min/1.73 m²). NSF may result in fatal or debilitating fibrosis affecting the skin, muscle, and internal organs. Report any diagnosis of NSF following Vueway administration to Bracco Diagnostics Inc. (1-800-257-5181) or FDA (1-800-FDA-1088 or www.fda.gov/medwatch).

Screen patients for acute kidney injury and other conditions that may reduce renal function. Features of acute kidney injury consist of rapid (over hours to days) and usually reversible decrease in kidney function, commonly in the setting of surgery, severe infection, injury or drug-induced kidney toxicity. Serum creatinine levels and estimated GFR may not reliably assess renal function in the setting of acute kidney injury. For patients at risk for chronically reduced renal function (e.g., age >60 years, diabetes mellitus or chronic hypertension), estimate the GFR through laboratory testing.

Among the factors that may increase the risk for NSF are repeated or higher than recommended doses of a GBCA and the degree of renal impairment at the time of exposure. Record the specific GBCA and the dose administered to a patient. For patients at highest risk for NSF, do not exceed the recommended Vueway dose and allow a sufficient period of time for elimination of the drug prior to re-administration. For patients receiving hemodialysis, physicians may consider the prompt initiation of hemodialysis following the administration of a GBCA in order to enhance the contrast agent's elimination [see Use in Specific Populations (8.6) and Clinical Pharmacology (12.3) in the full Prescribing Information]. The usefulness of hemodialysis in the prevention of NSF is unknown.

Hypersensitivity Reactions With GBCAs, serious hypersensitivity reactions have occurred. In most cases, initial symptoms occurred within minutes of GBCA administration and resolved with prompt emergency treatment.

- Before Vueway administration, assess all patients for any history of a reaction to contrast media, bronchial asthma and/or allergic disorders. These patients may have an increased risk for a hypersensitivity reaction to Vueway.
- Vueway is contraindicated in patients with history of hypersensitivity reactions to Vueway [see Contraindications (4) in the full Prescribing Information].
- Administer Vueway only in situations where trained personnel and therapies are promptly available for the treatment of hypersensitivity reactions, including personnel trained in resuscitation.
- During and following Vueway administration, observe patients for signs and symptoms of hypersensitivity reactions.

Gadolinium Retention Gadolinium is retained for months or years in several organs. The highest concentrations (nanomoles per gram of tissue) have been identified in the bone, followed by other organs (e.g. brain, skin, kidney, liver, and spleen). The duration of retention also varies by tissue and is longest in bone. Linear GBCAs cause more retention than macrocyclic GBCAs. At equivalent doses, gadolinium retention varies among the linear agents with gadodiamide causing greater retention than other linear agents such as gadoxetate disodium, and gadobenate dimeglumine. Retention is lowest and similar

among the macrocyclic GBCAs such as gadoterate meglumine, gadobutrol, gadoteridol, and gadopiclenol.

Consequences of gadolinium retention in the brain have not been established. Pathologic and clinical consequences of GBCA administration and retention in skin and other organs have been established in patients with impaired renal function [see Warnings and Precautions (5.1) in the full Prescribing Information]. There are rare reports of pathologic skin changes in patients with normal renal function. Adverse events involving multiple organ systems have been reported in patients with normal renal function without an established causal link to gadolinium.

While clinical consequences of gadolinium retention have not been established in patients with normal renal function, certain patients might be at higher risk. These include patients requiring multiple lifetime doses, pregnant and pediatric patients, and patients with inflammatory conditions. Consider the retention characteristics of the agent when choosing a GBCA for these patients. Minimize repetitive GBCA imaging studies, particularly closely spaced studies, when possible.

Acute Kidney Injury in patients with chronically reduced renal function, acute kidney injury requiring dialysis has occurred with the use of GBCAs. The risk of acute kidney injury may increase with increasing dose of the contrast agent. Do not exceed the recommended dose.

Extravasation and Injection Site Reactions Injection site reactions such as injection site pain have been reported in the clinical studies with Vueway [see Adverse Reactions (6.1) in the full Prescribing Information]. Extravasation during Vueway administration may result in tissue irritation [see Nonclinical Toxicology (13.2) in the full Prescribing Information]. Ensure catheter and venous patency before the injection of Vueway.

Interference with Visualization of Lesions Visible with Non-Contrast MRI As with any GBCA, Vueway may impair the visualization of lesions seen on non-contrast MRI. Therefore, caution should be exercised when Vueway MRI scans are interpreted without a companion non-contrast MRI scan.

ADVERSE REACTIONS

The following serious adverse reactions are discussed elsewhere in labeling:

- Nephrogenic Systemic Fibrosis [see Warnings and Precautions (5.1) in the full Prescribing Information]
- Hypersensitivity Reactions [see Contraindications (4) and Warnings and Precautions (5.2) in the full Prescribing Information]

Clinical Trials Experience Because clinical trials are conducted under widely varying conditions, adverse reaction rates observed in the clinical trials of a drug cannot be directly compared to rates in the clinical trials of another drug and may not reflect the rates observed in clinical practice.

The safety of Vueway was evaluated in 1,047 patients who received Vueway at doses ranging from 0.025 mmol/kg (one half the recommended dose) to 0.3 mmol/kg (six times the recommended dose). A total of 708 patients received the recommended dose of 0.05 mmol/kg. Among patients who received the recommended dose, the average age was 51 years (range 2 years to 88 years) and 56% were female. The ethnic distribution was 79% White, 10% Asian, 7% American Indian or Alaska native, 2% Black, and 2% patients of other or unspecified ethnic groups.

Overall, approximately 4.7% of subjects receiving the labeled dose reported one or more adverse reactions.

Table 1 lists adverse reactions that occurred in >0.2% of patients who received 0.05 mmol/kg Vueway.

TABLE 1. ADVERSE REACTIONS REPORTED IN >0.2% OF PATIENTS RECEIVING VUEWAY IN CLINICAL TRIALS	
Adverse Reaction	Vueway 0.05 mmol/kg (n=708) (%)
Injection site pain	0.7
Headache	0.7
Nausea	0.4
Injection site warmth	0.4
Injection site coldness	0.3
Dizziness	0.3
Local swelling	0.3

Adverse reactions that occurred with a frequency ≤ 0.2% in patients who received 0.05 mmol/kg Vueway included: maculopapular rash, vomiting, worsened renal impairment, feeling hot, pyrexia, oral paresthesia, dysgeusia, diarrhea, pruritus, allergic dermatitis, erythema, injection site paresthesia, Cystatin C increase, and blood creatinine increase.

Adverse Reactions in Pediatric Patients

One study with a single dose of Vueway (0.05 mmol/kg) was conducted in 80 pediatric patients aged 2 years to 17 years, including 60 patients who underwent a central nervous system (CNS) MRI and 20 patients who underwent a body MRI. One adverse reaction (maculopapular rash of moderate severity) in one patient (1.3%) was reported in the CNS cohort.

USE IN SPECIFIC POPULATIONS

Pregnancy Risk Summary There are no available data on Vueway use in pregnant women to evaluate for a drug-associated risk of major birth defects, miscarriage or other adverse maternal or fetal outcomes. GBCAs cross the human placenta and result in fetal exposure and gadolinium retention. The available human data on GBCA exposure during pregnancy and adverse fetal outcomes are limited and inconclusive (see Data). In animal reproduction studies, there were no adverse developmental effects observed in rats or rabbits with intravenous administration of Vueway during organogenesis (see Data). Because of the potential risks of gadolinium to the fetus, use Vueway only if imaging is essential during pregnancy and cannot be delayed. The estimated background risk of major birth defects and miscarriage for the indicated population(s) are unknown. All pregnancies have a background risk of birth defect, loss, or other adverse outcomes. In the U.S. general population, the estimated background risk of major birth defects and miscarriage in clinically recognized pregnancies is 2% to 4% and 15% to 20% respectively. Data Human Data Contrast enhancement is visualized in the placenta and fetal tissues after maternal GBCA administration. Cohort studies and case reports on exposure to GBCAs during pregnancy have not reported a clear association between GBCAs and adverse effects in the exposed neonates. However, a retrospective cohort study comparing pregnant women who had a GBCA MRI to pregnant women who did not have an MRI reported a higher occurrence of stillbirths and neonatal deaths in the group receiving GBCA MRI. Limitations of this study include a lack of comparison with non-contrast MRI and lack of information about the maternal indication for MRI. Overall, these data preclude

a reliable evaluation of the potential risk of adverse fetal outcomes with the use of GBCAs in pregnancy.

Animal Data Gadolinium Retention: GBCAs administered to pregnant non-human primates (0.1 mmol/kg on gestational days 85 and 135) result in measurable gadolinium concentration in the offspring in bone, brain, skin, liver, kidney, and spleen for at least 7 months. GBCAs administered to pregnant mice (2 mmol/kg daily on gestational days 16 through 19) result in measurable gadolinium concentrations in the pups in bone, brain, kidney, liver, blood, muscle, and spleen at one-month postnatal age.

Reproductive Toxicology: Animal reproduction studies conducted with gadopiclenol showed some signs of maternal toxicity in rats at 10 mmol/kg and rabbits at 5 mmol/kg (corresponding to 52 times and 57 times the recommended human dose, respectively). This maternal toxicity was characterized in both species by swelling, decreased activity, and lower gestation weight gain and food consumption.

No effect on embryo-fetal development was observed in rats at 10 mmol/kg (corresponding to 52 times the recommended human dose). In rabbits, a lower mean fetal body weight was observed at 5 mmol/kg (corresponding to 57 times the recommended human dose) and this was attributed as a consequence of the lower gestation weight gain.

Lactation Risk Summary There are no data on the presence of gadopiclenol in human milk, the effects on the breastfed infant, or the effects on milk production. However, published lactation data on other GBCAs indicate that 0.01% to 0.04% of the maternal gadolinium dose is excreted in breast milk. Additionally, there is limited GBCA gastrointestinal absorption in the breast-fed infant. Gadopiclenol is present in rat milk. When a drug is present in animal milk, it is likely that the drug will be present in human milk (see Data). The developmental and health benefits of breastfeeding should be considered along with the mother's clinical need for Vueway and any potential adverse effects on the breastfed infant from Vueway or from the underlying maternal condition. Data In lactating rats receiving single intravenous injection of [¹⁵²Gd]-gadopiclenol, 0.3% and 0.2% of the total administered radioactivity was transferred to the pups via maternal milk at 6 hours and 24 hours after administration, respectively. Furthermore, in nursing rat pups, oral absorption of gadopiclenol was 3.6%.

Pediatric Use The safety and effectiveness of Vueway for use with MRI to detect and visualize lesions with abnormal vascularity in the CNS (brain, spine, and associated tissues), and the body (head and neck, thorax, abdomen, pelvis, and musculoskeletal system) have been established in pediatric patients aged 2 years and older.

Use of Vueway in this age group is supported by evidence from adequate and well-controlled studies in adults with additional pharmacokinetic and safety data from an open-label, uncontrolled, multicenter, single dose study of Vueway (0.05 mmol/kg) in 80 pediatric patients aged 2 to 17 years. The 80 patients consisted of 60 patients who underwent a CNS MRI and 20 patients who underwent a body MRI [see Adverse Reactions (6.1) and Clinical Pharmacology (12.3) in the full Prescribing Information].

The safety and effectiveness of Vueway have not been established in pediatric patients younger than 2 years of age.

Geriatric Use Of the total number of Vueway-treated patients in clinical studies, 270 (26%) patients were 65 years of age and over, while 62 (6%) patients were 75 years of age and over. No overall differences in safety or efficacy were observed between these subjects and younger subjects.

This drug is known to be substantially excreted by the kidney, and the risk of adverse reactions to this drug may be greater in patients with impaired renal function. Because elderly patients are more likely to have decreased renal function, it may be useful to monitor renal function.

Renal Impairment in patients with renal impairment, the exposure of gadopiclenol is increased compared to patients with normal renal function. This may increase the risk of adverse reactions such as nephrogenic systemic fibrosis (NSF). Avoid use of GBCAs among these patients unless the diagnostic information is essential and not available with non-contrast MRI or other modalities. No dose adjustment of Vueway is recommended for patients with renal impairment. Vueway can be removed from the body by hemodialysis [see Warnings and Precautions (5.1, 5.3, 5.4) and Clinical Pharmacology (12.3) in the full Prescribing Information].

OVERDOSAGE

Among subjects who received a single 0.3 mmol/kg intravenous dose of gadopiclenol (6 times the recommended dose of Vueway), headache and nausea were the most frequently reported adverse reactions. Gadopiclenol can be removed from the body by hemodialysis [see Clinical Pharmacology (12.3) in the full Prescribing Information].

PATIENT COUNSELING INFORMATION Advise the patient to read the FDA-approved patient labeling (Medication Guide).

Nephrogenic Systemic Fibrosis Inform the patient that Vueway may increase the risk for NSF among patients with impaired elimination of the drugs and that NSF may result in fatal or debilitating fibrosis affecting the skin, muscle and internal organs.

Instruct the patients to contact their physician if they develop signs or symptoms of NSF following Vueway administration, such as burning, itching, swelling, scaling, hardening and tightening of the skin; red or dark patches on the skin; stiffness in joints with trouble moving, bending or straightening the arms, hands, legs or feet; pain in the hip bones or ribs; or muscle weakness [see Warnings and Precautions (5.1) in the full Prescribing Information].

Gadolinium Retention Advise patients that gadolinium is retained for months or years in brain, bone, skin, and other organs following Vueway administration even in patients with normal renal function. The clinical consequences of retention are unknown. Retention depends on multiple factors and is greater following administration of linear GBCAs than following administration of macrocyclic GBCAs [see Warnings and Precautions (5.3) in the full Prescribing Information].

Injection Site Reactions Inform the patient that Vueway may cause reactions along the venous injection site, such as mild and transient burning or pain or feeling of warmth or coldness at the injection site [see Warnings and Precautions (5.5) in the full Prescribing Information].

Pregnancy Advise pregnant women of the potential risk of fetal exposure to Vueway [see Use in Specific Populations (8.1) in the full Prescribing Information].

Rx only

US Patent No. 10,973,934
Manufactured for Bracco Diagnostics Inc. by Liebel-Flarsheim Company LLC - Raleigh, NC, USA 27616.
Toll Free: 1-877-272-2269 (U.S. only)
Revised November 2022

AJNR

AMERICAN JOURNAL OF NEURORADIOLOGY

AUGUST 2023
VOLUME 44
NUMBER 8
WWW.AJNR.ORG

Publication Preview at www.ajnr.org features articles released in advance of print. Visit www.ajnrblog.org to comment on AJNR content and chat with colleagues and AJNR's News Digest at <http://ajnrdigest.org> to read the stories behind the latest research in neuroimaging.

879 **PERSPECTIVES** *M. Wintermark*

REVIEW ARTICLE



880 **MR Imaging of Carotid Artery Atherosclerosis: Updated Evidence on High-Risk Plaque Features and Emerging Trends** *J.C. Benson, et al.*

EXTRACRANIAL VASCULAR

PRACTICE PERSPECTIVES



889 **Ecchordosis Physaliphora: Does It Even Exist?** *A.R. Stevens, et al.*

HEAD & NECK

GENERAL CONTENTS



894 **Performance of Automated ASPECTS Software and Value as a Computer-Aided Detection Tool** *J. Lambert, et al.*

ADULT BRAIN



901 **Effect of Radiographic Contrast Media Shortage on Stroke Evaluation in the United States** *A.I. Qureshi, et al.*

ADULT BRAIN

908 **Commentary**
The Iodinated Contrast Crisis of 2022: A Near Miss or a Missed Opportunity? *S.A. Amukotuwa, et al.*

ADULT BRAIN

910 **Brain Parcellation Repeatability and Reproducibility Using Conventional and Quantitative 3D MR Imaging** *J.B.M. Warntjes, et al.*

ADULT BRAIN



916 **Arterial Spin-Labeling MR Imaging for the Differential Diagnosis of Venous-Predominant AVMs and Developmental Venous Anomalies** *D.H. Yoo, et al.*

ADULT BRAIN INTERVENTIONAL



922 **Clinical Applications of Conebeam CTP Imaging in Cerebral Disease: A Systematic Review** *A.H.A. Zaid Al-Kaylani, et al.*

INTERVENTIONAL



928 **Effect of Platelet Function Testing Guidance on Clinical Outcomes for Patients with Intracranial Aneurysms Undergoing Endovascular Treatment** *X. Wang, et al.*

INTERVENTIONAL



934 **Outcomes of Preoperative Transophthalmic Artery Embolization of Meningiomas: A Systematic Review with a Focus on Embolization Agent** *M.A. Essibayi, et al.*

INTERVENTIONAL












939 **Endovascular Treatment of Cerebrovascular Lesions Using Nickel- or Nitinol-Containing Devices in Patients with Nickel Allergies** *J.F. Baranoski, et al.*

INTERVENTIONAL

AJNR (Am J Neuroradiol ISSN 0195–6108) is a journal published monthly, owned and published by the American Society of Neuroradiology (ASNR), 820 Jorie Boulevard, Oak Brook, IL 60523. Annual dues for the ASNR include approximately 19% for a journal subscription. The journal is printed by Intellicor Communications, 330 Eden Road, Lancaster, PA 17601; Periodicals postage paid at Oak Brook, IL and additional mailing offices. Printed in the U.S.A. POSTMASTER: Please send address changes to American Journal of Neuroradiology, P.O. Box 3000, Denville, NJ 07834, U.S.A. Subscription rates: nonmember \$452 (\$530 foreign) print and online, \$320 online only; institutions \$520 (\$594 foreign) print and basic online, \$1029 (\$1103 foreign) print and extended online, \$380 online only (basic), \$825 online only (extended); single copies are \$35 each (\$40 foreign). Indexed by PubMed/MEDLINE, BIOSIS Previews, Current Contents (Clinical Medicine and Life Sciences), EMBASE, Google Scholar, HighWire Press, Q-Sensei, RefSeek, Science Citation Index, SCI Expanded, ReadCube, and Semantic Scholar. Copyright © American Society of Neuroradiology.

I am a global citizen.
I am patient-centered care.
I am committed to health equity.
I am a teacher.
I am a life-long learner.
I am determined.
I am curious.
I am a collaborative team player.
I am a volunteer.
I am ASNR.

Don't miss out on the tools, resources and relationships you've come to rely on. Log in and renew your ASNR membership today! www.asnr.org

- 943 Mapping of Anatomic Variants of the Proximal Vertebral Artery in Relation to Embryology *H.F. Bueno, et al.* EXTRACRANIAL VASCULAR
-  951 Reliable Initial Trauma CT Findings of Supraclavicular Brachial Plexus Injury in Patients Sustaining Blunt Injuries *M.R. Povlow, et al.* HEAD & NECK
-  959 Somatostatin Receptor–PET/CT/MRI of Head and Neck Neuroendocrine Tumors *J.N. Rini, et al.* HEAD & NECK
-   967 Glutaric Aciduria Type I: Comparison between Diffusional Kurtosis Imaging and Conventional MR Imaging *B. Bian, et al.* PEDIATRICS FUNCTIONAL
-    974 Epileptogenic Tubers Are Associated with Increased Kurtosis of Susceptibility Values: A Combined Quantitative Susceptibility Mapping and Stereoelectroencephalography Pilot Study *A. Chari, et al.* PEDIATRICS FUNCTIONAL
- 983 Posterior Fossa Horns in Hurler Syndrome: Prevalence and Regression *S. Huang, et al.* PEDIATRICS
-  987 Deep Learning–Generated Synthetic MR Imaging STIR Spine Images Are Superior in Image Quality and Diagnostically Equivalent to Conventional STIR: A Multicenter, Multireader Trial *L.N. Tanenbaum, et al.* SPINE
-  994 Resisted Inspiration Improves Visualization of CSF-Venous Fistulas in Spontaneous Intracranial Hypotension *P.G. Kranz, et al.* SPINE

ONLINE FEATURES

MEMORIAL

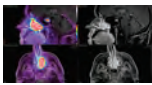
- E33 Professor Antonios Valavanis *I. Wanke, et al.*

LETTERS

- E35 Appreciation and Concerns Regarding the Published Study “CURES” *I. Arrese, et al.*
- E36 *Reply* *J. Raymond, et al.*
- E38 The Benefits of Ocular Ultrasound in Emergency Settings for the Evaluation of Orbital Compartment Syndrome *I. Mese, et al.*
- E40 *Reply* *C. Maier, et al.*

BOOK REVIEWS *R.M. Quencer, Section Editor*

Please visit www.ajnrblog.org to read and comment on Book Reviews.



Representative case of esthesioneuroblastoma demonstrating the ability of somatostatin receptor–PET/MRI to exquisitely delineate head and neck neuroendocrine tumor burden from Rini et al.

-  Indicates Editor's Choices selection
-  Indicates Fellows' Journal Club selection
-  Indicates open access to non-subscribers at www.ajnr.org
-  Indicates article with supplemental online data
-  Indicates article with supplemental online video
-  Evidence-Based Medicine Level 1
-  Evidence-Based Medicine Level 2

AJNR *go green*

***AJNR* urges American Society of Neuroradiology members to reduce their environmental footprint by voluntarily suspending their print subscription.**

The savings in paper, printing, transportation, and postage directly fund new electronic enhancements and expanded content.

The digital edition of *AJNR* presents the print version in its entirety, along with extra features including:

- Publication Preview
- Case Collection
- Podcasts
- The *AJNR* News Digest
- The *AJNR* Blog

It also reaches subscribers much faster than print. An electronic table of contents will be sent directly to your mailbox to notify you as soon as it publishes.

Readers can search, reference, and bookmark current and archived content 24 hours a day on www.ajnr.org.

ASNR members who wish to opt out of print can do so by using the *AJNR* Go Green link on the *AJNR* Website (<http://www.ajnr.org/content/subscriber-help-and-services>). Just type your name in the email form to stop print and spare our ecosystem.



The ASNR Career Center

The Go-To Job Site for Neuroradiology Employers and Job Seekers

For Job Seekers

- Access to an expanded network of jobs via the National Healthcare Career Network
- Confidential resume posting
- Professional online profile

For Employers

- Employer resources to help you recruit top talent
- Multiple pricing options, including free Fellowship listings
- Resume search

Start here: careers.asnr.org



JOIN US! COMPREHENSIVE NEURORADIOLOGY COURSE

February 1-3, 2024 • Cancun, Mexico / On-Demand

ASNR's Comprehensive Neuroradiology Course offers you three days of image-rich neuroradiology review focused on:

**Adult Brain Imaging | Head and Neck Imaging | Spine Imaging
Pediatric Neuroradiology | Advanced Imaging Techniques**

Join our award-winning faculty and engage in our interactive classroom environment, as well as during planned social and evening activities. Take advantage of a discounted, all-inclusive rate at the host hotel: the Hyatt Ziva Cancun!

Can't attend in person? An on-demand option is also available!

Get all of the details and register now at www.asnr.org/cnc24.

Meet the Faculty

Joshua Nickerson, MD

Division Chief of Neuroradiology, Associate Professor, Oregon Health & Science University

Tabassum Kennedy, MD

Division Chief of Neuroradiology, University of Wisconsin, Madison

Judith Gadde, DO, MBA

Pediatric Neuroradiologist and Director of Academic Innovation, Lurie Children's Hospital of Chicago

Mahmud Mossa-Basha, MD

Professor of Radiology, Vice Chair of Quality & Safety, and Medical Director of MRI, University of North Carolina School of Medicine

Wende Gibbs, MD, MA

Director of Spine Imaging and Intervention, Barrow Neurological Institute

Ashley Aiken, MD,

Director of Head and Neck Imaging and Professor of Radiology and Imaging Sciences, Emory University

Looking Back, Looking Forward

Dear Friends,

As the new Editor-in-Chief of the *American Journal of Neuroradiology (AJNR)*, I am committed to advancing the field of neuroradiology by providing all our readers with the most relevant and cutting-edge information relative to our discipline.

Looking back, the *AJNR* has been the leading neuroradiology publication for more than 40 years. Our journal has been instrumental in promoting excellence in research, education, and patient care. We have published research on a wide range of topics, from the latest imaging techniques to studies that address new clinical applications and relevant health policy issues. I am humbled by the work of our previous editorial teams, authors, and reviewers, who have made the *AJNR* the respected publication it is in the field of neuroradiology.

Looking forward, my priority as the new Editor-in-Chief is to continue this tradition of excellence and to build on the incredible legacy of the journal and the strengths of all the societies it represents: ASNR, ASFNR, ASHNR, ASPNR, and ASSR. I am

committed to ensuring that the *AJNR* remains at the forefront of neuroradiology education and research. Our journal will continue to provide high-quality, peer-reviewed articles that are relevant to patient care. As a global publication, the *AJNR* has a responsibility to serve the needs of neuroradiologists from around the world. I am committed to increasing our international reach and ensuring that the *AJNR* reflects the diverse perspectives of our readership.

I firmly believe that the *AJNR* should be the first journal selected to publish any neuroradiology article. Our commitment to providing the highest-quality research, promoting diversity and inclusion, and serving the needs of clinical neuroradiologists makes us the premier publication in our field.

In conclusion, I am honored to lead the *AJNR* and to work with our team to continue to advance neuroradiology through the publication of highly relevant articles. Together, we can make a meaningful difference in the lives of our patients and the communities we serve.

Sincerely,

M. Wintermark
Editor-in-Chief, American Journal of Neuroradiology

MR Imaging of Carotid Artery Atherosclerosis: Updated Evidence on High-Risk Plaque Features and Emerging Trends

J.C. Benson, L. Saba, G. Bathla, W. Brinjikji, V. Nardi, and G. Lanzino



ABSTRACT

SUMMARY: MR imaging is well-established as the criterion standard for carotid artery atherosclerosis imaging. The capability of MR imaging to differentiate numerous plaque components has been demonstrated, including those features that are associated with a high risk of sudden changes, thrombosis, or embolization. The field of carotid plaque MR imaging is constantly evolving, with continued insight into the imaging appearance and implications of various vulnerable plaque characteristics. This article will review the most up-to-date knowledge of these high-risk plaque features on MR imaging and will delve into 2 major emerging topics: the role of vulnerable plaques in cryptogenic strokes and the potential use of MR imaging to modify carotid endarterectomy treatment guidelines.

ABBREVIATIONS: CAS = carotid artery stent placement; CEA = carotid endarterectomy; ESUS = embolic stroke of undetermined source; HR = hazard ratio; IPH = intraplaque hemorrhage; K^{trans} = volume transfer constant; LRNC = lipid-rich necrotic core; QSM = quantitative susceptibility mapping; TRFC = thinning or rupture of the fibrous cap

Carotid artery atherosclerosis is a major contributor to ischemic strokes, responsible for up to 20% of strokes and TIAs.¹ Historically, carotid artery disease was classified on the basis of the degree to which a plaque narrowed an arterial lumen. However, it is now known that certain histologic characteristics make some plaques more susceptible than others to sudden symptomatic changes. Patients with these “vulnerable” plaque features have a 3 times higher incidence of ipsilateral neurologic ischemic events than those with stable plaques.²

The field of MR imaging of carotid artery atherosclerotic plaques continues to rapidly evolve. Thus, it is crucial that physicians keep up to date on the current applications of such imaging. This review will highlight the most recent developments in different types of high-risk plaque. It will also touch on 2 emerging topics: the use of carotid plaque imaging in the setting of cryptogenic strokes and how plaque imaging may influence future changes in treatment recommendations for carotid atherosclerosis.

Overview of MR Imaging of Carotid Plaque

MR imaging is the criterion standard for carotid artery plaque characterization and is best able to differentiate between “soft” plaque components, such as lipid material, and hemorrhage.³ However, variations in plaque imaging protocols exist, typically based on institutional preference. For example, some institutions elect not to use dedicated carotid surface coils, limiting the ability to evaluate the fibrous cap.⁴ In general, both pre- and postcontrast sequences are obtained without or with fat saturation.⁵ Many institutions now use 3D sequences (including 3D TOF, 3D MPRAGE, and 3D FSE; eg, sampling perfection with application-optimized contrasts by using different flip angle evolutions [SPACE sequence; Siemens] and/or Cube; GE Healthcare) to allow multiplanar reformatting.^{1,6}

Regardless of institutional preferences, consensus guidelines on MR imaging of plaque do exist. These include the use of 1.5T or 3T scanners, in-plane resolution of 0.6 mm, and effective blood suppression. At minimum, a plaque protocol should be able to identify intraplaque hemorrhage (IPH), lipid rich necrotic core (LRNC), degree of stenosis, fibrous cap condition (disruption and/or ulceration), and plaque burden and distribution.³

Updates on High-Risk Features

Numerous high-risk carotid artery plaque features have been extensively described. Each of these features increases the risk of a plaque being symptomatic, leading to future ischemic neurologic events or causing accelerated plaque growth. Here, we will review these one by one, with commentary on the histologic features, imaging appearance, and recent insights of each feature.

Received March 29, 2023; accepted after revision May 14.

From the Departments of Radiology (J.C.B., G.B., W.B.), Cardiovascular Medicine (V.N.), and Neurosurgery (G.L.), Mayo Clinic, Rochester, Minnesota; and Department of Medical Sciences (L.S.), University of Cagliari, Cagliari, Italy.

Please address correspondence to John C. Benson, MD, Department of Radiology, Mayo Clinic, 200 1st St SW, Rochester, MN 55902; e-mail: benson.john3@mayo.edu

Indicates open access to non-subscribers at www.ajnr.org

Indicates article with online supplemental data.

<http://dx.doi.org/10.3174/ajnr.A7921>

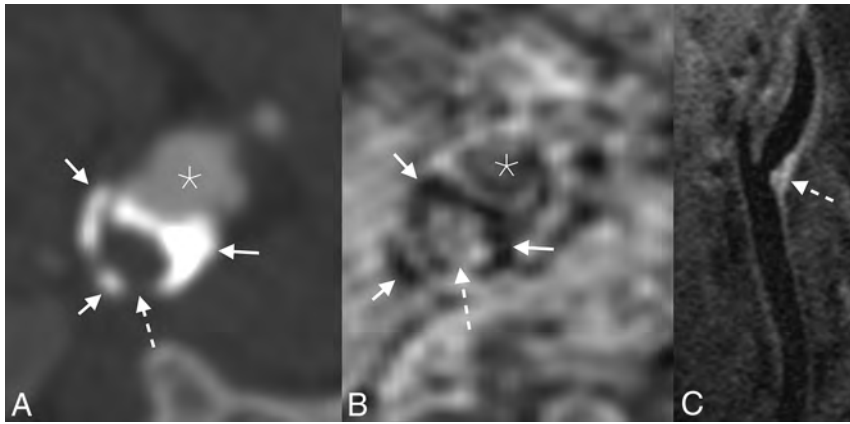


FIG 1. Example of an LRNC. Axial CTA image (A) demonstrates a peripherally calcified (*solid arrows*) plaque with a soft interior (*dashed arrow*). The corresponding axial-reformatted MPRAGE image (B) similarly demonstrates areas of calcifications with markedly low signal (*solid arrows*); the plaque interior lacks bright signal, ruling out hemorrhage (*dashed arrow*). T1 fat-saturated Cube image (C) shows hyperintense signal in the plaque interior (*dashed arrow*), compatible with an LRNC. Asterisks denote the vessel lumen.

Lipid-Rich Necrotic Core

An LRNC represents the earliest visible feature of vulnerable plaques. Atherosclerotic plaques begin as lipid streaks, in which lipid material deposits in the intima of arterial walls. Macrophages take up this lipid material, forming so-called “foam cells.” Excessive accumulation of such cells ultimately results in cell lysis and necrosis, leading to the formation of extracellular lipid pools, which eventually coalesce into an LRNC.⁷

On MR imaging, the LRNC tends to be mildly hypo- to mildly hyperintense to adjacent musculature on fat-suppressed T1-weighted images. LRNCs also lack markedly hyperintense signal on heavily T1-weighted images (namely MPRAGE images), signifying that superimposed plaque hemorrhage is absent (Fig 1). Specifically, LRNCs are slightly hypointense to adjacent muscle on MPRAGE images. Contrast-enhanced images can help distinguish an LRNC from the overlying fibrous cap; fibrous tissue enhances, while LRNCs do not.

In general, LRNC is less concerning than other high-risk plaque features. Nevertheless, LRNCs may be symptomatic. A 2020 meta-analysis, for example, found the hazard ratio (HR) of LRNC to be 2.73 (95% CI, 1.04–7.16) for recurrent stroke or TIA.⁸ In addition, LRNCs can increase in size or be precursors of higher-risk plaque features.⁹ Once a LRNC has formed, a plaque may become a higher grade, losing fibrous cap integrity or developing plaque hemorrhage or ulceration.

Treatment with high-intensity statins decreases the size of LRNCs, and this effect can be monitored in vivo using plaque imaging on MR imaging. The degree of expected lipid depletion is dependent on the duration of therapy. After 3 months, modest effects are typically observed.¹⁰ After 3 years, however, the LRNC volume and the percentage of overall plaque volume can decrease by as much as 50%.¹¹ This trend has been confirmed with a meta-analysis, in which no significant differences were found after 1–6 months or 7–12 months of therapy, but a significant decrease in LRNC volume was found after 1 year.¹²

Intraplaque Hemorrhage

IPH is thought to be caused by the breakdown of immature neovasculature, which commonly proliferates along the surface of a plaque. IPH remains the most validated imaging marker of a high-risk carotid artery plaque. It is a significant contributor to plaque growth, is associated with ipsilateral neurologic symptoms, and increases the risk of future strokes.

Historically, IPH was identifiable on T1-weighted MR images; hemorrhage was notably bright given the methemoglobin in the blood products. MPRAGE sequences were later developed to further highlight the T1 intensity within the IPH (Online Supplemental Data). More recently, some institutions have begun using simultaneous noncontrast angiography and intraplaque hemorrhage (SNAP) sequences, which provide high contrast between flowing blood and IPH.¹³

The association between IPH and ipsilateral neurologic ischemic events has been extensively documented.¹⁴ Recent studies have supported this evidence, with substantial HRs. A 2020 meta-analysis, for example, found the HR of IPH for recurrent stroke or TIA to be 7.14 (95% CI, 4.32–11.82).⁸ Another recent meta-analysis found that IPH increased the risk of ipsilateral stroke in both asymptomatic (HR = 7.9; 95% CI, 1.3–47.6) and symptomatic (HR = 10.2; 95% CI, 4.6–22.5) patients.¹⁵ Che et al¹⁶ found that IPH had a HR of 8.08 (95% CI, 3.65–17.91) for recurrent ischemic events. Some reports suggested that the brighter signal intensity in IPH was associated with increased ipsilateral ischemia.^{17,18} A more recent study, however, refuted these findings.¹⁹

More is now known about when to expect IPH: It is more common in older men, smokers, and patients with hyperlipidemia and hypertension.²⁰ IPH is also more common in the left-sided carotid arteries for reasons that remain unclear.²¹ Recent studies have confirmed such findings. van Dam-Nolen et al,²² in a cohort of patients with symptomatic plaques causing mild-to-moderate stenosis, found both the presence of IPH (HR = 2.12; 95% CI: 1.02–4.44) and total plaque volume (HR = 1.07; 95% CI, 1.00–1.15) to be associated with recurrent ipsilateral strokes.

In recent years, there has also been a better understanding that plaques with IPH are often symptomatic, even when nonstenotic. For example, Nardi et al²⁰ assessed a cohort of patients that had undergone carotid endarterectomy (CEA) for symptomatic carotid atherosclerosis, subdivided into patients with mild (<50%), moderate (50%–69%), and severe (\geq 70%) stenosis. The authors found that IPH was significantly more common in patients with mild stenosis (15.7%) than in those with moderate (3.9%) or severe (2.5%) stenosis. Another study found that IPH was associated with ipsilateral ischemia in patients with <30% stenosis (OR = 5.68; 95% CI, 1.49–21.69), but no such association was found in arteries with >30% stenosis.²³ Nevertheless, larger plaques are more likely to develop IPH: Increased stenosis is

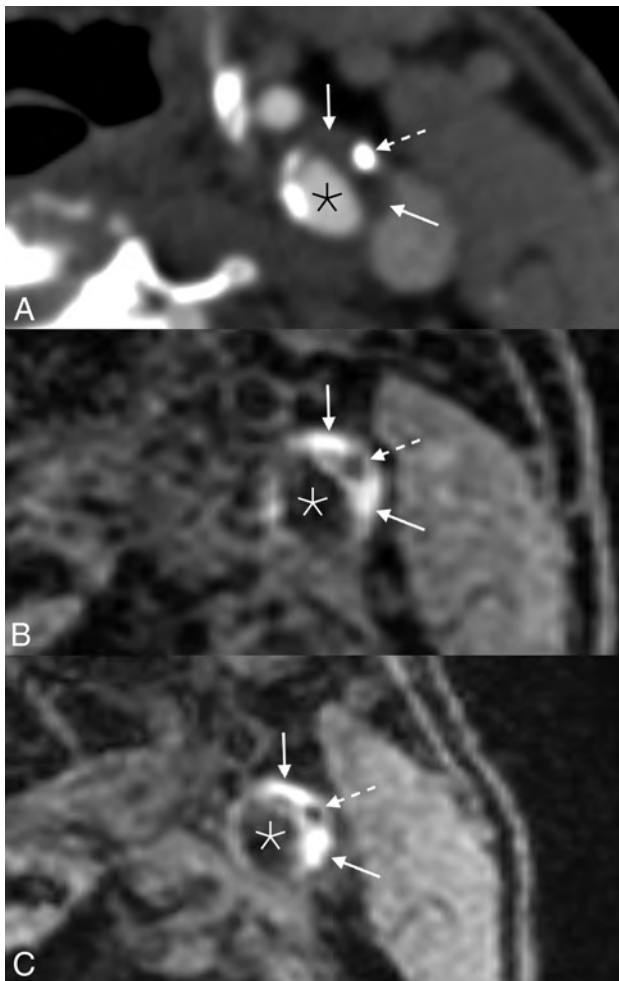


FIG 2. Example of persistent IPH in a 71-year-old man who presented with acute disorientation and unsteady gait. MR imaging of the brain at the time of admission (not shown) demonstrated multiple acute left cerebral infarcts. Axial CTA image (A) shows a mixed calcified (*dashed arrow*) and soft (*solid arrows*) plaque in the left ICA. Corresponding MPRAGE image (B) demonstrates IPH throughout the soft plaque components (*solid arrows*); the focal calcification is also noted (*dashed arrow*). The patient was started on dual antiplatelet therapy (aspirin and clopidogrel). One year later (C), the appearance of the IPH (*solid arrows*) and calcification (*dashed arrow*) was unchanged. Asterisks denote the vessel lumen.

independently associated with IPH on imaging (OR = 1.02; 95% CI, 1.01–1.03).²³

The signal related to IPH has drawn continued attention in studies across the years. In general, it seems increasingly clear that the MPRAGE signal related to IPH remains present on follow-up examinations in most patients. van den Bouwhuijsen et al,²⁴ for example, found that 94% of IPH remained present on subsequent examinations. Yamada et al,²⁵ similarly, found that 97% of plaques retained IPH on follow-up MRIs, with no significant change in volume noted with time (Fig 2). It is not clear why abnormal signal at the site of IPH persists across multiple examinations. Takaya et al²⁶ suggested that a relative lack of macrophages in a plaque would delay the degradation of blood products. Others believe that the signal reflects stagnant proteinaceous remnants of lytic blood and/or recurrent hemorrhage.²⁵ Signal characteristics on other sequences

may be used to determine the chronicity of blood products. Chu et al,²⁷ for example, found that chronic IPH was hypointense on T1WI, T2WI, and TOF. More recently, quantitative T1 mapping has been used to distinguish acute and chronic IPH, with moderate ($\kappa = 0.40$, $P = .028$) agreement in terms of imaging classification.²⁸

Finally, recent studies have sought to use quantitative susceptibility mapping (QSM) in carotid plaque imaging to better delineate IPH. QSM is able to differentiate between paramagnetic (eg, iron within hemoglobin) and diamagnetic (eg, calcium) materials.²⁹ Volumes of both IPH and calcification detected on QSM have already been shown to agree with findings on conventional plaque MRA techniques.³⁰ In addition, QSM may help distinguish IPH and LRNC, both of which are hyperintense on T1WI. Ikebe et al,³¹ for example, found that IPH had a significantly higher signal intensity than LRNC, while calcifications demonstrated expectedly low signal intensity.

Ulcerations

A plaque ulceration is a defect in the fibrous cap of a plaque, defined as being an indentation, erosion, or fissuring of the luminal surface of the plaque. These defects are due to weakening of the cap, often due to local inflammation or hemodynamic stress. The result is of substantial clinical concern: Ulcerations expose the inner plaque contents to the arterial blood. This exposure can both rapidly de-stabilize the plaque and allow plaque contents to embolize to the brain.

Although the description of ulceration on imaging varies among studies, most authors define an ulcer as a cavitation into a plaque measuring at least 1–2 mm (Online Supplemental Data).³² The prevalence of plaque ulceration in symptomatic patients is up to 27%. Larger and more stenotic plaques, plaques with higher volumes of LRNC and/or IPH, and plaques with loss of fibrous cap integrity are more likely to develop ulcerations.³³ Also, ulcerations are more likely to affect the portion of the plaque proximal to the region of maximum stenosis.³⁴

Historically, ulcerations have been considered one of the main sources of cerebral microemboli. Most recent studies have concurred with this concept, showing that ulcers increase the risk of ipsilateral neurologic ischemic events. A 2017 meta-analysis, for example, found ulcerations to be strongly associated with ipsilateral ischemia, with ORs ranging from 1.5 to 4.9.³⁵ A 2020 study found that patients with plaque ulceration had greater severity of ischemic strokes.³⁶

However, some recent data on the clinical importance of ulcerations have been contradictory. van Dam-Nolen et al,²² also using data from the Plaque At Risk (PARISK) study, found that the presence of plaque ulceration was not a determinant of stroke in symptomatic plaques with <70% stenosis. Fisher et al³⁷ found that the prevalence of ulceration was similar in plaques associated with ipsilateral and contralateral symptoms (34% and 42%, respectively). Nevertheless, the bulk of evidence supports the notion that ulcerated plaques are more likely to cause symptoms and increase a patient's risk of future strokes.

Loss of Fibrous Cap Integrity

Fibrous caps form early during atherosclerotic plaque development, in which smooth-muscle cells migrate toward the vessel

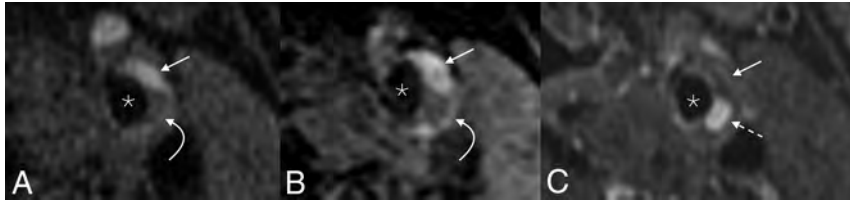


FIG 3. Example of pathologic plaque enhancement. Axial fat-saturated T1 Cube (A) and MPRAGE (B) images show a plaque in the left ICA, with both hemorrhagic (straight arrows) and nonhemorrhagic LRNC (curved arrows) regions. On the postgadolinium fat-saturated T1 Cube image (C), the LRNC component demonstrates marked enhancement (dashed arrow), while the hemorrhagic component does not (straight arrow). Asterisks denote the vessel lumen.

lumen. The cap is functionally protective: It separates the soft plaque components, eg, LRNC and IPH, from blood in the vessel lumen. A thick, well-formed cap can typically withstand pulsatile hemodynamic forces and is a marker of plaque stability, while a thinned or disrupted cap is a high-risk feature that portends future ischemic events. Specifically, cap disruption can lead to fissuring, ulceration, or rupture and can expose the thrombogenic components of a plaque to both platelets and coagulation factors in the bloodstream.

On MR imaging, a fibrous cap is located along the surface of a plaque and is typically hypointense on TOF images, isointense on T1 and T2, and enhances on postcontrast images. In general, assessment of the fibrous cap requires high-resolution carotid plaque surface coils; the accuracy of identifying the fibrous cap with a standard coil is limited.⁴ Even with high-resolution surface coil imaging, the fibrous cap can be difficult to accurately assess. On imaging, therefore, loss of cap integrity is often combined under the umbrella of thinning or rupture of the fibrous cap (TRFC).

TRFC has been repeatedly shown to be associated with neurologic ischemic events. Recent meta-analyses have confirmed these findings.³⁸ In addition, recent studies have assessed the significance of plaque surface irregularity without specifically looking at TRFC. Li et al,³⁹ for example, found that irregular surfaces were found in more than half of plaques and that irregularities were associated with LRNC and IPH, as well as subsequent vascular events (HR = 11.02; 95% CI, 2.65–45.85).

Plaque Enhancement

Unstable plaques are often characterized by inflammation and/or neoangiogenesis. These often coexist: Inflammatory cells are typically located near regions of fibrous cap disruption, where neovascularization also occurs. Histologic evidence of plaque inflammation—particularly greater numbers of macrophages—is associated with neurologic symptoms. For example, there is a direct correlation between the number of nonlacunar brain infarcts and the quantity of macrophages.⁴⁰

On imaging, both fibrous tissue (ie, the fibrous cap) and tissue near the vessel adventitial boundary typically demonstrate enhancement in all plaques. Necrotic tissue (ie, the LRNC) is usually nonenhancing. Enhancement superimposed over a LRNC is considered pathologic and a marker of plaque vulnerability (Fig 3).⁴¹ Millon et al⁴² specifically found central enhancement to be a marker of either plaque rupture or loose fibrosis.

Other authors have found that pathologic enhancement has been shown to represent either inflamed tissue or areas of neovascularization; thus, enhancement is often grouped together under the nomenclature of “plaque activity.”

Historically, studies have focused on establishing plaque enhancement as a high-risk, pathologic finding. It was shown to correspond to multiple histologic markers of vulnerability, including neovascularization, macrophages, and loose fibrosis.⁴² Enhancement is

also more common in symptomatic patients, while its absence is a negative predictor of cerebral ischemic events.⁴³

Recently, many studies have focused on the use of dynamic contrast-enhanced MR imaging to detect and characterize atherosclerotic neovascularization.⁴⁴ Dynamic contrast images allow the analysis of the intraplaque pharmacokinetic parameter, the volume transfer constant (K^{trans}), which is representative of microvascular density, permeability, and flow. Studies have shown, for instance, that K^{trans} is associated with plaque types on the basis of the American Heart Association classifications.⁴⁵ Nevertheless, K^{trans} remains an emerging research field and will need to be further refined before being regularly used in clinical practice.

Contrast enhancement in the adventitial layer of carotid plaque has also been associated with an increased risk of stroke. In a study of 58 patients with carotid atherosclerosis, Wasserman⁴⁶ found that patients with adventitial enhancement had a significantly higher rate of ipsilateral stroke. The presence of adventitial enhancement in carotid plaque may indicate the presence of inflammation or neovascularization, both of which have been linked to plaque instability and an increased risk of stroke. The ability to detect adventitial enhancement on contrast-enhanced MR imaging may thus provide an additional tool for identifying high-risk carotid plaques and guiding appropriate management strategies.

Calcifications

Calcifications are commonly observed in atherosclerotic plaques and are found in up to 90% of atheromas.⁴⁷ On MR imaging, calcifications are markedly hypointense on all sequences, sometimes described as being “jet black” in appearance (Online Supplemental Data). Unlike the previously described plaque components, calcifications are thought to have beneficial effects on atherosclerosis.⁴⁸ Hunt et al,⁴⁹ for example, found that patients with calcified atherosclerotic plaques were more likely to be asymptomatic ($P = .042$). Larger, bulky calcifications specifically are more likely to be found in asymptomatic patients.⁵⁰ Thus, plaque calcifications are a marker of plaque stability, representing a more quiescent, low-risk form of atherosclerosis.

Much of the recent data on this presumption have agreed with this hypothesis. The aforementioned PARISK study, for example, found no association between the proportion of calcification and the risk of stroke.²² A recent meta-analysis by Baradaran et al³⁵ found that the patients with calcified carotid plaques had a lower

incidence of stroke (OR = 0.5; 95% CI, 0.4–0.7). Zhang et al,⁵¹ in another meta-analysis, found calcified plaques to be much less likely to cause strokes than plaques with vulnerable features. Similarly, data from the Rotterdam Study found no association between carotid artery calcifications and stroke.⁵²

However, our understanding of this subject continues to evolve. Increasingly, it is thought that it is insufficient to characterize intraplaque calcifications solely on the basis of their binary presence or absence or total calcification volume.⁵³ Studies that use such simplified assessments failed to recognize the complex relationship between calcific and noncalcific components of atherosclerotic plaques. On CTA, for example, intraplaque calcifications have been categorized on the basis of their imaging appearances.⁵⁴ Using this classification, scattered microcalcifications can cause vulnerability by acting as an intraplaque stresser.⁵⁵ Moreover, the so-called rim sign, adventitial calcifications (<2-mm-thick) with a soft plaque component (≥ 2 mm), has been shown to be associated with intraplaque hemorrhage.^{56,57}

These classifications of intraplaque calcifications have not been validated on MR imaging and remain largely restricted to CT. Nevertheless, calcifications play a more nuanced role in atherosclerosis formation and stability than what was previously thought.

Emerging Trends

Many of the recent developments of carotid plaque imaging are beyond the scope of this review. However, there are 2 major emerging trends in MR imaging of carotid plaque that deserve specific review because they have the potential to substantially impact patient care: the role of vulnerable plaques in embolic strokes of undetermined source (ESUSs) and how MR imaging may influence treatment decisions. Here, we will give a brief review of these topics and discuss how recent literature may guide changes in diagnoses and/or treatment strategies.

ESUSs

ESUSs are defined as being embolic-type ischemic neurologic events in patients without a known etiology. On the basis of the definition established by the Trial of Org 10172 in Acute Stroke Treatment (TOAST),⁵⁸ “cryptogenic” strokes are restricted to patients with <50% stenosis of the ipsilateral carotid artery (ie, a “nonstenotic plaque”) who have no potential cardiogenic source of emboli and no other known stroke source. The terminology of such strokes varies. Some authors state that ESUSs constitute many of the so-called cryptogenic strokes, while others prefer that the term ESUSs replace the term “cryptogenic.”^{59,60} ESUSs account for 16%–25% of strokes, are prone to recurrence, and tend to occur in younger patients.⁵⁹

Increasingly, researchers believe that many ESUSs may originate from nonstenotic ipsilateral carotid plaques with vulnerable features. Coutinho et al⁶⁰ noted that large-but-nonstenotic plaques were significantly more common in the ipsilateral carotid arteries in patients with ESUSs. Subsequent studies supporting this theory have been primarily based on CTA-based trials. Data from both the Identifying New Approaches to Optimize Thrombus Characterization for Predicting Early Recanalization and Reperfusion With IV Alteplase and Other Treatments Using

Serial CT Angiography (INTERRSeCT) trial and the Systematic Evaluation of Patients Treated with Neurothrombectomy Devices for Acute Ischemic Stroke (STRATIS) registry, for example, found that nonstenotic plaques were significantly more common in the ipsilateral carotid artery compared with the contralateral side.^{61,62}

MR imaging data regarding plaque composition in the setting of ESUSs, however, remain sparse. Results from the Carotid Plaque Imaging in Acute Stroke (CAPIAS) study indicated that both a ruptured fibrous cap (HR = 4.91; 95% CI, 1.31–18.45) and IPH (HR = 4.37; 95% CI, 1.20–15.97) were associated with an increased risk of recurrent events in patients with ESUSs.⁶³ Other data from the same study found that high-risk plaque features were significantly more common in the artery ipsilateral to the infarcts compared with the contralateral artery (31% versus 12%, respectively).⁶⁴ Another study, by Larson et al,⁶⁵ found that patients with ESUSs and ipsilateral IPH had an annual rate of stroke recurrence of 9.5%; the rate was 2.5% in patients without IPH. Future studies, focusing on the MR imaging characteristics of plaques in patients with ESUSs should yield much more substantial data regarding the etiology of the strokes.

Carotid Plaque Composition and Treatment Guidelines

The decision regarding whether to perform a CEA is typically based on the degree of arterial stenosis and the risk of perioperative complications. Treatment guidelines are based on the results of the North American Symptomatic Carotid Endarterectomy Trial (NASCET) and the European Carotid Surgery Trial (ECST). By means of these studies, eligibility for CEA or stent placement in symptomatic patients depends on the severity of stenosis, with surgery not considered for patients with <50% stenosis.^{66,67} In the years that followed those trials, however, associations were found between the degree of stenosis and the presence of vulnerable plaque features.⁶⁸ Thus, the observed successes of the NASCET and ECST trials may have been partly due to treatment of high-risk plaques.

Because it is now known that many symptomatic plaques are nonstenotic by the NASCET criteria (Fig 4), there is a growing call for the modification of treatment guidelines. Specifically, many believe that imaging markers of plaque vulnerability should be considered in the determination of treatment eligibility. The most promising imaging features are IPH, ulceration, and maximum plaque thickness; LRNC, integrity of the fibrous cap, and some categories of intraplaque calcifications also have potential usefulness.⁵⁵

Early data suggest that CEA in patients with relatively small plaques is a viable option. Nardi et al⁶⁹ reported on a cohort of patients that underwent CEA for nonstenotic (<50%), symptomatic atherosclerotic plaques, 80% of which had IPH. The authors reported no intraoperative complications and an annualized rate of recurrent stroke after CEA of 1.5%. A systematic review of CEAs performed for nonstenotic carotid plaques found that patients had no recurrent ipsilateral ischemic events in any of the 138 studied patients (mean follow-up, 36 months).⁷⁰ Nevertheless, the issue remains hotly debated. Additional studies are still needed to assess the feasibility, safety, and clinical usefulness of performing CEAs on nonstenotic atherosclerotic lesions.



FIG 4. Example of a symptomatic nonstenotic plaque. Axial DWI (A and B) of the brain demonstrates multiple tiny acute infarcts in the right cerebral hemisphere (arrows). 3D reformatted gadolinium bolus image (C) demonstrates a nonstenotic plaque in the proximal right ICA (dashed oval). Axial CTA image (D) shows a soft, noncalcified plaque. On MRA, MPRAGE image (E) shows that most of this plaque is composed of hemorrhagic material (solid arrow), with a small hypointense component representing a nonhemorrhagic lipid necrotic core (dashed arrow). Pre- (F) and postcontrast (G) T1 Cube images demonstrate a LRNC (solid arrows). Asterisks denote the vessel lumen.

Carotid plaque MRA can also be used to guide the decision between CEA and carotid artery stent placement (CAS). Although this topic remains in the developing stage, the available data suggest that CEA should be preferred to CAS in the setting of vulnerable plaques because CAS can lead to a higher risk of periprocedural events, including cerebral embolism and restenosis.⁷¹⁻⁷³ A meta-analysis found that patients with IPH had higher composite outcomes of stroke, death, or myocardial infarction within 30 days of stent placement (8.1%) compared with those without IPH (2.1%) (OR = 4.45; 95% CI, 1.61-12.30; $P < .01$).⁷⁴

Finally, regarding medical management options, several recent trials have provided evidence strengthening conservative medical treatment of carotid disease, including the protective effects of high-dose statin therapy and anti-inflammatory therapy such as the interleukin-1 β innate immunity pathway.⁷⁵⁻⁷⁸ Recent meta-analyses provide evidence that atherosclerosis can be reversed with high-dose lipid-lowering therapy,⁷⁹ and high-dose statins may shift vulnerable plaque from high lipid content to a more stable calcified plaque.⁸⁰ Data from natural history studies suggest that IPH may override the beneficial effects of statin therapy, though the statin type and dose were neither randomized nor uniform.⁸¹ Currently, no prospective trials exist testing the hypothesis that the effects of IPH can be modified with very intensive lipid-lowering therapy.

Nevertheless, there is still a relative dearth of data on the topic of medical management for vulnerable carotid plaques, and definitive guidelines have yet to be established. Instead, many available conclusions have relied on expert opinion. For example, Holmes et al⁸² recommended that all patients with ESUSs should be treated with the same medications (high-dose statins and dual

antiplatelet therapy for 3 weeks and aspirin for a year) but that MRA should be used to determine further treatment pathways. Specifically, the authors opined that patients with IPH and/or ulceration and repeat strokes should be considered for CEA. Hackam,⁸³ similarly, opined that revascularization for treatment of asymptomatic carotid stenosis should be reserved for some patients with vulnerable plaques, but he did not distinguish between high- and low-risk plaques in his recommendations for medical management.

CONCLUSIONS

MR imaging of carotid artery atherosclerotic plaques is both complex and continually expanding. During recent years, there have been substantial advances in knowledge about many of the well-known plaque features, ranging from high-risk components such as IPH and TRFC to generally stabilizing features such as calcifications. As this field continues to expand, physicians will need to stay informed about how such imaging features may eventually impact management strategies and treatment guidelines.

Disclosure forms provided by the authors are available with the full text and PDF of this article at www.ajnr.org.

REFERENCES







1. Brinjikji W, Huston J, Rabinstein AA, et al. **Contemporary carotid imaging: from degree of stenosis to plaque vulnerability.** *J Neurosurg* 2016;124:27-42 CrossRef Medline
2. Kamtchum-Tatuene J, Wilman A, Saqqur M, et al. **Carotid plaque with high-risk features in embolic stroke of undetermined source: systematic review and meta-analysis.** *Stroke* 2020;51:311-14 CrossRef Medline

3. Saba L, Yuan C, Hatsukami TS, et al; Vessel Wall Imaging Study Group of the American Society of Neuroradiology. **Carotid artery wall imaging: perspective and guidelines from the ASNR Vessel Wall Imaging Study Group and Expert Consensus Recommendations of the American Society of Neuroradiology.** *AJNR Am J Neuroradiol* 2018;39:E9–31 CrossRef Medline
4. Brinjikji W, DeMarco JK, Shih R, et al. **Diagnostic accuracy of a clinical carotid plaque MR protocol using a neurovascular coil compared to a surface coil protocol.** *J Magn Reson Imaging* 2018;48:1264–72 CrossRef Medline
5. Fitzpatrick LA, Berkovitz N, Dos Santos MP, et al. **Vulnerable carotid plaque imaging and histopathology without a dedicated MRI receiver coil.** *Neuroradiol J* 2017;30:120–28 CrossRef Medline
6. Benson JC, Cheek H, Aubry MC, et al. **Cervical carotid plaque MRI: review of atherosclerosis imaging features and their histologic underpinnings.** *Clin Neuroradiol* 2021;31:295–306 CrossRef Medline
7. Gui Y, Zheng H, Cao RY. **Foam cells in atherosclerosis: novel insights into its origins, consequences, and molecular mechanisms.** *Front Cardiovasc Med* 2022;9:845942 CrossRef Medline
8. Deng F, Mu C, Yang L, et al. **Carotid plaque magnetic resonance imaging and recurrent stroke risk: a systematic review and meta-analysis.** *Medicine (Baltimore)* 2020;99:e19377 CrossRef Medline
9. Takaya N, Yuan C, Chu B, et al. **Association between carotid plaque characteristics and subsequent ischemic cerebrovascular events: a prospective assessment with MRI—initial results.** *Stroke* 2006;37:818–23 CrossRef Medline
10. Du R, Cai J, Zhao XQ, et al. **Early decrease in carotid plaque lipid content as assessed by magnetic resonance imaging during treatment of rosuvastatin.** *BMC Cardiovasc Disord* 2014;14:83 CrossRef Medline
11. Zhao XQ, Dong L, Hatsukami T, et al. **MR imaging of carotid plaque composition during lipid-lowering therapy: a prospective assessment of effect and time course.** *JACC Cardiovasc Imaging* 2011;4:977–86 CrossRef Medline
12. Brinjikji W, Lehman VT, Kallmes DF, et al. **The effects of statin therapy on carotid plaque composition and volume: a systematic review and meta-analysis.** *J Neuroradiol* 2017;44:234–40 CrossRef Medline
13. Wang J, Börnert P, Zhao H, et al. **Simultaneous noncontrast angiography and intraplaque hemorrhage (SNAP) imaging for carotid atherosclerotic disease evaluation.** *Magn Reson Med* 2013;69:337–45 CrossRef Medline
14. Geiger MA, Flumignan RL, Sobreira ML, et al. **Carotid plaque composition and the importance of non-invasive in imaging stroke prevention.** *Front Cardiovasc Med* 2022;9:885483 CrossRef Medline
15. Schindler A, Schinner R, Altaf N, et al. **Prediction of stroke risk by detection of hemorrhage in carotid plaques: meta-analysis of individual patient data.** *JACC Cardiovasc Imaging* 2020;13(2 Pt 1):395–406 CrossRef Medline
16. Che F, Mi D, Wang A, et al. **Extracranial carotid plaque hemorrhage predicts ipsilateral stroke recurrence in patients with carotid atherosclerosis: a study based on high-resolution vessel wall imaging MRI.** *BMC Neurol* 2022;22:237 CrossRef Medline
17. Wang X, Sun J, Zhao X, et al; CARE-II Study Investigators. **Ipsilateral plaques display higher T1 signals than contralateral plaques in recently symptomatic patients with bilateral carotid intraplaque hemorrhage.** *Atherosclerosis* 2017;257:78–85 CrossRef Medline
18. Yang D, Liu Y, Han Y, et al. **Signal of carotid intraplaque hemorrhage on MR T1-weighted imaging: association with acute cerebral infarct.** *AJNR Am J Neuroradiol* 2020;41:836–43 CrossRef Medline
19. Larson AS, Brinjikji W, Kroll NJ, et al. **Normalized intraplaque hemorrhage signal on MP-RAGE as a marker for acute ischemic neurological events.** *Neuroradiol J* 2022;35:112–18 CrossRef Medline
20. Nardi V, Benson J, Bois MC, et al. **Carotid plaques from symptomatic patients with mild stenosis is associated with intraplaque hemorrhage.** *Hypertens* 2022;79:271–82 CrossRef Medline
21. Larson AS, Brinjikji W, Savastano L, et al. **Left-sided carotid arteries have a higher prevalence of intraplaque hemorrhage than right-sided: an asymmetric conundrum.** *Neuroradiol J* 2020;33:494–500 CrossRef Medline
22. van Dam-Nolen DH, Truijman MT, van der Kolk AG, et al; PARISK Study Group. **Carotid plaque characteristics predict recurrent ischemic stroke and TIA: the PARISK (Plaque At RISK) study.** *JACC Cardiovasc Imaging* 2022;15:1715–26 CrossRef Medline
23. Larson AS, Brinjikji W, Savastano L, et al. **Carotid intraplaque hemorrhage and stenosis: at what stage of plaque progression does intraplaque hemorrhage occur, and when is it most likely to be associated with symptoms?** *AJNR Am J Neuroradiol* 2021;42:1285–90 CrossRef Medline
24. van den Bouwhuisen QJ, Selwaness M, Tang H, et al. **Change in carotid intraplaque hemorrhage in community-dwelling subjects: a follow-up study using serial MR imaging.** *Radiology* 2017;282:526–33 CrossRef Medline
25. Yamada N, Higashi M, Otsubo R, et al. **Association between signal hyperintensity on T1-weighted MR imaging of carotid plaques and ipsilateral ischemic events.** *AJNR Am J Neuroradiol* 2007;28:287–92 Medline
26. Takaya N, Yuan C, Chu B, et al. **Presence of intraplaque hemorrhage stimulates progression of carotid atherosclerotic plaques: a high-resolution magnetic resonance imaging study.** *Circulation* 2005;111:2768–75 CrossRef Medline
27. Chu B, Kampschulte A, Ferguson MS, et al. **Hemorrhage in the atherosclerotic carotid plaque: a high-resolution MRI study.** *Stroke* 2004;35:1079–84 CrossRef Medline
28. Qiao H, Li D, Cao J, et al. **Quantitative evaluation of carotid atherosclerotic vulnerable plaques using in vivo T1 mapping cardiovascular magnetic resonance: validation by histology.** *J Cardiovasc Magn Reson* 2020;22:38 CrossRef Medline
29. Ruetten PP, Cluroe AD, Usman A, et al. **Simultaneous MRI water-fat separation and quantitative susceptibility mapping of carotid artery plaque pre- and post-ultrasmall superparamagnetic iron oxide-uptake.** *Magn Reson Med* 2020;84:686–97 CrossRef Medline
30. Wang C, Zhang Y, Du J, et al. **Quantitative susceptibility mapping for characterization of intraplaque hemorrhage and calcification in carotid atherosclerotic disease.** *J Magn Reson Imaging* 2020;52:534–41 CrossRef Medline
31. Ikebe Y, Ishimaru H, Imai H, et al. **Quantitative susceptibility mapping for carotid atherosclerotic plaques: a pilot study.** *Magn Reson Med Sci* 2020;19:135–40 CrossRef Medline
32. Baradaran H, Gupta A. **Extracranial vascular disease: carotid stenosis and plaque imaging.** *Neuroimaging Clin N Am* 2021;31:157–66 CrossRef Medline
33. Dilba K, van Dam-Nolen DH, van Dijk AC, et al. **Plaque composition as a predictor of plaque ulceration in carotid artery atherosclerosis: the Plaque At RISK study.** *AJNR Am J Neuroradiol* 2021;42:144–51 CrossRef Medline
34. Rafailidis V, Chrysogonidis I, Tegos T, et al. **Imaging of the ulcerated carotid atherosclerotic plaque: a review of the literature.** *Insights Imaging* 2017;8:213–25 CrossRef Medline
35. Baradaran H, Al-Dasuqi K, Knight-Greenfield A, et al. **Association between carotid plaque features on CTA and cerebrovascular ischemia: a systematic review and meta-analysis.** *AJNR Am J Neuroradiol* 2017;38:2321–26 CrossRef Medline
36. Cao X, Yang Q, Tang Y, et al. **Normalized wall index, intraplaque hemorrhage and ulceration of carotid plaques correlate with the severity of ischemic stroke.** *Atherosclerosis* 2020;315:138–44 CrossRef Medline
37. Fisher M, Paganini-Hill A, Martin A, et al. **Carotid plaque pathology: thrombosis, ulceration, and stroke pathogenesis.** *Stroke* 2005;36:253–57 CrossRef Medline
38. Jiang B, He D, Zhang L, et al. **Risk prediction of cerebrovascular events with carotid plaque magnetic resonance analysis: a meta-analysis.** *J Neuroradiol* 2019;46:117–23 CrossRef Medline
39. Li J, Li D, Yang D, et al. **Irregularity of carotid plaque surface predicts subsequent vascular event: a MRI study.** *J Magn Reson Imaging* 2020;52:185–94 CrossRef Medline

40. Saba L, Lai L, Lucatelli P, et al. **Association between carotid artery plaque inflammation and brain MRI.** *J Neuroradiol* 2020;47:203–09 CrossRef Medline
41. Kerwin WS, Hatsukami T, Yuan C, et al. **MRI of carotid atherosclerosis.** *AJR Am J Roentgenol* 2013;200:W304–13 CrossRef Medline
42. Millon A, Boussel L, Brevet M, et al. **Clinical and histological significance of gadolinium enhancement in carotid atherosclerotic plaque.** *Stroke* 2012;43:3023–28 CrossRef Medline
43. Papini GD, Di Leo G, Bandirali M, et al. **Is carotid plaque contrast enhancement on MRI predictive for cerebral or cardiovascular events? A prospective cohort study.** *J Comput Assist Tomogr* 2017;41:321–26 CrossRef Medline
44. Cattaneo M, Sun J, Staub D, et al. **Imaging of carotid plaque neovascularization by contrast-enhanced ultrasound and dynamic contrast-enhanced magnetic resonance imaging.** *Cerebrovasc Dis* 2019;48:140–48 CrossRef Medline
45. Ge X, Zhou Z, Zhao H, et al. **Evaluation of carotid plaque vulnerability in vivo: correlation between dynamic contrast-enhanced MRI and MRI-modified AHA classification.** *J Magn Reson Imaging* 2017;46:870–76 CrossRef Medline
46. Wasserman BA. **Advanced contrast-enhanced MRI for looking beyond the lumen to predict stroke: building a risk profile for carotid plaque.** *Stroke* 2010;41:S12–16 CrossRef Medline
47. Ahmed M, McPherson R, Abruzzo A, et al. **Carotid artery calcification: what we know so far.** *Cureus* 2021;13:e18938 CrossRef Medline
48. Kwee RM. **Systematic review on the association between calcification in carotid plaques and clinical ischemic symptoms.** *J Vasc Surg* 2010;51:1015–25 CrossRef Medline
49. Hunt JL, Fairman R, Mitchell ME, et al. **Bone formation in carotid plaques: a clinicopathological study.** *Stroke* 2002;33:1214–19 CrossRef Medline
50. Shi X, Gao J, Lv Q, et al. **Calcification in atherosclerotic plaque vulnerability: friend or foe?** *Front Physiol* 2020;11:56 CrossRef Medline
51. Zhang Y, Bai Y, Xie J, et al. **Carotid plaque components and other carotid artery features associated with risk of stroke: a systematic review and meta-analysis.** *J Stroke Cerebrovasc Dis* 2022;31:106857 CrossRef Medline
52. Bos D, Arshi B, van den Bouwhuijsen QJ, et al. **Atherosclerotic carotid plaque composition and incident stroke and coronary events.** *J Am Coll Cardiol* 2021;77:1426–35 CrossRef Medline
53. Saba L, Nardi V, Cau R, et al. **Carotid artery plaque calcifications: lessons from histopathology to diagnostic imaging.** *Stroke* 2022;53:290–97 CrossRef Medline
54. Saba L, Chen H, Cau R, et al. **Impact analysis of different CT configurations of carotid artery plaque calcifications on cerebrovascular events.** *AJNR Am J Neuroradiol* 2022;43:272–79 CrossRef Medline
55. Bos D, van Dam-Nolen DH, Gupta A, et al. **Advances in multimodality carotid plaque imaging: AJR Expert Panel Narrative Review.** *AJR Am J Roentgenol* 2021;217:16–26 CrossRef Medline
56. Benson JC, Nardi V, Madhavan AA, et al. **Reassessing the carotid artery plaque “rim sign” on CTA: a new analysis with histopathologic confirmation.** *AJNR Am J Neuroradiol* 2022;43:429–34 CrossRef Medline
57. Eisenmenger LB, Aldred BW, Kim SE, et al. **Prediction of carotid intraplaque hemorrhage using adventitial calcification and plaque thickness on CTA.** *AJNR Am J Neuroradiol* 2016;37:1496–503 CrossRef Medline
58. Adams HP, Bendixen BH, Kappelle LJ, et al. **Classification of subtype of acute ischemic stroke: definitions for use in a multicenter clinical trial. TOAST—Trial of Org 10172 in Acute Stroke Treatment.** *Stroke* 1993;24:35–41 CrossRef Medline
59. Hart RG, Diener HC, Couotts SB, et al; Cryptogenic Stroke/ESUS International Working Group. **Embolic strokes of undetermined source: the case for a new clinical construct.** *Lancet Neurol* 2014;13:429–38 CrossRef Medline
60. Coutinho JM, Derkatch S, Potvin ARJ, et al. **Nonstenotic carotid plaque on CT angiography in patients with cryptogenic stroke.** *Neurology* 2016;87:665–72 CrossRef Medline
61. Ospel JM, Singh N, Marko M, et al. **Prevalence of ipsilateral nonstenotic carotid plaques on computed tomography angiography in embolic stroke of undetermined source.** *Stroke* 2020;51:1743–49 CrossRef Medline
62. Singh N, Ospel J, Mayank A, et al; STRATIS Investigators. **Nonstenotic carotid plaques in ischemic stroke: analysis of the STRATIS Registry.** *AJNR Am J Neuroradiol* 2021;42:1645–52 CrossRef Medline
63. Kopczak A, Schindler A, Sepp D, et al. **Complicated carotid artery plaques and risk of recurrent ischemic stroke or TIA.** *J Am Coll Cardiol* 2022;79:2189–99 CrossRef Medline
64. Kopczak A, Schindler A, Bayer-Karpinska A, et al. **Complicated carotid artery plaques as a cause of cryptogenic stroke.** *J Am Coll Cardiol* 2020;76:2212–22 CrossRef Medline
65. Larson AS, Nasr DM, Rizvi A, et al. **Embolic stroke of undetermined source: the association with carotid intraplaque hemorrhage.** *JACC Cardiovasc Imaging* 2021;14:506–08 CrossRef Medline
66. Chaturvedi S, Bruno A, Feasby T, et al; Therapeutics and Technology Assessment Subcommittee of the American Academy of Neurology. **Carotid endarterectomy—an evidence-based review: report of the Therapeutics and Technology Assessment Subcommittee of the American Academy of Neurology.** *Neurology* 2005;65:794–801 CrossRef Medline
67. **Randomised trial of endarterectomy for recently symptomatic carotid stenosis: final results of the MRC European Carotid Surgery Trial (ECST).** *Lancet* 1998;351:1379–87 CrossRef Medline
68. Barnett HJ, Taylor DW, Haynes RB, et al; North American Symptomatic Carotid Endarterectomy Trial Collaborators. **Beneficial effect of carotid endarterectomy in symptomatic patients with high-grade carotid stenosis.** *N Engl J Med* 1991;325:445–53 CrossRef Medline
69. Nardi V, Benson JC, Larson AS, et al. **Carotid artery endarterectomy in patients with symptomatic non-stenotic carotid artery disease.** *Stroke Vasc Neurol* 2022;7:251–57 CrossRef Medline
70. Larson A, Nardi V, Brinjikji W, et al. **Endarterectomy for symptomatic non-stenotic carotids: a systematic review and descriptive analysis.** *Stroke Vasc Neurol* 2022;7:6–12 CrossRef Medline
71. Tokunaga K, Tokunaga S, Hara K, et al. **Intraplaque high-intensity signal on time-of-flight magnetic resonance angiography and restenosis after carotid artery stenting.** *J Neurosurg* 2022;136:1029–34 CrossRef Medline
72. Yoshimura S, Yamada K, Kawasaki M, et al. **High-intensity signal on time-of-flight magnetic resonance angiography indicates carotid plaques at high risk for cerebral embolism during stenting.** *Stroke* 2011;42:3132–37 CrossRef Medline
73. Yoshimura S, Yamada K, Kawasaki M, et al. **Selection of carotid artery stenting or endarterectomy based on magnetic resonance plaque imaging reduced periprocedural adverse events.** *J Stroke Cerebrovasc Dis* 2013;22:1082–87 CrossRef Medline
74. Brinjikji W, Lehman VT, Huston J, et al. **The association between carotid intraplaque hemorrhage and outcomes of carotid stenting: a systematic review and meta-analysis.** *J Neurointerv Surg* 2017;9:837–42 CrossRef Medline
75. Naylor AR. **Time to rethink management strategies in asymptomatic carotid artery disease.** *Nat Rev Cardiol* 2012;9:116–24 CrossRef Medline
76. Ridker PM, Everett BM, Thuren T, et al; CANTOS Trial Group. **Antiinflammatory therapy with canakinumab for atherosclerotic disease.** *N Engl J Med* 2017;377:1119–31 CrossRef Medline
77. Abbott AL. **Medical (nonsurgical) intervention alone is now best for prevention of stroke associated with asymptomatic severe carotid stenosis: results of a systematic review and analysis.** *Stroke* 2009;40:e573–83 CrossRef Medline
78. Naylor AR, Gaines PA, Rothwell PM. **Who benefits most from intervention for asymptomatic carotid stenosis: patients or professionals?** *Eur J Vasc Endovasc Surg* 2009;37:625–32 CrossRef Medline
79. Ibrahimi P, Jashari F, Bajraktari G, et al. **Ultrasound assessment of carotid plaque echogenicity response to statin therapy: a systematic review and meta-analysis.** *Int J Mol Sci* 2015;16:10734–47 CrossRef Medline

80. Mujaj B, Bos D, Selwaness M, et al. **Statin use is associated with carotid plaque composition: the Rotterdam Study.** *Int J Cardiol* 2018;260:213–18 CrossRef Medline
81. Underhill HR, Yuan C, Yarnykh VL, et al. **Arterial remodeling in the subclinical carotid artery disease.** *JACC Cardiovasc Imaging* 2009;2:1381–89 CrossRef Medline
82. Holmes DR, Alkhouli MA, Klaas JP, et al. **Change of heart: the underexplored role of plaque hemorrhage in the evaluation of stroke of undetermined etiology.** *J Am Heart Assoc* 2022;11:e025323 CrossRef Medline
83. Hackam DG. **Optimal medical management of asymptomatic carotid stenosis.** *Stroke* 2021;52:2191–98 CrossRef Medline

Ecchordosis Physaliphora: Does It Even Exist?

 A.R. Stevens,  B.F. Branstetter IV,  P. Gardner,  T.M. Pearce,  G.A. Zenonos, and  K. Arani



ABSTRACT

SUMMARY: The term ecchordosis physaliphora (EP) has been used historically to describe a benign notochordal remnant with no growth potential, most commonly occurring in the central clivus. Unfortunately, the radiologic appearance of EP overlaps considerably with the appearance of low-grade chordomas, which do have the potential for growth. In this article, we review new pathologic terminology that better describes this family of diseases, and we propose new radiologic terms that better address the uncertainty of the radiologic diagnosis. The surgical importance of accurate terminology and the implications for patient care are discussed.

ABBREVIATIONS: BNCT = benign notochordal cell tumor; EP = ecchordosis physaliphora

Ecchordosis physaliphora (EP) is a term that has been traditionally used for a notochordal remnant that arises from ectopic rests, most commonly at the sphenoid-occipital synchondrosis of the clivus. It is characterized by a low proliferative index, a lack of bony invasion, small size, and no clinical symptoms.¹ It is usually discovered incidentally on neuroimaging performed for other reasons. Since the establishment of the defining histopathologic criteria, the pathology nomenclature has been revised from EP to benign notochordal cell tumor (BNCT).² Unfortunately, the radiologic and pathologic features of BNCT overlap those of clival chordoma, the malignant counterpart of EP, which similarly derives from notochordal remnants.³ Although attempts have been made to differentiate EP from chordoma, no definitive radiographic parameters have been validated. Furthermore, histologic features of these entities overlap and can be subjective in borderline cases. Therefore, we suggest that radiologists abandon the potentially misleading term EP in favor of the more modern terminology. Notochordal remnants are best understood as a spectrum of disease ranging from benign to low-grade to frankly malignant.

Case Presentation

A previously healthy 16-year-old girl underwent MR imaging for headaches. The examination findings were normal except for a

well-defined 5-mm T2-hyperintense prepontine mass with a dark rim and clival extension (Fig 1). A CT was performed for further characterization, showing a well-defined sclerotic margin to the clival component. There was no associated enhancement or mass effect. The interpreting radiologist stated that the lesion presumably represents ecchordosis physaliphora, and long-interval follow-up imaging was recommended.

The patient returned 4 years later with recurrent headaches and again underwent MR imaging (Fig 2). The lesion had marginally enlarged but retained all of its benign features. Because of the change in size, the neurosurgery team advised resection, and the patient agreed. The resection was accomplished with an endoscopic endonasal transclival resection.⁴ Histopathologic analysis (Fig 3) revealed a neoplasm composed of cells with multivacuolated (physaliphorous)-to-eosinophilic cytoplasm embedded in a myxoid background, with a chronic lymphocytic inflammatory infiltrate seen in fibrous septa separating the lobules of the tumor. There was a variable degree of nuclear enlargement, hyperchromasia, and nuclear membrane irregularities. Mitotic activity was sparse, and the Ki-67 proliferation index was very low (<1%), indicating indolent or benign disease. However, no amplification of 1p36 or 9p21 was detected with fluorescence in situ hybridization, so the tumor could not be classified as having minimal risk. Lobules of the tumor were identified intradurally as well as extending into the clivus, indicating some degree of aggressive features. Immunohistochemical staining for Brachyury showed strong, diffuse nuclear staining, confirming notochordal origin. When all of the histopathologic, genetic, and fluorescence stain data were taken into consideration, a diagnosis of low-grade chordoma was made, with a description of the relatively bland histologic features displayed by the tumor. Follow-up MR imaging 6 months later revealed no evidence of residual disease.

Received January 9, 2023; accepted after revision June 8.

From the Lake Erie College of Osteopathic Medicine (A.R.S.), Erie, Pennsylvania; and Departments of Radiology (B.F.B., K.A.), Otolaryngology (B.F.B.), Neurosurgery (P.G., G.A.Z.), and Pathology (T.M.P.), University of Pittsburgh School of Medicine, Pittsburgh, Pennsylvania.

Please address correspondence to Barton F. Branstetter IV, MD, University of Pittsburgh Medical Center, 200 Lothrop St, Pittsburgh, PA 15213; e-mail: BFB1@pitt.edu; @CharBranstetter

<http://dx.doi.org/10.3174/ajnr.A7932>

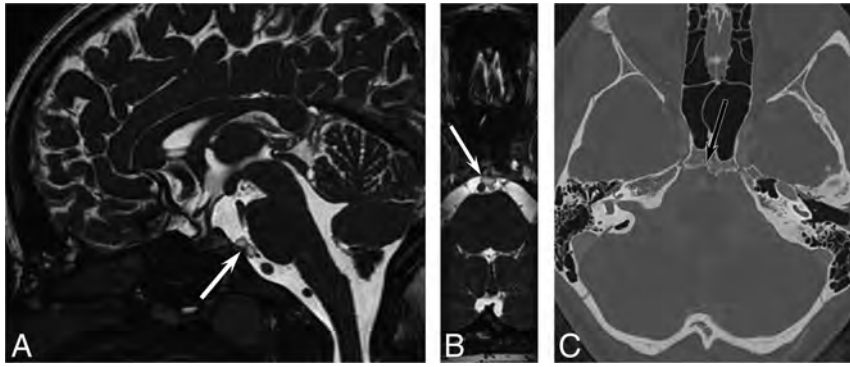


FIG 1. A 16-year-old girl with headaches. A, Sagittal steady-state free precession MR imaging shows a lobular, well-defined T2-hyperintense lesion (arrow) in the prepontine cistern. Axial reformatted image (B) shows a benign-appearing abutment to the clivus. Axial CT (C) shows slight remodeling of the posterior clivus without erosion.

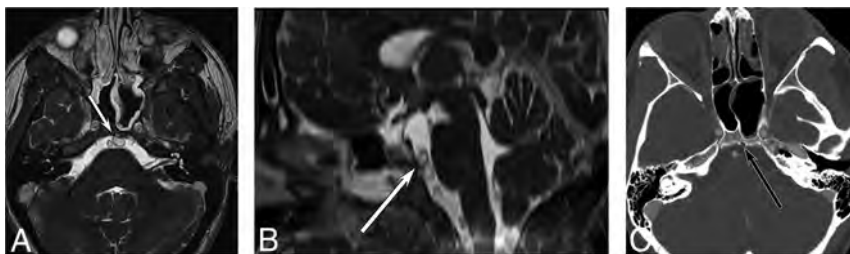


FIG 2. Follow-up imaging 4 years later. Axial steady-state free precession MR imaging (A) shows increased lesion size (arrow) with new involvement of the clivus. Sagittal reformat (B) shows increased superior-inferior extent. The clival involvement is confirmed on axial contrast-enhanced CT (C).

On a follow-up visit, the patient asked whether the lesion should have been resected when she first presented at age 16 and, in particular, whether the extent of surgery would have been less at that time.

Notochordal Embryology

Notogenesis is the formation of the embryologic notochord from precursor epiblasts during the third week of fetal development. The notochord initiates the process of neurulation, which results in the development of the CNS. On the formation of the brain and spine, the notochord regresses into the nucleus pulposus. Incomplete regression can result in persistence of isolated notochordal remnants, which are a potential source of neoplastic disease. Notochordal remnants usually remain near the midline, with a predilection for the sacrococcygeal region and the sphenoid-occipital synchondrosis.⁵⁻⁷ Both benign entities (BNCT) and malignant entities (chordoma) can occur in these locations, presumably originating from these remnants.

EP/BNCT

BNCTs (a term that encompasses both extraosseous lesions [EP] as well as intraosseous notochordal remnants) are typically asymptomatic, so the lesions are often discovered incidentally when imaging for other reasons. A radiologic hallmark of BNCT that can be detected on CT or MR imaging is a small bony stalk or pedicle projecting

from the basal portion of the clivus.⁸ Like other radiologic features, however, this parameter may only be used to suggest BNCT over other retroclival pathologies such as epidermoid or neuroenteric cysts.⁹ Other nonspecific MR imaging findings include T1-hypointensity, T2-hyperintensity, lack of gadolinium enhancement, and lack of bony erosion.¹⁰ A diagnosis of BNCT is often made presumptively on imaging without histopathologic proof, because excisional biopsy is considered overly invasive for a benign disease.

Histologically, BNCTs display sheets of physaliphorous cells, which are characterized by mucin-containing intracytoplasmic vacuoles and lack lobular architecture, fibrous septa, necrosis, and nuclear atypia that characterize chordomas. The lesions are often hypocellular, have bland nuclear features, and lack mitoses. BNCTs also have a low Ki-67 proliferation index, indicating low growth potential.^{11,12} However, there can be substantial overlap in the histology and immunophenotype of BNCT and chordoma, and the architectural features that help distinguish these entities may be difficult to appreciate on surgical samples of small lesions. Similar challenges can arise in distinguishing a BNCT from a chordoma in the lumbosacral spine, and the term “atypical notochordal cell tumor” has been recently proposed for cases that defy definitive classification.¹³

Chordoma

Chordomas are typically locally invasive, aggressive tumors that are presumed to arise from persistent notochordal cells. They can arise anywhere along the craniospinal axis, with a predilection for the base of the skull and sacrococcygeal region. Histologically, conventional chordomas are composed of the same physaliphorous cells seen in benign notochordal cell tumors, along with eosinophilic cytoplasm and intracytoplasmic vacuoles.¹⁴ Interspersed within the physaliphorous cells are variable amounts of myxoid material, which results in variable imaging characteristics for this tumor.¹⁵ The tumors typically have a capsule and grow in lobules separated by fibrous septa, often accompanied by an inflammatory infiltrate. The degree of nuclear pleomorphism and mitotic activity is highly variable, with conventional chordomas ranging from histologically bland tumors with mild nuclear atypia, sparse mitotic activity, and low proliferative activity, up to more overtly atypical, highly proliferative lesions. Poorly-differentiated chordomas are defined by loss of nuclear *INI-1* (*SMARCB1*) expression and often have increased cellularity and mitotic activity. A dedifferentiated chordoma consists of a frankly sarcomatous component juxtaposed with conventional chordomas. Poorly differentiated and dedifferentiated chordomas are quite rare, with

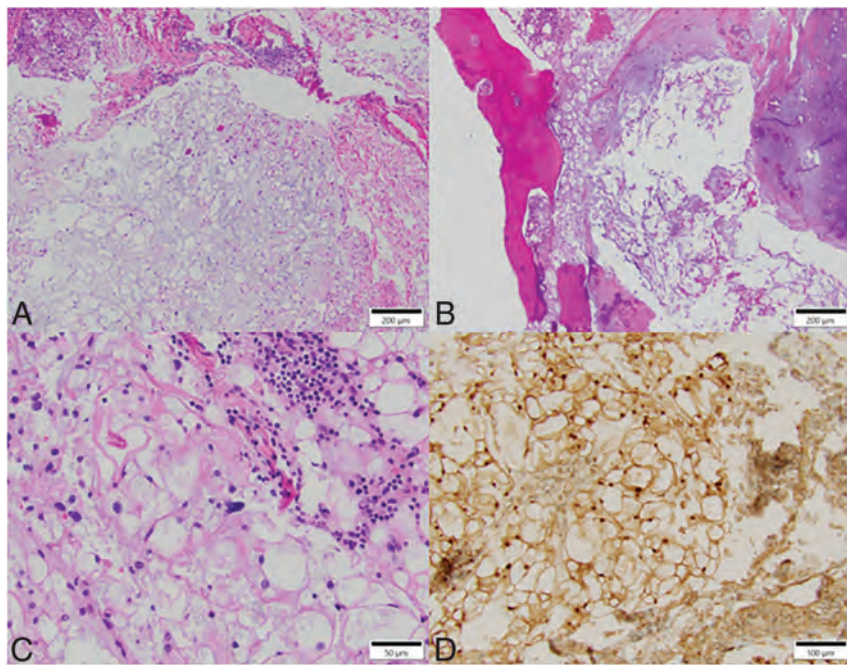


FIG 3. H&E-stained sections demonstrate a lobulated neoplasm composed of predominantly physaliphorous cells in a myxoid extracellular matrix, with a chronic inflammatory infiltrate centered in the fibrous septa (A) and extending to involve clival bone (B). Higher-power view shows cells with nuclear enlargement and atypia (C). An immunohistochemical stain for Brachyury shows strong diffuse nuclear staining in tumor cells (D).

conventional chordomas (including the chondroid subtype) accounting for ~95% of all tumors. Within conventional chordomas, histologic grading criteria to stratify tumor behavior do not exist, though molecular panels to improve prognostication have been recently developed.^{16,17} By definition, chordomas are considered malignant and are thus capable of locally destructive behavior and metastasis.¹⁸

The radiologic appearance of conventional chordoma depends on location, aggressivity, and molecular makeup. On MR imaging, chordomas are typically lobular, septate, and heterogeneous, showing hypointensity on T1-weighted images (but frequently containing high-signal foci) and hyperintensity on T2-weighted images. Enhancement after gadolinium administration is also heterogeneous and often septal, with myxoid areas enhancing poorly.¹⁹

Due to the infiltrative nature of these tumors, they often present clinically with pain and site-related neurologic symptoms. Cranial and skull base chordomas may present with headache or cranial nerve dysfunction. The most frequently affected cranial nerve is the abducens nerve (CN VI) because it is exposed to clival tumors while traveling through the Dorello canal along the posterior clivus in the clival venous plexus.²⁰ In rare cases, clival chordomas can present with rhinorrhea due to CSF leak.²¹ Craniocervical and cervical chordomas tend to present with nonspecific neck and upper-extremity pain. Dysphagia may be present due to mass effect. Thoracic, lumbar, and sacral chordomas tend to present with nonspecific dull pain.²²

Although chordomas have a slow rate of progression, they are associated with substantial morbidity from mass effect.²³ If a biopsy confirms the diagnosis of chordoma, en bloc resection

with wide margins is performed.²⁴ Chordomas have a high rate of recurrence, so adjuvant radiation and yearly MR imaging surveillance are often recommended.²⁵

Recent data suggest that homozygous 9p21 deletions (*p176/CDKN2A*) and 1p36 deletions can further risk-stratify chordomas, even within the “conventional chordoma” category, and are predictive of progression-free survival.^{16,17} These markers were also found to be relevant to seeding.²⁶ Depending on the prevalence of these deletions within the tumor cells, skull base chordomas can be further classified into an indolent group A, a highly aggressive group C, and an intermediate group B. According to this data set, radiation therapy did not confer any benefit after complete resections in groups A and B.¹⁷ Tumors in group A were more likely to be found in younger patients, were smaller, and were more likely to be asymptomatic on presentation. This group may encompass cases that would more accurately be described as EP or BNCT. Whether circulating tumor

DNA would have a role in differentiating EP/BNCT from chordomas remains to be determined.²⁷

Spectrum of Disease

Unfortunately, low-grade chordomas may have imaging features that overlap with the classic imaging appearance of BNCT. Imaging differentiation relies on sequential imaging, with BNCT remaining stable indefinitely and low-grade chordoma slowly enlarging. However, there is no established minimum rate of growth that indicates chordoma. Thus, it is difficult to recommend imaging intervals that would properly assess growth rates of a tumor with uncertain malignant potential. Furthermore, there are cases of presumed BNCTs that, on later excisional biopsy, are better classified as chordomas (as exemplified in the above case presentation). Several cases of BNCT have been published that displayed atypical characteristics, with resemblance to chordomas clinically or radiologically.²⁸⁻³⁰ Similarly, there are documented cases of chordoma that display a low proliferative index, a diameter of <2 cm, and a lack of any clinical symptoms, with detection occurring only incidentally.^{3,31-33}

Given the overlap in clinical, radiologic, and histopathologic findings for EP/BNCT and low-grade chordoma, the distinction between these entities may be arbitrary. Until histopathologic analysis is completed, radiologically characteristic lesions in typical locations are best described as “benign-appearing notochordal lesions,” to avoid ascribing expected behavior before repeat imaging. Repeat imaging, first after 6 months, then with larger intervals (doubling each time) as stability is established, is a more clinically relevant method for evaluating the malignant potential of these lesions and will allow more nuanced prognostic

Considerations for excisional biopsy of benign-appearing notochordal lesions

Considerations
Tumor size: >3 cm
Tumor margins: local invasion
Rate of growth: any appreciable growth on MR imaging
Radiology: bony erosion, enhancement
Patient age: <30 years
Surgical candidacy: lack of comorbidities
Symptoms: headache attributable to central skull base; cranial neuropathy
Patient preference

discussions with patients. Although many of these tumors will never require surgical intervention, a patient-centered approach can be used that factors in patient age, the presence of attributable symptoms, rate of tumor growth, changes in imaging characteristics, and patient preferences (Table). The potential for malignant transformation of benign lesions should be considered, and continued imaging surveillance should be pursued even in cases that do not demonstrate appreciable growth or development of symptoms. More research is needed to establish evidence-based criteria for surgical intervention.

CONCLUSIONS

The classic dichotomy of a benign notochordal remnant (ecchordosis physaliphora) and a malignant notochordal tumor (chordoma) is outdated. Notochordal lesions fall on a spectrum of disease from completely benign to aggressively malignant. Although aggressive disease can be identified radiologically, low-grade malignancies cannot be reliably distinguished from benign disease, and even benign disease has the occasional potential for malignant transformation. Repeat imaging, beginning at a 6-month interval, is recommended even for lesions that appear completely benign on MR imaging. The term benign-appearing notochordal lesion is a more accurate descriptive term that does not make undue assumptions about the clinical behavior of incidentally discovered lesions in the central clivus and skull base.

Disclosure forms provided by the authors are available with the full text and PDF of this article at www.ajnr.org.

REFERENCES

1. Park HH, Lee KS, Ahn SJ, et al. **Ecchordosis physaliphora: typical and atypical radiologic features.** *Neurosurg Rev* 2017;40:87–94 CrossRef Medline
2. Yamaguchi T, Suzuki S, Ishiwa H, et al. **Benign notochordal cell tumors: a comparative histological study of benign notochordal cell tumors, classic chordomas, and notochordal vestiges of fetal intervertebral discs.** *Am J Surg Pathol* 2004;28:756–61 CrossRef Medline
3. Rodriguez L, Colina J, Lopez J, et al. **Intradural prepontine growth: giant ecchordosis physaliphora or extraosseous chordoma?** *Neuropathology* 1999;19:336–40 CrossRef
4. Stippler M, Gardner PA, Snyderman CH, et al. **Endoscopic endonasal approach for clival chordomas.** *Neurosurgery* 2009;64:268–77; discussion 277–78 CrossRef Medline
5. de Bree K, de Bakker BS, Oostra RJ. **The development of the human notochord.** *PLoS One* 2018;13:e0205752 CrossRef Medline
6. Ramesh T, Nagula SV, Tardieu GG, et al. **Update on the notochord including its embryology, molecular development, and pathology: a primer for the clinician.** *Cureus* 2017;9:e1137 CrossRef Medline
7. Lawson L, Harfe BD. **Notochord to nucleus pulposus transition.** *Curr Osteoporos Rep* 2015;13:336–41 CrossRef Medline
8. Dias LA, Nakanishi M, Mangussi-Gomes J, et al. **Successful endoscopic endonasal management of a transclival cerebrospinal fluid fistula secondary to ecchordosis physaliphora: an ectopic remnant of primitive notochord tissue in the clivus.** *Clin Neurol Neurosurg* 2014;117:116–19 CrossRef Medline
9. Baek WK, Lachkar S, Iwanaga J, et al. **Comprehensive review of spinal neurenteric cysts with a focus on histopathological findings.** *Cureus* 2018;10:e3379 CrossRef Medline
10. Mehnert F, Beschorner R, Küker W, et al. **Retroclival ecchordosis physaliphora: MR imaging and review of the literature.** *AJNR Am J Neuroradiol* 2004;25:1851–55 Medline
11. Choudhri O, Feroze A, Hwang P, et al. **Endoscopic resection of a giant intradural retroclival ecchordosis physaliphora: surgical technique and literature review.** *World Neurosurg* 2014;82:912.e21–26 CrossRef Medline
12. Kandukuri SR, Lin F, Gui L, et al. **Application of immunohistochemistry in undifferentiated neoplasms: a practical approach.** *Arch Pathol Lab Med* 2017;141:1014–32 CrossRef Medline
13. Carter JM, Wenger DE, Rose PS, et al. **Atypical notochordal cell tumors: a series of notochordal-derived tumors that defy current classification schemes.** *Am J Surg Pathol* 2017;41:39–48 CrossRef Medline
14. Wasserman JK, Gravel D, Purgina B. **Chordoma of the head and neck: a review.** *Head Neck Pathol* 2018;12:261–68 CrossRef Medline
15. Egerbacher M, Böck P. **Myxoid tissue: its morphology, histochemistry, and relationship with other supporting tissues.** *Arch Histol Cytol* 1997;60:121–31 CrossRef Medline
16. Zenonos GA, Fernandez-Miranda JC, Mukherjee D, et al. **Prospective validation of a molecular prognostication panel for clival chordoma.** *J Neurosurg* 2019;130:1528–37 CrossRef Medline
17. Abdallah HM, Gersey ZC, Muthiah N, et al. **An integrated management paradigm for skull base chordoma based on clinical and molecular characteristics.** *J Neurol Surg B Skull Base* 2021;82:601–07 CrossRef Medline
18. Fernandez-Miranda JC, Gardner PA, Snyderman CH, et al. **Clival chordomas: a pathological, surgical and radiotherapeutic review.** *Head Neck* 2014;36:892–906 CrossRef Medline
19. Sung MS, Lee GK, Kang HS, et al. **Sacroccygeal chordoma: MR imaging in 30 patients.** *Skeletal Radiol* 2005;34:87–94 CrossRef Medline
20. Martin JJ, Niranjana A, Kondziolka D, et al. **radiosurgery for chordomas and chondrosarcomas of the skull base.** *J Neurosurg* 2007;107:758–64 CrossRef Medline
21. Alshammari J, Monnier P, Daniel RT, et al. **Clival chordoma with an atypical presentation: a case report.** *J Med Case Rep* 2012;6:410 CrossRef Medline
22. Young VA, Curtis KM, Temple HT, et al. **Characteristics and patterns of metastatic disease from chordoma.** *Sarcoma* 2015;2015:517657 CrossRef Medline
23. Smoll NR, Gautschi OP, Radovanovic I, et al. **Incidence and relative survival of chordomas: the standardized mortality ratio and the impact of chordomas on a population.** *Cancer* 2013;119:2029–37 CrossRef Medline
24. Walcott BP, Nahed BV, Mohyeldin A, et al. **Chordoma: current concepts, management, and future directions.** *Lancet Oncol* 2012;13:e69–76 CrossRef Medline
25. Rohatgi S, Ramaiya NH, Jagannathan JP, et al. **Metastatic chordoma: report of the two cases and review of the literature.** *Eurasian J Med* 2015;47:151–54 CrossRef Medline
26. Fernandes Cabral DT, Zenonos GA, Fernandez-Miranda JC, et al. **Iatrogenic seeding of skull base chordoma following endoscopic endonasal surgery.** *J Neurosurg* 2018;129:947–53 CrossRef Medline
27. Frederico SC, Darling C, Zhang X, et al. **Circulating tumor DNA: A potential aid in the management of chordomas.** *Front Oncol* 2022;12:1016385 CrossRef Medline

28. Ling SS, Sader C, Robbins P, et al. **A case of giant ecchordosis physaliphora: a case report and literature review.** *Otol Neurotol* 2007;28:931–33 CrossRef Medline
29. Sun R, Ajam Y, Campbell G, et al. **A rare case of ecchordosis physaliphora presenting with headache, abducens nerve palsy, and intracranial hypertension.** *Cureus* 2020;12:e8843 CrossRef Medline
30. Golden LD, Small JE. **Benign notochordal lesions of the posterior clivus: retrospective review of prevalence and imaging characteristics.** *J Neuroimaging* 2014;24:245–49 CrossRef Medline
31. Gonzalez-Martinez JA, Guthikonda M, Vellutini E, et al. **Intradural invasion of chordoma: two case reports.** *Skull Base* 2002;12:155–61 CrossRef Medline
32. Ciarpaglini R, Pasquini E, Mazzatenta D, et al. **Intradural clival chordoma and ecchordosis physaliphora: a challenging differential diagnosis: case report.** *Neurosurgery* 2009;64:E387–88; discussion E388 CrossRef Medline
33. Yuh SJ, Woulfe J, Corsten MJ, et al. **Diagnostic imaging dilemma of a clival lesion and its clinical management implications.** *J Neurol Surg B Skull Base* 2014;75:177–82 CrossRef Medline

Performance of Automated ASPECTS Software and Value as a Computer-Aided Detection Tool

J. Lambert, J. Demeestere, B. Dewachter, L. Cockmartin, A. Wouters, R. Symons, L. Boomgaert, L. Vandewalle, L. Scheldeman, P. Demaerel, and R. Lemmens



ABSTRACT

BACKGROUND AND PURPOSE: ASPECTS quantifies early ischemic changes in anterior circulation stroke on NCCT but has interrater variability. We examined the agreement of conventional and automated ASPECTS and studied the value of computer-aided detection.

MATERIALS AND METHODS: We retrospectively collected imaging data from consecutive patients with acute ischemic stroke with large-vessel occlusion undergoing thrombectomy. Five raters scored conventional ASPECTS on baseline NCCTs, which were also processed by RAPID software. Conventional and automated ASPECTS were compared with a consensus criterion standard. We determined the agreement over the full ASPECTS range as well as dichotomized, reflecting thrombectomy eligibility according to the guidelines (ASPECTS 0–5 versus 6–10). Raters subsequently scored ASPECTS on the same NCCTs with assistance of the automated ASPECTS outputs, and agreement was obtained.

RESULTS: For the total of 175 cases, agreement among raters individually and the criterion standard varied from fair to good (weighted κ = between 0.38 and 0.76) and was moderate (weighted κ = 0.59) for the automated ASPECTS. The agreement of all raters individually versus the criterion standard improved with software assistance, as did the interrater agreement (overall Fleiss κ = 0.15–0.23; $P < .001$ and .39 to .55; $P = .01$ for the dichotomized ASPECTS).

CONCLUSIONS: Automated ASPECTS had agreement with the criterion standard similar to that of conventional ASPECTS. However, including automated ASPECTS during the evaluation of NCCT in acute stroke improved the agreement with the criterion standard and improved interrater agreement, which could, therefore, result in more uniform scoring in clinical practice.

ABBREVIATION: CAD = computer-aided detection and diagnosis

ASPECTS was developed as a method to quantify early ischemic changes in the anterior circulation on NCCT. Low ASPECTS was associated with poor functional outcome and increased rates of symptomatic intracranial hemorrhage in patients with acute ischemic stroke who underwent thrombolysis.¹ ASPECTS was subsequently used to select patients with a higher pretreatment chance of achieving good functional outcome in randomized controlled trials on endovascular stroke

treatment and has been incorporated in the American Heart Association guidelines on the management of acute stroke for the selection of thrombectomy candidates in the early time window.² However, reported interrater agreement for ASPECTS varied considerably in previous publications.^{3–6} A systematic review on this topic concluded that there may be insufficient precision to use ASPECTS as a treatment decision guide.⁷ Automated software or artificial intelligence tools have been suggested in the literature as a possible solution for this problem.⁸ Several automated or semiautomated software packages based on artificial intelligence have been developed and validated in acute stroke diagnostics, and studies have shown that automated ASPECTS correlates with outcome in patients with large-vessel occlusions treated with mechanical thrombectomy.^{9,10} However, recently, a large study documented only moderate agreement of an automated ASPECTS tool compared with the expert raters. This finding argues against an artificial intelligence-only approach without case-by-case validation of the results by physicians.¹¹ In this study, we compared the agreement of automated ASPECTS and human raters with different

Received March 6, 2023; accepted after revision June 14.

From the Departments of Radiology (J.L., B.D., L.C., R.S., L.B., P.D.) and Neurology (J.D., L.V., L.S., R.S.), University Hospitals Leuven, Leuven, Belgium; Departments of Imaging and Pathology (J.L., B.D., P.D.), Neuroscience (J.D., A.W., L.V., L.S., R.L.), and Experimental Neurology (J.D., A.W., L.V., L.S., R.L.), Laboratory of Neurobiology, Katholieke Universiteit Leuven, University of Leuven, Leuven, Belgium; and Imelda Hospital (R.S.), Bonheiden, Belgium.

Please address correspondence to Julie Lambert, MD, Department of Radiology, University Hospitals Leuven, Herestraat 49, 3000 Leuven, Belgium; e-mail: julie.lambert@uzleuven.be

Indicates article with online supplemental data.

<http://dx.doi.org/10.3174/ajnr.A7956>

levels of experience levels with the criterion standard in scoring patients who underwent thrombectomy for anterior circulation acute ischemic stroke. In addition, we assessed the impact of the time interval between symptom onset and imaging on the performance of automated ASPECTS. Finally, we evaluated the benefit of automated software in assisting the raters while scoring ASPECTS, by providing software output in addition to the baseline NCCT. We examined the effect on the performance and agreement regarding the evaluation of these early ischemic changes.

MATERIALS AND METHODS

Patient Selection and Imaging Collection

We retrospectively collected imaging data of consecutive patients who underwent thrombectomy for acute ischemic stroke at the University Hospitals Leuven (Belgium) between 2015 and 2018, irrespective of the time from symptom onset. For transferred patients, we collected pretreatment imaging performed at the referral hospital. The scan protocol of the main referral centers for NCCT was like the scan protocol at the Leuven University Hospital. More detailed information about acquisition parameters can be found in the Online Supplemental Data. While 3 mm was the standard MPR soft-tissue section thickness for the thrombectomy center and also for both main referral centers, for some cases only 1- or 5-mm slices were available. For each case, the best available axial soft-tissue series was imported from the PACS system to the scoring platform. We did not apply angulation correction, filter, or fixed window settings.

ASPECTS Rating

Raters used the ViewDEX scoring platform (<https://academic.oup.com/rpd/article-abstract/139/1-3/42/1599429?redirectedFrom=fulltext>), which randomized cases, for ASPECT scoring.¹² Raters scored ASPECTS in both hemispheres, blinded to clinical information and follow-up imaging. They were able to view the images in the window levels of their preference. Each of 10 predefined regions of 1 side was scored as normal or abnormal (based on visible blurring of contours and swelling and/or hypodensity of the brain parenchyma) to obtain ASPECT scores.¹ If the rater selected the unaffected hemisphere to quantify ASPECTS, this was documented and another rating was requested for the affected side. The software of the automated ASPECTS was RAPID ASPECTS (iSchemaView). The images were remotely processed by the RAPID server. The cases for which the software rated the unaffected side were reprocessed on the server to obtain the score for the affected hemisphere.

The criterion standard was defined as the consensus rating of 2 experienced neuroradiologists (J.L. and P.D.), who also had access to the automated software. Each neuroradiologist scored the cases separately, and discordant cases were read together to reach consensus. This criterion standard rating was performed on high-definition external monitors, DICOM-calibrated, with appropriate lighting. Five raters individually rated the baseline NCCTs: rater 1 (a radiology resident [B.D.]), rater 2 (a stroke neurologist [J.D.]), rater 3 (a neurology resident [L.V.]), and raters 4 and 5 ([R.S.] and [L.B.], both radiologists with a special interest in neuroradiology).

For the evaluation of the software as a computer-aided detection and diagnosis (CAD) tool, we provided the raters with the same randomized images on the scoring platform several weeks after the initial reading. A file with both of their previous scores and the automated ASPECTS output (with images) was available for each case. Raters were then instructed to re-evaluate the scores of the NCCT with the knowledge of this additional software information and to make changes deemed appropriate.

Statistical Analysis. Weighted κ was calculated to assess the agreement between the overall ASPECT scores of individual raters as well as the agreement between the criterion standard ratings versus conventional and automated ASPECTS, respectively.

The interpretation of weighted κ values is identical to that of standard κ ,¹³ and the classification as proposed by Landis and Koch was applied.¹⁴ The Hotelling T-squared test was applied to compare weighted κ values, for example, to compare the inter-rater agreement for the readings with and without automated ASPECTS.¹⁵

The ASPECT scores were dichotomized according to guideline recommendations into 2 groups with either poor (0–5) or good (6–10) ASPECTS. The Cohen κ was used to calculate the agreement with the criterion standard for dichotomized ASPECTS.^{2,6} For the comparison of >2 raters, the Fleiss κ was applied. Additionally, sensitivity and specificity of the dichotomized scores of the raters compared with the criterion standard were calculated. Moreover, we calculated the area under the curve values as a measure of the accuracy and compared the area under the curve values without and with CAD by using the DeLong test.

To investigate the impact of time between symptom onset and imaging acquisition on interrater agreement, we binned patients into 3 time intervals (0–1 hour, 1–2 hours, 2–6 hours). All analyses were performed using SPSS v28.0 (IBM), except for the Hotelling T-squared test and the DeLong test, for which R statistical and computing software (<http://www.r-project.org/>) was used.

RESULTS

Demographics of the Study Cohort

We collected imaging data for 226 patients, of whom 52 were excluded (15 without an occlusion in the anterior circulation, 21 without NCCT, 11 with insufficient imaging quality, 2 with software-processing errors, and 3 who were double-registered in the database). Baseline characteristics for the 174 remaining patients are presented in Table 1. For 1 patient, we included 2 NCCTs because this person underwent 2 thrombectomies for a large-vessel occlusion, first in 1 hemisphere, followed by a second in the other hemisphere within a 3-day time interval. Time from symptom onset to imaging was known for 173 patients: Forty-six patients (27%) were imaged 0–1 hour after the onset of symptoms, 71 (41%) between 1 and 2 hours, 40 (23%) between 2 and 6 hours, and only 16 (9%) >6 hours after symptom onset.

Performance of Conventional ASPECTS Raters and Automated Software versus the Criterion Standard

The 175 NCCTs were scored by human raters (conventional ASPECTS) and processed by the automated software. An overview of all score ranges is provided in Table 2. The frequency of readers

Table 1: Patient characteristics

Characteristics	
No. of patients	174
Age (yr) ^a	72 (33–96)
Female sex (%)	94 (54%)
NIHSS ^b	18 (13–22)
Time from symptom onset to imaging (min) ^a	161 (5–1503)
No. of patients with known time interval from symptom onset to imaging	173
0–1 hour	46 (27%)
1–2 hours	71 (41%)
2–6 hours	40 (23%)
>6 hours	16 (9%)
NCCT acquired at referral hospital (%)	50 (29%)

^aData are mean (range).

^bData are median (interquartile range).

Table 2: ASPECTS ratings overview with medians, interquartile ranges, and dichotomized score proportions

Raters	Median (IQR)	0–5	6–10
Criterion standard	8 (7–10)	14%	86%
RAPID ASPECTS	7 (6–9)	17%	83%
Rater 1	9 (8–9)	7%	93%
Rater 1 with CAD	8 (7–9)	9%	91%
Rater 2	8 (6–10)	17%	83%
Rater 2 with CAD	8 (6–10)	19%	81%
Rater 3	9 (8–10)	8%	92%
Rater 3 with CAD	8 (7–10)	12%	88%
Rater 4	9 (7–10)	11%	89%
Rater 4 with CAD	8 (7–10)	14%	86%
Rater 5	8 (7–10)	11%	89%
Rater 5 with CAD	8 (6–9)	18%	82%

Note:—IQR indicates interquartile range.

scoring the unaffected side was low (rater 1: 3%; rater 2: 5%; rater 3: 0%; rater 4: 0%; rater 5: 1%) and similar to that of the software (2%). The intrarater agreement for a subset of 20 cases per reader is presented in the Online Supplemental Data.

We compared the individual rating with the criterion standard consensus scores.

The agreement with the criterion standard of conventional ASPECTS varied substantially among the raters, ranging between fair and good (rater 1: weighted $\kappa = 0.41$; rater 2: weighted $\kappa = 0.38$; rater 3: weighted $\kappa = 0.42$; rater 4: weighted $\kappa = 0.76$; rater 5: weighted $\kappa = 0.49$). Automated analysis resulted in moderate agreement with the criterion standard (weighted $\kappa = 0.59$). Agreement of the dichotomized ASPECTS of the software and raters compared with the criterion standard produced comparable results (automated ASPECTS: Cohen $\kappa = 0.51$; rater 1: Cohen $\kappa = 0.43$; rater 2: Cohen $\kappa = 0.42$; rater 3: Cohen $\kappa = 0.40$; rater 4: Cohen $\kappa = 0.74$; rater 5: Cohen $\kappa = 0.43$). Figure 1 shows the scatterplots of the 10-point-scale scores of both the automated software versus the criterion standard and the human raters versus the criterion standard. We conclude that for the separate software analysis, the automated scoring did not provide an advantage in scoring precision over the human raters.

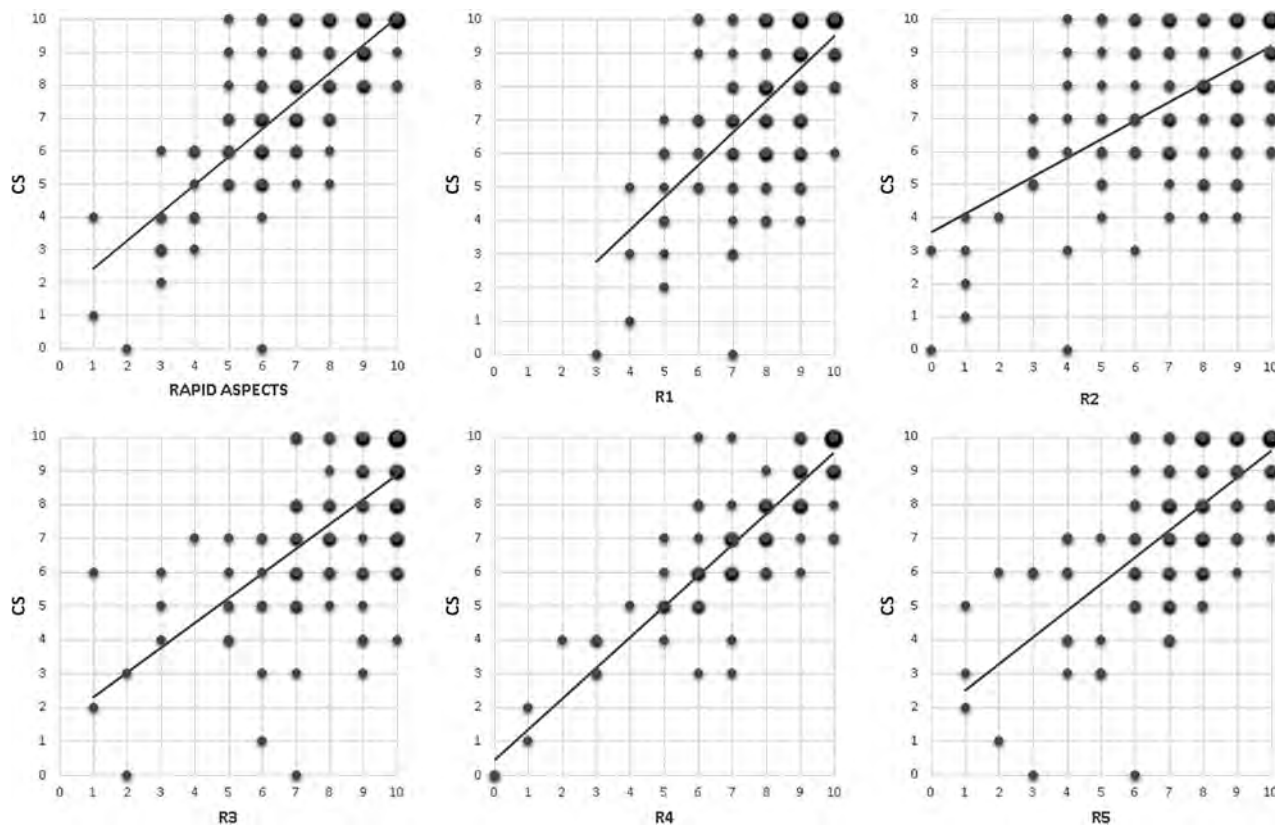


FIG 1. Scatterplots with trendlines of individual raters and automated software (x-axis) versus the criterion standard (y-axis). The size of each dot is proportionate to the number of cases with that combination of scores. R indicates rater.

Impact of Time from Symptom Onset to Imaging on ASPECT Scores

One-hundred fifty-seven patients (90% of the 174) presented within the 0- to 6-hour time window after stroke onset and were selected for this analysis. The median time between onset to imaging in this subgroup was 80 minutes (interquartile range = 55–66 minutes). We divided the patients into three groups according to time intervals: 0–1 hour, 1–2 hours, and 2–6 hours between onset and imaging. The agreement with the criterion

standard improved with time from symptom onset for the automated ASPECTS and 2 of 5 raters. These results are listed in Table 3.

Table 3: Impact of time from onset to imaging on ASPECTS

Paired Agreement	0–1 Hour	1–2 Hours	2–6 Hours	P Value
Rater 1 versus criterion standard	0.26	0.41	0.54	.10
Rater 2 versus criterion standard	0.38	0.42	0.32	.77
Rater 3 versus criterion standard	0.27	0.34	0.58	.03
Rater 4 versus criterion standard	0.72	0.68	0.84	.04
Rater 5 versus criterion standard	0.55	0.46	0.50	.71
Automated ASPECTS versus criterion standard	0.37	0.66	0.67	.002

Note:—Data are weighted κ values.

Table 4: Overall scores agreement with the expert criterion standard for readings without and with CAD

Overall Scores	Weighted κ without CAD	Weighted κ with CAD	P Value
Rater 1 versus criterion standard	0.41 (0.04)	0.58 (0.03)	<.001
Rater 2 versus criterion standard	0.38 (0.05)	0.52 (0.05)	.001
Rater 3 versus criterion standard	0.42 (0.04)	0.68 (0.03)	<.001
Rater 4 versus criterion standard	0.76 (0.03)	0.84 (0.02)	<.001
Rater 5 versus criterion standard	0.49 (0.04)	0.57 (0.04)	.04

Note:—Standard errors of the κ coefficients are in parentheses.

Table 5: Dichotomized scores agreement with the criterion standard for readings without and with CAD

Dichotomized Scores	Cohen κ without CAD	Cohen κ with CAD	P Value
Rater 1 versus criterion standard	0.43 (0.11)	0.61 (0.09)	.12
Rater 2 versus criterion standard	0.42 (0.09)	0.63 (0.08)	.02
Rater 3 versus criterion standard	0.40 (0.10)	0.55 (0.09)	.19
Rater 4 versus criterion standard	0.74 (0.08)	0.86 (0.06)	.07
Rater 5 versus criterion standard	0.43 (0.10)	0.58 (0.09)	.14

Note:—Standard errors of the κ coefficients are in parentheses.

Automated ASPECTS for Computer-Aided Detection. We identified an improvement in agreement with the criterion standard for the conventional ASPECTS ratings with the use of automated ASPECTS output as CAD. The Online Supplemental Data show the scatterplots of all raters without and with CAD, compared with the criterion standard.

For rater 1, the weighted κ increased from 0.41 to 0.58; for rater 2, from 0.38 to 0.52; for rater 3, from 0.42 to 0.68; for rater 4, from 0.76 to 0.84; and for rater 5, from 0.49 to 0.57 (Tables 4 and 5). For dichotomized ASPECTS, we could not identify this significantly improved agreement of the CAD ratings for most raters, though an increasing trend of the Cohen κ values was observed for all raters (0.43–0.61, $P = .12$ for rater 1; 0.42–0.63, $P = .02$ for rater 2; 0.40–0.55, $P = .19$ for rater 3; 0.74–0.86, $P = .07$ for rater 4; and 0.43–0.58, $P = .14$ for rater 5; Tables 4 and 5). The diagnostic performance of the dichotomized readings for each reader is provided in the Online Supplemental Data. Overall, the accuracy (area under the curve) improved with the assistance of the automated software from 0.72 to 0.82 ($P = .004$). Also, the overall Fleiss κ for the interrater agreement of all 5 raters improved with CAD from 0.15 to 0.23 ($P < .001$). We identified the same increase for the overall Fleiss κ of the binary scores with CAD (from 0.39 to

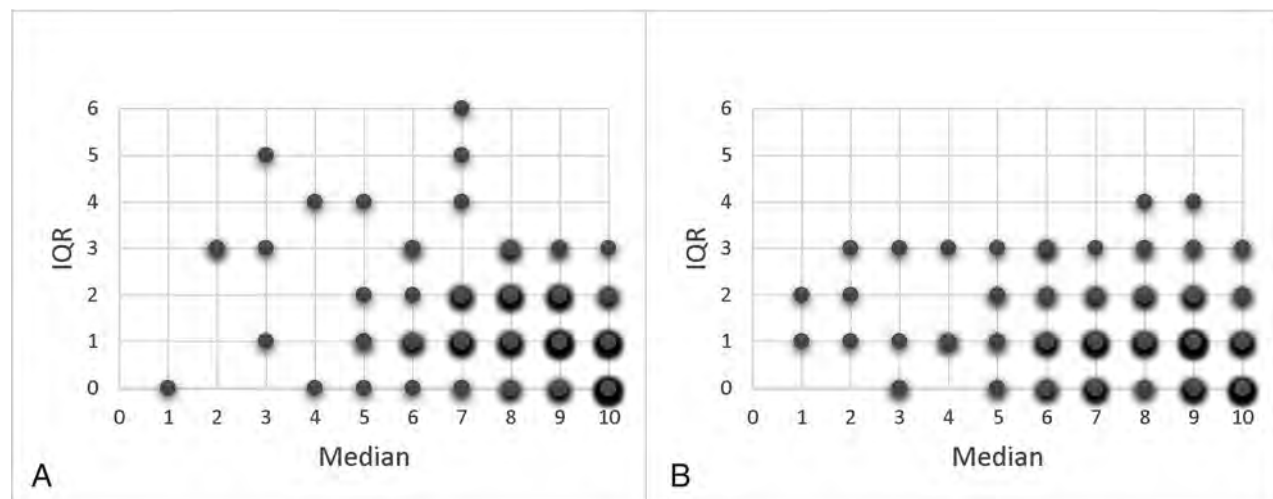


FIG 2. Score distribution plots illustrating the improvement of the interrater agreement of the 5 raters without (A) and with (B) CAD. The intra-class correlation coefficient of the raters was 0.55 (95% CI, 0.48–0.62) without CAD compared with 0.73 (95% CI, 0.68–0.78) with CAD. IQR indicates interquartile range.

0.55; $P = .01$). The reduction in variability for the ASPECTS rating with CAD is illustrated in Fig 2.

DISCUSSION

We compared the performance of automated ASPECTS software with human readers and identified moderate agreement for most visual assessments and automated ASPECTS compared with the criterion standard. Providing readers with the automated software such as CAD improved the agreement with the criterion standard and accuracy. Most important, the interrater agreement increased with the assistance of the output from the software, suggesting enhanced uniformity in reading ASPECTS by CAD.

The performance of the automated software in comparison with the consensus score is in line with previous studies revealing similar, moderate agreement in conventional assessment of baseline NCCT by raters and automated software analysis compared with experts.^{11,16-18} Some studies analyzing results for the individual regions did identify differences in agreement depending on the ASPECTS region.^{19,20} Two previous validation studies on RAPID ASPECTS software showed an outperformance of the software versus the human raters.^{21,22} A first study found RAPID ASPECTS to be more accurate than experienced raters in patients with large hemispheric infarcts compared with a diffusion-weighted imaging ASPECTS, which, of course, differs from our methodology.²²

A second study showed near-perfect agreement with a criterion standard.²¹ Agreement with the criterion standard in our study was lower, possibly due to methodologic differences related to the definition of the criterion standard. First, the criterion standard expert raters in our study were exposed to only baseline NCCT data, while in the other study, follow-up MR imaging, which revealed the final infarct location, was included. Also, the NCCT acquisition and reconstructions sometimes slightly differed among cases in our data (as a reflection of imaging included from multiple centers), while this was standardized in the other study. Section thickness possibly affects human raters and automated ASPECTS differently. Thinner slices can improve the performance of automated analyses resulting from the higher resolution, but these could also negatively affect human performance because the resolution will differ from imaging data evaluated in daily clinical practice.²³ Surprisingly, while most hospitals are evolving to thinner slices, a recent study on the validation of 2 automated ASPECTS software programs found 5 mm to be the optimal section thickness.^{18,24}

Several publications reported on the interrater variability of ASPECTS.³⁻⁶ A study with 100 raters found high variability among even experienced radiologists and neuroradiologists.²⁵ In many hospitals, stroke care is provided by less experienced raters (particularly in out-of-office hours). Therefore, we studied the potential role of automated software to assist readers in improving agreement with the criterion standard but also accuracy and interrater agreement because these may be of great benefit.

Our results revealing increased agreement with a consensus criterion standard in readers assisted by the automated ASPECTS have been reported previously.²⁶ This information may not be extrapolated to all available packages because suboptimal software

tools may even negatively influence readers, thereby decreasing their performance.²⁷

To our knowledge, previous studies did not report on the effect of automated ASPECTS on overall interrater agreement. We hypothesize that part of the reason for the amelioration of the interrater agreement reported here is due to the visualization of the automated ASPECTS on 2 standardized slices with uniform angulation, filter, and windowing. Presenting this uniform set of selected images by the software might counteract part of the image variability that ASPECTS raters encounter when evaluating NCCTs.

In clinical management of acute ischemic stroke, agreement on a dichotomized ASPECTS (good versus poor) may be more relevant because it is used to assess eligibility for thrombectomy.²⁸ In this study, we defined ASPECTS as good versus poor on the basis of the current guidelines. Although one might assume the interrater variability to be less in the dichotomized approach, the individual κ values were rather similar for the weighted and Cohen κ . We assume the imbalance of our data set; the more normal ASPECTS areas than ischemic areas as well as the low proportion of ASPECT scores of <3 can partially explain this. Considering the recently published trials in large-core patients, a similar analysis would be of interest after dichotomizing ASPECTS in <3 compared with ≥ 3 .^{29,30} Because our population was skewed toward higher ASPECTS, we could, unfortunately, not perform this dichotomized low ASPECTS analysis in this cohort.

Our study has several limitations. First, we included only patients who underwent thrombectomy. Although in our clinical center, we typically do not exclude patients from thrombectomy presenting in the 0- to 6-hour time window solely on the basis of poor ASPECTS, it is possible that patients with low ASPECTS are underrepresented in this cohort, possibly affecting interrater agreement. Second, we wanted the experienced raters to have access to the automated ASPECTS output for the consensus criterion standard rating because they could have all imaging information. Potentially, this choice could have introduced bias toward the automated software results, but we assumed experienced readers to be less prone to this bias. Third, the sample size may have been too small and homogeneous in relation to the time between onset to imaging (patients imaged beyond 6 hours after symptom onset were underrepresented) to robustly study the role of time from onset to imaging on the performance of human and automated ratings. We believe that future studies should focus on including patients in the later time window to study the effect of the time between onset and imaging on the agreement of ASPECTS reading.

Another limitation of our study is that we evaluated only 1 vendor software type. A different automated ASPECTS software program (Brainomix; <https://www.brainomix.com/>) was shown to be noninferior to neuroradiologists in several studies.^{16,31,32} A comparison between Brainomix and Frontier software found higher agreement of the raters with Brainomix than with Frontier.¹⁷ A study comparing 3 different automated ASPECTS tools reported on a convincing grade of agreement among them, underscoring the potential of all 3 for decision support.¹⁸

The current discussion on introducing artificial intelligence in clinical practice is often directed at evaluating software as a replacement for human raters. Alternatively, we could focus on the software as a decision-aiding tool in clinical practice. In clinical scenarios, frequently a patient with presumed stroke is not immediately assessed by a criterion standard expert. Therefore, our study with raters of different backgrounds, all working in the acute stroke flow, is clinically relevant. The introduction of artificial intelligence for ASPECTS could benefit many patients because it can potentially support raters with lower levels of expertise. Because even intrarater agreement of ASPECTS is known to be low,⁷ the advantage of the software (if, of course, accurate) is providing reproducible assistance. ASPECTS with assistance of artificial intelligence has the potential to improve the accuracy of various raters over all hospital settings, especially in the absence of the expert raters. The results of our study are suggestive of such a benefit, though its potential needs to be confirmed on a larger scale by future studies. These studies could focus on reading ASPECTS in patients presenting in later time windows beyond 6 hours to assess the performance of the automated software and the value of the output in assisting readers in scoring ASPECTS. In addition, these studies could include physicians from various disciplines involved in acute stroke care with differences in expertise to validate the improvement in performance and agreement.

CONCLUSIONS

We determined automated ASPECTS and human raters to have similar agreement compared with the criterion standard. Using the automated ASPECTS output as a CAD tool improved the agreement with the criterion standard, accuracy, and interrater agreement. Our findings suggest that the application of this automated analysis as an assistance tool for reading NCCTs in patients with acute ischemic stroke will result in more uniform and accurate scoring of ASPECTS.

Disclosure forms provided by the authors are available with the full text and PDF of this article at www.ajnr.org.

REFERENCES

1. Barber PA, Demchuk AM, Zhang J, et al. **Validity and reliability of a quantitative computed tomography score in predicting outcome of hyperacute stroke before thrombolytic therapy.** *Lancet* 2000;355:1670–74 CrossRef Medline
2. Powers WJ, Rabinstein AA, Ackerson T, et al. **Guidelines for the Early Management of Patients with Acute Ischemic Stroke: 2019 Update to the 2018 Guidelines for the Early Management of Acute Ischemic Stroke—A Guideline For Healthcare Professionals from the American Heart Association/American Stroke Association.** *Stroke* 2019;50:E344–418 CrossRef Medline
3. Coutts SB, Demchuk AM, Barber PA, et al; VISION Study Group. **Interobserver variation of ASPECTS in real time.** *Stroke* 2004;35:e103–05 CrossRef Medline
4. Gupta AC, Schaefer PW, Chaudhry ZA, et al. **Interobserver reliability of baseline noncontrast CT Alberta Stroke Program Early CT score for intra-arterial stroke treatment selection.** *AJNR Am J Neuroradiol* 2012;33:1046–49 CrossRef Medline
5. McTaggart RA, Jovin TG, Lansberg MG, et al; DEFUSE 2 Investigators. **Alberta stroke program early computed tomographic scoring performance in a series of patients undergoing**

- computed tomography and MRI: reader agreement, modality agreement, and outcome prediction.** *Stroke* 2015;46:407–12 CrossRef Medline
6. Nicholson P, Hilditch CA, Neuhaus A, et al. **Per-region interobserver agreement of Alberta Stroke Program Early CT Scores (ASPECTS).** *J Neurointerv Surg* 2020;12:1069–71 CrossRef Medline
7. Farzin B, Fahed R, Guilbert F, et al. **Early CT changes in patients admitted for thrombectomy: intrarater and interrater agreement.** *Neurology* 2016;87:249–56 CrossRef Medline
8. Wilson AT, Dey S, Evans JW, et al. **Minds treating brains: understanding the interpretation of non-contrast CT ASPECTS in acute ischemic stroke.** *Expert Rev Cardiovasc Ther* 2018;16:143–45 PMC] CrossRef Medline
9. Pfaff J, Herweh C, Schieber S, et al. **E-ASPECTS correlates with and is predictive of outcome after mechanical thrombectomy.** *AJNR Am J Neuroradiol* 2017;38:1594–99 CrossRef Medline
10. Olive-Gadea M, Martins N, Boned S, et al. **Baseline ASPECTS and e-ASPECTS correlation with infarct volume and functional outcome in patients undergoing mechanical thrombectomy.** *J Neuroimaging* 2019;29:198–202 CrossRef Medline
11. Mair G, White P, Bath PM, et al. **External validation of e-ASPECTS software for interpreting brain CT in stroke.** *Ann Neurol* 2022;92:943–57 CrossRef Medline
12. Håkansson M, Svensson S, Zachrisson S, et al. **ViewDEX: an efficient and easy-to-use software for observer performance studies.** *Radiat Prot Dosimetry* 2010;139:42–51 CrossRef Medline
13. McHugh ML. **Interrater reliability: the κ statistic.** *Biochem Med (Zagreb)* 2012;22:276–82 Medline
14. Landis JR, Koch GG. **The measurement of observer agreement for categorical data.** *Biometrics* 1977;33:159–74 Medline
15. Vanbelle S. **Comparing dependent κ coefficients obtained on multilevel data.** *Biom J* 2017;59:1016–34 CrossRef Medline
16. Sundaram VK, Goldstein J, Wheelwright D, et al. **Automated ASPECTS in acute ischemic stroke: a comparative analysis with CT perfusion.** *AJNR Am J Neuroradiol* 2019;40:2033–38 CrossRef Medline
17. Goebel J, Stenzel E, Guberina N, et al. **Automated ASPECT rating: comparison between the Frontier ASPECT Score software and the Brainomix software.** *Neuroradiology* 2018;60:1267–72 CrossRef Medline
18. Hoelter P, Muehlen I, Goelitz P, et al. **Automated ASPECT scoring in acute ischemic stroke: comparison of three software tools.** *Neuroradiology* 2020;62:1231–33 CrossRef Medline
19. Neuhaus A, Seyedsaadat SM, Mihal D, et al. **Region-specific agreement in ASPECTS estimation between neuroradiologists and e-ASPECTS software.** *J Neurointerv Surg* 2020;12:720–23 CrossRef Medline
20. Austein F, Wodarg F, Jürgensen N, et al. **Automated versus manual imaging assessment of early ischemic changes in acute stroke: comparison of two software packages and expert consensus.** *Eur Radiol* 2019;29:6285–92 CrossRef Medline
21. Maegerlein C, Lehm M, Friedrich B, et al. **Automated calculation of the Alberta Stroke Program Early CT Score: feasibility and reliability.** *Radiology* 2019;291:141–48 CrossRef Medline
22. Albers GW, Wald MJ, Mlynash M, et al. **Automated calculation of Alberta Stroke Program Early CT Score: validation in patients with large hemispheric infarct.** *Stroke* 2019;50:3277–79 CrossRef Medline
23. Löffler MT, Sollmann N, Mönch S, et al. **Improved reliability of automated ASPECTS evaluation using iterative model reconstruction from head CT scans.** *J Neuroimaging* 2021;31:341–44 CrossRef Medline
24. Chen Z, Shi Z, Lu F, et al. **Validation of two automated ASPECTS software on non-contrast computed tomography scans of patients with acute ischemic stroke.** *Front Neurol* 2023;14 CrossRef Medline
25. van Horn N, Kniep H, Broocks G, et al. **ASPECTS interobserver agreement of 100 investigators from the TENSION study.** *Clin Neuroradiol* 2021;31:1093–100 CrossRef Medline

26. Delio PR, Wong ML, Tsai JP, et al. **Assistance from automated ASPECTS software improves reader performance.** *J Stroke Cerebrovasc Dis* 2021;30:105829 CrossRef Medline
27. Ernst M, Bernhardt M, Bechstein M, et al. **Effect of CAD on performance in ASPECTS reading.** *Inform Med Unlocked* 2020;18:100295 CrossRef
28. Cagnazzo F, Derraz I, Dargazanli C, et al. **Mechanical thrombectomy in patients with acute ischemic stroke and ASPECTS \leq 6: a meta-analysis.** *J Neurointerv Surg* 2020;12:350–55 CrossRef Medline
29. Huo X, Ma G, Tong X, et al; ANGEL-ASPECT Investigators. **Trial of Endovascular Therapy for Acute Ischemic Stroke with Large Infarct.** *N Engl J Med* 2023;388:1272–83 CrossRef Medline
30. Sarraj A, Hassan AE, Abraham MG, et al; SELECT2 Investigators. **Trial of Endovascular Thrombectomy for Large Ischemic Strokes.** *N Engl J Med* 2023;388:1259–71 CrossRef Medline
31. Herweh C, Ringleb PA, Rauch G, et al. **Performance of e-ASPECTS software in comparison to that of stroke physicians on assessing CT scans of acute ischemic stroke patients.** *Int J Stroke* 2016;11:438–45 CrossRef Medline
32. Nagel S, Sinha D, Day D, et al. **e-ASPECTS software is non-inferior to neuroradiologists in applying the ASPECT score to computed tomography scans of acute ischemic stroke patients.** *Int J Stroke* 2017;12:615–22 CrossRef Medline

Effect of Radiographic Contrast Media Shortage on Stroke Evaluation in the United States

 A.I. Qureshi,  A. Grintal,  A.C. DeGaetano,  M. Goren,  A. Lodhi, D. Golan, and  A.E. Hassan



ABSTRACT

BACKGROUND AND PURPOSE: We performed this study to identify the effect of the nationwide iodinated contrast media shortage due to reduction in GE Healthcare production, initiated on April 19, 2022, on the evaluation of patients with stroke.

MATERIALS AND METHODS: We analyzed the data on 72,514 patients who underwent imaging processed with commercial software in a sample of 399 hospitals in United States from February 28, 2022, through July 10, 2022. We quantified the percentage change in the daily number of CTAs and CTPs performed before and after April 19, 2022.

RESULTS: The daily counts of individual patients who underwent CTAs decreased (a 9.6% reduction, $P = .002$) from 1.584 studies per day per hospital to 1.433 studies per day per hospital. The daily counts of individual patients who underwent CTPs decreased (a 25.9% reduction, $P = .003$) from 0.484 studies per day per hospital to 0.358 studies per day per hospital. A significant reduction in CTPs using GE Healthcare contrast media (43.06%, $P < .001$) was seen but not in CTPs using non-GE Healthcare contrast media (increase by 2.93%, $P = .29$). The daily counts of individual patients with large-vessel occlusion decreased (a 7.69% reduction) from 0.124 per day per hospital to 0.114 per day per hospital.

CONCLUSIONS: Our analysis reported changes in the use of CTA and CTP in patients with acute ischemic stroke during the contrast media shortage. Further research needs to identify effective strategies to reduce the reliance on contrast media–based studies such as CTA and CTP without compromising patient outcomes.

ABBREVIATIONS: LVO = large-vessel occlusion; PHI = patient health information; rCBF = regional CBF; Tmax = time-to-maximum


On April 19, 2022, GE Healthcare notified medical facilities that orders for its iodinated contrast media products for CT would be rationed after a coronavirus disease 2019 (COVID-19) outbreak resulted in lockdown of its production facility in Shanghai, China.^{1,2} The lockdown resulted in the interruption of the production of the iodinated contrast media iohexol (Omnipaque; GE Healthcare) at the primary GE Healthcare manufacturing facility.² Although there were other suppliers such as Bracco Diagnostics, Bayer AG, and Guerbet for iodinated contrast media, they were unable to rapidly increase production to meet the demand for iodinated contrast media. CT imaging including CTA and CTP using IV

contrast media was the main technique for identification of patients with acute ischemic stroke who may be candidates for endovascular treatment at that time.^{3,4} Several strategies were introduced to modify the neuroimaging protocols for patients with acute ischemic stroke in various institutions, including selecting fewer patients for CTA and CTP after initial screening based on clinical criteria and a noncontrast CT scan, modifying the protocol for acquisition of CTA and CTP, and/or using MR imaging to triage patients with acute ischemic stroke.⁵⁻⁸ Although there are reports on the effect of the shortage of contrast media,^{9,10} the effect on a larger scale on neuroimaging evaluation of patients with stroke has not been quantified.

Received November 10, 2022; accepted after revision May 31, 2023.

From the Zeenat Qureshi Stroke Institute and Department of Neurology (A.I.Q., A.L.), University of Missouri, Columbia, Missouri; Viz.ai (A.G., A.C.D., M.G., D.G.), San Francisco, California; Department of Neuroscience (A.E.H.), Valley Baptist Medical Center, Harlingen, Texas; and Department of Neurology (A.E.H.), University of Texas Rio Grande Valley School of Medicine, Harlingen, Texas.

Please address correspondence to Adnan I. Qureshi, MD, Department of Neurology, University of Missouri, One Hospital Dr CE507, Columbia, MO 65212; e-mail: qureshai@gmail.com

 Indicates article with online supplemental data.

<http://dx.doi.org/10.3174/ajnr.A7924>

MATERIALS AND METHODS

We analyzed the data collected in a commercial neuroimaging data base associated with the Viz.ai software platform (viz.ai) as a surrogate for the quantity of neuroimaging evaluations that hospitals provided for patients with acute ischemic stroke. In routine use, neuroimaging for acute ischemic stroke comprising noncontrast CT, CTA of the head and neck, and/or CTP of the brain is transmitted in real-time from the point of acquisition to a local

DICOM gateway that forwards the scans to the cloud hosting Viz.ai imaging software. Images are transmitted to the Viz.ai server in DICOM format with associated metadata that include patient age, sex, site of imaging, and date and the time of image acquisition. These data are processed by the Viz.ai server and sent to the appropriate clinical teams for patient care. Data are then anonymized by the Viz.ai server and transmitted to a central data warehouse. Viz.ai ensured compliance with Health Insurance Portability and Accountability Act (HIPAA) Privacy and Security Rule and Breach Notification Rule¹¹ to protect sensitive patient health information (PHI). Viz.ai used a secure end-to-end process, securing PHI at both the hospital firewall and cloud Advanced Wireless Services network (<https://k21academy.com/amazon-web-services/aws-solutions-architect/networking-fundamental/>), with biometric, multifactorial access and a secure de-identification process. Viz.ai shared Customer Data in accordance with the Customer Agreement and in compliance with applicable law and legal process. The analysis of de-identified data does not constitute human subject research as defined at 45 CFR 46.102 (<https://www.ecfr.gov/current/title-45/subtitle-A/subchapter-A/part-46/subpart-A/section-46.102>) and therefore did not require institutional review board review.¹²

Patient-Related Variables

We divided patients' ages into 4 groups: younger than 40 years, 40–59 years, 60–79 years, and 80 years of age or older. Two measures of stroke severity were used, defined by 2 imaging parameters on CTP: time-to-maximum (Tmax) > 6 seconds and regional cerebral blood flow (rCBF) < 30%. For both parameters, patients were divided into 4 groups based on the affected volume as 0 mL, 1–30 mL, 31–60 mL, 61–90 mL, 91–119 mL, and ≥120 mL. Imaging data included automatically calculated volumes of rCBF of <30% and hypoperfusion from CTP data. Hypoperfusion volume, which corresponds to areas of the brain that are critically hypoperfused regardless of reversibility, is estimated within Viz.ai as regions with Tmax of the residue function of >6 seconds.

Contrast Media Used

The contrast source information was based only on studies in which contrast media could be identified on the basis of DICOM information. The contrast agent information was calculated from the Contrast/Bolus Agent Attribute DICOM tag (0018,0010) in which Omnipaque and iodixanol (Visipaque) agents counted as GE Healthcare contrast agents and iopamidol (Isovue; Bracco Diagnostics) and ioversol (Optiray; Guerbet) counted as non-GE Healthcare contrast agents. Only 16 institutions (4% of total institutions in the analysis) used both GE Healthcare and non-GE Healthcare contrast, and only 3 institutions had >20 patients and used the alternate contrast in >10% of the total patients. The data were too small to be analyzed as a separate group, and institutions were classified on the basis of the predominant contrast used.

Hospital Characteristics

The hospitals were divided into Comprehensive Stroke Centers, Primary Stroke Centers, Thrombectomy-Capable Stroke Centers, and Acute Stroke Ready Hospitals according to definitions provided by The Joint Commission.¹³ Both Comprehensive Stroke

Centers and Thrombectomy-Capable Stroke Centers are required to perform 15 mechanical thrombectomies during the past 12 months (or 30 during past 24 months), but a Comprehensive Stroke Center is additionally required to treat 20 patients with subarachnoid hemorrhage, perform endovascular or surgical treatment for 15 patients with intracranial aneurysms, and administer IV thrombolytics 25 times annually.

Additional Variables

Large-Vessel Occlusion Alert. The large-vessel occlusion (LVO) alert feature is based on automated detection of LVO located in the ICA and the MCA (M1 and M2 segments).

Data and Statistical Analysis

Outcome data were measured as daily counts of patients per hospital who underwent CTA for acute ischemic stroke using the Viz.ai platform, including all hospitals. The percentage decline was calculated from the ratio of daily counts of patients per hospital before and after April 19, 2022, as well as for each individual month prior (March) and after (May, June, and July) that date. We performed a subgroup analysis of hospitals that perform CTPs for acute ischemic stroke using the Viz.ai platform. We used the Mann Kendall test for trend to determine statistical significance. The data in various strata defined by patient characteristics (age, sex, stroke severity), hospital characteristics (Primary or Comprehensive Stroke Centers, Thrombectomy-Capable, or Stroke Ready Centers), and contrast media used (GE Healthcare and non-GE Healthcare) were plotted on a weekly basis from February 28, 2022, through July 10, 2022.

RESULTS

We analyzed the anonymized data on 72,514 patients (including 79,053 studies) who underwent imaging processed with Viz.ai software in a sample of 399 hospitals in the United States from February 28, 2022, through July 10, 2022 (Online Supplemental Data). The daily counts of individual patients who underwent CTAs decreased (a 9.6% reduction, $P = .002$) from 1.584 studies per day per hospital before April 19, 2022, to 1.433 studies per day per hospital after April 19, 2022. The daily counts of individual patients who underwent CTA decreased from 1.585 studies per day per hospital in March to 1.427 studies per day per hospital in May, 1.408 studies per day per hospital in June, and 1.367 studies per day per hospital in July (Fig 1A). The lowest CTA count was 3798 individual patients observed between June 6 and 12. A significant reduction in CTAs performed was seen in patients 40–59 years of age ($P < .001$), 60–79 years of age ($P < .001$), 80 years of age or older ($P = .002$), but not in those younger than 40 years of age ($P = .09$) (Online Supplemental Data).

The daily counts of individual patients who underwent CTPs decreased (a 25.9% reduction, $P = .003$) from 0.484 studies per day per hospital before April 19 to 0.358 studies per day per hospital after April 19 in 185 hospitals that performed CTPs. The daily counts of individual patients who underwent CTP decreased from 0.484 studies per day per hospital in March to 0.346 studies per day per hospital in May, 0.333 studies per day per hospital in June, and 0.350 studies per day per hospital in July

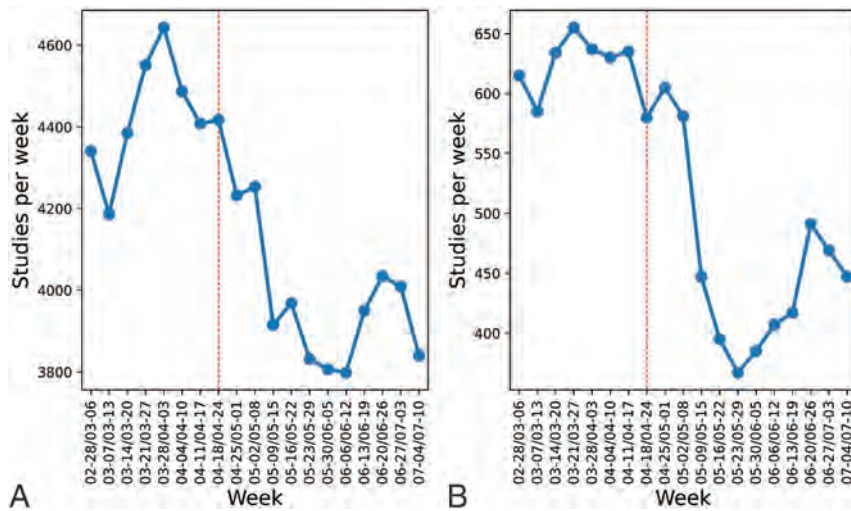


FIG 1. The weekly trend in daily counts of unique patients undergoing the study is presented. CTA (A) and CTP (B).

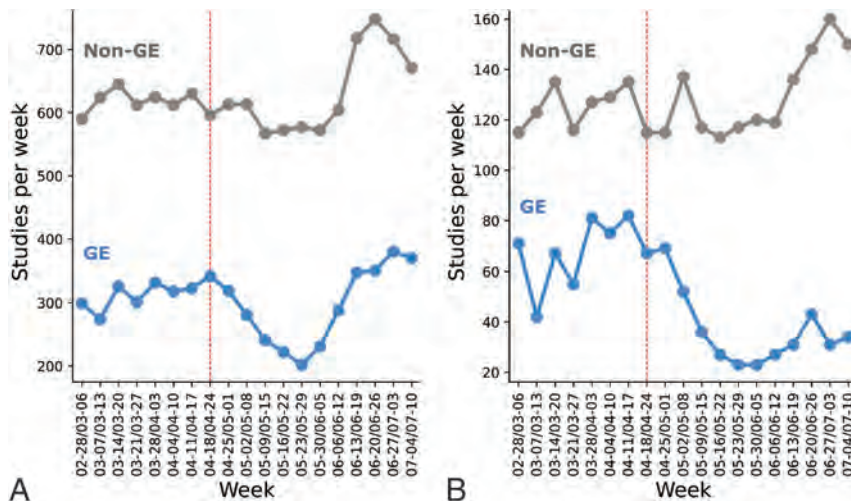


FIG 2. The weekly trend in daily counts of unique patients undergoing the study is presented according to manufacturer of contrast media used, CTA (A) and CTP (B). GE indicates GE Healthcare.

(Fig 1B). The lowest CTP count was 367 individual patients observed between May 23 and 29. A significant reduction in CTPs performed was seen in patients with Tmax values of zero ($P = .004$), <30 mL ($P = .004$), and 90–119 mL ($P = .003$), but not in those with values of 31–60 mL ($P = .14$), 61–90 mL ($P = .85$), and >120 mL ($P = .62$). A significant reduction in CTPs performed was seen in patients with rCBF values of zero ($P = .007$), <30 mL ($P = .04$), and 61–90 mL ($P = .04$), but not in those with values of 31–60 mL ($P = .16$), 90–119 mL ($P = .52$), and >120 mL ($P = .47$).

A nonsignificant reduction in CTAs using GE Healthcare contrast media was seen (12.42%, $P = .32$) but was not seen in CTAs using non-GE Healthcare contrast media (2.11%, $P = .55$) before and after April 19 in an analysis of data from 99 hospitals that provided the manufacturer of contrast media (Fig 2A). A significant reduction in CTPs using GE Healthcare contrast media

(43.06%, $P < .001$) was seen but not in CTPs using non-GE Healthcare contrast media (increased by 2.93%, $P = .29$) (Fig 2B). Among hospitals that used GE Healthcare contrast media, the daily counts of individual patients who underwent CTA decreased (a 25.06% reduction) in May from 0.550 studies per day per hospital in March to 0.412 studies per day per hospital in May. Among hospitals that used non-GE Healthcare contrast media, the daily counts of individual patients who underwent CTAs decreased (a 11.40% reduction) in May from 1.062 studies per day per hospital in March to 0.941 studies per day per hospital in May.

The daily counts of individual patients who underwent CTA decreased in Comprehensive Stroke Centers (a 11.36% reduction, $P = .027$) and Primary Stroke Centers (a 11.57% reduction, $P < .001$) but not in Thrombectomy-Capable Stroke Centers or Acute Stroke Ready Hospitals (a 2.27% decrease, $P = .72$, and a 1.86% increase, $P = .48$, respectively) before April 19 to after April 19 in an analysis of data from 130 hospitals, which provided certification status. The daily count of individual patients who underwent CTP decreased in Primary Stroke Centers (40.39%, $P = .004$) and Comprehensive Stroke Centers (31.94%, $P = .004$), with a nonsignificant increase in Acute Stroke Ready Hospitals (17.14%, $P = .48$) and Thrombectomy-Capable Stroke Centers (11.11%, $P = .056$).

In Comprehensive Stroke Centers, the daily counts of individual patients who underwent CTA decreased (a 17.32% reduction) from 4.043 studies per day per hospital in March to 3.343 studies per day per hospital in May (Fig 3A). The daily counts of individual patients who underwent CTA in June, 3.669 studies per day per hospital, and July, 2.404 studies per day per hospital, remained lower than in March. A corresponding pattern appears in CTPs in these centers with a 42.71% reduction in May, from 0.924 studies per day per hospital in March to 0.534 studies per day per hospital in May. The daily counts of individual patients who underwent CTP in June, 0.628 studies per day per hospital, and July, 0.615 studies per day per hospital, remained lower than in March (Fig 3B).

Overall, 6260 studies had alerts (positive LVO detection), and 72,793 studies did not have alerts. The proportion of patients with LVO alerts (ICA, M1 or M2) among those undergoing CTA did not change before and after April 19 (7.82% versus 7.98%, $P = .054$). However, the daily counts of individual patients with

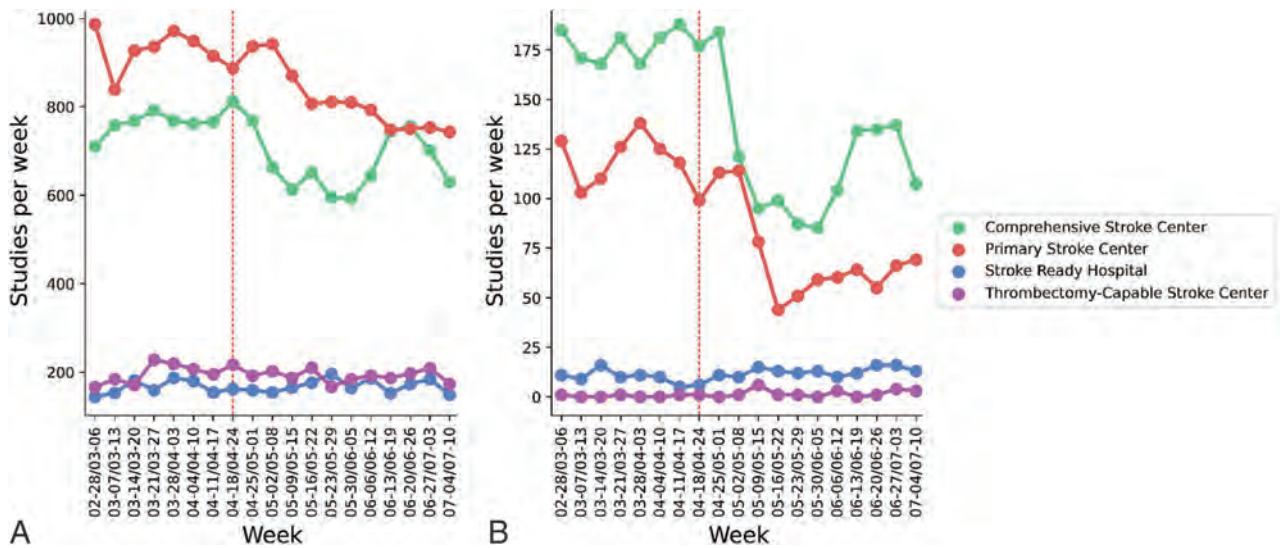


FIG 3. The weekly trend in daily counts of unique patients undergoing the study is presented according to type of hospital. CTA (A) and CTP (B).

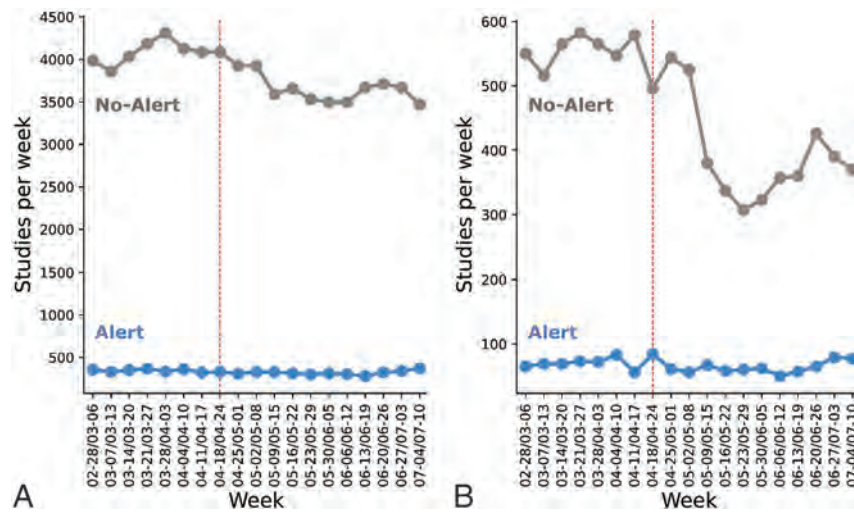


FIG 4. The weekly trend in daily counts of unique patients with LVO alert is presented. CTA (A) and CTP (B).

LVO decreased (a 7.69% reduction) from 0.124 per day per hospital before April 19 to 0.114 per day per hospital after April 19. The daily counts of individual patients with LVO in March (0.125 per day per hospital) remained higher than in May (0.112 per day per hospital) and June (0.110 per day per hospital); however, they increased in July (0.129 per day per hospital) (Fig 4). The proportions of patients with LVO alert according to hospital type before and after April 19 was as follows: Comprehensive Stroke Centers (9.47% and 9.75), Primary Stroke Centers (7.4% and 7.17%), Thrombectomy-Capable Stroke Center (8.68% and 7.82%), and Stroke Ready Hospitals (6.61% and 7.53%). Among patients who underwent CTP, the LVO alert rate increased from 12.56% to 16.09% after April 19 without any disproportionate changes in strata defined by CTP parameters of $T_{max} > 6$ seconds and $rCBF < 30\%$ (Online Supplemental Data).

DISCUSSION

Our analysis provides a quantitative estimate of the effect of contrast media shortage on the performance of CTA and CTP in patients with acute ischemic stroke derived from a large sample of health care systems in the United States. The daily counts of individual patients who underwent CTA decreased (a 9.6% reduction) after April 19. The magnitude of reduction was smaller than expected, presumably because many facilities routinely store variable amounts of GE Healthcare contrast media. There was also the availability of products by other contrast media suppliers such as iohexol and iopamidol and GE Healthcare's ability to provide approximately 20% of the demand.² Furthermore, increased use

of unenhanced imaging or alternate tests such as MR imaging and ultrasound for other body systems preserving contrast for CTA and CTP and use of reduced contrast media volume in CTA and CTP in patients with acute ischemic stroke may have resulted in a smaller (than expected) magnitude of reduction.^{6,8} Although the reduction in daily counts of individual patients undergoing CTA was seen immediately after April 19, the reduction in daily counts of individual patients undergoing CTP was not seen until the middle of May, suggesting that the reductions on various components of multimodal CT evaluations were not the same. The daily counts of individual patients undergoing CTA or CTP demonstrated an increase in counts toward the end of June, but the counts remained well below the counts seen before April 19. The lag in recovery was seen despite GE Healthcare reporting that production was up to 60% of baseline production by May 21, 2022, and up to 100% by June 8,

2022,¹⁴ and may be attributable to delays in distribution chains and/or continuation of acute stroke imaging protocols in institutions that avoided use of contrast media–based CTA and CTP.

The reduction in daily counts of individual patients undergoing CTA was consistent in various strata defined by the patient's age, with possibly a lesser reduction in patients younger than 40 years of age. There appeared to be a greater reduction in CTP in patients with either rCBF < 30% or Tmax > 6-second volume of zero or <30 mL. These parameters correlate with minor or resolving neurologic deficits,^{15,16} indicating that patients with ischemic strokes with minor deficits or those with TIAs were less likely to undergo CTPs during the period of contrast media shortage. The selective exclusion of patients with minor or resolving neurologic deficits from undergoing CTP appears to be one of the strategies to reduce the need for contrast because these patients are unlikely to be candidates for endovascular treatment.³

Reductions in daily counts of individual patients undergoing CTA and particularly CTP using GE Healthcare contrast media was seen but not in daily counts of individual patients undergoing CTA and CTP using non-GE Healthcare contrast media. There was an increase in daily counts of individual patients undergoing studies using non-GE Healthcare contrast media by late June to greater counts than those before April 19, suggesting that more institutions may have started using non-GE Healthcare contrast media to avoid any future reductions in supply. Overall, non-GE Healthcare contrast media was more commonly used in a study sample of hospitals before April 19, which may have reduced the overall impact of the contrast media shortage.

When stratified on the basis of the characteristics of hospitals, the reduction in daily counts of individual patients undergoing CTA and CTP was highest in Comprehensive Stroke Centers and Primary Stroke Centers. An important part of this magnitude of reduction was the much larger volume of studies performed in Comprehensive Stroke Centers. Comprehensive Stroke Centers have a large proportion of patients undergoing interventional procedures requiring contrast media, which may result in contrast media availability for the performance of CTA.^{17,18} Comprehensive Stroke Centers are usually based in larger hospitals with competing needs for contrast media–based imaging studies for patients with trauma and cardiac disease.^{19,20} The reduction in CTAs and CTPs at Comprehensive Stroke Centers may be partly attributed to more effective triage of patients with acute ischemic stroke, including the use of pre-hospital LVO-detection tools, transport paradigms, in-hospital workflows, acute stroke neuroimaging protocols, and angiography suite workflows.²¹ Comprehensive Stroke Centers may have greater access to emergent MR imaging and cerebral angiography, allowing substitution of or bypassing CTA and CTP for emergent neuroimaging in patients with acute ischemic stroke.

We did not identify any differences in the proportion of patients with LVO alerts among those undergoing CTA before or after April 19, despite the reduction in CTAs performed. The daily counts of individual patients with LVO alerts in March (0.125 per day per hospital) was higher than that seen in May (0.112 per day per hospital) and June (0.110 per day per hospital). The possibility of suboptimal detection of LVOs and adverse

effects on the quality of care is not supported by single-center studies.^{9,22} We cannot further analyze this possibility because the total number of patients with acute ischemic stroke presenting to the hospitals was not available, preventing us from determining the fraction of patients with acute ischemic stroke undergoing CTA before and after April 19. We found a greater reduction in daily counts of individual patients undergoing CTA among patients with less severe strokes (based on imaging criteria), also suggesting that patients at lower risk of LVO were selectively excluded from CTA. If we were to assume that only patients at a higher risk of LVO after initial screening based on clinical criteria and noncontrast CT were undergoing CTA and CTP, the proportion of LVO alerts should be higher. Therefore, it is more likely that other imaging modalities substituted for CTA and CTP.^{23–25}

There are several issues that require consideration before interpretation of the findings. The sample is based on all the 399 hospitals that use the Viz.ai imaging platform. The results presented here may not be reflective of practices at those hospitals that use the alternate Rapid.AI platform (<https://www.rapidai.com/about>)^{26,27} or do not use any imaging software despite CTA acquisitions. Several analyses such as those for reduction in daily counts of individual patients undergoing CTA according to the manufacturer of contrast media were performed on a smaller sample of patients. The comparison between CTA and CTP performed before and April 19 was restricted to the year 2022. A comparison with the same time period in 2021 was not reliable because the number of hospitals using the Viz.ai platform had increased and we could not adjust for differences in hospital number and characteristics in such a comparison. The short period of observation before contrast media shortage reduces the data available for analysis, subsequently reducing the power of the study and increasing the margin of error,²⁸ and reducing the inability to exclude seasonal fluctuations in the incidence of acute ischemic stroke.²⁹ The LVO alert and quantitation of infarction volume and hypoperfusion were based on using an automated algorithm, which has been previously validated.^{30,31} In an analysis of 650 CTAs performed in patients with acute ischemic stroke,³⁰ Viz.ai demonstrated a sensitivity of 82%, specificity of 94%, positive predictive value of 77%, and negative predictive value of 95% for the detection of LVO compared with an independent neuro-radiologist's interpretation. In another analysis of 2544 CTAs performed in patients with acute ischemic stroke in 139 US hospitals,³¹ Viz.ai demonstrated a sensitivity of 96% and specificity of 94% for the detection of LVO compared with an independent radiologist's interpretation.

However, we acknowledge that detection of LVOs was not based on the interpretation of an independent neuroradiologist in our study and cannot exclude the possibility of false-positive and false-negative alerts. The anonymized data used in the analysis do not provide any access to patient records and other imaging modalities used. We were unable to document the magnitude of increase in the use of other imaging or diagnostic approaches (such as MR imaging) during the study period. We were also unable to determine whether there were changes in the criteria for selecting patients for CTA and CTP after April 19 and whether there were any differences in quality indicators such as in the time interval between hospital arrival and endovascular

treatment or in patient outcomes. We were also unable to assess whether institutions changed the dose of contrast media administered and used a lower dose after April 19. A single-center study⁹ did not identify any change in the rates of successful reperfusion, average time to recanalization, average radiation dose, and favorable outcome at discharge before and after the contrast media shortage. We also acknowledge that mitigation strategies at institutions may be dynamic and various strategies (as mentioned earlier) may have been used at different time points. We are also unable to comment on the effect of the contrast media shortage on CTA performed for other indications such as for detection of intracranial aneurysms or traumatic vascular injuries.

CONCLUSIONS

Our analysis reported changes in the use of CTA and CTP in patients with acute ischemic stroke and identified some of the factors that influenced the change in use during contrast media shortage. Future studies should go into greater depth in studying the contrast media shortage–related changes with particular emphasis on the effect on the quality of care and patient outcomes. Several strategies were implemented in various institutions during the contrast media shortage, including increased use of alternate tests such as MR imaging, reducing contrast media volume, and increased reliance on clinical criteria and noncontrast CT scans.^{6,8,9} Data accrued during the period of contrast media shortage may help in identifying effective strategies to reduce reliance on contrast media–based studies such as CTA and CTP²³ without compromising patient outcomes.

Disclosure forms provided by the authors are available with the full text and PDF of this article at www.ajnr.org.

REFERENCES

- Iohexol Injection. 2023. <https://www.ashp.org/drug-shortages/current-shortages/drug-shortage-detail.aspx?id=830&loginreturnUrl=SSOCheckOnly>. Accessed 12–10, 2022
- Grist TM, Canon CL, Fishman EK, et al. **Short-, mid-, and long-term strategies to manage the shortage of iohexol.** *Radiology* 2022;304:289–93 CrossRef Medline
- Powers WJ, Rabinstein AA, Ackerson T, et al. **Guidelines for the Early Management of Patients with Acute Ischemic Stroke: 2019 Update to the 2018 Guidelines for the Early Management of Acute Ischemic Stroke—a Guideline for Healthcare Professionals from the American Heart Association/American Stroke Association.** *Stroke* 2019;50:e344–418 CrossRef Medline
- Turc G, Bhogal P, Fischer U, et al. **European Stroke Organisation (ESO): European Society for Minimally Invasive Neurological Therapy (ESMINT) Guidelines on Mechanical Thrombectomy in Acute Ischaemic Stroke Endorsed by Stroke Alliance for Europe (SAFE).** *Eur Stroke J* 2019;4:6–12 CrossRef Medline
- Considerations for Imaging Contrast Shortage Management and Conservation.** 2022. <https://www.ashp.org/drug-shortages/shortage-resources/considerations-for-imaging-contrast-shortage-management?loginreturnUrl=SSOCheckOnly>. Accessed 12–10 2022
- Davenport MS, Chu P, Szczykutowicz TP, et al. **Comparison of strategies to conserve iodinated intravascular contrast media for computed tomography during a shortage.** *JAMA* 2022;328:476–78 CrossRef Medline
- Wang CL, Asch D, Cavallo J, et al. **Statement from the ACR Committee on Drugs and Contrast Media on the intravenous iodinated contrast media shortage.** *J Am Coll Radiol* 2022;19:834–35 CrossRef Medline
- Bammer R, Amukotuwa SA. **Navigating supply chain disruptions of iodinated contrast agent for neuroimaging and how business intelligence can help the decision process.** *AJNR Am J Neuroradiol* 2022;43:944–50 CrossRef Medline
- Almallouhi E, Sattur M, Lajthia O, et al. **Contrast conservation measures during the global iohexol contrast shortage crisis did not affect stroke thrombectomy outcomes.** *J Neurointerv Surg* 2022 July 26 [Epub ahead of print] CrossRef Medline
- Amukotuwa SA, Jackson D, Bammer R. **Iodinated contrast media conservation measures during a global shortage: effect on contrast media use at a large health system.** *AJR Am J Roentgenol* 2022;219:983 CrossRef Medline
- Guidance Regarding Methods for De-identification of Protected Health Information in Accordance with the Health Insurance Portability and Accountability Act (HIPAA) Privacy Rule. <https://www.hhs.gov/hipaa/for-professionals/privacy/special-topics/de-identification/index.html>. Accessed February 20, 2023
- Ferretti A, Ienca M, Hurst S, et al. **Big data, biomedical research, and ethics review: new challenges for IRBs.** *Ethics Hum Res* 2020;42:17–28 CrossRef Medline
- The Joint Commission. **Stroke Certification.** <https://www.jointcommission.org/what-we-offer/certification/certifications-by-setting/hospital-certifications/stroke-certification/>. Accessed February 20, 2023
- GE Healthcare Issues Update on Iodinated Contrast Media.** 2022. <https://www.itnonline.com/content/ge-healthcare-issues-update-iodinated-contrast-media>. Accessed December 10, 2022
- Boxerman JL, Jayaraman MV, Mehan WA, et al. **Clinical stroke penumbra: use of National Institutes of Health Stroke Scale as a surrogate for CT perfusion in patient triage for intra-arterial middle cerebral artery stroke therapy.** *AJNR Am J Neuroradiol* 2012;33:1893–1900 CrossRef Medline
- Furlanis G, Ajcović M, Stragapede L, et al. **Ischemic volume and neurological deficit: correlation of computed tomography perfusion with the National Institutes of Health Stroke Scale Score in acute ischemic stroke.** *J Stroke Cerebrovasc Dis* 2018;27:2200–07 CrossRef Medline
- Alberts MJ, Latchaw RE, Selman WR, et al; Brain Attack Coalition. **Recommendations for comprehensive stroke centers.** *Stroke* 2005;36:1597–616 CrossRef Medline
- Grigoryan M, Chaudhry SA, Hassan AE, et al. **Neurointerventional procedural volume per hospital in United States.** *Stroke* 2012;43:1309–14 CrossRef Medline
- Guidera SA, Aggarwal S, Walton JD, et al. **Mechanical thrombectomy for acute ischemic stroke in the cardiac catheterization laboratory.** *JACC Cardiovasc Interv* 2020;13:884–91 CrossRef Medline
- Khan AA, Chaudhry SA, Hassan AE, et al. **Potential synergy between advanced primary stroke centers and level I or II trauma centers in the United States.** *Am J Emerg Med* 2012;30:1535–39 CrossRef Medline
- Ospel JM, Dmytriw AA, Regenhardt RW, et al. **Recent developments in pre-hospital and in-hospital triage for endovascular stroke treatment.** *J Neurointerv Surg* 2022 Oct 14 [Epub ahead of print] CrossRef Medline
- Salazar G, Mossa-Basha M, Kohi MP, et al. **Short-term mitigation steps during the iohexol contrast shortage: a single institution's approach.** *J Am Coll Radiol* 2022;19:841–45 CrossRef Medline
- Nguyen TN, Abdalkader M, Nagel S, et al. **Noncontrast computed tomography vs computed tomography perfusion or magnetic resonance imaging selection in late presentation of stroke with large-vessel occlusion.** *JAMA Neurol* 2022;79:22–31 CrossRef Medline
- Requena M, Olivé-Gadea M, Muchada M, et al. **Direct to angiography suite without stopping for computed tomography imaging for patients with acute stroke: a randomized clinical trial.** *JAMA Neurol* 2021;78:1099–1107 CrossRef Medline
- Mayer SA, Viarasilpa T, Panyavachiraporn N, et al. **CTA-for-all: impact of emergency computed tomographic angiography for all**

- patients with stroke presenting within 24 hours of onset. *Stroke* 2020;51:331–34 CrossRef Medline
26. Kansagra AP, Goyal MS, Hamilton S, et al. **Collateral effect of Covid-19 on stroke evaluation in the United States.** *N Engl J Med* 2020;383:400–401 CrossRef Medline
 27. Kansagra AP, Goyal MS, Hamilton S, et al. **Stroke imaging utilization according to age and severity during the COVID-19 pandemic.** *Radiology* 2021;300:E342–44 CrossRef Medline
 28. Boyko EJ. **Observational research: opportunities and limitations.** *J Diabetes Complications* 2013;27:642–48 CrossRef Medline
 29. Oberg AL, Ferguson JA, McIntyre LM, et al. **Incidence of stroke and season of the year: evidence of an association.** *Am J Epidemiol* 2000;152:558–64 CrossRef Medline
 30. Chatterjee A, Somayaji NR, Kabakis IM. **Artificial intelligence detection of cerebrovascular large vessel occlusion: nine month, 650 patient evaluation of the diagnostic accuracy and performance of the Viz.ai LVO algorithm.** *Stroke* 2019;50(Suppl 1):AWMP16-AWMP16 CrossRef
 31. Golan D, Shalitin O, Mates J, et al. **AI-powered stroke triage system performance in the wild.** *J Exp Stroke Transl Med* 2020;12:3

The Iodinated Contrast Crisis of 2022: A Near Miss or a Missed Opportunity?

The unprecedented global shortage of iodinated contrast media (ICM), commencing in late April 2022, was a direct result of excessive global reliance on one manufacturer, GE Healthcare, which produced much of its most widely used ICM, iohexol (Omnipaque), at a facility in Shanghai, China.^{1,2} When Shanghai was plunged into a coronavirus disease 2019 (COVID-19) lockdown, production ceased abruptly. Just-in-time inventory management and production strategies, aimed at reducing costs, left the world with no stockpile to turn to, while GE Healthcare's other factory in Ireland and other ICM vendors did not have the capacity to scale up production at such short notice to meet the global demand. Fortunately, because Shanghai came out of lockdown and GE Healthcare's factory returned to full operating capacity in June, the period of critical ICM scarcity lasted just a few months. However, this near miss taught us some important lessons when it comes to critical medical supplies: Diversification is essential, even if it is costly, and health care services must consider self-sufficiency in the face of vulnerable global supply chains, whether it be through local production or amassing sufficient stockpiles.

Early in the crisis, professional interest groups and journals, including the American College of Radiology and the *American Journal of Roentgenology*, issued guidance to affected health care services on how to rationalize ICM usage and conserve supplies for indications essential to patient care.^{2,3} One of these critical indications is acute ischemic stroke (AIS). ICM is required for guiding endovascular thrombectomy and also for diagnosis because most centers in North America rely on multimodal CT, with CTA and CTP, to triage patients presenting with suspected ischemic stroke to treatment. We provided guidance, published in this journal, on how to both reduce and avoid ICM usage in AIS imaging.¹ Approaches included the following: modifying CT scan protocols to allow CTA and CTP to be performed with smaller volumes of ICM; improving triage to multimodal stroke CT by mandating that stroke neurologists, rather than trainees or emergency physicians, assess patients; and using MR imaging instead of CT. Individual institutions were advised to tailor their strategy, depending on their ICM supplies, availability of local expertise, and access to emergent MR imaging.

Now that the crisis is over, we are presented with a unique opportunity to review and study the impact of these interventions.

What did we learn? Can we get away with doing fewer multimodal stroke CT scans? Is diversion to MR imaging feasible, and should we be using this technique instead?

The study by Qureshi et al⁴ in this issue of the *American Journal of Neuroradiology* sheds some light on the subject. The authors provide a quantitative estimate of the effect of the ICM shortage on the use of multimodal stroke CT by reviewing processing logs of the 399 hospital install-base of the Viz.ai (<https://www.viz.ai/>) software in the United States. There was a significant reduction in the volume of CTAs and CTPs performed, of 9.6% and 25.9%, respectively, compared with the period before the crisis. There was a disproportionately high reduction in the number of CTPs yielding either no perfusion lesion or a small one, suggesting that multimodal stroke CT was avoided in patients with mild deficits and transient symptoms. Instead, only those patients with more severe symptoms, suggesting a larger volume of eloquent tissue at risk and thus a higher likelihood of a large-vessel occlusion (LVO), were triaged to CTA and CTP.

This practice aligns with the original purpose of CTP, to select patients for endovascular treatment. However, patients with LVOs can present with mild symptoms, due to involvement of the nondominant hemisphere or good collaterals.⁵ Furthermore, medium-vessel occlusions, which typically present with milder deficits, are increasingly considered for thrombectomy because even mild deficits can cause severe disability in individual patients.⁶ Thus, this strategy may have resulted in worse outcomes for some patients. An audit of stroke clinic data, including follow-up imaging, is needed to ascertain whether treatable strokes, including those due to LVOs, were missed by scanning fewer patients. In addition, multimodal CT is used increasingly in patients with milder symptoms to exclude a vascular cause for presentation. Reassurance provided by normal scan findings may allow patients to be discharged home from the emergency department with early outpatient follow-up. This is, therefore, a valuable opportunity to review our practice and examine the impact of more stringent criteria for triage to multimodal CT on stroke care, including hospitalization rates.

The crisis also provided health care systems with a golden opportunity to revisit using emergent MR imaging for triage of AIS

patients to treatment. While CT is easier to access in the emergent setting, MR imaging with DWI is the criterion standard for identifying infarcted brain tissue.⁷⁻⁹ It is, therefore, the standard-of-care first-line imaging technique for assessing patients with AIS in Europe and some centers in North America. DSC PWI was the method used for delineating the ischemic penumbra in early thrombectomy studies, and MR imaging diffusion-perfusion mismatch to select patients for thrombectomy has been well-validated.¹⁰ MR imaging also has the advantage of offering an entirely noninvasive technique, which requires no contrast agent injection, for assessing the penumbra: arterial spin-labeling perfusion.¹¹

Because our institution, a comprehensive stroke center, had access to a software that is FDA-cleared for performing MR imaging-based mismatch analysis, RapidAI (<https://www.rapidai.com/>), we seized the opportunity to implement a fast (around 5 minutes) acute stroke MR imaging protocol. While we were able to divert some patients to MR imaging, we encountered several obstacles: First, access to emergent MR imaging was more challenging than anticipated. Due to the high demand for MR imaging examinations, both our inpatient and outpatient scanners were heavily overbooked, making it challenging even to fit in a short scan. We also found that our MR imaging technologists are less accustomed to emergent workflows and fast scan turnaround than our CT technologists. We learned, therefore, that while emergent MR imaging for triage to thrombectomy is feasible, it requires a streamlined workflow with staggered bookings and sufficient time to “squeeze in” patients with stroke. Plenty of practice is also needed to embed these fast workflows and bring MR imaging technologists up to speed. Audits from institutions that switched to predominantly or exclusively MR imaging, including the effect on door-to-needle times, would therefore be needed “to identify effective strategies to reduce reliance on contrast media-based studies, such as CTAs/CTPs, without compromising patient outcomes,” as suggested by the authors.

Unfortunately, because Viz.ai does not have FDA clearance for LVO detection and mismatch analysis on MR imaging, the authors did not have access to data on MR imaging scan numbers to determine whether diversion occurred in their installed bases and, if so, to what extent. In addition, the impact of using MR imaging instead of CT on door-to-needle time could not be assessed because the software was not used for care co-ordination of these patients, leading to a loss of valuable data on workflow on which health care systems may rely.

In conclusion, the study from Qureshi et al⁴ provides us with a glimpse of the effect of the ICM crisis on acute stroke imaging in the United States. However, it also raises many important

questions that must be answered through audits of individual health care services in order to not miss a valuable opportunity to gain insights that can improve stroke care.

REFERENCES

1. Bammer R, Amukotuwa SA. Navigating supply chain disruptions of iodinated contrast agent for neuroimaging and how business intelligence can drive decisions. *AJNR Am J Neuroradiol* 2022;43:944–50 CrossRef Medline
2. Cavallo J, Pahade J. Practice management strategies for imaging facilities facing an acute iodinated contrast media shortage. *AJR Am J Roentgenol* 2022;219:666–70 CrossRef Medline
3. ACR Committee on Drugs and Contrast Media Brief Statement on Nomenclature for Symptoms Associated with Gadolinium-Based Contrast Agent Exposure (SAGE). https://www.acr.org/-/media/ACR/Files/Clinical-Resources/SAGE-Paragraph_-_FINAL.pdf. Accessed May 13, 2022
4. Qureshi AI, Grintal A, DeGaetano AC, et al. Effect of radiographic contrast media shortage on stroke evaluation in the United States. *AJNR Am J Neuroradiol* 2023;44:901–07 CrossRef Medline
5. Maas MB, Furie KL, Lev MH, et al. National Institutes of Health Stroke Scale score is poorly predictive of proximal occlusion in acute cerebral ischemia. *Stroke* 2009;40:2988–93 CrossRef Medline
6. Saver JL, Chapot R, Agid R, et al; Distal Thrombectomy Summit Group. Thrombectomy for distal, medium vessel occlusions: a consensus statement on present knowledge and promising directions. *Stroke* 2020;51:2872–84 CrossRef Medline
7. Campbell BC, Purushotham A, Christensen S, et al; EPITHET-DEFUSE Investigators. The infarct core is well represented by the acute diffusion lesion: sustained reversal is infrequent. *J Cereb Blood Flow Metab* 2012;32:50–56 CrossRef Medline
8. Gill R, Sibson NR, Hatfield RH, et al. A comparison of the early development of ischaemic damage following permanent middle cerebral artery occlusion in rats as assessed using magnetic resonance imaging and histology. *J Cereb Blood Flow Metab* 1995;15:1–11 CrossRef Medline
9. Gonzalez RG, Schaefer PW, Buonanno FS, et al. Diffusion-weighted MR imaging: diagnostic accuracy in patients imaged within 6 hours of stroke symptom onset. *Radiology* 1999;210:155–62 CrossRef Medline
10. Lansberg MG, Straka M, Kemp S, et al; DEFUSE 2 Study Investigators. MRI profile and response to endovascular reperfusion after stroke (DEFUSE 2): a prospective cohort study. *Lancet Neurol* 2012;11:860–67 CrossRef Medline
11. Zaharchuk G, El Mogy IS, Fischbein NJ, et al. Comparison of arterial spin labeling and bolus perfusion-weighted imaging for detecting mismatch in acute stroke. *Stroke* 2012;43:1843–48 CrossRef Medline

©S.A. Amukotuwa
R. Bammer

Department of Diagnostic Imaging
Department of Radiology
Monash University, Melbourne, Australia

<http://dx.doi.org/10.3174/ajnr.A7940>

Brain Parcellation Repeatability and Reproducibility Using Conventional and Quantitative 3D MR Imaging

J.B.M. Warntjes, P. Lundberg, and A. Tisell

ABSTRACT

BACKGROUND AND PURPOSE: Automatic brain parcellation is typically performed on dedicated MR imaging sequences, which require valuable examination time. In this study, a 3D MR imaging quantification sequence to retrieve R_1 and R_2 relaxation rates and proton density maps was used to synthesize a T1-weighted image stack for brain volume measurement, thereby combining image data for multiple purposes. The repeatability and reproducibility of using the conventional and synthetic input data were evaluated.

MATERIALS AND METHODS: Twelve subjects with a mean age of 54 years were scanned twice at 1.5T and 3T with 3D-QALAS and a conventionally acquired T1-weighted sequence. Using SyMRI, we converted the R_1 , R_2 , and proton density maps into synthetic T1-weighted images. Both the conventional T1-weighted and the synthetic 3D-T1-weighted inversion recovery images were processed for brain parcellation by NeuroQuant. Bland-Altman statistics were used to correlate the volumes of 12 brain structures. The coefficient of variation was used to evaluate the repeatability.

RESULTS: A high correlation with medians of 0.97 for 1.5T and 0.92 for 3T was found. A high repeatability was shown with a median coefficient of variation of 1.2% for both T1-weighted and synthetic 3D-T1-weighted inversion recovery at 1.5T, and 1.5% for T1-weighted imaging and 4.4% for synthetic 3D-T1-weighted inversion recovery at 3T. However, significant biases were observed between the methods and field strengths.

CONCLUSIONS: It is possible to perform MR imaging quantification of R_1 , R_2 , and proton density maps to synthesize a 3D-T1-weighted image stack, which can be used for automatic brain parcellation. Synthetic parameter settings should be reinvestigated to reduce the observed bias.

ABBREVIATIONS: 3D-QALAS = 3D-quantification using an interleaved Look-Locker acquisition sequence with T2 preparation pulse; BPV = brain parenchymal volume; CoV = coefficient of variation; ICV = intracranial volume; NQ = NeuroQuant; PD = proton density; syTIWI = synthetic 3D-T1-weighted inversion recovery

Various postprocessing programs can be used to quantify specific features of the brain, such as the size of structures or lobes, or tissue characteristics of the entire brain. Unfortunately, each program typically is associated with its own dedicated MR imaging sequence required for optimal performance. To minimize the examination time burden, we aimed to investigate whether quantitative MR imaging data can be used to synthesize the necessary T1-weighted images for automatic brain parcellation. A 3D quantification sequence, called 3D-QALAS, was recently adapted

from cardiac^{1,2} to brain applications³⁻⁶ and can measure the R_1 and R_2 relaxation rates and proton density (PD) at high resolution in a relatively short scan time. By means of these parameter maps, global brain volumes and local tissue characteristics can be measured. Brain parcellation programs such as NeuroQuant (CorTech Labs),⁷⁻¹² however, cannot work with these maps directly but require a 3D-T1-weighted image stack as input. Such images can be generated from the R_1 , R_2 , and PD maps using synthetic MR imaging.¹³⁻¹⁵ It may, therefore, be possible to collect both the quantitative maps and the necessary input for brain parcellation in a single sequence.

Aims of this study 1) were to compare volume estimation using either a conventionally acquired T1-weighted sequence or a synthesized T1-weighted image stack for NeuroQuant, 2) to compare the volume estimation using NeuroQuant and SyMRI (SyntheticMR), 3) and to investigate the repeatability and reproducibility of volume estimation of NeuroQuant and SyMRI at 1.5T and 3T.

Received November 18, 2022; accepted after revision June 14, 2023.

From the Centre for Medical Image Science and Visualization (J.B.M.W.), Department of Radiation Physics (P.L., A.T.), and Department of Health, Medicine and Caring Sciences (P.L., A.T.), Linköping University, Linköping, Sweden; and SyntheticMR (J.B.M.W.), Linköping, Sweden.

Please address correspondence to J.B.M. Warntjes, MD, Center for Medical Imaging Science and Visualisation, Linköping University Hospital, 58185 Linköping, Sweden; e-mail: marcel.warntjes@cmiv.liu.se

<http://dx.doi.org/10.3174/ajnr.A7937>

MATERIALS AND METHODS

Subjects

Twelve volunteers, 6 women and 6 men, were prospectively included in the study. Their age was 54 (SD, 14) years, ranging from 29 to 70 years of age (median, 53 years). No medical information was provided other than that they were self-reported healthy, and no subject was excluded on the basis of image appearance, motion artifacts, or potential other issues. The regional ethics review board approved the study (Linköping University, Dnr 2015 13–31). Informed written consent was obtained from all volunteers.

MR Imaging Acquisition Methods

For the NeuroQuant sequence, the recommended settings for the 3D-T1-weighted inversion recovery were used. At 1.5T, a sagittal acquisition was acquired with an FOV = 230 mm and matrix = 192, providing 1.2-mm isotropic resolution, reconstructed to 1.0-mm resolution (matrix = 240), with a coverage of 160 slices. TE was 4.0 ms, TR was 8.6 ms, and the flip angle was 8°. The shot interval was 2300 ms (ETL 153), and the inversion prepulse delay was 1000 ms. For 3T, the parameters were identical, except that the shot interval was 2500 ms and the flip angle was 9° instead. The scan time was 6 minutes 10 seconds for both field strengths.

3D-QALAS consists of 5 segmented 3D gradient-echo acquisitions that are acquired in parallel. The TE was 2.3 ms, and the TR was 5.0 ms, repeated 150 times, resulting in an acquisition time of 750 ms for each acquisition 1–5. The delay time between the acquisitions was set to 150 ms, making the total cycle time $5 \times 900 \text{ ms} = 4.5$ seconds. The flip angle was 4°. Before the first acquisition, an R₂-sensitizing phase was applied, consisting of a hard 90° radiofrequency pulse, 4 adiabatic 180° refocusing pulses, and a hard –90 pulse (TE = 100 ms). Before the second acquisition, an R₁ sensitizing phase was applied, consisting of an adiabatic inversion pulse. The sagittal acquisition orientation, the FOV of 230 mm, the acquisition matrix of 192, the reconstruction matrix of 240, and the number of slices of 160 were set identical to those of the conventional acquisition. The scan time was matched to 6 minutes 10 seconds using a sensitivity encoding factor of 2.2.

The scanners were a 1.5T dStream Achieva and a 3T Ingenia (Philips Healthcare), with a patched software, Release 5.3.0. All subjects were scanned twice and removed from the scanner between the 2 examinations, at both field strengths, resulting in 8 data sets per patient, with a total of 96 scans.

Processing

Processing of the 3D-QALAS data was performed by a prototype version (18Q3) of SyMRI. Processing time was 20 seconds on a regular laptop, generating R₁, R₂, and PD maps to create the synthetic 3D-T1-weighted inversion recovery (syT1WI) images with the recommended settings from NeuroQuant (shot interval/delay time = 2300/1000 ms and 2500/100 ms at 1.5T and 3T, respectively). The intracranial volume, brain parenchymal volume (BPV), white matter volume, gray matter volume, and CSF volume were automatically calculated by SyMRI. At the time of volume analysis, a newer version of the prototype was released, which was used instead (22Q2).

The 96 T1-weighted and syT1WI image stacks were uploaded to NeuroQuant, and a PDF report was obtained in about 15 minutes per data set. The report provided 13 items: forebrain parenchyma, cortical gray matter, superior lateral ventricle, inferior lateral ventricle, hippocampus, amygdala, caudate, putamen, pallidum, thalamus, cerebellum, intracranial volume, and BPV. The BPV was defined as the sum of the forebrain parenchyma, cortical gray matter, hippocampus, amygdala, caudate, putamen, pallidum, thalamus, and cerebellum. Gray matter, white matter, and CSF volumes were not specified as separate items, and for this study, the gray matter volume was calculated as the sum of cortical gray matter, hippocampus, amygdala, caudate, putamen, pallidum, thalamus, and half the volume of the cerebellum. White matter volume was calculated as BPV minus gray matter volume; and CSF volume, as intracranial volume (ICV) minus BPV.

Statistics

In this study, repeatability was defined as the investigation of multiple measurements using the same method at the same field strength. Repeatability was expressed as a coefficient of variation (CoV), the ratio of the SD, and the mean of the measurements. Reproducibility was defined as the investigation of multiple measurements using different measurements or on different field strengths. The reproducibility was investigated using Bland-Altman statistics (mean, bias, SD) and the correlation coefficient *r*. Differences in reproducibility were evaluated using a paired *t* test, in which *P* < .05 was considered significant.

RESULTS

The typical appearance of the conventional and synthetic 3D-T1-weighted images is shown in Fig 1 in sagittal, coronal, and axial reformats. Visual inspection shows a very similar white matter–gray matter contrast, but a somewhat sharper appearance in the synthetic images. Of the 96 data sets uploaded to NeuroQuant, 9 failed to provide segmentation results (9.4%), 5 were based on conventional T1-weighted images (2 at 1.5T and 3 at 3T), and 4 were based on syT1WI (all at 3T). All SyMRI volumes produced a segmentation result.

As shown in Table 1, processing with conventional and synthetic T1-weighted images resulted in a consistently smaller ICV for the syT1WI images, on average, 61 mL for 1.5T and 116 mL for 3T (3.8% and 7.2%, respectively) and a smaller BPV (–49 mL and –103 mL, respectively). A Bland-Altman plot for ICV and BPV is shown in Fig 2. The smaller volumes for the syT1WI images are also observed in all brain structures. For most structures, however, the bias was not significant due to the relatively large variation of the segmentation results with respect to their mean volume. Both bias and SD were generally larger at 3T than at 1.5T. A high correlation was found for all the brain structures, with a median of *r* = 0.97 for 1.5T and *r* = 0.92 for 3T.

In Table 2, the repeatability of the segmentation volumes is shown for measurements 1 and 2 at the same field strengths. A small CoV was observed for all brain structures, with a median CoV of 1.2% for both T1-weighted and syT1WI at 1.5T and 1.5% for T1-weighted and 4.4% for syT1WI at 3T. A large CoV, exceeding 10%, was found for the pallidum using T1-weighted imaging at 1.5T and for the lateral ventricles using syT1WI at 3T.

The segmentation results for WM, GM, CSF, BPV, and ICV were compared between 1.5T and 3T. In Table 3, the mean, bias, SD, and correlation coefficient are listed for the conventional T1W (NQ), syT1WI, and SyMRI. Significant differences were observed between the field strengths, especially for the syT1WI NQ. The mean bias for syT1WI was 68 mL, while for T1-weighted imaging, it was only 23 mL. The mean SD of the syT1WI, however, was 22 mL, while for T1-weighted imaging, it was 79 mL. For SyMRI, the mean SD was 22 mL. The correlation of the volumes was lowest for the T1-weighted NQ (mean, 0.82)

and highest for syT1WI NQ (mean, 0.96) and SyMRI (mean, 0.96). For illustration, the ICV and BPV are shown in a Bland-Altman plot in Fig 3. The repeatability is shown in Table 4, providing low CoV values for both field strengths.

DISCUSSION

Our study showed that it is possible to generate synthetic syT1WIs on the basis of quantification maps of R_1 , R_2 , and PD, which are readily processed by NeuroQuant as if they were conventionally acquired T1-weighted images. Four data sets of the 48 with syT1WI data failed to provide a result, though that may be normal behavior in view of the 5 of the 48 conventional T1-weighted image stacks that also failed. Most of the failed stacks were acquired at 3T, but the numbers were too small to be decisive on whether field strength played a role.

A significant bias in the segmentation results between T1-weighted imaging and syT1WI was observed, in combination with a low SD and a high correlation coefficient between them (Table 1). A similar observation was made when comparing the methods on both field strengths (Table 3). These results suggest a field strength-dependent systematic error rather than a random error. The likely reason is the slightly different contrast in the conventional T1-weighted image and syT1WI images. Most voxels in the data sets experience some level of partial volume effect of gray matter, white matter, and CSF, and a slight contrast change could lead to substantial volume changes. To



FIG 1. Representative example of a sagittal, coronal, and axial reformat of the 3D-T1-weighted image stack at 1.2-mm isotropic resolution at a scan time of 6 minutes 10 seconds. The subject is a man, 54 years of age. Upper row (A), conventional T1-weighted NeuroQuant sequence. Lower row (B), synthetic T1-weighted image, created from the R_1 , R_2 , and PD maps (SyMRI 22Q2).

Table 1: Reproducibility of volume estimation of various brain structures using NeuroQuant with either a conventional or synthetic T1-weighted image stack as input^a

	syT1WI-T1-Weighted NQ 1.5T				syT1WI-T1-Weighted NQ 3T			
	Mean (mL)	Bias (mL)	SD (mL)	<i>r</i>	Mean (mL)	Bias (mL)	SD (mL)	<i>r</i>
Forebrain parenchyma	1084	-37	14	1.00	1041	-80	34	0.98
Cortical gray matter	506	8.3	14	0.98	492	-25	17	0.97
Superior lateral ventricle	29	-2.2	1.4	0.99	27	0.8	3.7	0.84
Inferior lateral ventricle	1.7	0.0	0.2	0.97	1.7	-0.1	0.3	0.78
Hippocampus	7.5	-0.8 ^b	0.3	0.97	7.4	-0.7 ^b	0.3	0.94
Amygdala	3.3	-0.2	0.2	0.95	3.5	-0.6 ^b	0.2	0.84
Caudate	6.0	0.1	0.5	0.87	6.0	-0.3	0.6	0.83
Putamen	11	-2.1 ^b	0.5	0.94	11	-2.2 ^b	0.6	0.87
Pallidum	1.4	0.1	0.2	0.84	1.7	-0.1	0.1	0.90
Thalamus	15	-0.3	0.8	0.90	15	-2.1 ^b	0.6	0.96
Cerebellum	145	-7.3	2.3	0.98	141	-16 ^b	4.2	0.90
ICV	1619	-61 ^b	17	1.00	1610	-116 ^b	19	0.99
BPV	1273	-49 ^b	16	1.00	1226	-103 ^b	36	0.98
WMV	651	-50	22	0.97	622	-82	64	0.98
GMV	621	1	13	0.99	608	-62	72	0.97
CSFV	346	-13	20	0.93	384	-10	25	0.82

Note:—WMV indicates white matter volume; GMV, gray matter volume; CSFV, CSF volume.

^a Expressed as mean volume, bias, and SD of the difference and correlation coefficient *r*, at 1.5T and 3T.

^b Significant ($P < .05$).

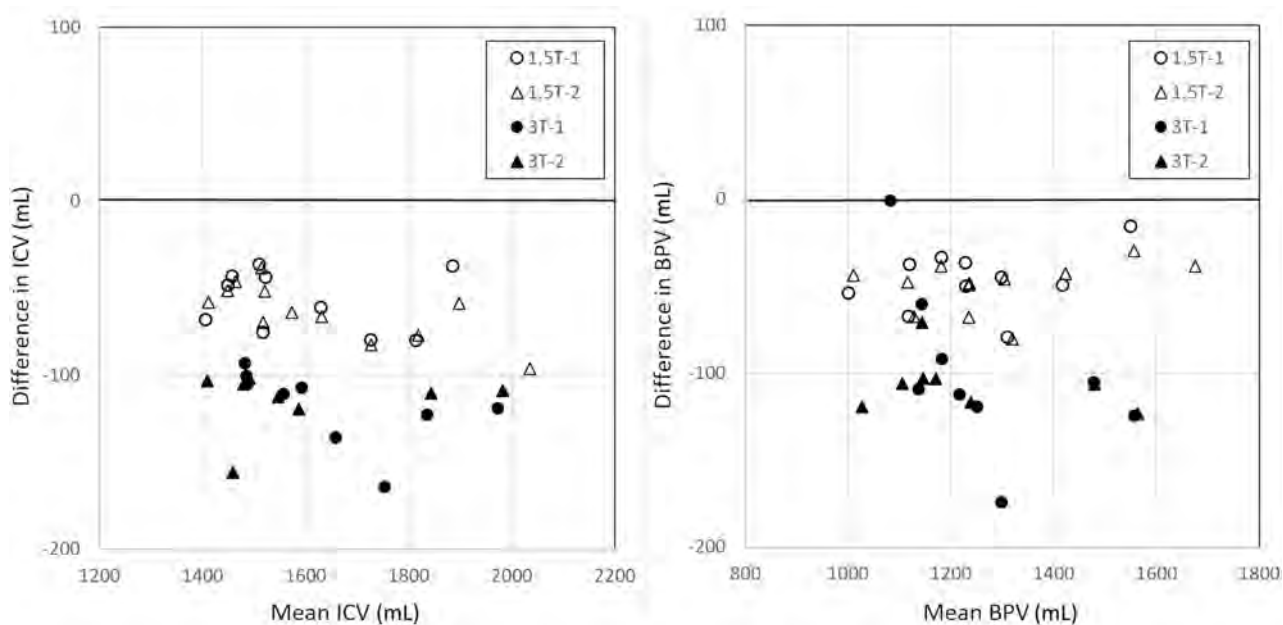


FIG 2. Bland-Atman plot with NQ segmentation results for ICV and BPV, in which T1-weighted and syTIWI were pooled as input data to focus on reproducibility at 2 different field strengths, irrespective of acquisition type. Measurements 1 (circles) and 2 (triangles) were plotted separately for both field strengths. There is a substantial bias, with lower ICV and BPV when using syTIWI. The bias is larger at 3T than at 1.5T.

Table 2: Repeatability of volume estimation of various brain structures using NeuroQuant with either a conventional or synthetic T1-weighted image stack as input^a

	T1-Weighted 1.5T	syTIWI 1.5T	T1-Weighted 3T	syTIWI 3T
Forebrain parenchyma	0.6	0.7	0.6	4.0
Cortical gray matter	1.2	1.0	1.5	4.4
Superior lateral ventricle	1.1	1.2	1.0	18.2
Inferior lateral ventricle	5.6	4.6	3.5	21.3
Hippocampus	1.2	1.2	2.4	3.8
Amygdala	3.6	2.3	4.0	5.2
Caudate	4.0	2.0	2.9	6.4
Putamen	2.6	1.3	1.6	6.2
Pallidum	12.8	5.3	8.8	6.3
Thalamus	3.4	2.9	3.3	6.1
Cerebellum	0.7	0.9	1.0	2.9
ICV	0.4	0.3	0.3	1.5
BPV	0.5	0.6	0.5	3.7
WMV	1.2	0.7	1.0	3.7
GMV	0.9	0.9	1.2	4.0
CSFV	2.1	2.4	1.6	6.0

Note:—WMV indicates white matter volume; GMV, gray matter volume; CSFV, CSF volume.

^a Expressed as coefficient of variation (%), at 1.5T and 3T.

illustrate this point, we placed ROIs in the frontal cortical gray matter and frontal white matter in the conventional and synthetic T1-weighted images, providing estimates of the observed local signal intensity. If contrast is defined as the difference in the signals divided by the mean [$2 \times (S1-S2) / (S1 + S2)$], the conventional T1-weighted image showed a gray matter/white matter contrast of 0.414, and for the synthetic gray matter/white matter contrast, it was 0.385 at 1.5T. The TE, TR, and TI of the synthetic images can be manipulated to alter the contrast. On manipulation, the gray matter/white matter contrast changed $-0.38\%/ms$ for TE, $0.025\%/ms$ for TR, and $-0.113\%/ms$ for TI.

It can be speculated that identical contrasts could be obtained with either a 116-ms longer TR or a 3.1-ms shorter TI

or a combination thereof. At 3T, the conventional T1-weighted imaging had a gray matter/white matter contrast of 0.560, and the synthetic gray matter/white matter contrast was 0.511. The synthetic contrast showed a change of gray matter/white matter contrast of $-0.24\%/ms$ for TE, $0.030\%/ms$ for TR, and $-0.171\%/ms$ for TI. Identical contrast could be obtained with either a 165-ms longer TR or a 11.3-ms shorter TI or a combination thereof. This illustration shows that especially the inversion delay time has a very sensitive effect on contrast, and the difference in the signal intensity of gray matter and white matter will alter substantially on a minor change of TI on the order of 10–20 ms. Noise (or SNR) should have a random effect

on the segmentation procedure and is, therefore, less likely to result in a bias.

In the setup used for the study, the syTIWI processing results showed a higher precision (mean SD, 22 mL versus 79 mL) but a lower accuracy (mean bias, 68 mL versus 23 mL) than T1-weighted imaging. SyMRI showed both high precision (mean SD, 22 mL) and high accuracy (mean bias, 10 mL) between 1.5T and 3T. It may be possible to optimize the chosen scanner settings for the syTIWI to somewhat different values to better match the contrast in the conventional T1-weighted images, thereby reducing the observed bias and obtaining a more similar result in brain parcellation. The level of optimizing must be higher for 3T than for 1.5T. Once the systematic

Table 3: Reproducibility of volume estimation of WM, GM, CSF, BPV, and ICV using NeuroQuant and SyMRI, between 1.5T and 3T^a

	T1-Weighted NQ 1.5T-3T				syT1WI NQ 1.5T-3T				SyMRI 1.5T-3T			
	Mean	Bias	SD	<i>r</i>	Mean	Bias	SD	<i>r</i>	Mean	Bias	SD	<i>r</i>
WM	661	27 ^b	65	0.83	613	58 ^b	23	0.97	547	0	39	0.89
GM	622	-6	58	0.83	609	55 ^b	14	0.98	669	-7	33	0.95
CSF	368	-41 ^b	34	0.76	359	-45 ^b	22	0.88	236	1	16	0.97
BPV	1284	21	119	0.84	1223	113 ^b	31	0.98	1258	21 ^b	13	1.00
ICV	1652	-20	120	0.86	1581	68 ^b	20	0.99	1494	21 ^b	9	1.00

^a Expressed as mean, bias, and SD of the difference and correlation coefficient *r*.

^b Significant (*P* < .05).

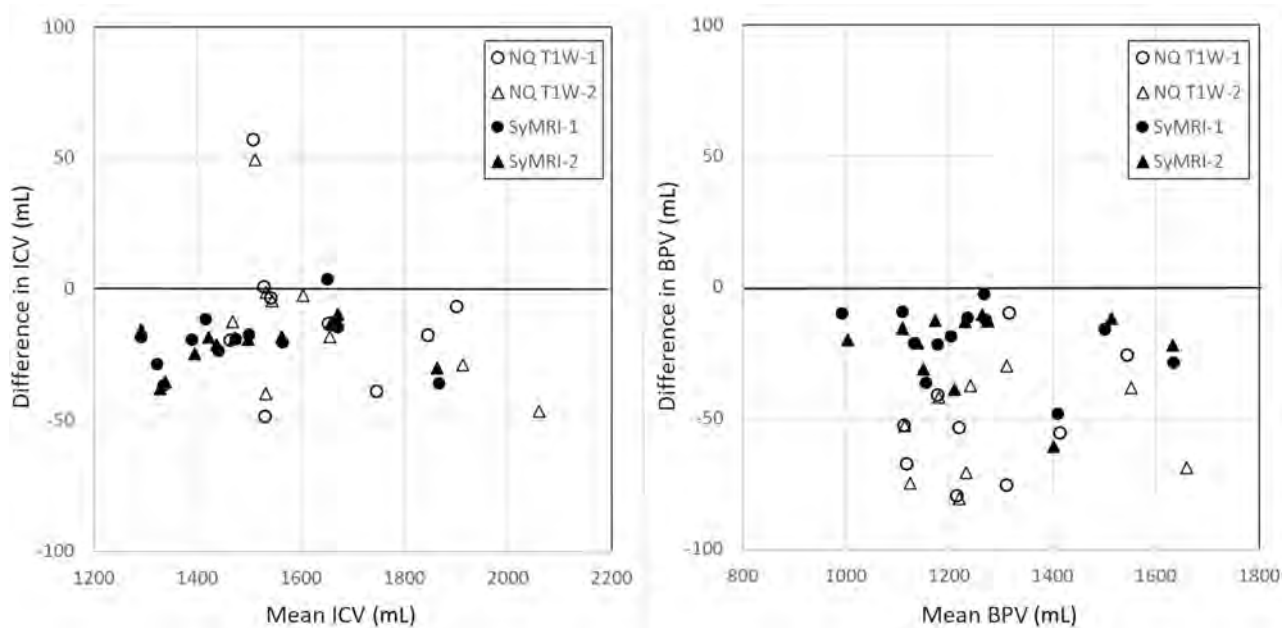


FIG 3. Bland-Atman plot with segmentation results for ICV and BPV in which data from 1.5T and 3T were pooled to focus on the reproducibility for the 2 different acquisition methods, irrespective of field strength NQ T1-weighted imaging and SyMRI. Measurements 1 (circles) and 2 (triangles) are plotted separately for both methods. There is a bias, with lower ICV and BPV when using 3T. The bias is largest for the BPV using NQ T1-weighted imaging.

Table 4: Repeatability of the volume estimation of WM, GM, CSF, BPV, and ICV using NeuroQuant and SyMRI^a

	T1-Weighted NQ 1.5T	syT1WI NQ 1.5T	SyMRI 1.5T	T1-Weighted NQ 3T	syT1WI NQ 3T	SyMRI 3T
WM	1.2	0.7	4.8	1.0	3.7	4.4
GM	0.9	0.9	4.6	1.2	4.0	4.4
CSF	2.1	2.4	3.5	1.6	6.0	3.3
BPV	0.5	0.6	0.7	0.5	3.7	0.6
ICV	0.4	0.3	0.4	0.3	1.5	0.1

^a Expressed as CoV for 1.5T and 3T.

error is reduced, the precision is of the highest importance for clinical use.

The results indicated inferior performance concerning both reproducibility and repeatability at 3T in comparison with 1.5T. On inspection, however, our observed values at 3T may have been dominated by 2 extreme cases of segmentation results. The first case was a woman 70 years of age who at 1.5T had BPVs of 1027 and 1032 mL using T1-weighted imaging, while syT1WI provided 973 and 988 mL, reflective of the average 49-mL bias as seen in Table 1. At 3T, however, 1 case of T1-weighted imaging failed, and the other gave a much higher 1383 mL. For the syT1WI, 1 case also failed, and the other gave a much lower 836 mL. All brain structures were similarly scaled. The second

case was a woman 74 years of age, in whom, for example, the superior lateral ventricle had a mean volume of all measurements of 36.5 (SD, 1.1) mL, while 1 measurement provided 23.1 (-12 SD) mL. Measurements were similar for the inferior lateral ventricles, which had 2.08 (SD, 0.15) mL, while one had 1.24 (SD, -5.4) mL.

Combining brain parcellation with R_1 , R_2 , and PD maps can provide local characteristics of brain tissue. This result may improve precision diagnosis owing to the objective characterization of both the size and content of each brain structure. Time efficiency to retrieve all the information is important to make the procedure clinically relevant. The studied procedure can reduce the required imaging time to a single acquisition.

A limitation in our study was that the original design dictated that no subject was to be excluded on any grounds such as medical issues or imaging artifacts. The 9 failed NeuroQuant data sets, however, did not provide a result and could, therefore, not be included into the analysis. Omitting 9 pairs could have varying effects for the comparisons. Also, the analysis may be affected by a few extreme cases. The study was not repeated using other scanner settings for syT1WI images to evaluate the effect on bias due to economic reasons. The suggested optimization to reduce the observed bias remains a topic for future work.

CONCLUSIONS

Our study has shown that MR imaging quantification maps of R_1 and R_2 relaxation and PD can be used to generate a synthetic 3D-T1-weighted image stack that can be used for automatic brain parcellation. A high correlation between the volume results using either conventional or synthetic data and a high repeatability for each method were observed. The exact image parameters to generate the synthetic T1-weighted images must be reinvestigated to reduce the observed bias between the 2 methods.

Disclosure forms provided by the authors are available with the full text and PDF of this article at www.ajnr.org.

REFERENCES

1. Kvernby S, Warntjes M, Haraldsson H, et al. **Simultaneous three-dimensional myocardial T1 and T2 mapping in one breath hold with 3D-QALAS.** *J Cardiovasc Magn Reson* 2014;16:102 CrossRef Medline
2. Kvernby S, Warntjes M, Engvall J, et al. **Clinical feasibility of 3D-QALAS: single breath-hold 3D myocardial T1- and T2-mapping.** *Magn Reson Imaging* 2017;38:13–20 CrossRef Medline
3. Fujita S, Hagiwara A, Hori M, et al. **Three-dimensional high-resolution simultaneous quantitative mapping of the whole brain with 3D-QALAS: an accuracy and repeatability study.** *Magn Reson Imaging* 2019;63:235–43 CrossRef Medline
4. Fujita S, Hagiwara A, Takei N, et al. **Accelerated isotropic multi-parametric imaging by high spatial resolution 3D-QALAS with compressed sensing: a phantom, volunteer, and patient study.** *Invest Radiol* 2021;56:292–300 CrossRef Medline
5. Fujita S, Yokoyama K, Hagiwara A, et al. **3D quantitative synthetic MRI in the evaluation of multiple sclerosis lesions.** *AJNR Am J Neuroradiol* 2021;42:471–78 CrossRef Medline
6. Fujita S, Hagiwara A, Hori M, et al. **3D quantitative synthetic MRI-derived cortical thickness and subcortical brain volumes: scan-rescan repeatability and comparison with conventional T1-weighted images.** *J Magn Reson Imaging* 2019;50:1834–42 CrossRef Medline
7. Ochs AL, Ross DE, Zannoni MD, et al; Alzheimer's Disease Neuroimaging Initiative. **Comparison of automated brain volume measures obtained with NeuroQuant and FreeSurfer.** *J Neuroimaging* 2015;25:721–27 CrossRef Medline
8. Lee JY, Oh SW, Chung MS, et al. **Clinically available software for automatic brain volumetry: comparisons of volume measurements and validation of intermethod reliability.** *Korean J Radiol* 2021;22:405–14 CrossRef Medline
9. Pareto D, Sastre-Garriga J, Alberich M, et al. **Brain regional volume estimations with NeuroQuant and FIRST: a study in patients with a clinically isolated syndrome.** *Neuroradiology* 2019;61:667–74 CrossRef Medline
10. Brinkmann BH, Guragain H, Kenney-Jung D, et al. **Segmentation errors and intertest reliability in automated and manually traced hippocampal volumes.** *Ann Clin Transl Neurol* 2019;6:1807–14 CrossRef Medline
11. Stelmokas J, Yassay L, Giordani B, et al. **Translational MRI volumetry with NeuroQuant: effects of version and normative data on relationships with memory performance in healthy older adults and patients with mild cognitive impairment.** *J Alzheimers Dis* 2017;60:1499–510 CrossRef Medline
12. Tanpitukpongse TP, Mazurowski MA, Ikhen J, et al; Alzheimer's Disease Neuroimaging Initiative. **Predictive utility of marketed volumetric software tools in subjects at risk for Alzheimer disease: do regions outside the hippocampus matter?** *AJNR Am J Neuroradiol* 2017;38:546–52 CrossRef Medline
13. Bobman SA, Riederer SJ, Lee JN, et al. **Cerebral magnetic resonance image synthesis.** *AJNR Am J Neuroradiol* 1985;6:265–69 Medline
14. Riederer SJ, Lee JN, Farzaneh F, et al. **Magnetic resonance image synthesis: clinical implementation.** *Acta Radiol Suppl* 1986;369:466–68 Medline
15. Redpath TW, Smith FW, Hutchison JM. **Magnetic resonance image synthesis from an interleaved saturation recovery/inversion recovery sequence.** *Br J Radiol* 1988;61:619–24 CrossRef Medline

Arterial Spin-Labeling MR Imaging for the Differential Diagnosis of Venous-Predominant AVMs and Developmental Venous Anomalies

D.H. Yoo, C.-H. Sohn, H.-S. Kang, Y.D. Cho, and K.M. Kim



ABSTRACT

BACKGROUND AND PURPOSE: Venous-predominant AVMs are almost identical in appearance to developmental venous anomalies on conventional MR imaging. Herein, we compared and analyzed arterial spin-labeling findings in patients with developmental venous anomalies or venous-predominant AVMs, using DSA as the criterion standard.

MATERIALS AND METHODS: We retrospectively collected patients with either DVAs or venous-predominant AVMs, each available on both DSA and arterial spin-labeling images. Arterial spin-labeling imaging was visually assessed for the presence of hyperintense signal. CBF measured at the most representative section was normalized to the contralateral gray matter. The temporal phase of developmental venous anomalies or venous-predominant AVMs was measured on DSA as a delay between the first appearance of the intracranial artery and the lesion. Correlation between the normalized CBF and the temporal phase was evaluated.

RESULTS: Analysis of 15 lesions (13 patients) resulted in categorization into 3 groups: typical venous-predominant AVMs (temporal phase, <2 seconds), intermediate group (temporal phase between 2.5 and 5 seconds), and classic developmental venous anomalies (temporal phase, >10 seconds). Arterial spin-labeling signal was markedly increased in the typical venous-predominant AVM group, while there was no discernible signal in the classic developmental venous anomaly group. In the intermediate group, however, 3 of 6 lesions showed mildly increased arterial spin-labeling signal. The normalized CBF on arterial spin-labeling and the temporal phase on DSA were moderately negatively correlated: $r(13) = 0.66, P = .008$.

CONCLUSIONS: Arterial spin-labeling may predict the presence and amount of arteriovenous shunting in venous-predominant AVMs, and using arterial spin-labeling enables confirmation of typical venous-predominant AVMs without DSA. However, lesions with an intermediate amount of shunting suggest a spectrum of vascular malformations ranging from purely vein-draining developmental venous anomalies to venous-predominant AVMs with overt arteriovenous shunting.

ABBREVIATIONS: ASL = arterial spin-labeling; DVA = developmental venous anomaly; GKS = gamma knife surgery; nCBF = normalized CBF; SWAN = T2 star-weighted angiography; TCV = temporal phase in regard to the cortical vein (on DSA); TP = temporal phase (on DSA); vpAVM = venous-predominant AVM

Developmental venous anomaly (DVA) is the most frequently encountered cerebral vascular malformation, with a reported incidence of approximately 2%–3%. DVAs are usually incidentally detected and appear as a caput medusa or umbrella-like medullary veins collecting into a single common draining vein (stem vein).^{1,2} A venous-predominant AVM (vpAVM), a rare form of AVM, is almost identical in appearance to DVAs on conventional MR

imaging. This type of AVM has no definable nidus, and early venous drainage is the only feature that distinguishes it from a DVA.^{3,4} However, whereas a DVA is of little clinical significance, a vpAVM may cause venous hypertension or hemorrhage.⁴⁻⁶ Whether symptomatic or incidentally detected, a vpAVM is conventionally diagnosed through DSA, which poses a risk to patients because it is an invasive procedure involving iodinated contrast and radiation exposure.

Arterial spin-labeling (ASL) is a noninvasive MR imaging technique used to assess cerebral circulation by magnetically labeling inflowing blood.⁷ The availability and application of ASL have steadily increased, and its usefulness in evaluating arteriovenous shunting of intracranial AVMs is well-recognized.^{8,9} We hypothesized that ASL would effectively represent the presence and degree of shunting in vpAVM, thus enabling a diagnosis of vpAVM without the use of contrast or invasive DSA. SWI has

Received March 6, 2023; accepted after revision June 5.

From the Departments of Radiology (D.H.Y., C.-H.S., Y.D.C.) and Neurosurgery (H.-S.K., K.M.K.), Seoul National University Hospital, Seoul National University College of Medicine, Seoul, Korea.

Please address correspondence to Chul-Ho Sohn, MD, PhD, Department of Radiology, Seoul National University Hospital, Seoul National University College of Medicine, 101 Daehak-ro, Jongno-gu, Seoul, 03080, Korea; e-mail: neurorad63@gmail.com



Indicates article with online supplemental data.

<http://dx.doi.org/10.3174/ajnr.A7922>

also been reported to serve as an accurate tool for detection of arteriovenous shunting.^{10,11} The purpose of the present study was to compare and analyze ASL and SWI findings in patients with DVA or vpAVM, using DSA as the criterion standard.

MATERIALS AND METHODS

Patient Selection

This study was approved by the local ethics review board; written informed consent was waived due to its retrospective nature. We searched the PACS data base at our center between January 2016 and December 2019 for MR images that included ASL sequences acquired from a 3T MR imaging system (Discovery 750; GE Healthcare). To screen patients for a DVA or vpAVM, we used keywords as follows: “developmental venous anomaly,” “DVA,” “venous angioma,” “arteriovenous malformation,” “AVM,” and “venous-predominant.” Next, we selected only those with available DSA images. Patients with coexisting disease that could hinder proper evaluation of the ASL signal were excluded. Medical records were reviewed to collect demographics and clinical data.

Image Acquisition

A multiphase ASL protocol was the most frequently used sequence in our institution, with the best image quality. Thus, we limited our series to those who underwent this protocol to ensure homogeneity of the study population. We applied the following parameters: TR/TE = 5871/11.0 ms; number of averages = 1; section thickness = 6 mm; number of slices = 26–28; readout = 4 spiral arms × 640 samples; FOV = 240 × 240 mm²; matrix = 128 × 128; and voxel resolution = 3.8 × 3.8 6.0 mm. Details of the technique used to acquire multiphase ASL images are described in a previous report.¹² Along with ASL, all patients were examined with T2 star-weighted angiography (SWAN). The SWAN parameters were TE = 21.5 ms; TR = 37.3 ms; flip angle = 300°; thickness = 1.2 mm; matrix = 416 × 256; FOV = 220 × 220; number of slices = 120.

DSA was performed on either an Innova IGS 630 (GE Healthcare) system or AlluraClarity (Philips Healthcare). After puncture of the femoral artery and insertion of a 5F arterial sheath, selective catheterization of the dominant vertebral artery and bilateral internal carotid arteries was performed. A bolus of 7–9 mL of contrast media was injected at an injection rate of 5–6 mL/s by a contrast delivery system. The image-acquisition frequency was in 3 phases: 4 frames per second for the first 3 seconds, then 2 frames per second for the next 3 seconds, and then 1 frame per second (0.5 frames per second in AlluraClarity) thereafter.

Image Analysis

The size of the lesion (largest dimension) was measured on an enhanced T1 image. The signal intensity of the lesion (caput medusa or umbrella-like draining vein) was visually assessed on SWI as either dark or high. ASL imaging was used to visually assess whether hyperintense signal was detected at the location where DVA or vpAVM was noted on contrast-enhanced imaging. In addition, ROIs were drawn in the most representative sections of the ASL quantitative CBF map (at the corresponding

location that matched the caput medusa or umbrella-like draining vein on the contrast-enhanced image) to determine the CBF of the DVA or vpAVM (CBF_{lesion}). To adjust for interindividual variation, we drew additional ROIs within the gray matter of normal contralateral parenchyma at the same section levels (CBF_{gray}). Subsequently, normalized CBF (nCBF) was calculated as $nCBF = CBF_{lesion} / CBF_{gray}$.¹³

Using DSA, we endeavored to quantify arteriovenous shunting using 2 different ways to measure the temporal phase in which the lesions were visualized. First, we calculated the delay between the first visualization of the intracranial artery (carotid genu in the anterior circulation, V4 segment of the vertebral artery in the posterior circulation) and the first appearance of the lesion (DVA or vpAVM). Hence, we used the following equation: Temporal Phase of the Lesion (TP, sec) = Timeframe of Appearance of the Lesion – Timeframe of Intracranial Artery Visualization. Second, the time of detection of the lesion was measured against the first visualization of the cortical vein (temporal phase in regard to the cortical vein [TCV]). The earlier appearance of the lesion was translated to a negative value. We evaluated the correlation between the nCBF and TP by calculating the Pearson correlation coefficient.

RESULTS

Both DSA and multiphase ASL images were available in 17 patients who had lesions with a caput medusa or umbrella-like appearance on contrast-enhanced MR imaging. Four patients were excluded due to comorbidities limiting normal intracranial perfusion; these included Moyamoya disease, stenotic intracranial vasculitis, severe carotid stenosis, and a dural AVF with severe cortical reflux. Clinical and lesion characteristics as well as imaging features are summarized in the Online Supplemental Data. At the time of DSA, 6 patients (cases 1–6) were diagnosed with 8 vpAVMs (2 lesions in cases 4 and 6), while 7 patients (cases 7–13) were diagnosed with DVAs. There were 7 men and 6 women, with a mean age of 46.4 years (range, 20–72 years) at the time of the ASL image acquisition.

Two patients diagnosed with vpAVM presented with hemorrhage (cases 1 and 3), while 4 patients presented with unrelated symptoms. Signs of intracranial hypotension (diffuse meningeal thickening, engorged dural sinus, and so forth) were observed on MR images of case 6. Seven lesions were detected during diagnostic work-up of various comorbidities (syncope in case 7, carotid disease in case 8, a separate AVM in cases 9 and 11, an unruptured aneurysm in cases 10 and 12, and a meningioma in case 13). Two patients presenting with hemorrhage (cases 1 and 3) underwent gamma knife surgery (GKS). In case 3, image analysis was performed on the residual vpAVM 3 years after the first GKS session. GKS was also performed for a separate AVM in cases 9 and 11. All patients remained event-free during the mean follow-up period of 73.9 months (median, 33 months; range, 3–571 months).

After meticulous analysis of the DSA images, we categorized study cases into 3 groups according to TP and TCV on DSA. The first group consisted of “typical vpAVM,” which showed the characteristic appearance of early venous drainage, with the TP of <2 seconds and negative-value TCV (cases 1–5). Lesions in the second group did not exhibit overt arteriovenous shunting

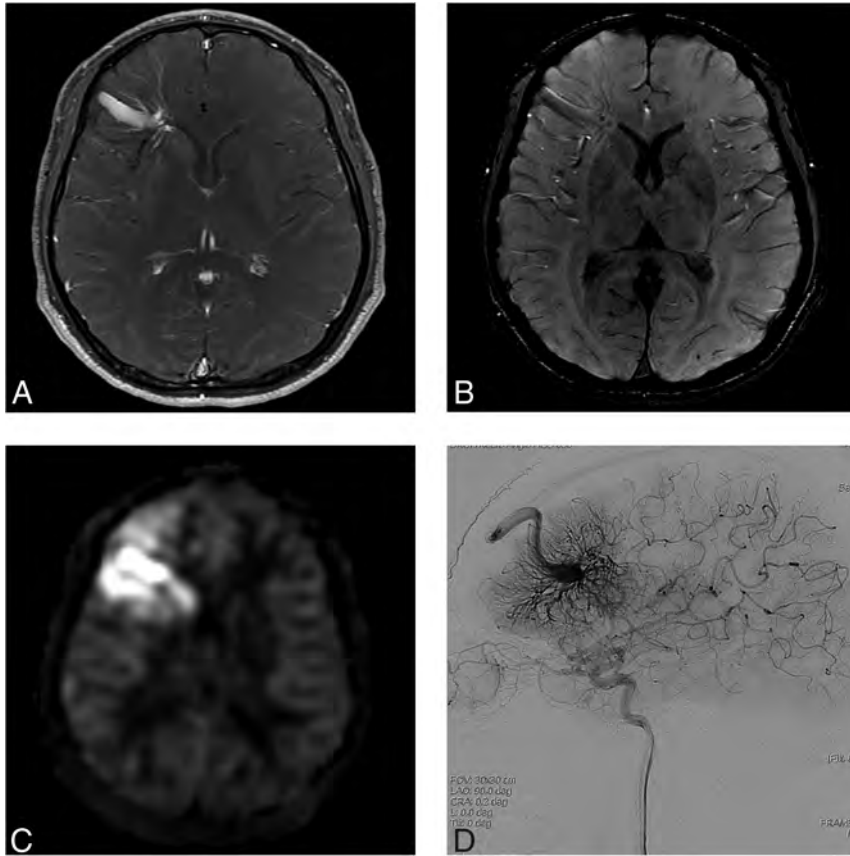


FIG 1. A 31-year-old man presenting with dizziness (case 4). *A*, Contrast-enhanced T1-weighted axial MR imaging shows a DVA-like lesion in the left frontal lobe. *B*, On SWI, both hyperintense and hypointense signal is present in the collecting vein, while only hypointense signal is present in the dilated medullary veins. *C*, The ASL quantitative CBF image demonstrates hyperintense signal intensity in the collecting vein and parenchyma corresponding to the location of the lesion, suggesting a vpAVM. *D*, On DSA, a caput medusae appearance of medullary veins draining to the superior sagittal sinus via a collecting cortical vein is visualized in the arterial phase.

and resembled DVAs. These lesions were first observed during the late capillary or early venous phase, deemed the “intermediate stage,” TP between 2.5 and 5 seconds and TCV between 0 and 3 seconds (cases 6 to 10). In the third group, lesions manifested themselves at the late venous phase with the appearance of a “classic DVA,” TP of >10 seconds and TCV of >5 seconds (cases 11–13).

It was evident that visually, ASL signal was markedly increased in the typical vpAVM group, while there was no discernible signal from lesions in the classic DVA group. In the intermediate group, however, 3 of 6 lesions (cases 6 [2 lesions] and 9) showed increased ASL signal; the other 3 lesions did not. Moreover, in those 3 lesions with increased ASL signal, the intensity was not as prominent as those observed in the typical vpAVM group. The nCBF was <2 in those 3 lesions from the intermediate group. The nCBF in the typical vpAVM group was >2, except in case 3, probably because a small residual portion of the lesion remained after GKS. Representative images from illustrative cases are shown in Figs 1–3.

The distribution of nCBF and TP values for the 3 groups of lesions is shown in Fig 4. The nCBF on ASL and TP on DSA were moderately negatively correlated across all groups: $r(13) = 0.66, P = .008$. On SWI, only 3 of 6 lesions in the typical vpAVM

group exhibited hyperintense signal in the dilated medullary veins, whereas all lesions in the intermediate and classic DVA groups had hypointense signal.

DISCUSSION

Detection of vpAVMs has become more frequent recently due to the increased availability of advanced imaging modalities. Various nomenclatures used to indicate vpAVM include transitional venous anomaly, DVA with an arterial component, and atypical DVA.^{6,14–16} Although the natural course of a vpAVM is poorly understood due to its low incidence, it is generally considered to carry a considerable risk of hemorrhage. Dilated medullary veins converging to a collecting vein is not infrequently encountered on enhanced MR imaging and is usually designated as a DVA in a routine clinical setting. Indeed, most of these lesions are DVAs; a previous study reported that only 8% of lesions with a DVA-like appearance on MR imaging showed increased ASL signal.¹⁷ Given that ASL is increasingly included as a regular sequence in MR imaging, we aimed to investigate the accuracy of ASL in distinguishing a vpAVM from a DVA.

Our study is the first to use DSA in study cases with DVA or vpAVM to fully validate ASL. The study results show the following: 1) A lesion with a

caput medusae appearance on contrast-enhanced MR imaging could be a vpAVM or DVA but could also be a lesion with intermediate shunting; and 2) ASL effectively predicts the presence of a vpAVM on MR imaging, and ASL signal intensity (nCBF) correlates well with how early the lesion appears on DSA (ie, the degree of arteriovenous shunting).

ASL imaging uses magnetically labeled water protons in arterial blood as an endogenous tracer to evaluate cerebral perfusion. Because there is no need for administration of a gadolinium-based contrast agent in dynamic susceptibility contrast-enhanced perfusion imaging, the risk of nephrogenic systemic fibrosis in patients with decreased renal function is nonexistent. As with an intracranial AVM, the utility of ASL in various other cerebrovascular conditions, including dural arteriovenous fistula, Moyamoya disease, and meningioma, has been well-documented.^{13,18,19} Most patients with cerebral vascular lesions in our institution currently undergo multiphase ASL. Multiphase ASL was initially introduced and used to evaluate perfusion in patients with stenotic lesions because the CBF value based on conventional ASL is underestimated due to the long arterial transit time. A previous study showed that the multiphase ASL technique can overcome the effect of delayed transit time on perfusion maps.¹² In nonstenotic vascular territory,

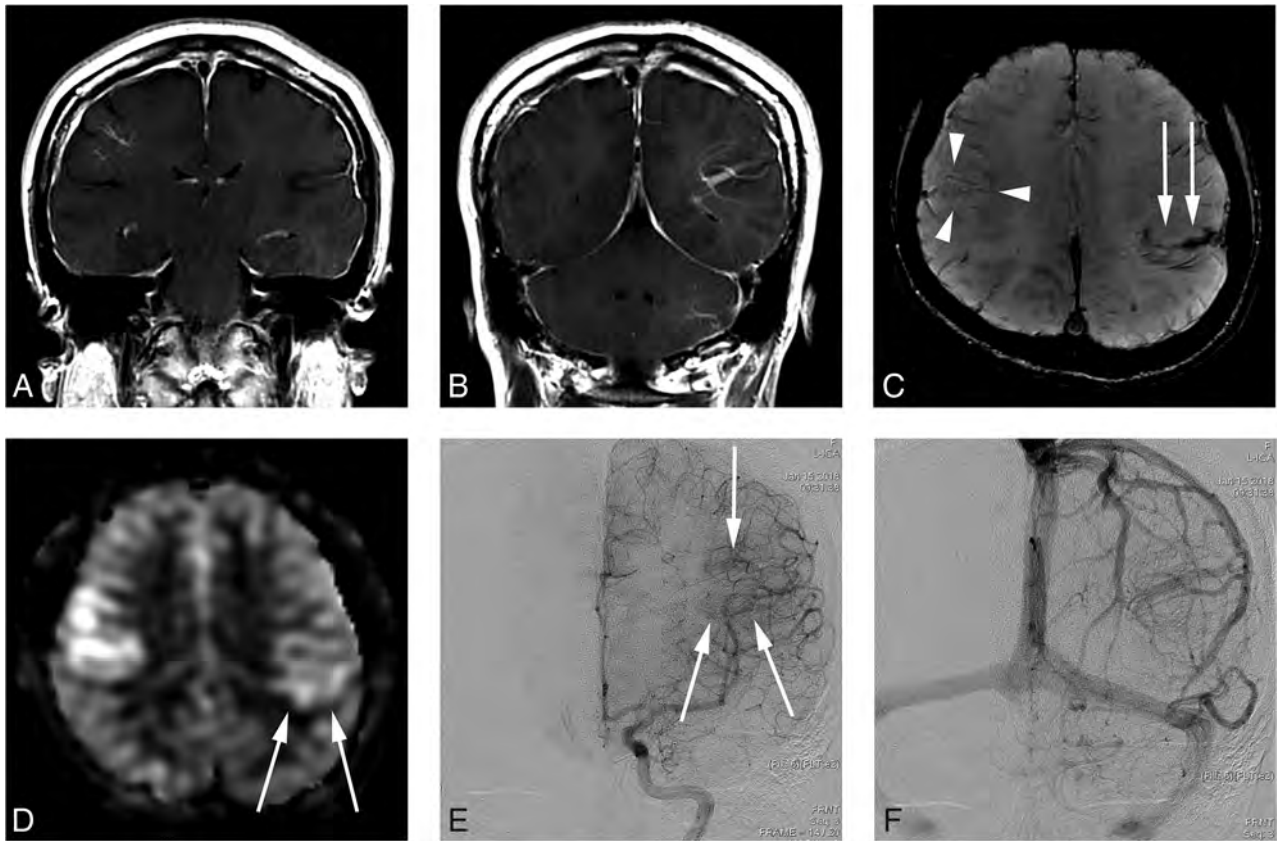


FIG 2. A 34-year-old woman presenting with a headache (case 6). *A* and *B*, Contrast-enhanced T1-weighted coronal MR imaging shows a DVA-like lesion in the bilateral parietal lobes. *C*, SWI demonstrates only hypointense signal in both the right (*arrowheads*) and left (*arrow*) lesions. *D*, The ASL quantitative CBF image demonstrates mildly hyperintense signal intensity in the parenchyma, corresponding to the location of the lesion. The left-sided lesion exhibits particularly subtle signal (*arrows*). *E*, In the late arterial phase of DSA, dilated medullary veins are gradually and subtly visualized (*arrows*). *F*, In the venous phase, dilated medullary veins draining to a collecting vein typical of a DVA are seen.

however, CBF values from both conventional and multiphase ASL showed high concordance levels with CBF values from DSC MR imaging. Therefore, although multiphase ASL may not be as widely used as conventional ASL, the findings from multiphase ASL in our study may well be applicable to conventional ASL.

Earlier studies have reported that arteriovenous shunting manifests as hyperintense signal intensity on SWI because arterial and venous circulation appear hyperintense (due to rapid flow) and hypointense (due to slow flow and deoxyhemoglobin), respectively.^{10,11} However, in 3 of 6 typical vpAVMs in our study, SWI indicated a DVA, with hypointense signal at the dilated medullary veins, though iso- to hyperintense signal could be detected at a stem vein in 2 cases. This finding suggests that ASL is capable of distinguishing a vpAVM from a DVA more accurately than SWI. The mechanism of how hypointense signal could be present in vpAVM (especially in such a high-flow lesion as in case 4, Fig 1) is not clear. It might be that some vpAVMs also drain normally circulated parenchymal venous flow, thus functioning as a DVA as well.⁶ The arteriovenous shunt flow may not be enough to rapidly wash out venous drainage in dilated medullary veins, resulting in hypointense signal from venous blood that is rich in deoxyhemoglobin.

Although lesions were clinically diagnosed as either DVAs or vpAVMs at the time of the DSA study, retrospective analysis of

DSA images for the present study indicated 3 distinct groups based on the degree of arteriovenous shunting. This finding suggests a spectrum of vascular malformations with varying hemodynamic characteristics, ranging from purely vein-draining DVAs to vpAVMs with overt arteriovenous shunting. This spectrum could possibly be explained by potential interrelation between DVAs and AVMs. It is well-known that DVAs and cavernous malformations commonly coexist, because venous hypertension and angiogenic proliferation caused by abnormal vascular anatomy of the DVA may lead to formation of the cavernous malformation.²⁰ Likewise, it is thought that thrombosis in venous radicles of a DVA may generate a fistula, similar to hypothetic dural arteriovenous fistula development, via various processes such as inflammation, venous hypertension, or angiogenesis.^{5,20}

The intermediate group lesions in our series may represent either lesions in the transitional stage from a DVA to a vpAVM or a vpAVM with progression of fistula formation terminated at a point of a low amount of shunting. The former supposition is supported by a case report in which previously nonexistent arteriovenous shunting developed into a DVA after 5 years.²¹ However, the possibility of the latter hypothesis cannot be completely excluded because there is no other report of a DVA developing into a vpAVM. In addition, follow-up ASL imaging was available in 3 cases in our study in which there was no evident change in ASL

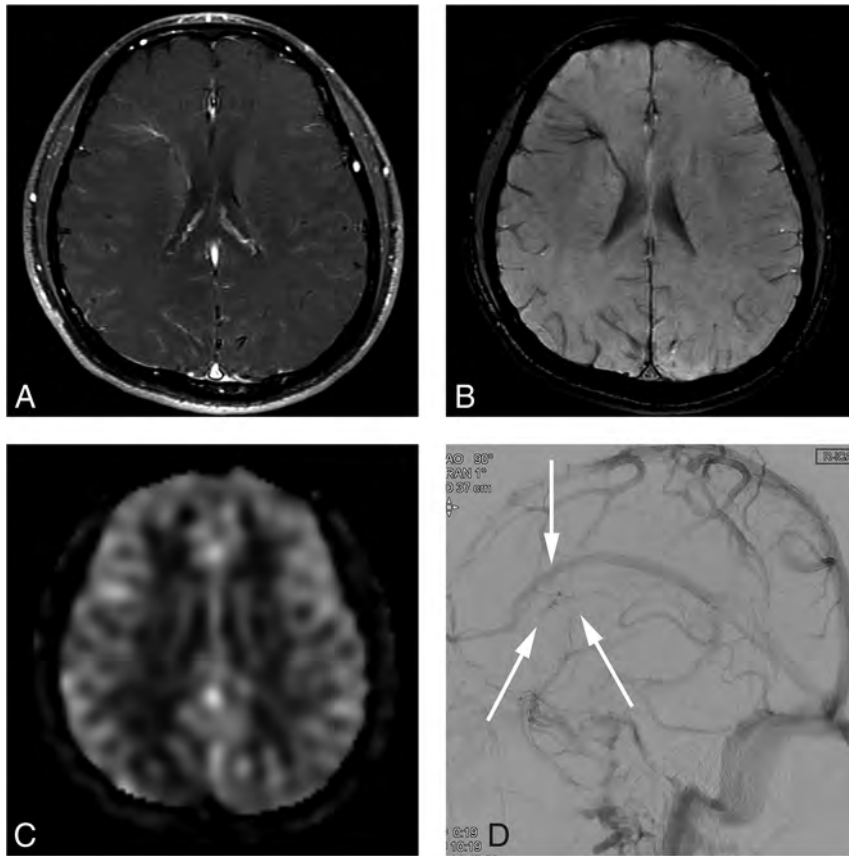


FIG 3. A 29-year-old man presenting with an AVM in the left occipital lobe (case 11). *A*, Contrast-enhanced T1-weighted axial MR imaging shows a DVA-like lesion in the right frontal lobe. *B*, SWI shows hypointense signal in the lesion. *C*, An ASL quantitative CBF image demonstrates no identifiable signal corresponding to the lesion. *D*, On DSA, the lesion is first visualized in the late venous phase (arrows), as is typically seen in a classic DVA.

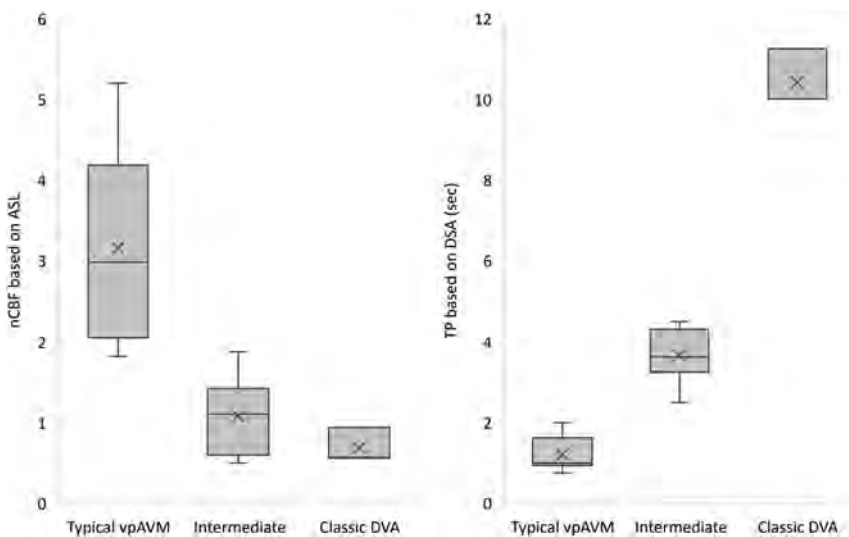


FIG 4. Box-and-whisker display of nCBF and TP for the 3 groups of lesions. The *line* across the boxes denotes the median value, whereas the *ends* of the boxes represent the first and third quartiles (not applied in the classic DVA group due to the small number of cases). The *ends* of each plot indicate the smallest and largest values. *x* denotes average value. *Sec* indicates second.

signal (1 in each group: case four, 36 months; case nine, 46 months; case thirteen, 4 months).

In any case, ASL imaging enabled instant visual detection of vpAVMs. In addition, our study results indicate that the nCBF effectively reflects the degree of arteriovenous shunting. The moderately negative correlation of $r(13) = 0.66$ between nCBF and TP on DSA may have been attenuated by the locational variation of DVAs. The nCBF of DVAs located near the cerebral cortex was measured to be near 1 due to normal cerebral perfusion, while the value was much lower (about 0.5) in DVAs located in deep cerebral matter.

Management strategies for a vpAVM are not well-established due to the small number of cases and paucity of data on treatment outcome. In cases of repetitive or extensive hemorrhagic lesions, surgical removal can be considered, though incomplete resection due to poor localization may lead to venous infarction or massive hemorrhage. In cases of symptomatic high-flow vpAVM, GKS may alleviate hemodynamic stress, though complete obliteration is seldom achieved.^{3,4} Endovascular treatment plays a limited role in vpAVMs because the lesions exhibit diffuse distribution without a definite dominant arterial feeder. De Maria et al⁵ have advocated conservative management, even in the presence of hemorrhage. They argued that hemorrhage is due to venous infarction by the thrombosis of one of the large collecting veins rather than the presence of a weak point in the vessels. It is generally accepted that conservative management will suffice for hemodynamically stable or asymptomatic lesions. In our case series, there was no bleeding in both hemorrhagic and nonhemorrhagic lesions during a relatively long follow-up period (mean, 73.9 months). Therefore, the clinical implication of an incidentally detected vpAVM is unclear. However, physicians should be aware of the possibility of a future hemorrhagic presentation and caution patients with vpAVMs about this. Meanwhile, in patients presenting with intracerebral hemorrhage by a ruptured vpAVM, ASL has the potential to suggest an

arteriovenous shunt in the initial work-up with MR imaging, even if a small lesion is partially obscured by mass effect from the hematoma.²²

There are some limitations to the present study primarily due to the retrospective nature of the study. First, DSA is not usually performed in patients with DVAs, and we were able to recruit only a small number of selected cases of DVAs in which DSA was performed to evaluate a separate disease. Therefore, our DVA cases are subject to nonrepresentative sampling and selection bias. Second, in cases of vpAVMs, a higher frame rate on DSA (eg, 7 frames per second) for the purpose of this study would have provided a more sensitive analysis of the shunt. However, only DSA images acquired with routine protocol were available.

Third, MRA was not evaluated in our study, though various MRA techniques could be used to detect arteriovenous shunt lesions. In our institution, contrast-enhanced MRA and 4D MRA were not routinely used; while TOF-MRA was mostly used in daily practice, the whole brain up to vertex was not covered. Future study comparing ASL and MRA sequences in detecting a vpAVM would produce more comprehensive results. Finally, analysis of ASL and DSA images depended on subjective and inconsistent visual assessment, without computerized measurement. Therefore, parameters such as the ROI drawn on ASL or the first appearance of the lesion or cortical vein on DSA are subject to slight inaccuracy. Despite these shortcomings, this study suggests that ASL has a clear role in screening overt vpAVMs in patients with dilated medullary veins converging to a collecting vein on contrast-enhanced MR imaging.

CONCLUSIONS

DVA and vpAVM are not readily discernible on contrast-enhanced or susceptibility-weighted MR imaging. ASL may predict the presence and amount of arteriovenous shunting in vpAVM, and using ASL enables confirmation of a vpAVM without DSA. However, the existence of a lesion with an intermediate amount of shunting should be considered. These lesions exhibit iso- or subtly increased signal on ASL, and their nature should be further investigated.

Disclosure forms provided by the authors are available with the full text and PDF of this article at www.ajnr.org.

REFERENCES

1. Gokce E, Acu B, Beyhan M, et al. **Magnetic resonance imaging findings of developmental venous anomalies.** *Clin Neuroradiol* 2014;24:135–43 CrossRef Medline
2. Aoki R, Srivatanakul K. **Developmental venous anomaly: benign or not benign.** *Neurol Med Chir (Tokyo)* 2016;56:534–43 CrossRef Medline
3. Im SH, Han MH, Kwon BJ, et al. **Venous-predominant parenchymal arteriovenous malformation: a rare subtype with a venous drainage pattern mimicking developmental venous anomaly.** *J Neurosurg* 2008;108:1142–47 CrossRef Medline
4. Jeon JP, Kim JE, Ahn JH, et al. **Long-term treatment outcome of venous-predominant arteriovenous malformation.** *J Neurosurg* 2016;124:1100–06 CrossRef Medline
5. De Maria L, Lanzino G, Flemming KD, et al. **Transitional venous anomalies and DVAs draining brain AVMs: a single-institution**

- case series and review of the literature.** *J Clin Neurosci* 2019;66:165–77 CrossRef Medline
6. Picart T, Dumot C, Guyotat J, et al. **Arteriovenous malformation drained into a developmental venous anomaly: a case report and up-dated literature review.** *Neurochirurgie* 2020;66:471–76 CrossRef Medline
7. Haller S, Zaharchuk G, Thomas DL, et al. **Arterial spin labeling perfusion of the brain: emerging clinical applications.** *Radiology* 2016;281:337–56 CrossRef Medline
8. Sunwoo L, Sohn CH, Lee JY, et al. **Evaluation of the degree of arteriovenous shunting in intracranial arteriovenous malformations using pseudo-continuous arterial spin labeling magnetic resonance imaging.** *Neuroradiology* 2015;57:775–82 CrossRef Medline
9. Kodera T, Arai Y, Arishima H, et al. **Evaluation of obliteration of arteriovenous malformations after stereotactic radiosurgery with arterial spin labeling MR imaging.** *Br J Neurosurg* 2017;31:641–47 CrossRef Medline
10. Jagadeesan BD, Delgado Almandoz JE, Moran CJ, et al. **Accuracy of susceptibility-weighted imaging for the detection of arteriovenous shunting in vascular malformations of the brain.** *Stroke* 2011;42:87–92 CrossRef Medline
11. Hodel J, Leclerc X, Kalsoum E, et al. **Intracranial arteriovenous shunting: detection with arterial spin-labeling and susceptibility-weighted imaging combined.** *AJNR Am J Neuroradiol* 2017;38:71–76 CrossRef Medline
12. Yun TJ, Sohn CH, Yoo RE, et al. **Transit time corrected arterial spin-labeling technique aids to overcome delayed transit time effect.** *Neuroradiology* 2018;60:255–65 CrossRef Medline
13. Yoo RE, Yun TJ, Cho YD, et al. **Utility of arterial spin labeling perfusion magnetic resonance imaging in prediction of angiographic vascularity of meningiomas.** *J Neurosurg* 2016;125:536–43 CrossRef Medline
14. Oran I, Kiroglu Y, Yurt A, et al. **Developmental venous anomaly (DVA) with arterial component: a rare cause of intracranial haemorrhage.** *Neuroradiology* 2009;51:25–32 CrossRef Medline
15. Roh JE, Cha SH, Lee SY, et al. **Atypical developmental venous anomaly associated with single arteriovenous fistula and intracerebral hemorrhage: a case demonstrated by superselective angiography.** *Korean J Radiol* 2012;13:107–10 CrossRef Medline
16. Zhang M, Telischak NA, Fischbein NJ, et al. **Clinical and arterial spin-labeling brain MRI features of transitional venous anomalies.** *J Neuroimaging* 2018;28:289–300 CrossRef Medline
17. Iv M, Fischbein NJ, Zaharchuk G. **Association of developmental venous anomalies with perfusion abnormalities on arterial spin-labeling and bolus perfusion-weighted imaging.** *J Neuroimaging* 2015;25:243–50 CrossRef Medline
18. Amukotuwa SA, Marks MP, Zaharchuk G, et al. **Arterial spin-labeling improves detection of intracranial dural arteriovenous fistulas with MRI.** *AJNR Am J Neuroradiol* 2018;39:669–77 CrossRef Medline
19. Lee S, Yun TJ, Yoo RE, et al. **Monitoring cerebral perfusion changes after revascularization in patients with moyamoya disease by using arterial spin-labeling MR imaging.** *Radiology* 2018;288:565–72 CrossRef Medline
20. Aboian MS, Daniels DJ, Rammos SK, et al. **The putative role of the venous system in the genesis of vascular malformations.** *Neurosurg Focus* 2009;27:E9 CrossRef Medline
21. Piliipenko Y, Kononov A, Okishev D, et al. **Formation during lifetime of arteriovenous shunt in developmental venous anomaly that caused intracerebral hemorrhage.** *World Neurosurg* 2018;119:168–71 CrossRef Medline
22. Hak JF, Boulouis G, Kerleroux B, et al. **Arterial spin-labeling for the etiological workup of intracerebral hemorrhage in children.** *Stroke* 2022;53:185–93 CrossRef Medline

Clinical Applications of Conebeam CTP Imaging in Cerebral Disease: A Systematic Review

 A.H.A. Zaid Al-Kaylani,  R.C.L. Schuurmann,  W.D. Maathuis,  R.H.J.A. Slart,  J.-P.P.M. de Vries, and  R.P.H. Bokkers



ABSTRACT

BACKGROUND: Perfusion imaging with multidetector CT is integral to the evaluation of patients presenting with ischemic stroke due to large-vessel occlusion. Using conebeam CT perfusion in a direct-to-angio approach could reduce workflow times and improve functional outcome.

PURPOSE: Our aim was to provide an overview of conebeam CT techniques for quantifying cerebral perfusion, their clinical applications, and validation.

DATA SOURCES: A systematic search was performed for articles published between January 2000 and October 2022 in which a conebeam CT imaging technique for quantifying cerebral perfusion in human subjects was compared against a reference technique.

STUDY SELECTION: Eleven articles were retrieved describing 2 techniques: dual-phase ($n = 6$) and multiphase ($n = 5$) conebeam CTP.

DATA ANALYSIS: Descriptions of the conebeam CT techniques and the correlations between them and the reference techniques were retrieved.

DATA SYNTHESIS: Appraisal of the quality and risk of bias of the included studies revealed little concern about bias and applicability. Good correlations were reported for dual-phase conebeam CTP; however, the comprehensiveness of its parameter is unclear. Multiphase conebeam CTP demonstrated the potential for clinical implementation due to its ability to produce conventional stroke protocols. However, it did not consistently correlate with the reference techniques.

LIMITATIONS: The heterogeneity within the available literature made it impossible to apply meta-analysis to the data.

CONCLUSIONS: The reviewed techniques show promise for clinical use. Beyond evaluating their diagnostic accuracy, future studies should address the practical challenges associated with implementing these techniques and the potential benefits for different ischemic diseases.

ABBREVIATIONS: CBCT = conebeam CT; ICC = intraclass correlation coefficient; LVO = large-vessel occlusion; PBV = parenchymal blood volume; r = relative

Perfusion imaging with multidetector CT has become part of the standard diagnostic evaluation for patients presenting


with symptoms of acute ischemic stroke.¹ In patients beyond the conventional treatment time windows, it is used to select patients who may benefit from IV thrombolysis and/or endovascular therapy.²⁻⁴ Time from symptom onset to treatment has been shown to be one of the most significant modifiable factors affecting clinical outcome.⁵⁻⁷

For patients suspected of having a cerebral large-vessel occlusion (LVO), studies have investigated whether the time to treatment can be reduced by transferring the patients directly to the angiosuite and bypassing the initial stroke triage in the emergency department. Considerable reductions in door-to-puncture times have been demonstrated with a direct-to-angio approach. These studies focused on the ability of using conebeam CT (CBCT) to detect intracerebral hemorrhage and an LVO.⁸⁻¹⁴

Received January 2, 2023; accepted after revision June 11.

From Department of Radiology (A.H.A.Z.A., R.H.J.A.S., R.P.H.B.), Medical Imaging Center, Department of Surgery (A.H.A.Z.A., R.C.L.S., J.-P.P.M.d.V.), Division of Vascular Surgery, and Department of Nuclear Medicine and Molecular Imaging (R.H.J.A.S.), University Medical Center Groningen, University of Groningen, Groningen, the Netherlands; and Department of Biomedical Photonic Imaging (W.D.M., R.H.J.A.S.), Faculty of Science and Technology, University of Twente, Enschede, the Netherlands.

Please address correspondence to Reinoud P.H. Bokkers, MD, Medical Imaging Center, Department of Radiology, Hanzeplein 1, Postbus 30 001 (EB 44), 9700 RB, Groningen, the Netherlands; e-mail: r.p.h.bokkers@umcg.nl

 Indicates article with online supplemental data.

<http://dx.doi.org/10.3174/ajnr.A7930>

New CBCT perfusion techniques, such as dual-phase¹⁵ and multiphase¹⁶ CBCT imaging, have also been recently introduced and found to be able to detect perfusion deficits in patients with an LVO. For a reliable evaluation of perfusion deficits in the late time window, CBCTs must, however, have a diagnostic accuracy and precision comparable with those of multidetector CTP imaging.

This systematic review provides an overview of CBCT techniques for quantifying cerebral perfusion techniques, their clinical applications, and validation with other reference techniques.

MATERIALS AND METHODS

This systematic review was conducted in accordance with the Preferred Reporting Items for Systematic Review and Meta-Analysis (PRISMA) statement (Online Supplemental Data).¹⁷ This systematic review and the corresponding search strategy have been registered in the PROSPERO registry (registration number: CRD42021243288). The review and search strategy were formulated using the Population, Intervention, Comparison, and Outcomes framework. Due to the heterogeneity in the methodology, interventions, and outcomes of the retrieved studies, they could not be grouped. Therefore, the studies were narrowed down to those investigating CBCT techniques for cerebral perfusion imaging. Furthermore, due to the heterogeneity in the studies included in the review, no meta-analysis was performed. Descriptions of the techniques, their applications, and correlations with the reference techniques were reported.

Literature Search

EMBASE, PubMed, the Cochrane Library, and the Cumulative Index of Nursing and Allied Health were searched for eligible studies on CBCT perfusion imaging techniques. The search was performed with the help of Medical Subject Heading terms, free text, and Boolean operators. Additional articles were retrieved through cross-checking references in the relevant literature. The full search strategy can be found in the Online Supplemental Data. Studies published before January 2000 were excluded because the technology before that time is considered outdated.

Titles and abstracts of the studies were independently reviewed by 2 authors (A.H.A.Z.A., W.D.M.) by means of Rayyan software (Rayyan Systems).¹⁸ The reviewers were blinded to the authors and journal titles. Items in which there was disagreement were discussed by the 2 reviewers to reach a consensus for inclusion. If consensus could not be reached, adjudication was provided from a third reviewer (R.P.H.B.).

Selection Criteria

Articles including a CBCT imaging technique for quantifying perfusion in the brain were eligible. The CBCT techniques had to be compared with another perfusion imaging technique using a different modality. Furthermore, the studies were required to report the correlations between the CBCT technique and the reference technique. The selected articles included only human subjects and were not limited to a language. Online translation services were used to translate studies in languages other than English. Exclusion criteria were studies with <10 subjects, case reports, case series studies, review articles, conference abstracts,

letters to the editors, commentaries, and studies without full text availability.

Data Extraction and Quality Assessment

The study details from the relevant articles were extracted using a predefined form and categorized according to the CBCT perfusion imaging technique. We extracted the following data: study year, study design, number of patients, diagnoses, CBCT technique, reference technique, the measured perfusion parameters, and correlations among them. Data were collected using the Rayyan software.¹⁸ The Quality Assessment of Diagnostic Accuracy Studies tool¹⁹ was used for appraisal of quality and the risk of bias and was conducted by 1 reviewer (A.H.A.Z.A.).

Results and Description of Techniques

The search resulted in 6165 records, of which 993 were duplicates. After detailed evaluation of the titles and abstracts, 355 articles were selected for full-text assessment. Of these articles, 52 were excluded due to lack of comparison with a reference technique, 291 were excluded because of different outcomes, and 5 were excluded because the measurements were performed in different organs. Four articles were retrieved through cross-checking references in the relevant literature. Eleven articles were found to be eligible for inclusion. An outline of the review process can be found in the Online Supplemental Data.

Six of the 11 articles investigated dual-phase CBCT perfusion in patients with cerebral ischemia. The 5 remaining studies investigated multiphase CBCT perfusion, 2 of which were in patients undergoing carotid artery stent placement, and 3 were in patients with acute ischemic stroke due to LVO. The included study characteristics and the quality and risk of bias appraisal of the included studies are shown in the Online Supplemental Data. Most of the studies in this review demonstrated little-to-no concern about the applicability and risk of bias.

CBCT Perfusion Imaging

Dual-Phase CBCT Perfusion. Dual-phase CBCT perfusion is a 3D technique from which the perfusion parameter parenchymal blood volume (PBV) is derived. These perfusion maps are derived by acquiring two 3D volumes¹⁵ and are based on a single compartment model.^{20,21}

First, an initial noncontrast mask volume is acquired, after which injection of a contrast medium is started by using a prolonged injection protocol that floods the arteries, tissues, and veins with contrast. On the basis of DSA observation between the scans, the fill run is manually started when opacification of the veins becomes visible to ensure the presence of a steady state of contrast in the entirety of the image for the duration of the acquisition. The acquisition is illustrated in the Online Supplemental Data.

The images are derived by means of postprocessing in which the mask and fill runs are reconstructed separately.¹⁵ First the 2 volumes are coregistered, after which the noncontrast mask volume is subtracted from the contrast-enhanced volume. An algorithm is then applied to segment out air and bone. Afterward, the steady-state arterial input function is automatically calculated.

The image volume is normalized by applying a final scaling. To reduce pixel noise, a smoothing filter is applied.

Calculation of PBV requires the time curves for contrast in tissue, artery, and vein, which is not possible with a CBCT. Using the steady-state method, PBV can then be inferred to be equal to multidetector CT-derived CBV. However, PBV has been shown to be a composite perfusion parameter, exhibiting properties similar to both CBV and CBF.²²

Clinical Applications. In this systematic review, 6 prospective studies were retrieved that investigated the use of dual-phase CBCT perfusion for the assessment of cerebral hemodynamic status in 106 patients. Five studies investigated patients with signs of acute ischemic stroke, and 1 study investigated patients with delayed cerebral ischemia after aneurysmal SAH.

In patients with acute cerebrovascular signs, all 5 studies compared CBCT CBV with CTP CBV. Struffert et al²³⁻²⁵ performed 3 prospective studies in 48 patients. CTP was performed before treatment in all studies, and PBV was calculated after treatment with a time difference between the 2 acquisitions from 95 minutes to 24 hours. Correlations between CBCT CBV and CTP CBV ranged from $r = 0.72$ to $r = 0.90$. Two studies prospectively studied both PBV and CTP CBV in 32 patients with signs of cerebrovascular ischemia and reported comparable good correlations between the 2 techniques.^{26,27} Furthermore, no treatment was performed in the time interval between the scans.

Kamran et al²² compared relative (r) PBV ($rPBV = \text{right PBV/left PBV}$) measurements with $rCBF$ derived from MRI-PWI and $rCBV$ in 26 patients with delayed cerebral ischemia after aneurysmal SAH. Delayed cerebral ischemia was defined as clinical deterioration lasting ≥ 2 hours without imaging evidence of rebleeding or hydrocephalus and no other medical causes. Clinical deterioration occurred an average of 7 days after aneurysmal SAH. Moderate-to-good correlations were reported between $rPBV$ and MRI-PWI $rCBF$ ($r = 0.85$ and $r = 0.78$), and $rPBV$ versus MRI-PWI $rCBV$ ($r = 0.72$ and $r = 0.69$) was reported for cortical and subcortical voxels of interest, respectively. The average time between the scans was 124 minutes.

Multiphase CBCT Perfusion. Multiphase CBCT perfusion is a technique in which perfusion parameters, such as CBV, CBF, MTT, and TTP, are derived by acquiring multiple sequential volumes after injection of contrast. Time-density curves are then generated throughout the brain tissue to calculate parametric perfusion maps.

Acquisition is based on the work of Royalty et al.²⁸ Before contrast injection, 2 high-speed baseline scans (clockwise and counterclockwise) are performed to obtain mask images. A contrast bolus is then injected, after which 7 or 8 high-speed bidirectional scans are obtained. The average rotation time is approximately 5 seconds, with 1 second between the rotations, resulting in a sampling time of 6 seconds. A motion-correction algorithm based on mutual information is used to decrease movement artifacts.^{29,30} The acquisition protocol is outlined in the Online Supplemental Data.

After manual selection of the arterial input function, parametric perfusion maps of TTP, CBV, CBF, and MTT are calculated,

similar to CTP by means of a modified deconvolution algorithm.^{16,31,32}

Clinical Applications. Five studies were retrieved in this review that prospectively compared multiphase CBCT perfusion with MR perfusion or CTP. A total of 69 patients were included.

Lin et al³³ evaluated the feasibility of quantifying oligemia in 10 patients with carotid stenosis before treatment. Relative and absolute values of TTP, MTT, CBF, and CBV were compared with those of MR perfusion. For the relative values, the correlations were moderate-to-good: $rTTP$ ($r = 0.75$), $rCBF$ ($r = 0.79$), and $rCBV$ ($r = 0.50$). For the absolute measurements, the correlations were poor-to-moderate: TTP ($r = 0.56$), MTT ($r = 0.47$), CBF ($r = 0.43$), and CBV ($r = 0.47$). No correlations were reported for $rMTT$ between CBCT and MR perfusion.

Chen et al³⁴ evaluated the feasibility of using CBCT to monitor cerebral hemodynamics during carotid artery stent placement in 13 patients. Relative and absolute TTP, CBV, MTT, and CBF were measured before and after treatment by both MR perfusion and CBCT. They reported no correlations in the absolute parameters. Before stent placement, there was moderate-to-good correlation for $rTTP$ ($r = 0.58$) and $rCBF$ ($r = 0.73$). After stent placement, none of the parameters were correlated between CBCT and MR perfusion.

Struffert et al³⁵ investigated the feasibility and qualitative comparability of multiphase CBCT perfusion in 12 patients with LVO and perfusion mismatch presenting beyond 4.5 hours of symptom onset. The scans with CBCT and MR perfusion were obtained within 30 minutes of each other. The results were evaluated by 2 reviewers (A and B). For reviewer A, the correlation was moderate for CBV ($r = 0.49$) and good for CBF ($r = 0.97$), MTT ($r = 0.96$), and TTP ($r = 0.96$). For reviewer B, the correlation was poor for CBV ($r = 0.40$) and good for CBF ($r = 0.98$), MTT ($r = 0.95$), and TTP ($r = 0.97$).

Kurmann et al³⁶ prospectively compared preinterventional volumes of ischemic core, penumbra, and mismatch between multiphase CBCT perfusion and CTP in 20 patients with LVO. Scans were obtained with a maximum of a 2-hour delay in between. The infarct core threshold was set at $rCBF < 30\%$ and $rCBF < 45\%$ for CTP and multiphase CBCT, respectively. The penumbra threshold was set at a time-to-maximum of > 6 seconds. They reported good ($r^2 = 0.84$) correlations for conventional $rCBF (< 30\%)$ and multiphase CBCT $rCBF (< 45\%)$. The correlation was poor ($r^2 = 0.33$) for mismatch volumes and moderate ($r^2 = 0.57$) for penumbra volumes.

Ortega-Gutierrez et al³⁷ prospectively compared perfusion maps between multiphase CBCT perfusion and CTP in 14 patients with acute ischemic stroke due to LVO. The median time between the scans was 42 minutes. The comparison was made using 3 methods: Method 1 was based on placing matched ROIs in the anterior circulation, method 2 was based on placement of matched ROIs in the 10 areas of the MCA corresponding to the ASPECTS,³⁸ and method 3 was based on manual drawing of ROIs in areas with visually apparent perfusion abnormalities. For the first method, the correlation was good (intraclass correlation coefficient [ICC] = 0.77) for MTT and moderate (ICC = 0.58, ICC = 0.65, ICC = 0.52) for CBF, CBV, and time-to-maximum/TTP,

respectively. For the second method, the correlation was poor (ICC = 0.32) for time-to-maximum/TTP, and moderate (ICC = 0.51, ICC = 0.57, ICC = 0.62) for CBF, CBV, and MTT, respectively. For the third method, the correlation was poor (ICC = 0.15) for time-to-maximum/TTP, moderate (ICC = 0.70) for CBF, and good (ICC = 0.83, ICC = 0.95) for MTT and CBV, respectively.

DISCUSSION

This systematic review provides an overview of the currently available CBCT techniques to image tissue perfusion in the brain. We identified 11 studies based on a dual-phase ($n = 6$) or multiphase ($n = 5$) CBCT perfusion imaging techniques. Moderate-to-good correlations were reported between the CBCT techniques and the reference techniques; however, most of the studies demonstrated a large time interval between the scans and included small heterogeneous cohorts.

Studies of endovascular therapy in the late time window (6–24 hours after stroke onset) and intravenous thrombolysis^{2–4} have relied on CTP or multimodal MR imaging (diffusion-weighted and perfusion-weighted imaging) to identify patients with small ischemic core volumes and relatively large penumbra volumes. The studies in this review suggest that CBCT perfusion imaging can be used for assessing cerebral ischemic disease, either as adjuncts to conventional imaging for intraoperative monitoring or a substitute for conventional CTP in a direct-to-angio approach. A recent meta-analysis of the direct-to-angio approach demonstrated its safety and effectivity in decreasing door-to-treatment times.³⁹ However, none of the included studies in this review investigated the diagnostic accuracy of CBCT perfusion imaging in terms of quantitative assessment of perfusion or its ability to distinguish core from penumbra in acute ischemic stroke.

The studies in this review that investigated dual-phase CBCT perfusion demonstrated the feasibility of this technique to provide real-time assessment of the perfusion parameter PBV and reported good correlations between PBV and CTP CBV. Furthermore, it has been demonstrated that PBV could potentially predict final infarct volume in patients with stroke.²⁵ On the other hand, PBV is not yet fully understood as a perfusion parameter and has been demonstrated to be a composite parameter, incorporating both CBV and CBF.²² The implications for its ability to select patients for revascularisation therapy are, therefore, unknown. Future studies should focus on investigating the comprehensiveness of PBV and its clinical applicability.

Multiphase CBCT perfusion is a technique that can assess multiple perfusion parameters.^{40,41} However, the limited temporal resolution of CBCTs may affect the quantification of the perfusion parameters.^{42–45} The studies in this review have demonstrated the feasibility of this technique in patients with chronic ($n = 2$) and acute ($n = 3$) ischemia. The reported correlations between CBCT and MR perfusion ranged from poor to good for all perfusion parameters, but in some instances, they did not correlate at all.^{33–35} In studies investigating the technique in patients with stroke with LVO, weak correlations for penumbra and mismatch volumes from CBCT and CTP were reported,³⁶ and weak-to-good correlations were reported between perfusion parameters from CBCT and CTP.^{36,37} Multiphase CBCT

perfusion demonstrates promising accuracy and applicability in patients with stroke with LVO; however, the current evidence is limited. Future studies should aim to investigate the diagnostic accuracy and include large homogeneous cohorts, a standardized acquisition protocol, and comparison with a criterion standard, such as PET perfusion imaging.

Both reported CBCT perfusion techniques require a lower dose of contrast and radiation than conventional CT for acquiring the same data. A multidetector CT stroke protocol consists of perfusion imaging, noncontrast CT, and angiographic imaging, resulting in a total dose of approximately 8–9 mSv for an entire evaluation.^{46–48} Multiphase CBCT perfusion requires a total effective radiation dose of 4.6 mSv.^{33–35} Furthermore, with this technique, additional reconstructions can be applied in the same acquisition only to the mask runs and only to the fill runs to provide soft-tissue and dynamic angiographic imaging, respectively.²³ Therefore, a single multiphase CBCT acquisition could provide data that are analogous to a full multidetector CT stroke protocol for around half the radiation dose. A dual-phase CBCT scan provides PBV measurements, in addition to large-vessel and soft-tissue reconstructions, which could reliably assess the patency of large vessels, the presence of vasospasms, and the presence of intracranial hemorrhage.^{22,49}

While the direct-to-angio approach has proved safe and feasible in reducing door-to-puncture times, it faces numerous limitations with regard to practicalities and applicability. In patients with acute ischemic stroke, the initial triage is aimed at ruling out intracerebral hemorrhage and confirming LVOs. Prolonged selection protocols identify only a minority of patients who may not benefit from treatment, leaving most at risk.⁸ On the other hand, simplifying the selection process may increase the number of patients undergoing angiography who would not benefit from the procedure.⁹ This potential disadvantage should be carefully considered when implementing measures to reduce complexity. Furthermore, standardized clinical scales must be introduced and in-hospital organization should be realized to optimize the benefit of such an approach and achieve better outcomes.⁵⁰

This selected literature has limitations. First, the heterogeneity between and within the techniques, the C-arm systems, and post-processing methods made it difficult to draw conclusions and impossible to apply meta-analysis to the data. Second, a large heterogeneity exists with regard to the terminology; numerous terms could be used to describe the same technique/system. Last, none of the studies in this review investigated the diagnostic accuracy of the CBCT techniques against conventional methods.

CONCLUSIONS

The CBCT techniques in this review demonstrate the potential for implementation in clinical practice. Dual-phase CBCT perfusion could be used as an adjunct to conventional diagnostic methods, potentially improving overall outcome and safety, with the advantage of reduction of contrast medium and radiation dose. However, it does not provide a full assessment of brain perfusion parameters, and the comprehensiveness of PBV remains unclear. Multiphase CBCT perfusion provides an assessment of multiple brain perfusion parameters and could reduce door-to-puncture times substantially and improve functional outcome in

a direct-to-angio approach. On the other hand, multiphase CBCT has low temporal resolution, and its parameters did not consistently correlate with the reference technique. In addition to investigating their performance and diagnostic accuracy, future studies should address the practical challenges associated with implementing these techniques and the potential benefits for different ischemic diseases.

Disclosure forms provided by the authors are available with the full text and PDF of this article at www.ajnr.org.

REFERENCES

1. Powers WJ, Rabinstein AA, Ackerson T, et al. **Guidelines for the Early Management of Patients with Acute Ischemic Stroke: 2019 Update to the 2018 Guidelines for the Early Management of Acute Ischemic Stroke—A Guideline for Healthcare Professionals From the American Heart Association/American Stroke Association.** *Stroke* 2019;50:e344–418 CrossRef Medline
2. Ma H, Campbell B. V, Parsons MW, et al; EXTEND Investigators. **Thrombolysis guided by perfusion imaging up to 9 hours after onset of stroke.** *N Engl J Med* 2019;380:1795–803 CrossRef Medline
3. Nogueira RG, Jadhav AP, Haussen DC, et al; DAWN Trial Investigators. **Thrombectomy 6 to 24 hours after stroke with a mismatch between deficit and infarct.** *N Engl J Med* 2018;378:11–21 CrossRef Medline
4. Albers GW, Marks MP, Kemp S, et al; DEFUSE 3 Investigators. **Thrombectomy for stroke at 6 to 16 hours with selection by perfusion imaging.** *N Engl J Med* 2018;378:708–18 CrossRef Medline
5. Saver JL, Goyal M, van der Lugt A, et al; HERMES Collaborators. **Time to treatment with endovascular thrombectomy and outcomes from ischemic stroke: a meta-analysis.** *JAMA* 2016;316:1279–88 CrossRef Medline
6. Meretoja A, Keshkaran M, Saver JL, et al. **Stroke thrombolysis.** *Stroke* 2014;45:1053–58 CrossRef Medline
7. Dargazanli C, Consoli A, Barral M, et al. **Impact of modified TIC1 3 versus modified TIC1 2b reperfusion score to predict good outcome following endovascular therapy.** *AJNR Am J Neuroradiol* 2017;38:90–96 CrossRef Medline
8. Mendez B, Requena M, Aires A, et al. **Direct transfer to angio-suite to reduce workflow times and increase favorable clinical outcome.** *Stroke* 2018;49:2723–27 CrossRef Medline
9. Ribo M, Boned S, Rubiera M, et al. **Direct transfer to angiosuite to reduce door-to-puncture time in thrombectomy for acute stroke.** *J Neurointerv Surg* 2018;10:221–24 CrossRef Medline
10. Brehm A, Tsogkas I, Maier IL, et al. **One-stop management with perfusion for transfer patients with stroke due to a large-vessel occlusion: feasibility and effects on in-hospital times.** *AJNR Am J Neuroradiol* 2019;40:1330–34 CrossRef Medline
11. Sarraj A, Goyal N, Chen M, et al. **Direct to angiography vs repeated imaging approaches in transferred patients undergoing endovascular thrombectomy.** *JAMA Neurol* 2021;78:916–26 CrossRef Medline
12. Psychogios MN, Bähr M, Liman J, et al. **One stop management in acute stroke: first mothership patient transported directly to the angiography suite.** *Clin Neuroradiol* 2017;27:389–91 CrossRef Medline
13. Bousslama M, Haussen DC, Grossberg JA, et al. **Flat-panel detector CT assessment in stroke to reduce times to intra-arterial treatment: a study of multiphase computed tomography angiography in the angiography suite to bypass conventional imaging.** *Int J Stroke* 2021;16:63–72 CrossRef Medline
14. Requena M, Olivé-Gadea M, Muchada M, et al. **Direct to angiography suite without stopping for computed tomography imaging for patients with acute stroke: a randomized clinical trial.** *JAMA Neurol* 2021;78:1099–107 CrossRef Medline
15. Zellerhoff M, Deuerling-Zheng Y, Strother CM, et al. **Measurement of cerebral blood volume using angiographic C-arm systems.** In: *Proceedings of SPIE, The International Society for Optical Engineering* 7262, February 26, 2009. Lake Buena Vista, Florida CrossRef
16. Ganguly A, Fieselmann A, Marks M, et al. **Cerebral CT perfusion using an interventional C-arm imaging system: cerebral blood flow measurements.** *AJNR Am J Neuroradiol* 2011;32:1525–31 CrossRef Medline
17. Moher D, Shamseer L, Clarke M, et al; PRISMA-P Group. **Preferred reporting items for systematic review and meta-analysis protocols (PRISMA-P) 2015 statement.** *Syst Rev* 2015;4:1 CrossRef Medline
18. Ouzzani M, Hammady H, Fedorowicz Z, et al. **Rayyan: a web and mobile app for systematic reviews.** *Syst Rev* 2016;5:210 CrossRef Medline
19. Whiting PF, Rutjes AW, Westwood ME, et al; QUADAS-2 Group. **QUADAS-2: a revised tool for the quality assessment of diagnostic accuracy studies.** *Ann Intern Med* 2011;155:529–36 CrossRef Medline
20. Klotz E, König M. **Perfusion measurements of the brain: using dynamic CT for the quantitative assessment of cerebral ischemia in acute stroke.** *Eur J Radiol* 1999;30:170–84 CrossRef Medline
21. Axel L. **Cerebral blood flow determination by rapid-sequence computed tomography: theoretical analysis.** *Radiology* 1980;137:679–86 CrossRef Medline
22. Kamran M, Byrne JV. **C-arm flat detector computed tomography parenchymal blood volume imaging: the nature of parenchymal blood volume parameter and the feasibility of parenchymal blood volume imaging in aneurysmal subarachnoid haemorrhage patients.** *Neuroradiology* 2015;57:937–49 CrossRef Medline
23. Struffert T, Deuerling-Zheng Y, Kloska S, et al. **Flat detector CT in the evaluation of brain parenchyma, intracranial vasculature, and cerebral blood volume: a pilot study in patients with acute symptoms of cerebral ischemia.** *AJNR Am J Neuroradiol* 2010;31:1462–69 CrossRef Medline
24. Struffert T, Deuerling-Zheng Y, Kloska S, et al. **Cerebral blood volume imaging by flat detector computed tomography in comparison to conventional multislice perfusion CT.** *Eur Radiol* 2011;21:882–89 CrossRef Medline
25. Struffert T, Deuerling-Zheng Y, Engelhorn T, et al. **Feasibility of cerebral blood volume mapping by flat panel detector CT in the angiography suite: first experience in patients with acute middle cerebral artery occlusions.** *AJNR Am J Neuroradiol* 2012;33:618–25 CrossRef Medline
26. Zhang Q, Wang B, Han J, et al. **Feasibility study of perfusion imaging using flat detector CT with an intra-arterial injection protocol compared to conventional multi-slice perfusion CT with an intravenous injection protocol.** *Interv Neuroradiol* 2013;19:409–15 CrossRef Medline
27. Zhang Y-W, Hong B, Huang Q-H, et al. **The feasibility and clinical application of flat-panel detector computer tomography in evaluating cerebral blood volume: an initial prospective study.** *J Interv Radiol (China)* 2012;21:265–69 CrossRef
28. Royalty K, Manhart M, Pulfer K, et al. **C-arm CT measurement of cerebral blood volume and cerebral blood flow using a novel high-speed acquisition and a single intravenous contrast injection.** *AJNR Am J Neuroradiol* 2013;34:2131–38 CrossRef Medline
29. Bizais Y, Barillot C, Di Paola R, eds. *Information Processing in Medical Imaging: Computational Imaging and Vision (CIVI, volume 3).* Springer; 1995.
30. Viola P, Wells WM III. **Alignment by maximization of mutual information.** *International Journal of Computer Vision* 1997;24:137–54 CrossRef
31. Fieselmann A, Kowarschik M, Ganguly A, et al. **Deconvolution-based CT and MR brain perfusion measurement: theoretical model revisited and practical implementation details.** *Int J Biomed Imaging* 2011;2011:467563 CrossRef Medline
32. Fieselmann A, Ganguly A, Deuerling-Zheng Y, et al. **Interventional 4-D C-arm CT perfusion imaging using interleaved scanning and partial reconstruction interpolation.** *IEEE Trans Med Imaging* 2012;31:892–906 CrossRef Medline
33. Lin CJ, Guo WY, Chang FC, et al. **Using flat-panel perfusion imaging to measure cerebral hemodynamics: a pilot feasibility study in**

- patients with carotid stenosis. *Medicine (Baltimore)* 2016;95:e3529 CrossRef Medline
34. Chen LW, Lin CJ, Guo WY, et al. **Evaluating cerebral hemodynamics using quantitative digital subtraction angiography and flat-detector computed tomography perfusion imaging: a comparative study in patients with carotid stenosis.** *J Chin Med Assoc* 2018;81:977–84 CrossRef Medline
 35. Struffert T, Deuerling-Zheng Y, Kloska S, et al. **Dynamic angiography and perfusion imaging using flat detector CT in the angiography suite: a pilot study in patients with acute middle cerebral artery occlusions.** *AJNR Am J Neuroradiol* 2015;36:1964–70 CrossRef Medline
 36. Kurmann CC, Kaesmacher J, Cooke DL, et al. **Evaluation of time-resolved whole brain flat panel detector perfusion imaging using RAPID ANGIO in patients with acute stroke: comparison with CT perfusion imaging.** *J Neurointerv Surg* 2023;15:387–92 CrossRef Medline
 37. Ortega-Gutierrez S, Quispe-Orozco D, Schafer S, et al. **Angiography suite cone-beam CT perfusion for selection of thrombectomy patients: a pilot study.** *J Neuroimaging* 2022;32:493–501 CrossRef Medline
 38. Barber PA, Demchuk AM, Zhang J, et al. **Validity and reliability of a quantitative computed tomography score in predicting outcome of hyperacute stroke before thrombolytic therapy.** *Lancet* 2000;355:1670–74 CrossRef Medline
 39. Requena M, Olivé M, García-Tornel Á, et al. **Time matters.** *Stroke* 2020;51:1766–71 CrossRef Medline
 40. Wintermark M, Sincic R, Sridhar D, et al. **Cerebral perfusion CT: technique and clinical applications.** *J Neuroradiol* 2008;35:253–60 CrossRef Medline
 41. de Lucas EM, Sánchez E, Gutiérrez A, et al. **CT protocol for acute stroke: tips and tricks for general radiologists.** *Radiographics* 2008;28:1673–87 CrossRef Medline
 42. Wintermark M, Smith WS, Ko NU, et al. **Dynamic perfusion CT: optimizing the temporal resolution and contrast volume for calculation of perfusion CT parameters in stroke patients.** *AJNR Am J Neuroradiol* 2004;25:720–29 Medline
 43. Wiesmann M, Berg S, Bohner G, et al. **Dose reduction in dynamic perfusion CT of the brain: effects of the scan frequency on measurements of cerebral blood flow, cerebral blood volume, and mean transit time.** *Eur Radiol* 2008;18:2967–74 CrossRef Medline
 44. Kämena A, Streitparth F, Grieser C, et al. **Dynamic perfusion CT: optimizing the temporal resolution for the calculation of perfusion CT parameters in stroke patients.** *Eur J Radiol* 2007;64:111–18 CrossRef Medline
 45. Abels B, Klotz E, Tomandl BF, et al. **CT perfusion in acute ischemic stroke: a comparison of 2-second and 1-second temporal resolution.** *AJNR Am J Neuroradiol* 2011;32:1632–39 CrossRef Medline
 46. Mnyusiwalla A, Aviv RI, Symons SP. **Radiation dose from multidetector row CT imaging for acute stroke.** *Neuroradiology* 2009;51:635–40 CrossRef Medline
 47. Diekmann S, Siebert E, Juran R, et al. **Dose exposure of patients undergoing comprehensive stroke imaging by multidetector-row CT: comparison of 320-detector row and 64-detector row CT scanners.** *AJNR Am J Neuroradiol* 2010;31:1003–09 CrossRef Medline
 48. Cohnen M, Wittsack HJ, Assadi S, et al. **Radiation exposure of patients in comprehensive computed tomography of the head in acute stroke.** *AJNR Am J Neuroradiol* 2006;27:1741–45 Medline
 49. Kamran M, Nagaraja S, Byrne JV. **C-arm flat detector computed tomography: the technique and its applications in interventional neuro-radiology.** *Neuroradiology* 2010;52:319–27 CrossRef Medline
 50. Sun CJ, Ribo M, Goyal M, et al. **Door-to-puncture: a practical metric for capturing and enhancing system processes associated with endovascular stroke care, preliminary results from the rapid reperfusion registry.** *J Am Heart Assoc* 2014;3:e000859 CrossRef Medline

Effect of Platelet Function Testing Guidance on Clinical Outcomes for Patients with Intracranial Aneurysms Undergoing Endovascular Treatment

X. Wang, L. Luo, Y. Wang, and Z. An



ABSTRACT

BACKGROUND: Platelet function testing has been proposed to better adjust individualized antiplatelet treatment for patients undergoing endovascular treatment for intracranial aneurysms. Its clinical significance needs to be comprehensively evaluated.

PURPOSE: Our aim was to evaluate the impact of platelet function testing–guided versus standard antiplatelet treatment in patients receiving endovascular treatment for intracranial aneurysms.

DATA SOURCES: PubMed, EMBASE, and the Cochrane Library of clinical trials were searched from inception until March 2023.

STUDY SELECTION: Eleven studies comprising 6199 patients were included.

DATA ANALYSIS: ORs with 95% CIs were calculated using random effects models.

DATA SYNTHESIS: The platelet function testing–guided group was associated with a decreased rate of symptomatic thromboembolic events (OR = 0.57; 95% CI, 0.42–0.76; $I^2 = 26\%$). No significant difference was found in asymptomatic thromboembolic events (OR = 1.07; 95% CI, 0.39–2.94; $I^2 = 48\%$), hemorrhagic events (OR = 0.71; 95% CI, 0.42–1.19; $I^2 = 34\%$), intracranial hemorrhagic events (OR = 0.61; 95% CI, 0.03–10.79; $I^2 = 62\%$), morbidity (OR = 0.53; 95% CI, 0.05–5.72; $I^2 = 86\%$), and mortality (OR = 1.96; 95% CI, 0.64–5.97; $I^2 = 0\%$) between the 2 groups. Subgroup analysis suggested that platelet function testing–guided therapy may contribute to fewer symptomatic thromboembolic events in patients who received stent-assisted coiling (OR = 0.43; 95% CI, 0.18–1.02; $I^2 = 43\%$) or a combination of stent-assisted and flow-diverter stent placement (OR = 0.61; 95% CI, 0.36–1.02; $I^2 = 0\%$) or who changed from clopidogrel to other thienopyridines (OR = 0.64; 95% CI, 0.40–1.02; $I^2 = 18\%$), though the difference did not reach statistical significance.

LIMITATIONS: Heterogeneous endovascular treatment methods and adjusted antiplatelet regimens were limitations.

CONCLUSIONS: Platelet function testing–guided antiplatelet strategy significantly reduced the incidence of symptomatic thromboembolic events without any increase in the hemorrhagic events for patients undergoing endovascular treatment for intracranial aneurysms.

ABBREVIATIONS: EVT = endovascular treatment; HPR = high on-treatment platelet reactivity; IA = intracranial aneurysm; LTA = light transmission aggregometry; PFT = platelet function testing; RCT = randomized controlled trial

In recent years, the use of endovascular treatment (EVT) for intracranial aneurysms (IAs) gained increasing attention due to its less invasive nature and associated improved clinical outcomes.^{1–4}

Despite advancements in techniques and technology,¹ thromboembolic events remain a major concern, leading to the adoption of conventional dual antiplatelet therapy as the standard regimen.⁵ However, a considerable proportion of patients (ranging from 15% to 55.3%) may develop high on-treatment platelet reactivity (HPR),^{6–9} which increases the risk of thromboembolic events.^{5,10}

Platelet function testing (PFT) has been proposed as a means to adjust individualized antiplatelet strategies for patients with HPR.¹¹ However, the use of PFT for EVT in patients with IAs remains controversial, and its clinical significance needs comprehensive evaluation. Several studies have demonstrated that PFT

Received April 11, 2023; accepted after revision June 1.

From the Departments of Pharmacy (X.W., Z.A.) and Neurosurgery (Y.W.), Beijing Chao-Yang Hospital, Capital Medical University, Beijing, China; and Department of Pharmacy (L.L.), Beijing Huairou Hospital, Beijing, China.

Dr. Y. Wang and Z. An are the co-senior authors of this research.

Please address correspondence to Zhuoling An, PhD, Department of Pharmacy, Beijing Chao-Yang Hospital, Capital Medical University, No. 8 Gongtintan Rd, Chaoyang District, Beijing, China; e-mail: anzhuoling@163.com

Indicates article with online supplemental data.

<http://dx.doi.org/10.3174/ajnr.A7923>

can reduce thromboembolic events in patients undergoing EVT for IAs.^{5,12,13} Conversely, other studies have not shown a significant reduction in such events^{14,15} and have suggested that the increased intensity of the antiplatelet treatment may lead to an increased incidence of bleeding events.⁵ Furthermore, there is inconsistency in the literature regarding the impact of PFT on clinical outcomes such as morbidity. Aoun et al¹⁶ found significantly reduced postoperative permanent morbidity, while Brinjikji et al¹⁷ found higher rates of morbidity in patients who underwent Pipeline Embolization Device (PED; Medtronic) replacement.

Unlike previous meta-analyses that focused on specific procedures (mainly PED treatment)^{18,19} or compared individual studies with or without PFT,^{19,20} our study uniquely selected studies reporting both PFT-guided and standard groups for any endovascular procedures. We aimed to comprehensively evaluate the effect of PFT on patients with IAs undergoing EVT by comparing those who underwent PFT and those who did not. This approach will fill a notable gap in the literature and add valuable insight to the existing body of research.

MATERIALS AND METHODS

Protocol and Registration

We followed the Preferred Reporting Items for Systematic reviews and Meta-Analyses (PRISMA) guideline²¹ to perform this meta-analysis. This systematic review and meta-analysis was prospectively registered at the international prospective register of systematic reviews (PROSPERO) before searching.

Literature Research

PubMed, EMBASE, and the Cochrane Library of clinical trials data bases were searched from inception until March 2023 with no language restrictions. The terms were ([intracranial] OR [cerebral] AND [aneurysm]) AND ([platelet function test] OR [light transmittance aggregometry] OR [LTA] OR [vasodilator stimulated phosphoprotein] OR [VASP] OR [VerifyNow] OR [Thromboelastography]). The detailed search terms are available in the Online Supplemental Data.

Study Selection

Two independent reviewers (X.W. and L.L.) through EndNote (Version 9.3.2; <https://endnote.com/downloads>) performed manual screening and scanning for eligibility. The Population, Intervention, Comparison, and Outcomes Study (PICOS) principle was used to select included studies. The inclusion criteria were presented as follows: 1) Population: patients underwent endovascular treatment for intracranial aneurysm; 2) Intervention: patients received PFT and accordingly adjusted antiplatelet strategy; 3) Comparison: patients received standard antiplatelet strategy without taking the PFT; 4) Outcomes: symptomatic thromboembolic events, asymptomatic thromboembolic events, hemorrhagic events, intracranial hemorrhage, morbidity, and mortality; and 5) Study: cohort studies or randomized controlled trials (RCTs). We also hand-searched the reference lists of all included studies for potentially relevant citations. The outcome definitions of symptomatic thromboembolic events in the individual studies are listed in the Online Supplemental Data.

Quality Assessment

Two reviewers independently performed the quality assessment using the Newcastle-Ottawa Scale and the Cochrane Collaboration tool for assessing the risk of bias²² for cohort studies and RCTs, respectively. Disagreements on study quality assessment were discussed with another reviewer (Z.A. and Y.W.) until a consensus was reached.

Data Extraction

Two investigators (X.W. and L.L.) independently extracted data for eligible studies. The characteristic data obtained for each study included the first author, year of publication, study design, type of aneurysms, endovascular procedure, PFT method, initial and adjusted antiplatelet strategy, number of patients who received an adjustment in the adjusted group, sample size, and outcomes.

Statistical Analysis

ORs with 95% CIs were calculated with R statistical and computing software (Version 4.0.5; <http://www.r-project.org>). Heterogeneity across the studies was assessed using the Cochran Q test; the percentage of total variability attributable to heterogeneity was quantified by the I^2 value. An I^2 of <50% indicates low or moderate heterogeneity, and >50% indicates high heterogeneity.²² The random effects model with inverse-variance weighting was used for all analyses. P values < .05 were considered significant. Subgroup analysis was performed for symptomatic thromboembolic events and hemorrhagic events according to the endovascular procedure, initial antiplatelet treatment, adjusted strategy, and race. A difference between the estimates of these subgroups was considered significant for the P value between subgroups of <.10.²³ To evaluate the stability of the results, we performed a sensitivity analysis by sequentially removing every single study from the pooled effect estimates including all cohort studies.

RESULTS

Three hundred seventy-nine studies were found after data base searching, of which 75 duplicated studies were excluded. After screening for title and abstract, 224 studies were removed and 80 were full-text screened (Online Supplemental Data). Eleven studies with 6199 patients in total were finally included in the systematic review and meta-analysis (Online Supplemental Data).^{5,12-17,24-27} One study⁵ was an RCT, and the other 10 were cohort studies. The endovascular treatment consisted of stent-assisted coiling, flow-diverter stent placement, and combinations of coiling, stent/balloon-assisted coiling, and flow-diverter stent placement. Types of platelet testing included VerifyNow (Accumetrics), light transmission aggregometry (LTA), multiple electrode aggregometry, INNOVANCE PFA-100 P2Y platelet function assay (Siemens), whole-blood aggregometry testing, and thromboelastography-platelet mapping. The proportion of patients who received antiplatelet strategy adjustment in the tested group ranged from 15.8% to 69.9%.

Quality Assessment

Only 1 study¹⁵ scored 4 on the Newcastle-Ottawa Scale because it was a conference abstract with little detailed information about

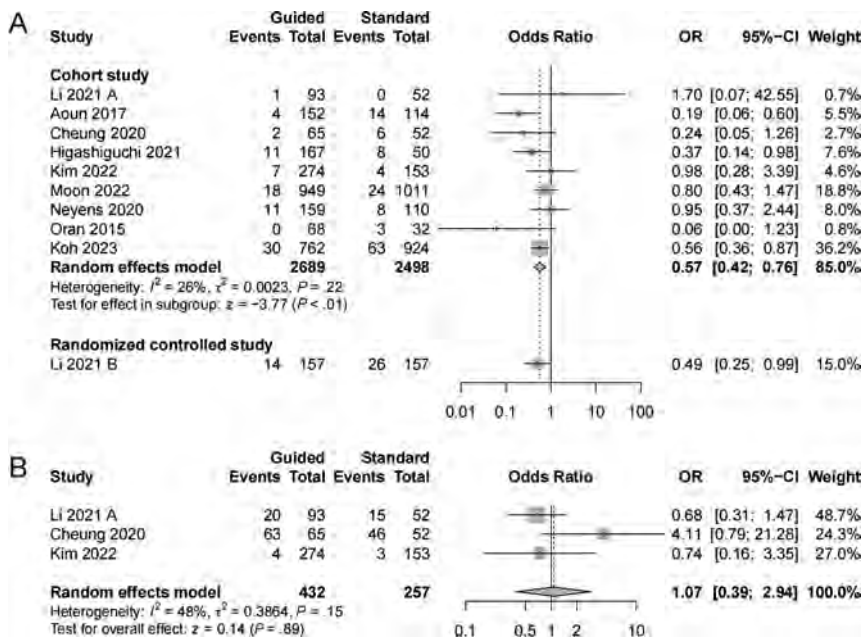


FIG 1. Forest plot of symptomatic thromboembolic events and asymptomatic thromboembolic events comparing the PFT-guided group with the standard group. A, Symptomatic thromboembolic events. B, Asymptomatic thromboembolic events.

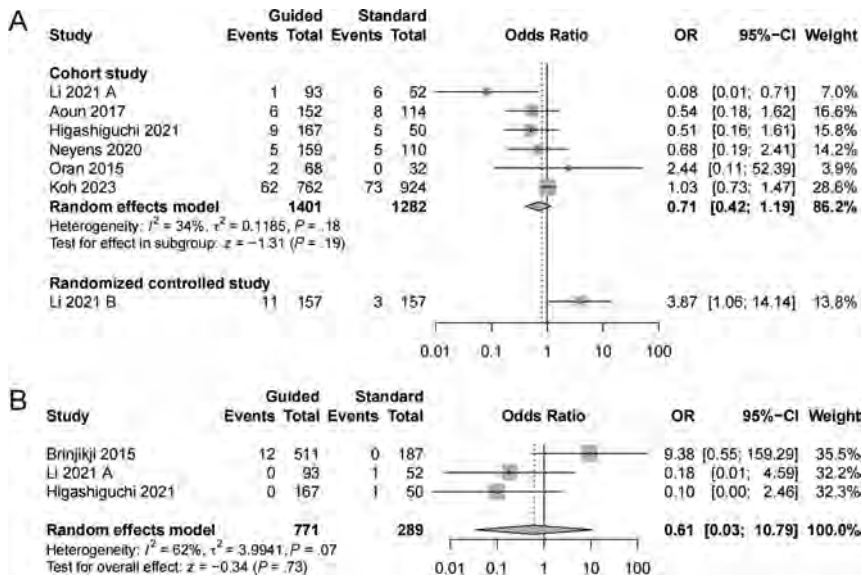


FIG 2. Forest plot of hemorrhagic events and intracranial hemorrhagic events comparing the PFT-guided group with the standard group. A, Hemorrhagic events. B, Intracranial hemorrhagic events.

the study design. The other 10 cohort studies scored 8–9 (Online Supplemental Data). For the RCT study, all potential biases were evaluated as low except for the performance bias for its open-label design (Online Supplemental Data).

Thromboembolic Events

Ten studies^{5,12-16,24-27} reported symptomatic thromboembolic events, including 9 cohort studies and 1 RCT. The guided group

was associated with a decreased rate of symptomatic thromboembolic events compared with the standard group in cohort studies (OR = 0.57; 95% CI, 0.42–0.76; $I^2 = 26\%$) (Fig 1A). Three cohort studies^{13,14,25} reported asymptomatic thromboembolic events, and no significant difference was found between the 2 groups (OR = 1.07; 95% CI, 0.39–2.94; $I^2 = 48\%$) (Fig 1B).

Hemorrhagic Events

Seven studies^{5,12,16,24-27} evaluated hemorrhagic events, including 6 cohort studies and 1 RCT. We found no significant association between the guided and standard groups (OR = 0.71; 95% CI, 0.42–1.19; $I^2 = 34\%$) in cohort studies (Fig 2A). Similarly, no difference was found in intracranial hemorrhagic events (OR = 0.61; 95% CI, 0.03–10.79; $I^2 = 62\%$) (Fig 2B).

Morbidity and Mortality

We found no association of morbidity (OR = 0.53; 95% CI, 0.05–5.72; $I^2 = 86\%$) between guided and standard groups (Online Supplemental Data). The mortality rate was comparable between the guided and the standard groups in cohort studies (OR = 1.96; 95% CI, 0.64–5.97; $I^2 = 0\%$) (Online Supplemental Data).

Subgroup Analysis (Data Base)

The results of the subgroup analysis for all cohort studies are presented in the Online Supplemental Data. Subgroup analyses were performed for symptomatic thromboembolic events and hemorrhagic events because other outcomes included only a few studies.

We found a slight but not significantly decreased risk of symptomatic thromboembolic events in the guided group compared with the standard group in subgroups using stent-assisted coiling (OR = 0.43; 95% CI, 0.18–1.02; $I^2 = 43\%$) and combined treatment (OR = 0.61; 95% CI, 0.36–1.02; $I^2 = 0\%$). There was no difference in symptomatic events between the 2 groups for patients who underwent PED stent placement (OR = 0.35; 95% CI, 0.03–4.64; $I^2 = 66\%$).

Additionally, the guided group showed a slightly lower incidence, though not significant, of symptomatic thromboembolic events compared with the standard group when clopidogrel was changed to other thienopyridines (OR = 0.64; 95% CI, 0.40–1.02;

$I^2 = 18\%$). We found that neither changing the dual antiplatelet therapy dose (OR = 0.33; 95% CI, 0.05–2.12; $I^2 = 36\%$) nor adding other drugs into the antiplatelet strategy (OR = 0.35; 95% CI, 0.03–4.78; $I^2 = 64\%$) was associated with a lower incidence of symptomatic events.

PFT-guided treatment significantly reduced the incidence of symptomatic thromboembolic events in both Asian (OR = 0.62; 95% CI, 0.45–0.86; $I^2 = 0\%$) and white groups (OR = 0.32; 95% CI, 0.11–0.92; $I^2 = 5.5\%$).

Moreover, the PFT-guided group was not associated with a significant impact on hemorrhagic events regarding subgroups according to the endovascular procedure, adjustment strategy, or race compared with the standard group.

Sensitivity Analysis

The significance of the results changed when the study by Koh et al²⁷ was excluded from the analysis of hemorrhagic events and the study by Brinjikji et al¹⁷ was excluded from the analysis of morbidity. The exclusion of any individual study included in the analysis did not significantly impact the overall findings of other outcomes (Online Supplemental Data).

DISCUSSION

The results of this meta-analysis, which included data from 6199 patients, indicated that the use of PFT-guided antiplatelet strategies in patients undergoing EVT for IAs significantly reduced the risk of symptomatic thromboembolic events without any increased risk of hemorrhagic events compared with the standard group. We found no significant impact of PFT-guided antiplatelet strategies on the incidence of morbidity and mortality.

In the subgroup analysis, we observed a notable trend toward a reduction in symptomatic thromboembolic events in the guided group of patients who received stent-assisted coiling or a combination of stent-assisted and flow-diverter stent placement, though the difference did not reach statistical significance. This finding suggests that PFT-guided therapy may have potential benefits for these specific subgroups of patients. However, the impact of PFT guidance on patients undergoing PED stent placement did not result in significant clinical outcomes, consistent with previous meta-analyses focused on PED-treated patients.¹⁹ Although a recent RCT⁵ reported reduced thromboembolic events with PFT guidance in this context (7.9% in the guided group and 20% in the standard group), further exploration and confirmation are needed due to the limited number of studies available for subgroup analysis and potential confounding factors.

Notably, we found that the replacement of clopidogrel with other adenosine diphosphate inhibitors had a tendency to reduce thromboembolic events, while other treatment adjustments did not show a significant association with this outcome. These findings highlight the importance of individualizing the antiplatelet strategy on the basis of PFT results, particularly in terms of selecting the most appropriate adenosine diphosphate inhibitor. Because it has been proved that high-dose clopidogrel could not overcome the clopidogrel hyporesponsiveness in a cardiac study,²⁸ clinicians mainly replaced clopidogrel with other thienopyridines such as prasugrel^{12,15,29} and ticagrelor.^{5,13} Several studies suggested a better antithrombotic effect with a higher risk of hemorrhagic

events of those novel P2Y₁₂ inhibitors compared with clopidogrel.^{30–32} The explanation for the elevated risk of hemorrhagic events could be the greater inhibition of platelet function and lower interindividual variability of the response to medication. Evidence from coronary trials revealed the association between those P2Y₁₂ inhibitors and a higher hemorrhage incidence, so clopidogrel remained the first choice. On the other hand, patients with HPR who lack sufficient antiplatelet treatment might have an increased risk of in-stent thrombosis,^{33,34} resulting in additional operations. Hence, PFT provided an optimal way to monitor the platelet function and evaluate whether to switch to other antiplatelet strategies.

Furthermore, our analysis demonstrated the efficacy of PFT in reducing thromboembolic events without increasing bleeding risks in both Asian and white populations. This result suggests that PFT can be a valuable tool for optimizing antiplatelet therapy in diverse patient populations.

The phenotyping assay used varied among studies, highlighting the lack of consensus among different PFT tests in identifying patients with HPR. VerifyNow was the most commonly used PFT method among all the methods.³⁵ It is a point-of-care PFT method that uses a concept similar to LTA, because LTA is known as the criterion standard for PFT but with limited clinical use due to its lack of standardization and time-consuming preparation process.³⁵ At present, the ideal cutoff value for VerifyNow remains controversial and is mainly adapted or extrapolated from cardiology literature.³⁵ There is no denying that the result of the PFT test itself is not stable due to many challenges, namely the transport of fresh blood for testing within a very short time frame.³⁵ Future studies regarding more standardized methodologic-specific processes are needed to allow better reproducible tests and adequate thresholds.

Although the PFT has been proved useful for guiding antiplatelet escalation and de-escalation for antiplatelet strategy after percutaneous coronary intervention, it is recommended that it be performed only in specific clinical scenarios such as with a high thromboembolic/hemorrhagic risk instead of on a routine basis.³⁶ To optimize the efficacy and safety of individualized antiplatelet treatment strategies, it is important to consider significant clinical and procedural variables when integrating PFT as an adjunct to antiplatelet therapy for patients underwent EVT treatment for IAs. Additionally, further evaluation is needed to focus on optimal PFT methods and establish appropriate cutoff values that accurately identify patients who would benefit from tailored antiplatelet treatment, appropriate adjustment strategies, and cost-benefit ratios in real-world implementation. Further well-designed controlled studies should be conducted to test this hypothesis.

To our knowledge, this study is the first systematic review and meta-analysis evaluating PFT in EVT for IAs for guiding antiplatelet treatment, incorporating studies that included both a PFT-guided group and a standard group. The confirmation of its beneficial effect in our study could allow further exploration of standardized PFT-guided antiplatelet strategies and their cost-effectiveness, which could have important implications for clinical practice.

However, it is important to acknowledge the limitations of our study. First, there were variations in procedural characteristics, such as the use of stent-assisted coiling or flow-diverter

stents, as well as differences in antiplatelet strategies across the included studies. Despite these differences, the heterogeneity among studies for all outcomes was low-to-moderate. Furthermore, our subgroup analyses based on endovascular procedures, adjustment strategy, and race did not show significant differences between subgroups in terms of symptomatic thromboembolic and hemorrhagic events. Second, most of the included studies were cohort studies, with only 1 RCT available. Cohort studies using real-world data can provide valuable insight into the clinical relevance and overall benefit of PFT in guiding daily treatment decisions. These studies capture a broader patient population and reflect the effectiveness of PFT in routine clinical practice. Future well-designed RCTs focusing on different procedural or antiplatelet strategy settings would further contribute to the existing evidence base.

CONCLUSIONS

In patients undergoing EVT for IAs, the PFT-guided antiplatelet strategy significantly reduced the incidence of symptomatic thromboembolic events without any increase in the hemorrhagic events. Further studies focused on a standardized PFT-guided antiplatelet strategy and different procedures are needed.

Disclosure forms provided by the authors are available with the full text and PDF of this article at www.ajnr.org.

REFERENCES

- Pierot L, Wakhloo AK. **Endovascular treatment of intracranial aneurysms: current status.** *Stroke* 2013;44:2046–54 CrossRef Medline
- Molyneux AJ, Kerr RS, Yu LM, et al; International Subarachnoid Aneurysm Trial (ISAT) Collaborative Group. **International subarachnoid aneurysm trial (ISAT) of neurosurgical clipping versus endovascular coiling in 2143 patients with ruptured intracranial aneurysms: a randomised comparison of effects on survival, dependency, seizures, rebleeding, subgroups, and aneurysm occlusion.** *Lancet* 2005;366:809–17 CrossRef Medline
- Pierot L, Spelle L, Vitry F; ATENA Investigators. **Immediate clinical outcome of patients harboring unruptured intracranial aneurysms treated by endovascular approach: results of the ATENA study.** *Stroke* 2008;39:2497–504 CrossRef Medline
- Thompson BG, Brown RD Jr, Amin-Hanjani S, et al; American Stroke Association. **Guidelines for the Management of Patients with Unruptured Intracranial Aneurysms: A Guideline for Healthcare Professionals from the American Heart Association/American Stroke Association.** *Stroke* 2015;46:2368–400 CrossRef Medline
- Li W, Zhu W, Wang A, et al. **Effect of adjusted antiplatelet therapy on preventing ischemic events after stenting for intracranial aneurysms.** *Stroke* 2021;52:3815–25 CrossRef Medline
- Hwang G, Huh W, Lee JS, et al. **Standard vs modified antiplatelet preparation for preventing thromboembolic events in patients with high on-treatment platelet reactivity undergoing coil embolization for an unruptured intracranial aneurysm: a randomized clinical trial.** *JAMA Neurol* 2015;72:764–72 CrossRef Medline
- Delgado Almandoz JE, Kadkhodayan Y, Crandall BM, et al. **Variability in initial response to standard clopidogrel therapy, delayed conversion to clopidogrel hyper-response, and associated thromboembolic and hemorrhagic complications in patients undergoing endovascular treatment of unruptured cerebral aneurysms.** *J Neurointerv Surg* 2014;6:767–73 CrossRef Medline
- Fifi JT, Brockington C, Narang J, et al. **Clopidogrel resistance is associated with thromboembolic complications in patients undergoing neurovascular stenting.** *AJNR Am J Neuroradiol* 2013;34:716–20 CrossRef Medline
- Flechtenmacher N, Kämmerer F, Dittmer R, et al. **Clopidogrel resistance in neurovascular stenting: correlations between light transmission aggregometry, VerifyNow, and the Multiplate.** *AJNR Am J Neuroradiol* 2015;36:1953–58 CrossRef Medline
- Yang H, Li Y, Jiang Y. **Insufficient platelet inhibition and thromboembolic complications in patients with intracranial aneurysms after stent placement.** *J Neurosurg* 2016;125:247–53 CrossRef Medline
- Favaloro EJ, Lippi G, Franchini M. **Contemporary platelet function testing.** *Clin Chem Lab Med* 2010;48:579–98 CrossRef Medline
- Higashiguchi S, Sadato A, Nakahara I, et al. **Reduction of thromboembolic complications during the endovascular treatment of unruptured aneurysms by employing a tailored dual antiplatelet regimen using aspirin and prasugrel.** *J Neurointerv Surg* 2021;13:1044–48 CrossRef Medline
- Cheung NK, Carr MW, Ray U, et al. **Platelet function testing in neurovascular procedures: tool or gimmick?** *Interv Neurol* 2020;8:123–34 CrossRef Medline
- Kim GJ, Heo Y, Moon EJ, et al. **Thromboembolic events during endovascular coiling for unruptured intracranial aneurysms: clinical significance of platelet reactivity unit and adjunctive cilostazol.** *Clin Neurol Neurosurg* 2022;213:107133 CrossRef Medline
- Moon EJ, Kwon B, Song Y, et al. **The necessity of monitoring platelet response and adjusting antiplatelet agents for endovascular treatment of unruptured intracranial aneurysms: a single-center, retrospective, cohort study.** In: *Proceedings of the 14th Congress of the European Society of Minimally Invasive Neurological Therapy*, September 2022, Nice, Provence-Alpes-Cote d Azur, France. CrossRef
- Aoun SG, Welch BG, Pride LG, et al. **Contribution of whole platelet aggregometry to the endovascular management of unruptured aneurysms: an institutional experience.** *J Neurointerv Surg* 2017;9:974–77 CrossRef Medline
- Brinjikji W, Lanzino G, Cloft HJ, et al. **Platelet testing is associated with worse clinical outcomes for patients treated with the Pipeline Embolization Device.** *AJNR Am J Neuroradiol* 2015;36:2090–95 CrossRef Medline
- Ajadi E, Kabir S, Cook A, et al. **Predictive value of Platelet Reactivity Unit (PRU) value for thrombotic and hemorrhagic events during flow diversion procedures: a meta-analysis.** *J Neurointerv Surg* 2019;11:1123–28 CrossRef Medline
- Skukalek SL, Winkler AM, Kang J, et al. **Effect of antiplatelet therapy and platelet function testing on hemorrhagic and thrombotic complications in patients with cerebral aneurysms treated with the Pipeline Embolization Device: a review and meta-analysis.** *J Neurointerv Surg* 2016;8:58–65 CrossRef Medline
- Gonzalez SM, Iordanou J, Adams W, et al. **Effect of stent porosity, platelet function test usage, and dual antiplatelet therapy duration on clinical and radiographic outcomes after stenting for cerebral aneurysms: a meta-analysis.** *World Neurosurg* 2023;171:159 CrossRef Medline
- Moher D, Liberati A, Tetzlaff J, et al; PRISMA Group. **Preferred reporting items for systematic reviews and meta-analyses: the PRISMA statement.** *BMJ* 2009;339:b2535 CrossRef Medline
- Higgins JP, Altman DG, Gotzsche PC, et al; Cochrane Statistical Methods Group. **The Cochrane Collaboration's tool for assessing risk of bias in randomised trials.** *BMJ* 2011;343:d5928 CrossRef Medline
- Richardson M, Garner P, Donegan S. **Interpretation of subgroup analyses in systematic reviews: a tutorial.** *Clin Epidemiol Glob Health* 2019;7:192–98 CrossRef
- Oran I, Cinar C, Bozkaya H, et al. **Tailoring platelet inhibition according to multiple electrode aggregometry decreases the rate of thrombotic complications after intracranial flow-diverting stent implantation.** *J Neurointerv Surg* 2015;7:357–62 CrossRef Medline
- Li Y, Zhang X, Guo Z, et al. **Standard vs. modified antiplatelet therapy based on thromboelastography with platelet mapping for preventing bleeding events in patients undergoing stent-assisted coil for**

- a ruptured intracranial aneurysm. *Front Neurol* 2021;11:615829 CrossRef Medline
26. Neyens R, Donaldson C, Andrews C, et al. **Platelet function testing with a VerifyNow-directed personalized antiplatelet strategy and associated rates of thromboembolic complications after Pipeline embolization for complex cerebral aneurysms.** *World Neurosurg* 2020;138:e674–82 CrossRef Medline
27. Koh JS, Hwang G, Park JC, et al; KoNES Registry Investigators. **Tailored antiplatelet therapy in stent assisted coiling for unruptured aneurysms: a nationwide registry study.** *J Neurointerv Surg* 2023 Jan 3 [Epub ahead of print] CrossRef Medline
28. Price MJ, Berger PB, Teirstein PS, et al; GRAVITAS Investigators. **Standard- vs high-dose clopidogrel based on platelet function testing after percutaneous coronary intervention: the GRAVITAS randomized trial.** *JAMA* 2011;305:1097–105 CrossRef Medline
29. McTaggart RA, Choudhri OA, Marcellus ML, et al. **Use of thromboelastography to tailor dual-antiplatelet therapy in patients undergoing treatment of intracranial aneurysms with the Pipeline Embolization Device.** *J Neurointerv Surg* 2015;7:425–30 CrossRef Medline
30. Wang Y, Meng X, Wang A, et al; CHANCE-2 Investigators. **Ticagrelor versus clopidogrel in CYP2C19 loss-of-function carriers with stroke or TIA.** *N Engl J Med* 2021;385:2520–30 CrossRef Medline
31. Wang A, Meng X, Tian X, et al; CHANCE-2 Investigators. **Bleeding risk of dual antiplatelet therapy after minor stroke or transient ischemic attack.** *Ann Neurol* 2022;91:380–88 CrossRef Medline
32. Wang A, Meng X, Tian X, et al. **Ticagrelor aspirin vs clopidogrel aspirin in CYP2C19 loss-of-function carriers with minor stroke or TIA stratified by risk profile.** *Neurology* 2023;100:e497–504 CrossRef Medline
33. Pinto Slottow TL, Bonello L, Gavini R, et al. **Prevalence of aspirin and clopidogrel resistance among patients with and without drug-eluting stent thrombosis.** *Am J Cardiol* 2009;104:525–30 CrossRef Medline
34. Bouman HJ, van Werkum JW, Breet NJ, et al. **A case-control study on platelet reactivity in patients with coronary stent thrombosis.** *J Thromb Haemost* 2011;9:909–16 CrossRef Medline
35. Kim KS, Fraser JF, Grupke S, et al. **Management of antiplatelet therapy in patients undergoing neuroendovascular procedures.** *J Neurosurg* 2018;129:890–905 CrossRef Medline
36. Sibbing D, Aradi D, Alexopoulos D, et al. **Updated expert consensus statement on platelet function and genetic testing for guiding P2Y₁₂ receptor inhibitor treatment in percutaneous coronary intervention.** *JACC Cardiovasc Interv* 2020;12:1521–37 CrossRef Medline

Outcomes of Preoperative Transophtalmic Artery Embolization of Meningiomas: A Systematic Review with a Focus on Embolization Agent

M.A. Essibayi, M. Zakirova, K.M. Phipps, C.D. Patton, R. Fluss, D. Khatri, E. Raz, M. Shapiro, A.A. Dmytriw, N. Haranhalli, V. Agarwal, and D.J. Altschul



ABSTRACT

BACKGROUND: Transophtalmic artery embolization of intracranial meningiomas is thought to be associated with a high complication risk.

PURPOSE: With advances in endovascular techniques, we systematically reviewed the current literature to improve our understanding of the safety and efficacy of transophtalmic artery embolization of intracranial meningiomas.

DATA SOURCES: We performed a systematic search using PubMed from inception until August 3, 2022.

STUDY SELECTION: Twelve studies with 28 patients with intracranial meningiomas embolized through the transophtalmic artery were included.

DATA ANALYSIS: Baseline and technical characteristics and clinical and safety outcomes were collected. No statistical analysis was conducted.

DATA SYNTHESIS: The average age of 27 patients was 49.5 (SD, 13) years. Eighteen (69%) meningiomas were located in the anterior cranial fossa, and 8 (31%), in the sphenoid ridge/wing. Polyvinyl alcohol particles were most commonly ($n = 8$, 31%) used to preoperatively embolize meningiomas, followed by *n*-BCA in 6 (23%), Onyx in 6 (23%), Gelfoam in 5 (19%), and coils in 1 patient (4%). Complete embolization of the target meningioma feeders was reported in 8 (47%) of 17 patients; partial embolization, in 6 (32%); and suboptimal embolization, in 3 (18%). The endovascular complication rate was 16% (4 of 25), which included visual impairment in 3 (12%) patients.

LIMITATIONS: Selection and publication biases were limitations.

CONCLUSIONS: Transophtalmic artery embolization of intracranial meningiomas is feasible but is associated with a non-negligible complication rate.

ABBREVIATIONS: OPH = ophthalmic artery; PVA = polyvinyl alcohol

Intracranial meningiomas are often highly vascular tumors, accounting for 13%–26% of primary intracranial neoplasms.¹ Intracranial meningiomas can be associated with seizures, headaches, vision loss, or focal neurologic deficits.² Surgical resection is the primary technique of treatment, which may result in

serious blood loss.¹ Increased blood loss is linked to worse patient outcomes.³ Transarterial embolization of the tumor is an effective strategy to reduce intraoperative blood loss and facilitate the removal of meningiomas by shortening the operation time and increasing the likelihood of complete resection.⁴

Blood supply to meningiomas commonly arises from dural branches of the external and internal carotid and vertebral arteries, as well as from pial sources.⁵ However, some meningiomas, specifically those located in the anterior and middle skull base, may be supplied by dural branches of the ophthalmic

Received February 4, 2023; accepted after revision June 11.

From the Department of Neurological Surgery (M.A.E., M.Z., K.M.P., R.F., D.K., N.H., V.A., D.J.A.), Montefiore Medical Center, and D. Samuel Gottesman Library (C.D.P.), Albert Einstein College of Medicine, Bronx, New York; Department of Radiology (M.A.E.), Mayo Clinic, Rochester, Minnesota; Bernard and Irene Schwartz Neurointerventional Radiology Section (E.R., M.S.), Center for Stroke and Cerebrovascular Diseases, New York University Langone Health, New York, New York; Neuroendovascular Program (A.A.D.), Massachusetts General Hospital & Brigham and Women's Hospital, Harvard Medical School, Boston, Massachusetts; and Neurovascular Centre (A.A.D.), Departments of Medical Imaging & Neurosurgery, St. Michael's Hospital, University of Toronto, Toronto, Ontario, Canada.

M.A. Essibayi, M. Zakirova, and K.M. Phipps contributed equally to this work.

Please address correspondence to David J. Altschul, MD, Department of Neurological Surgery, Montefiore Medical Center, Albert Einstein College of Medicine, 3316 Rochambeau Ave, Bronx, NY 10467; e-mail: daltschu@montefiore.org; @DavidAltschulMD; @MAEssibayi; @monteinsteinrcl

Indicates article with online supplemental data.

<http://dx.doi.org/10.3174/ajnr.A7935>

artery, such as the ethmoid, recurrent meningeal, and deep recurrent meningeal arteries.^{5,6} Embolization via the ophthalmic artery (OPH) route poses a risk of retinal ischemia and visual deficits.⁶ Given this hazard, preoperative embolization of OPH is rarely performed.

To better understand the efficacy and safety profile of trans-ophthalmic artery embolization of intracranial meningiomas, we reviewed the published literature regarding the type and location of meningiomas embolized, the type of embolic material used, and the type and frequency of procedural complications associated with OPH embolization of meningiomas.

MATERIALS AND METHODS

Search Strategy

A medical librarian searched the medical literature according to the Preferred Reporting Items for Systematic Reviews and Meta-Analyses (PRISMA) guidelines.¹² Search strategies used a combination of keywords and standardized index terms that included [(“embolization, therapeutic” OR “embolism” OR “embolization” OR “embolisation” OR “embolotherapy”) AND (“meningioma” OR “meningeal Neoplasms” OR “meningeal tumor” OR “meningeal tumor” OR “meningeal cancer” OR “meningeal neoplasm”)]. Searches were run on August 3, 2022, in the PubMed (MEDLINE) data base. Included articles met all inclusion criteria (published in English, reported data for a consecutive series of patients with meningiomas receiving embolization through the ophthalmic artery, a branch of the ICA, before surgical resection with an identifiable report of primary outcomes). Reviews, guidelines, technical notes, comments, conference abstracts, animal studies, and editorials were excluded.

Study Selection Process

Title, abstract, and full-text screenings were conducted by 2 (M.Z. and K.M.P.) authors using EndNote (https://support.clarivate.com/Endnote/s/article/Download-EndNote?language=en_US). Conflicts were resolved by a senior author (M.A.E. or D.J.A.).

Data Extraction and Outcome Measures

Baseline patient and tumor characteristics and technical information about the embolization procedure were extracted from each article. Outcomes were analyzed for embolization material, the reported postembolization devascularization rate, complications, postoperative surgical resection grades, and complications and clinical outcomes. Clinical outcomes were classified as favorable, disability (permanent neurologic complication), or death.

Statistical Analysis and Risk of Bias Assessment

The continuous variables were summarized using means (SDs), and categorical variables were summarized using frequencies and proportions. No statistical comparisons were performed. The data analyses were performed using Excel 365 software (Microsoft).

The risk of bias among included studies was assessed using the Joanna Briggs Institute Critical Appraisal Tool for case reports (https://www.researchgate.net/figure/The-Joanna-Briggs-Institute-JBI-critical-appraisal-checklist-for-studies-reporting_fig2_322317583). In addition, the risk of bias within this systematic review was performed using the ROBIS tool (<https://abstracts.cochrane.org/introduction-robis-tool-assess-risk-bias-systematic-review>).

cochrane.org/introduction-robis-tool-assess-risk-bias-systematic-review).

RESULTS

Study Selection and Baseline Characteristics and Risk of Bias

After the initial review of 472 references collected from the PubMed library search, 12 studies with 28 patients (Online Supplemental Data) were included in this systematic review.^{1,5-15} A flow chart of the screening process is illustrated in the Online Supplemental Data. The risk of bias was low in 10 and high in 2 studies (Online Supplemental Data). Publication bias and heterogeneity among studies were not evaluated due to the nature of the included studies, which were case reports, and due to the very small sample size. The risk of bias within this systematic review was medium. The risk of bias within the synthesis and findings was unclear because no statistical evaluation of publication bias and heterogeneity was performed due to the reasons mentioned earlier (Online Supplemental Data).

The average age of 27 patients was 49.5 (SD, 13) years, with 13 (48%) women (Online Supplemental Data). The most common symptom on presentation was visual disturbance (50%; 7 of 14), followed by organic psychological disorder/dementia (36%), headache (29%), hemiparesis (21%), anosmia (14%), and apathy (14%) (Online Supplemental Data).

Eighteen (69%) meningiomas were located in the anterior cranial fossa, and 8 (31%), in the sphenoid ridge/wing. Eleven (42%) meningiomas were fed by a single arterial feeder. The ethmoidal arteries were the most commonly embolized ophthalmic branches (60%), followed by other meningeal branches (40%, recurrent, accessory, or anterior arteries) (Online Supplemental Data).

Technical Characteristics

Polyvinyl alcohol (PVA) particles overall ($n = 8$, four without coils and 4 with coils) were the most commonly (31%) used material to preoperatively embolize meningiomas, followed by *n*-BCA in 6 (23%), Onyx (Covidien) in 6 (23%) patients, Gelfoam (Pfizer) in 5 (19%), and primary coil embolization in 1 patient (4%) (Online Supplemental Data). Among 8 patients receiving PVA particles, the particle size was reported in 3 patients, including 90–180 μm and 150–300 μm in 2 meningiomas embolized via PVA particles alone and 1 meningioma embolized with a combination of 120- to 250- μm PVA particles and coils. Microcatheters included Tracker 18 (Target Therapeutics) in 7 (54%) patients and Marathon (Covidien) in 6 (46%). Seven studies with 15 patients did not report the type of microcatheter used.

Meningiomas embolized with PVA particles were predominantly located in the anterior cranial fossa and were of the meningothelial histopathologic type. A higher prevalence of fibroblastic meningiomas was reported among the *n*-BCA and Onyx groups (Online Supplemental Data).

Outcomes

Embolization outcomes were not reported in 9 patients. Eight (47%) of 17 patients received complete embolization of target meningioma feeders, 6 (32%) had partial embolization, and 3 (18%) were suboptimally embolized (Online Supplemental Data).

Complications were not reported in 3 patients from 2 studies. The overall endovascular complication rate was 16% (4 of 25 cases), which included visual impairment in 3 (12%, quadrantanopsia or hemianopsia in 2, and total vision loss in 1) and peritumoral hemorrhage/oculomotor nerve palsy in 1 (4%) (Online Supplemental Data). In addition, loss of retinal blush occurred in 1 (4%) patient but without clinical sequelae.

Surgical outcomes were reported among 15 cases. Postoperative complete meningioma excision was descriptively reported in 14 (93%). Simpson scale grades were reported by only 2 studies with 5 patients, including 1 (20%) meningioma with grade I, 3 (60%) with grade II, and 1 (20%) with grade IV (Online Supplemental Data). On the postoperative histopathologic evaluation of resected meningiomas, 4 (50%) of 8 meningiomas were a meningothelial type, 2 (25%) were fibroblastic, one (13%) was transitional, and one (13%) was atypical (Online Supplemental Data).

Clinical outcomes were reported among only 9 patients. Postoperative clinical outcomes were favorable or improved in 8 of 9 (89%) patients, and one (11%) died due to progressive brain edema. No long-term follow-up was reported among any patients in the included studies.

Outcomes by Embolization Agent

Among 4 patients with meningiomas embolized with PVA, 2 showed suboptimal embolization outcomes, defined as delayed opacification of the occluded vessel (Online Supplemental Data). Varying results of PVA \pm coils and *n*-BCA were reported among the studies included. Complete or partial embolization of the feeders was reported after Onyx and *n*-BCA embolization of 5 and 3 meningiomas, respectively. One (17%, of 6 receiving Onyx) patient experienced total vision loss after Onyx, and another patient had a loss of retinal blush on an angiogram after Onyx embolization with a microcatheter positioned distal to the origin of the central retinal artery but without visual sequelae. One patient with a sphenoid wing meningioma was embolized using Onyx and experienced total vision loss after the procedure. Two (40%) patients with meningiomas embolized via Gelfoam experienced partial visual impairment after the procedure. The first patient with an olfactory groove meningioma embolized through the posterior ethmoidal artery experienced postprocedural quadrantanopsia. The second patient with a sphenoid wing meningioma embolized through both the posterior ethmoid and anterior choroidal arteries and ICA perforators using Gelfoam powder developed hemianopsia, which the authors attributed to anterior choroidal artery embolization. Complete tumor resection was achieved in most cases with different embolization materials. However, only 1 patient with a 5.5-cm sphenoid wing meningioma embolized using coils alone had a postsurgical Simpson grade of IV. No difference in clinical outcomes and mortality by embolization material was reported except for 1 mortality event of a patient with sphenoid wing meningioma embolized using *n*-BCA who died after surgical resection because of brain edema.

DISCUSSION

To date, few case reports of patients with meningiomas undergoing OPH embolization have been reported. To the best of our knowledge, this systematic review is the first to comprehensively

summarize the available literature evidence on the outcomes of OPH embolization of skull base meningiomas, with a vision loss of 12%.

The role of preoperative transarterial embolization for meningioma resection remains controversial. While it can improve resection rates and reduce intraoperative blood loss, the procedure comes with the risk of serious complications. A meta-analysis published in 2021 included 34 studies with 1782 preoperatively embolized meningiomas and found no significant difference in technical and safety outcomes of preoperative embolization versus nonembolization of meningiomas.¹⁶ Akimoto et al,¹⁷ in a recent retrospective propensity-matched analysis of 186 patients with World Health Organization grade 1 meningiomas, compared the outcomes of 42 patients receiving embolization with 42 patients who did not undergo embolization before the operation. The authors found that the embolization group had favorable recurrence-free survival (49.4 versus 24.1 months, $P = .049$) and less intraoperative blood loss (mean 178 [SD, 203] mL versus 221 [SD, 165] mL, $P = .009$) compared with the nonembolization group. However, they found no significant differences in Simpson IV resection (33.3% versus 28.6%, $P = .637$) or overall perioperative complications (21.4% versus 11.9%, $P = .241$). Notably, middle cranial fossa meningiomas supplied by the meningohypophyseal and inferolateral trunks have been safely embolized.¹⁸

Meningiomas with primary arterial supply from the ophthalmic artery are located in the skull base,¹² as we found in this study, which included meningiomas located in the olfactory groove and sphenoid wing. Meningiomas in these locations are large and highly vascularized, with multiple feeders from the ophthalmic artery such as ethmoidal arteries (most commonly) and other arteries.^{19,20} Thus, surgical treatment of these lesions carries a high risk of complications. Transcranial surgical resection of these meningiomas comes with a higher potential risk than meningiomas primarily supplied by external carotid sources. The expanded transnasal endoscopic approach to treating anterior skull base meningiomas has increased in use during the past decade. While this technique is extremely useful in limiting brain retraction and its secondary consequences, the ability to control bleeding is technically more complex than traditional open surgical approaches. As a result, transarterial embolization may have a more valuable role when deciding to use endoscopic approaches for meningioma resection.

While ophthalmic artery feeder embolization comes with a clear and serious risk of vision loss, advances in microcatheters and microwires may make this approach safer and more feasible now compared with the past. Terada et al,⁵ in 1996, reported a rate of posttreatment visual impairment of 25% among 4 meningiomas embolized with Gelfoam powder, PVA particles, and/or microcoils through the ophthalmic artery. Trivelatto et al⁶ described promising safety outcomes of Onyx for the embolization of meningiomas fed by the ophthalmic artery, which they attributed to the nonadhesive characteristics and the low precipitation rate of Onyx, allowing more controlled injection.^{21,22} The authors suggested that successful embolization of the OPH branches with a low risk of inadvertent central retinal artery occlusion can only be achieved when the microcatheter tip is positioned safely and Onyx injections are performed very slowly and intermittently to avoid excessive reflux.

On the other hand, other reports mentioned that preservation of central retinal artery occlusion could be better achieved when PVA particles of $>300\ \mu\text{m}$ are used, considering that the central retinal artery is narrower than $300\ \mu\text{m}$.^{5,23} Nevertheless, precautions were reported to be necessary because the PVA particles have a high potential to fragment into smaller pieces during the mixing process and occlude the central retinal artery with retrograde filling. Most included cases received PVA embolization with particles with sizes between 80 and $300\ \mu\text{m}$. Furthermore, no visual impairment was reported among the patients who received PVA particles or *n*-BCA.

The microcatheter used to deliver the embolization material plays a crucial role in safely completing the embolization procedure. Half of the included patients had details reported of the microcatheter used, including Tracker 18 in 7 (54%) patients and Marathon in the rest. Among 3 patients with severe visual complications, 2 had meningiomas embolized with Gelfoam delivered by a Tracker 18 microcatheter and 1 had a meningioma embolized with Onyx, but the microcatheter used was not reported. The Tracker 18 microcatheter is an old microcatheter with a relatively large inner diameter (0.024 inch). Injury to the central retinal artery can be caused by accidental embolization due to improper catheter position or excessive reflux to the point of origin of the central retinal artery. Superselective microcatheter injection, with a detailed analysis of the vascular anatomy, is essential for understanding the safe position of the embolic injection and preventing this potential complication.

A second cause of injury to the central retinal artery can be the inadvertent dissection of the OPH secondary to vascular access or the formation of a clot around the microcatheter. Injection of vasodilators such as verapamil and administration of a heparin bolus may help to reduce the risk of inadvertent vascular injury during access to the OPH. Preoperative embolization of skull base meningiomas through the OPH can be much more feasible and safer with the recently introduced microcatheters (eg, Headway Duo microcatheter; MicroVention). Finally, some investigators mentioned that provocative tests before embolization might be beneficial for embolization decisions;⁵ nevertheless, other reports of false-negative or -positive tests are available.^{5,13}

Investigation of the effect of OPH embolization on the postoperative surgical outcomes of skull base meningiomas through this systematic review is difficult due to the small sample size, a serious amount of missing data, high heterogeneity, and lack of postoperative outcome reports by included studies. In this study, the postoperative complete resection rate was 93% among 15 cases, which is higher than or similar to reported gross total removal rates after transcranial resection of skull base meningiomas with no preoperative embolization (69%–100%).^{24–26} Furthermore, the surgical treatment resulted in good clinical outcomes, with only 1 death due to brain edema. However, this comparison is invalid due to the limitations mentioned earlier. Furthermore, other operative outcomes, such as surgical complications and intraoperative blood loss, were not reported. Thus, evaluation of the benefits of embolization on those outcomes is impossible. Further studies on endovascular and surgical nuances of OPH embolization of skull base meningiomas are required to evaluate these effects.

In conclusion, caution must be exercised before the embolization of OPH branches, considering the advantages and disadvantages of the embolization procedure. This can be achieved through preprocedural casewise evaluation of the need for the meningioma embolization based on factors such as tumor size, location, vascularity, and anatomic variations of the OPH (origin and proximity of the tumor to the central retinal artery) to facilitate surgical resection and decrease intraoperative complications. Furthermore, an initial provocative test can be used to assess the tolerance of OPH branch occlusion and subsequently make the final decision about embolization. However, published studies have inconclusive results based on a limited number of cases, and the outcomes of embolization attempts of meningiomas fed by the OPH may have gone unreported. Therefore, the literature evidence needs to be more robust to give recommendations.

Limitations

This systematic review includes only the reported cases in the literature, which may lead to selection bias and may not be an accurate representation of the procedure-related complications or outcomes. Furthermore, a considerable amount of heterogeneity is present due to several factors, including tumor-related (size, location, vascularity), anatomic (origin and branches of the ophthalmic artery), and technical factors (microcatheter used, embolization agents).

CONCLUSIONS

OPH embolization of meningiomas is feasible and efficient. However, its safety remains a matter of concern. Advances in embolization techniques and materials are expected to facilitate and improve the outcomes of this procedure. Although not generalizable due to this limited, very small sample of the study, embolization materials such as PVA are safely deployable and have relatively fewer complications than liquid agents, which have better technical outcomes. Finally, most included studies were case reports published before 2015. Thus, further studies investigating the outcomes of the preoperative embolization of meningiomas through the ophthalmic artery in the current endovascular era are warranted.

Disclosure forms provided by the authors are available with the full text and PDF of this article at www.ajnr.org.

REFERENCES

1. Gruber A, Killer M, Mazal P, et al. **Preoperative embolization of intracranial meningiomas: a 17-years single center experience.** *Minim Invasive Neurosurg* 2000;43:18–29 CrossRef Medline
2. Fricconet G, Espíndola Ala VH, Lemnos L, et al. **Pre-surgical embolization of intracranial meningioma with Onyx: a safety and efficacy study.** *J Neuroradiol* 2020;47:353–57 CrossRef Medline
3. Rajagopalan V, Chouhan RS, Pandia MP, et al. **Effect of intraoperative blood loss on perioperative complications and neurological outcome in adult patients undergoing elective brain tumor surgery.** *J Neurosci Rural Pract* 2019;10:631–40 CrossRef Medline
4. Shah AH, Patel N, Raper DM, et al. **The role of preoperative embolization for intracranial meningiomas.** *J Neurosurg* 2013;119:364–72 CrossRef Medline
5. Terada T, Kinoshita Y, Yokote H, et al. **Preoperative embolization of meningiomas fed by ophthalmic branch arteries.** *Surg Neurol* 1996;45:161–66 CrossRef Medline

6. Trivelatto F, Nakiri GS, Manisor M, et al. **Preoperative Onyx embolization of meningiomas fed by the ophthalmic artery: a case series.** *AJNR Am J Neuroradiol* 2011;32:1762–66 CrossRef Medline
7. Ohnishi H, Miyachi S, Murao K, et al. **Infiltrated embolization of meningioma with dilute cyanoacrylate glue.** *Neurol Med Chir (Tokyo)* 2017;57:44–50 CrossRef Medline
8. Kawaji H, Koizumi S, Sakai N, et al. **Evaluation of tumor blood flow after feeder embolization in meningiomas by arterial spin-labeling perfusion magnetic resonance imaging.** *J Neuroradiol* 2013;40:303–06 CrossRef Medline
9. Lefkowitz M, Giannotta SL, Hieshima G, et al. **Embolization of neurosurgical lesions involving the ophthalmic artery.** *Neurosurgery* 1998;43:1298–303 CrossRef Medline
10. Matsumaru Y, Alvarez H, Rodesch G, et al. **Embolisation of branches of the ophthalmic artery.** *Interv Neuroradiol* 1997;3:239–45 CrossRef Medline
11. Nishiguchi T, Iwakiri T, Hayasaki K, et al. **Post-embolisation susceptibility changes in giant meningiomas: multiparametric histogram analysis using non-contrast-enhanced susceptibility-weighted PRESTO, diffusion-weighted and perfusion-weighted imaging.** *Eur Radiol* 2013;23:551–61 CrossRef Medline
12. Przybylowski CJ, Baranoski JF, See AP, et al. **Preoperative embolization of skull base meningiomas: outcomes in the Onyx era.** *World Neurosurg* 2018;116:e371–79 CrossRef Medline
13. Suzuki K, Nagaishi M, Matsumoto Y, et al. **Preoperative embolization for skull base meningiomas.** *J Neurol Surg B Skull Base* 2017;78:308–14 CrossRef Medline
14. Torres GT, Kini A, Al Othman B, et al. **Acute vision loss after ophthalmic artery embolization of meningioma.** *J Neuroophthalmol* 2019;39:520–22 CrossRef Medline
15. Yoon YS, Ahn JY, Chang JH, et al. **Pre-operative embolisation of internal carotid artery branches and pial vessels in hypervascular brain tumours.** *Acta Neurochir (Wien)* 2008;150:447–52; discussion 452 CrossRef Medline
16. Jumah F, AbuRmilah A, Raju B, et al. **Does preoperative embolization improve outcomes of meningioma resection? A systematic review and meta-analysis.** *Neurosurg Rev* 2021;44:3151–63 CrossRef Medline
17. Akimoto T, Ohtake M, Miyake S, et al. **Preoperative tumor embolization prolongs time to recurrence of meningiomas: a retrospective propensity-matched analysis.** *J Neurointerv Surg* 2022 Jul 8. [Epub ahead of print] CrossRef Medline
18. Raz E, Cavalcanti DD, Sen C, et al. **Tumor embolization through meningohypophyseal and inferolateral trunks is safe and effective.** *AJNR Am J Neuroradiol* 2022;43:1142–47 CrossRef Medline
19. Hentschel SJ, DeMonte F. **Olfactory groove meningiomas.** *Neurosurg Focus* 2003;14:1–5 CrossRef Medline
20. Saeed P, van Furth WR, Tanck M, et al. **Natural history of sphenoorbital meningiomas.** *Acta Neurochir (Wien)* 2011;153:395–402 CrossRef Medline
21. Shi ZS, Feng L, Jiang XB, et al. **Therapeutic embolization of meningiomas with Onyx for delayed surgical resection.** *Surg Neurol* 2008;70:478–81 CrossRef Medline
22. Rossitti S. **Preoperative embolization of lower-falx meningiomas with ethylene vinyl alcohol copolymer: technical and anatomical aspects.** *Acta Radiol* 2007;48:321–26 CrossRef Medline
23. Horton JA, Kerber CW. **Lidocaine injection into external carotid branches: provocative test to preserve cranial nerve function in therapeutic embolization.** *AJNR Am J Neuroradiol* 1986;7:105–08 Medline
24. De Jesús O, Sekhar LN, Parikh HK, et al. **Long-term follow-up of patients with meningiomas involving the cavernous sinus: recurrence, progression, and quality of life.** *Neurosurgery* 1996;39:915–20; discussion 919–20 CrossRef Medline
25. Couldwell WT, Fukushima T, Giannotta SL, et al. **Petroclival meningiomas: surgical experience in 109 cases.** *J Neurosurg* 1996;84:20–28 CrossRef Medline
26. Nanda A, Vannemreddy P. **Recurrence and outcome in skull base meningiomas: do they differ from other intracranial meningiomas?** *Skull Base* 2008;18:243–52 CrossRef Medline

Endovascular Treatment of Cerebrovascular Lesions Using Nickel- or Nitinol-Containing Devices in Patients with Nickel Allergies

J.F. Baranoski, J.S. Catapano, C. Rutledge, T.S. Cole, N. Majmundar, E.A. Winkler, V.M. Srinivasan, A.P. Jadhav, A.F. Ducruet, and F.C. Albuquerque

ABSTRACT

SUMMARY: Nickel is used in many cerebral endovascular treatment devices. However, nickel hypersensitivity is the most common metal allergy, and the relative risk of treatment in these patients is unknown. This retrospective analysis identified patients with nickel or metal allergies who underwent cerebral endovascular treatment with nickel-containing devices. Seven patients with nickel and/or other metal allergies underwent treatment with 9 nickel-containing devices. None experienced periprocedural complications. No patient received treatment with corticosteroids or antihistamines. At a mean clinical follow-up for all patients of 22.8 months (range, 10.5–38.0 months), no patients had symptoms attributable to nickel allergic reactions. The mean radiographic follow-up for all patients at 18.4 months (range, 2.5–37.5 months) showed successful treatment of the targeted vascular pathologies, with no evidence of in-stent stenosis or other allergic or hypersensitivity sequelae. The treatment of cerebrovascular lesions with a nickel-containing device resulted in no adverse outcomes among these patients and was safe and effective.

ABBREVIATION: DAPT = dual antiplatelet therapy

Nickel hypersensitivity is the most commonly documented metal allergy, with an estimated prevalence of 10% to 15% in the general population, predominantly affecting women.^{1,2} Nickel is used in the manufacturing of most new endovascular treatment devices for intracranial aneurysms, including nitinol-containing flow-diverting stents, self-expanding stents, and intrasaccular occlusion devices.³⁻⁷ Because these devices are increasingly used, the relative risk of adverse events when they are used in patients with nickel and other metal allergies should be more fully elucidated.

In the cardiac literature, particularly in retrospective studies, nickel allergy has been associated with an increased incidence of in-stent stenosis.^{8,9} However, prospective studies have not confirmed this relationship.¹⁰⁻¹² Nevertheless, some concern remains regarding the questionable risk of using these devices in patients with documented metal allergies.¹³

In the cerebrovascular literature, a limited number of studies have addressed the use of nickel-containing devices in patients

with nickel allergies. Some reports have documented possible associated complications,^{3,4,6,14-16} while others have reported no serious adverse outcomes in this patient population.^{5,7}

In this study, we sought to review the perioperative management and outcomes of patients with documented nickel and other metal allergies who underwent endovascular cerebrovascular pathology treatment with nickel-containing devices.

Case Series

We performed a retrospective analysis using data from our prospectively collected endovascular database and identified patients with a documented nickel allergy or other metal allergy who underwent treatment with a permanently implanted nickel-containing device from July 2018 through March 2021. Institutional review board approval for the study was obtained. The requirement for informed consent for study participation was waived due to the retrospective nature of the study and the low risk to participants. All patients had given prior informed written consent for their treatment. From the database, we extracted demographic, clinical, and radiologic data, including angiographic results, medications, complications, and follow-up clinical and radiologic outcomes. All patient data were appropriately anonymized to maintain confidentiality.


Endovascular Procedures

Endovascular treatment procedures were performed with the patients placed under general anesthesia with neurophysiologic

Received September 16, 2022; accepted after revision June 11, 2023.

From the Department of Neurosurgery, Barrow Neurological Institute, St. Joseph's Hospital and Medical Center, Phoenix, Arizona.

Please address correspondence to Felipe C. Albuquerque, MD, c/o Neuroscience Publications, Barrow Neurological Institute, St. Joseph's Hospital and Medical Center, 350 W Thomas Rd, Phoenix, AZ 85013; e-mail: Neuropub@barrowneuro.org; @BaranoskiJake; @calebcuts; @tylcole; @NeilMajMD; @EWinklerMDPhD; @visishis; @AshuPJadhav; @ducruetaf; @fcalbuquerque51; @BarrowNeuro

 Indicates article with online supplemental data.

<http://dx.doi.org/10.3174/ajnr.A7936>

monitoring. Dermatologic testing was not performed to confirm the self-reported metal allergies of patients. The patients were not pretreated prophylactically with corticosteroids or antihistamines. Intraprocedural heparin was administered to all patients to maintain the goal of an activated clotting time 2–3 times that of baseline. All patients were receiving a dual antiplatelet therapy (DAPT) regimen at the time of device deployment, and this regimen was continued for at least 6 months after treatment.

Included Patients and Outcomes

Seven patients (mean age, 61.7 years; range, 40s–80s) with documented nickel allergies (4 patients) or other metal allergies (3 patients) who had 9 vascular lesions (7 saccular aneurysms, 1 blister or fusiform aneurysm, and 1 intracranial dissection) underwent treatment with a total of 9 nickel-containing devices (7 flow-diverting stents and 2 self-expanding intracranial stents) during 8 treatment sessions. All 7 patients were receiving a DAPT regimen at the time of treatment, with an adequate response verified on hematologic assays. DAPT was continued for at least 6 months in all 7 patients. No patient experienced any periprocedural complications, including any apparent allergic reactions, thromboembolic events, or in-stent stenoses. No patient received periprocedural prophylactic treatment with either corticosteroids or antihistamines for documented nickel or metal allergies.

Clinical, radiologic, and angiographic follow-up was performed at the interventionalist's discretion and in accordance with practice patterns. Clinical follow-up available for all 7 patients (mean, 22.8 months; range, 10.5–38.0 months) found no evidence of procedure-related neurologic symptoms or symptoms attributable to nickel or metal allergic reactions. Angiographic follow-up was available for 6 patients (mean, 5 months; range, 0.5–14.5 months). In 5 of these 6 patients, follow-up angiography demonstrated complete resolution of their 7 vascular lesions (complete obliteration of 6 saccular aneurysms and no dissection-associated flow aberration), with no evidence of in-stent stenosis, vasculitis-like changes, or other vessel pathology. In 1 of these 6 patients, short-interval follow-up angiography at 2 weeks demonstrated decreased aneurysm filling with marked contrast stagnation in a ruptured fusiform aneurysm after flow-diverting stent placement. Follow-up noninvasive imaging findings (MR imaging or MRA for 4 patients, CTA for 3 patients) were available for all 7 patients (mean, 18.4 months; range, 2.5–37.5 months).

None of these 7 patients showed any evidence of adverse outcomes attributable to nickel or metal allergy reactions, including increased small-vessel disease, WM lesions, vasculitis, or attributable ischemic changes (Online Supplemental Data).

DISCUSSION

Cases of cutaneous allergic reactions to metallic orthopedic and surgical implants are well documented.^{17,18} However, the evidence that endovascularly placed intravascular devices can induce a deleterious allergic response is more debatable. Although studies in the cardiology literature have associated nickel allergies with an increased incidence of in-stent stenosis,^{8,9,13} prospective studies have not confirmed this relationship.^{10–12} Nonetheless,

neuroendovascular surgeons and interventionalists may be wise to be concerned about placing nickel-containing devices in patients who have reported nickel or other metal allergies.¹⁹ Despite the overall prevalence of nickel allergies within the general population (10%–15%)^{1,2} and the increased use of nickel-containing devices for the treatment of cerebrovascular lesions, relatively few studies have been published on the subject.

Tonetti et al³ reported the successful treatment with a nickel-containing flow-diverting stent of 2 patients who had cutaneous nickel allergies; neither patient demonstrated any allergic reactions or in-stent stenosis at prolonged follow-up. As in our series of 7 patients, neither of their 2 patients had received periprocedural prophylactic treatment with steroids or antihistamines. Similarly, Wallace et al⁷ reported that, in a series of 20 patients with metal allergies who underwent cerebral aneurysm treatment with nickel-containing flow-diverting stents, there were no apparent allergic reactions despite the lack of periprocedural prophylactic treatment with steroids or antihistamines. Our series further supports these results, because we found no evidence of allergic or other adverse clinical reactions among our patients. Moreover, we found that, in all 6 patients with angiographic follow-up, complete obliteration of the vascular lesion was demonstrated without adverse sequelae.

Although our results suggest that neuroendovascular treatment with nickel-containing devices may be safe in patients with nickel or other metal allergies, other authors have reported some cases of adverse effects possibly attributable to allergic reactions to metal. Fujii et al¹⁴ reported a case of delayed in-stent stenosis in a patient with a cobalt allergy who was treated with a nickel-containing flow-diverting stent. Other authors have reported cases of diffuse cerebral edema with seizures or focal neurologic deficits after placement of a nickel-containing device.^{13,15} However, the exact etiology in these cases has not been fully elucidated. Fortunately, the patients in these cases were successfully treated with systemic steroids, which resulted in radiologic and clinical resolution of their symptoms.^{13,15} Similarly, other authors have reported radiographic sequelae, including foci of MR imaging enhancement in the catheterized territory that developed in the weeks after the procedure and responded to steroid treatment.^{16,20,21} Together, these findings suggest that a delayed, steroid-responsive hypersensitivity-like reaction is possible after endovascular treatment; however, the exact etiology remains to be fully elucidated. On the basis of our results and those of other authors, we believe that there is a low relative risk of severe allergic reactions after treatment with nickel-containing neuroendovascular devices.

However, precautionary steps to help mitigate any potential risk should be considered. We did not pursue nickel allergy patch testing for the patients in our series who reported having a nickel allergy before their treatment with a nickel-containing device; however, performing a patch test before an elective treatment may be a reasonable approach. Other authors recommend this strategy to enable better patient counseling and to provide an opportunity to consider treatment alternatives.²² However, others have reported that patch testing was of very limited clinical utility for patients undergoing endovascular treatment.¹¹ The incidence of nickel hypersensitivities is likely underreported in retrospective

studies. To better address this area of concern and to assist in future analyses and patient counseling, we have implemented a policy of explicitly asking all patients about any potential metal allergies or hypersensitivities when they are scheduled to undergo an elective endovascular treatment in which a nickel-containing device is part of the treatment plan.

One potential reason for the lack of frequent consequential adverse reactions after placement of nickel-containing cerebrovascular stents in patients with reported nickel allergies is that the commonly used neurovascular stents do not actually release nickel ions. The release of nickel ions is necessary to induce a nickel hypersensitivity response via immune cell activation. Recent *in vitro* work by Vanent et al²³ determined that commonly used nickel-containing cerebrovascular stents—including those used in our series—do not actually release nickel ions. These findings correlate with our clinical results because the lack of free nickel ion release from the stents would preclude a clinical hypersensitivity response. Taken together, these results suggest that patients with a nickel allergy who require endovascular treatment for cerebrovascular lesions may be safely treated with nickel-containing stents. This conclusion is supported by the general observation that the percentage of patients with adverse effects after treatment with nickel-containing devices (generally reported as markedly <10%^{24–27}) is notably less than the estimated prevalence of nickel allergy or hypersensitivity within the general population (10%–15%).²⁸ However, neither our results nor the previously reported data preclude a causal relationship between a metal or nickel allergy and any adverse reaction. Therefore, to more comprehensively address the relative risk and possible causation, larger prospective databases are required that systematically document allergy status and identify potential clinical and imaging sequelae.

Our study was limited by its retrospective nature and the small patient cohort. Limitations included a lack of rigid standardization of clinical and radiologic follow-up timing, technique, and granularity. These limitations may have obscured minor clinical or radiologic sequelae. Furthermore, we ascertained the presence of a cutaneous metal allergy from a retrospective chart review rather than from formal dermatologic allergy testing. Although we review allergies for all patients as part of our standard inpatient and clinic history and physical, it is possible that the sensitivity and specificity of this methodology produce both false-positive and false-negative results. It is important to note that, in light of population statistics, the number of patients with reported nickel or other metal allergies or hypersensitivities in our study likely underestimates the actual number of patients with such hypersensitivities. Future prospective studies are warranted that are designed to describe the safety and efficacy of nickel-containing devices in neurosurgery, the potential role of patch testing for nickel allergies, and the possible benefit of prophylactic treatment.

CONCLUSIONS

In this small case series, the endovascular treatment of cerebrovascular lesions with a nickel-containing device in 7 patients with documented nickel or other metal allergies did not result in any adverse outcomes and was safe and effective overall. Further research in this area is warranted.

ACKNOWLEDGMENT

We thank the staff of Neuroscience Publications at Barrow Neurological Institute for assistance with manuscript preparation.

Disclosure forms provided by the authors are available with the full text and PDF of this article at www.ajnr.org.

REFERENCES

1. Thyssen JP, Menne T. **Metal allergy: a review on exposures, penetration, genetics, prevalence, and clinical implications.** *Chem Res Toxicol* 2010;23:309–18 CrossRef Medline
2. Thyssen JP, Linneberg A, Menne T, et al. **The epidemiology of contact allergy in the general population—prevalence and main findings.** *Contact Dermatitis* 2007;57:287–99 CrossRef Medline
3. Marcos-Gonzalez A, Spoerl D, Darbellay B, et al. **Hypersensitivity to an intracerebral stent and symptomatic cerebral lesions: a possible link?** *J Dermatol* 2017;44:1187–88 CrossRef Medline
4. Park HS, Nakagawa I, Yokoyama S, et al. **Nickel-associated delayed multiple white matter lesions after stent-assisted coil embolization of intracranial unruptured aneurysm.** *J Neurointerv Surg* 2018;10:e1 CrossRef Medline
5. Tonetti DA, Perez JL, Ozpinar A, et al. **Use of pipeline endovascular device in patients with nickel allergies.** *World Neurosurg* 2018;120:349–51 CrossRef Medline
6. Ulus S, Yakupoğlu A, Kararslan E, et al. **Reversible intracranial parenchymal changes in MRI after MCA aneurysm treatment with stent-assisted coiling technique: possible nickel allergy.** *Neuroradiology* 2012;54:897–99 CrossRef Medline
7. Wallace AN, Delgado Almandoz JE, Kayan Y, et al. **Pipeline treatment of intracranial aneurysms is safe and effective in patients with cutaneous metal allergy.** *World Neurosurg* 2019;123:e180–85 CrossRef Medline
8. Koster R, Vieluf D, Kiehn M, et al. **Nickel and molybdenum contact allergies in patients with coronary in-stent restenosis.** *Lancet* 2000;356:1895–97 CrossRef Medline
9. Aliğaoglu C, Turan H, Erden I, et al. **Relation of nickel allergy with in-stent restenosis in patients treated with cobalt chromium stents.** *Ann Dermatol* 2012;24:426–29 CrossRef Medline
10. Iijima R, Ikari Y, Amiya E, et al. **The impact of metallic allergy on stent implantation: metal allergy and recurrence of in-stent restenosis.** *Int J Cardiol* 2005;104:319–25 CrossRef Medline
11. Norgaz T, Hobikoglu G, Serdar ZA, et al. **Is there a link between nickel allergy and coronary stent restenosis?** *Tohoku J Exp Med* 2005;206:243–46 CrossRef Medline
12. Romero-Brufau S, Best PJ, Holmes DR, Jr, et al. **Outcomes after coronary stent implantation in patients with metal allergy.** *Circ Cardiovasc Interv* 2012;5:220–26 CrossRef Medline
13. Guéroult AM, Al-Balah A, Davies AH, et al. **Nickel hypersensitivity and endovascular devices: a systematic review and meta-analysis.** *Heart* 2022;108:1707–15 CrossRef Medline
14. Fujii S, Fujita K, Yamaoka H, et al. **Refractory in-stent stenosis after flow diverter stenting associated with delayed cobalt allergic reaction.** *J Neurointerv Surg* 2022;14:e4 CrossRef Medline
15. Tsang AC, Nicholson P, Pereira VM. **Nickel-related adverse reactions in the treatment of cerebral aneurysms: a literature review.** *World Neurosurg* 2018;115:147–53 CrossRef Medline
16. Shotar E, Law-Ye B, Baronnet-Chauvet F, et al. **Non-ischemic cerebral enhancing lesions secondary to endovascular aneurysm therapy: nickel allergy or foreign body reaction? Case series and review of the literature.** *Neuroradiology* 2016;58:877–85 CrossRef Medline
17. Haddad SF, Helm MM, Meath B, et al. **Exploring the incidence, implications, and relevance of metal allergy to orthopaedic surgeons.** *J Am Acad Orthop Surg Glob Res Rev* 2019;3:e023 CrossRef Medline
18. King L Jr, Fransway A, Adkins RB. **Chronic urticaria due to surgical clips.** *N Engl J Med* 1993;329:1583–84 CrossRef Medline

19. Apostolos A, Gregoriou S, Drakopoulou M, et al. **Correspondence on “Nickels and tines: the myth of nickel allergy in intracranial stents” by Vanent et al.** *J Neurointerv Surg* 2022;14:1286–87 CrossRef Medline
20. Lobotesis K, Mahady K, Ganesalingam J, et al. **Coiling-associated delayed cerebral hypersensitivity: is nickel the link?** *Neurology* 2015;84:97–99 CrossRef Medline
21. Oh SW, Shin NY, Lee HJ, et al. **Delayed enhancing lesions after coil embolization of aneurysms: clinical experience and benchtop analyses.** *J Neurointerv Surg* 2017;9:1243–47 CrossRef Medline
22. Jeswani S, Alexander MJ. **Nickel allergy: a reason for concern?** *J Neurointerv Surg* 2011;3:2–4 CrossRef Medline
23. Vanent KN, Federico EM, Bass DI, et al. **Nickels and tines: the myth of nickel allergy in intracranial stents.** *J Neurointerv Surg* 2022;14:1244–47 CrossRef Medline
24. Phillips TJ, Wenderoth JD, Phatouros CC, et al. **Safety of the Pipeline embolization device in treatment of posterior circulation aneurysms.** *AJNR Am J Neuroradiol* 2012;33:1225–31 CrossRef Medline
25. Feng MT, Wen WL, Feng ZZ, et al. **Endovascular embolization of intracranial aneurysms: to use stent(s) or not? Systematic review and meta-analysis.** *World Neurosurg* 2016;93:271–78 CrossRef Medline
26. Mocco J, Fargen KM, Albuquerque FC, et al. **Delayed thrombosis or stenosis following Enterprise-assisted stent-coiling: is it safe? Midterm results of the interstate collaboration of Enterprise stent coiling.** *Neurosurgery* 2011;69:908–13; discussion 913–14 CrossRef Medline
27. Guimaraens L, Vivas E, Saldana J, et al. **Efficacy and safety of the dual-layer flow-diverting stent (FRED) for the treatment of intracranial aneurysms.** *J Neurointerv Surg* 2020;12:521–25 CrossRef Medline
28. Levitt MR, Vanent KN, Federico EM, et al. **Response to: Correspondence on “Nickels and tines: the myth of nickel allergy in intracranial stents” by Apostolos et al.** *J Neurointerv Surg* 2022;14:1287–88 CrossRef Medline

Mapping of Anatomic Variants of the Proximal Vertebral Artery in Relation to Embryology

H.F. Bueno and E.A. Nimchinsky

ABSTRACT

BACKGROUND AND PURPOSE: Variations in the origins and courses of the vertebral arteries are relatively rare but may be clinically meaningful. We hypothesize a relationship between variant origins of the vertebral arteries and their levels of entry to the foramina transversaria.

MATERIALS AND METHODS: In this retrospective study of CT angiograms, we document the frequency and types of vertebral artery variants, correlating origins with levels of entry to the foramina transversaria.

RESULTS: Vertebral artery variants were observed in 18.7% of a sample of 460 CT angiograms of the neck. Right-sided variants were less common than left (44.2% versus 68.6%, with 12.8% bilateral) and more common than previously thought. The most common variant on both sides was a variant origin proximal to the normal vertebral artery origin and entry at C5. Most right vertebral arteries originating within 2 cm of the origin of the right subclavian artery and left vertebral arteries originating between the left common carotid and subclavian arteries were “high-entry” variants. Most “low-entry” variants, entering at C7, took origin from the arch just distal to the left subclavian artery or at a common origin with the costocervical trunk. Multiple origins or accessory vertebral arteries were also described, and each moiety followed the same rules described for single origins. A map of vertebral artery origins mirrored the map of aortic arch embryology.

CONCLUSIONS: Vertebral artery variants follow certain well-defined patterns that correlate with the embryology of the aortic arch and great vessels.

ABBREVIATIONS: CCT = costocervical trunk; FT = foramen transversarium; ISA = intersegmental artery; LCCA = left common carotid artery; LSCA = left subclavian artery; LVA = left vertebral artery; RSCA = right subclavian artery; RVA = right vertebral artery; SCA = subclavian artery; VA = vertebral artery

The vertebral artery (VA) normally takes origin from the subclavian artery (SCA) and enters the foramen transversarium (FT) of the C6 vertebral body. This pattern is found on both sides in most cases, with estimates ranging from 82.7% to 99%.¹⁻⁶ Variations from this configuration are sufficiently uncommon to warrant case reports on a regular basis,⁷⁻¹⁰ and several studies have tried to compile these variations through meta-analysis¹¹ or literature review.¹² Most larger studies with primary data have described variants either at the site of origin of the VA or the site of entry into the FT. A much smaller number of studies have studied both systematically in concert, and these have noted that left VAs originating directly from the aortic arch may enter the

FT at levels other than C6 with greater frequency.^{1-5,13-18} Of these, 1 study³ noted that those originating distally on the arch enter at C7. Most of these studies found marked variability in right-sided FT entry but little variability in right vertebral artery (RVA) origins,^{1-5,13-18} a perplexing difference that has not been explained. One notable exception^{3,7} is that origins on the very proximal right SCA (RSCA) tend to have a higher entry point, but this was not quantified.

More uncommon still are multiple origins of the VAs. These are most frequently described in case reports, though 1 large series found them in only 0.3% of cases.¹⁹ Adachi noted, on the basis of his cadaveric series (cited in Bordes et al²⁰), that “accessory” left VAs originate directly from the aortic arch and that accessory right VAs originate more proximally on the SCA. However, the origins and entry points of VAs with multiple origins also have not, to date, been described systematically.

In summary, although a wide range of variations has historically and repeatedly been noted in VA origins and entry points, a systematic approach that could organize and unify these disparate variants has yet to be proposed.

Received February 1, 2023; accepted after revision June 15.

From the Department of Radiology, Rutgers-New Jersey Medical School, Newark, New Jersey.

Please address correspondence to Esther A. Nimchinsky, MD, PhD, Department of Radiology, New Jersey Medical School, Rutgers, The State University of New Jersey, MSB Room F-506, 185 South Orange Ave, Newark, NJ 07103; e-mail: nimchins@njms.rutgers.edu

<http://dx.doi.org/10.3174/ajnr.A7942>

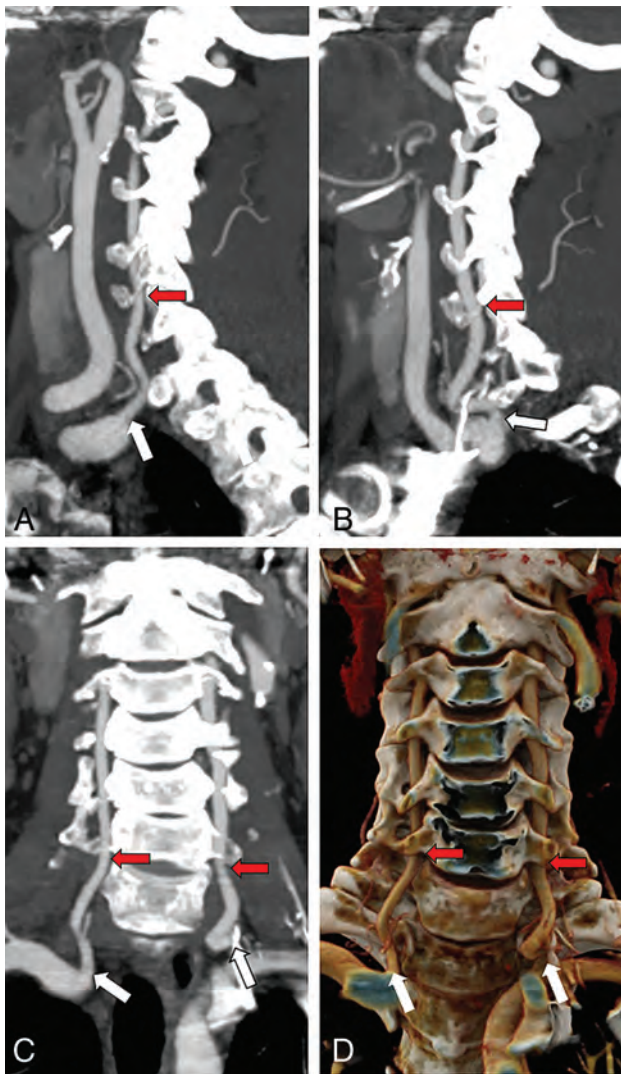


FIG 1. Normal anatomy of the cervical VAs. Sagittal MIPs of the right (A) and left (B) VAs and both in the coronal plane (C), as well as a coronal 3D rendering (D) show the origin of both VAs from the SCAs (white arrows) and their entry into the FT at C6 (red arrows).

This issue is important because variant courses of the VAs may predispose to intraoperative complications, including injury to an “unprotected” VA that is not within the FT^{21,22} or a VA whose origin from the aortic arch reduces the space available for placement of a stent.^{23,24} In addition, direct origin of the left vertebral artery (LVA) from the aortic arch has been associated with an increased risk of dissection,²⁵ making recognition of this variant particularly important.

Here we describe a series of VA variants encountered during the course of normal neuroradiologic duties at an inner-city hospital in the United States (University Hospital, Newark, NJ). We describe their origins and points of entry into the FT and propose a unifying hypothesis linking these patterns with the embryology of the great vessels.

MATERIALS AND METHODS

CTAs of the neck were obtained for a variety of indications, including stroke, trauma, nontraumatic hemorrhage, vertigo,

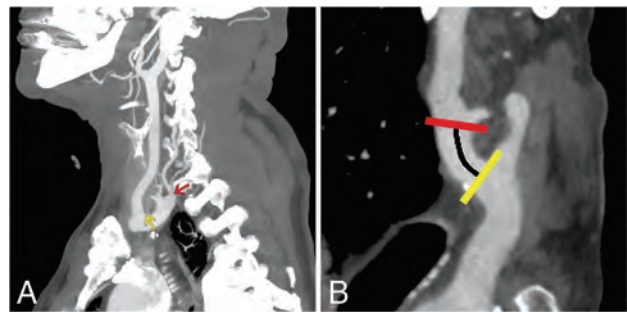


FIG 2. Quantification of the distance from the right SCA origin to the origin of the RVA. A, Sagittal MIPs show the origins of the RSCA (yellow arrow), defined as the distal wall of the origin of the right common carotid artery and the RVA (red arrow). B, Curved planar reformat shows a straightened SCA with estimation of the distance to the RVA origin along the SCA (black line indicates distance; yellow line, RSCA origin; red line, RVA origin).

abnormal findings on carotid Doppler ultrasound, and follow-up for findings noted on earlier studies. CTA was performed according to institutional procedures, by using either a 64- or 128-section scanner (LightSpeed VCT or Revolution GSI, respectively; GE Healthcare) with bolus tracking following administration of Omnipaque 350 (GE Healthcare) into the venous system at a rate of 4 mL/s. Slices (0.625-mm-thick) were obtained from below the aortic arch through the circle of Willis or through the entire head, depending on the indication. Coronal and sagittal reformats were obtained, and MIPs were generated. 3D volume-rendered reformats were generated using dedicated software (Syngo Via; Siemens) (Fig 1). The same software was used to generate the images in subsequent images. Measurements of distances along the parent arteries to the origins of the VAs were obtained by generating curved planar reformats and measuring linear distances along the parent vessels (Fig 2). Cases with VA variants were identified and compiled in a deidentified file on a Health Insurance Portability and Accountability Act-compliant encrypted server. This study was exempted from institutional review board review by the Rutgers University Institutional Review Board (Pro 2022000874).

RESULTS

To describe the frequency of variants of VA origin or FT entry in our population, we reviewed an unselected consecutive series of 493 CTAs of the neck, representing all such studies performed during a 3-month period. Of these, 33 were excluded because of patient duplication (a patient scanned more than once in the trial period), an inadequate bolus, excessive motion, or beam-hardening artifacts, making it impossible to ascertain the origin and/or entry point of either VA. In the remaining 460 studies, 86 cases (18.7%) were identified with VA variants. Two-thirds (67.4%) of the variant population presented for a wide range of neurologic conditions, including stroke, intracranial hemorrhage, and surveillance or pre- or postoperative evaluation for treatment of an aneurysm, known dissection, or tumor, while 32.6% presented with trauma. These presentations were comparable with the presenting conditions in the parent population (69.2% for neurologic indications versus 30.2% for trauma). The demographic properties of this subpopulation (59.3% men, mean age, 51.2 years; 40.7% women, mean age, 59 years) were also similar to those of

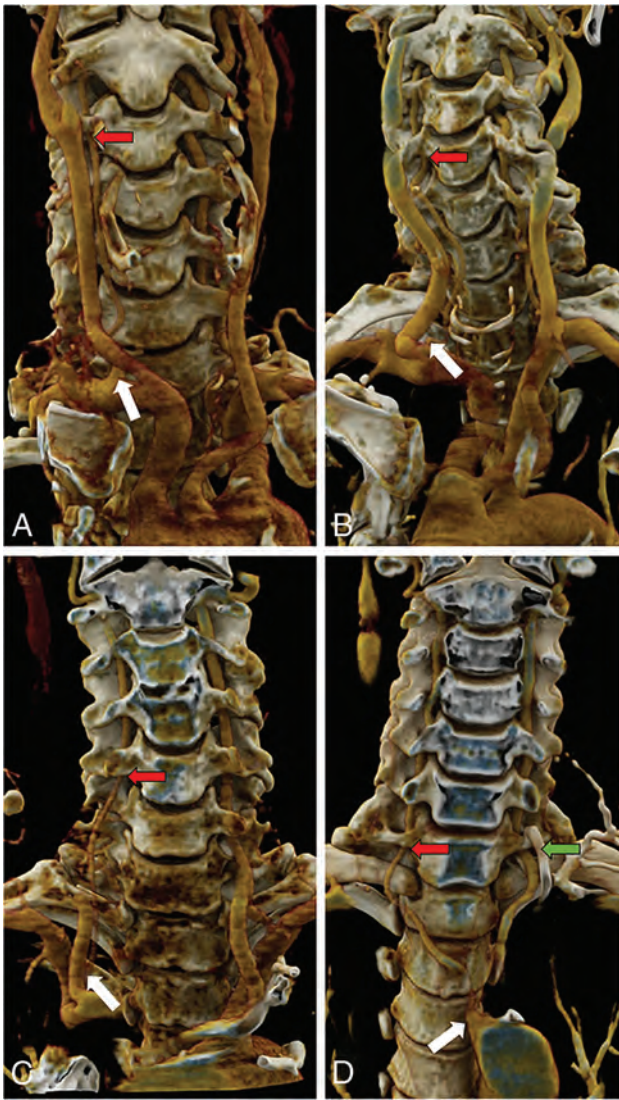


FIG 3. RVA variants. RVA origin within 2 cm of the RSCA origin (*white arrows*) entering the FT (*red arrows*) at C3 (A), C4 (B), or C5 (C). D. The RVA originates from the distal aortic arch (*white arrow*), crosses along the upper thoracic vertebral bodies, and enters the FT at C7 (*red arrow*). Note that in this case, the left VA also enters the FT at C7 (*green arrow*), having originated as the fourth branch from the aortic arch (not shown).

the parent population (55.2% men, mean age, 53.6 years; 44.8% women, mean age, 59.3 years).

Thirty-nine cases demonstrated variants in entry to the FT on the right (8.5% of the total sample and 44.8% of the variant cases, Fig 3), and 59 demonstrated variants in origin and/or entry on the left (12.8% of the total sample and 67.8% of the variant cases, Fig 4). These numbers include 11 with bilateral variants (2.4% of the total sample and 12.8% of the variant cases), so 28 had variants only on the right; 48, only on the left; and 11, bilaterally. These are summarized in Table 1. Three accessory VAs (0.65% of the total sample and 3.5% of the variant cases) were identified in this sample, as well as a single case of triplicated origin (0.22% of the total sample and 1.2% of the variant cases). Considering the frequency of cases with unilateral variants (5.9% on the right and 10.4% on the left), the expected frequency of bilateral

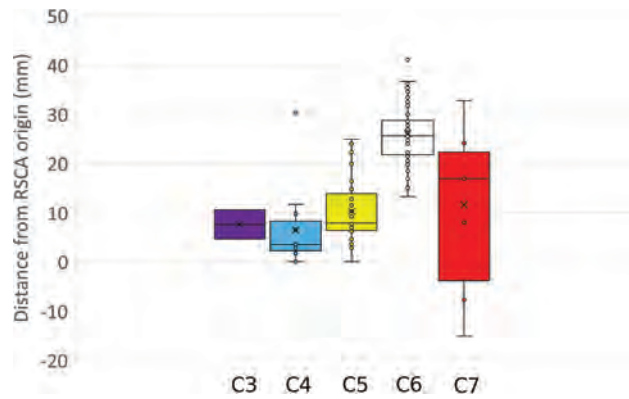


FIG 4. Box-and-whisker plot showing the distance from the origin of the RSCA for right VAs entering the FT from C3 through C7. Although there is some overlap, high-entry VAs originate more proximally than arteries entering at C6. There is more heterogeneity in low-entry VAs, which may originate from the aortic arch (negative numbers on this figure) or along the RSCA. For this figure, all low-entry VAs are considered together, without regard for whether they share a common origin with the CCT.

Table 1: Distribution of variant VA origins and entries to the FT in a consecutive series of 493 cases^a

	C4	C5	C6	C7
Right				
Proximal SCA	6	22	0	3
SCA	0	2	48	2
Arch	0	0	0	0
Left				
SCA	1	6	27	2
Arch ^b	4	30	3	0
SCA posterior wall	0	0	0	5
4th branch arch	0	0	0	7

^aThe 3 cases of duplicated origins in this sample are not included in this table. Note that no right VAs originating from the aortic arch, and no VAs on either side entering at C3 were seen in this sample.

^bIndicates the portion of the arch between the left common carotid and subclavian arteries.

variants, assuming independence of the events, was 0.0061, though the observed frequency was 0.024, indicating a 3.9-fold increased likelihood of bilateral variants than would be predicted if the events were independent. We note that in this series, we encountered 6 cases of aberrant right SCAs (1.3%), and 1 right-sided arch (0.20%), within ranges described in the literature.^{26,27}

To supplement these observations, we added additional cases of variant VAs that had been accrued in a nonsystematic fashion during the preceding 2 years during the course of routine work in the same hospital. These were added to increase the number of observations of these variants, some of which are extremely rare. Thirty-nine cases demonstrated 1 or both VAs entering the FT at a level other than C6, and 9 angiograms demonstrated accessory vessels for 1 or both VAs (Fig 5). In 3 of these, the contralateral VA had an atypical level of entry (all on the left), yielding a total of 42 single atypical VAs. Of these 42 single VAs, 20 (48%) were on the right side and 30 (71%) were on the left, similar to the relative frequencies in our exhaustive sample. Because this was not an unbiased sample, frequencies relative to the population cannot be calculated.

When we reviewed all 125 cases with variant arteries, the most common pattern on the right was origin from the RSCA,

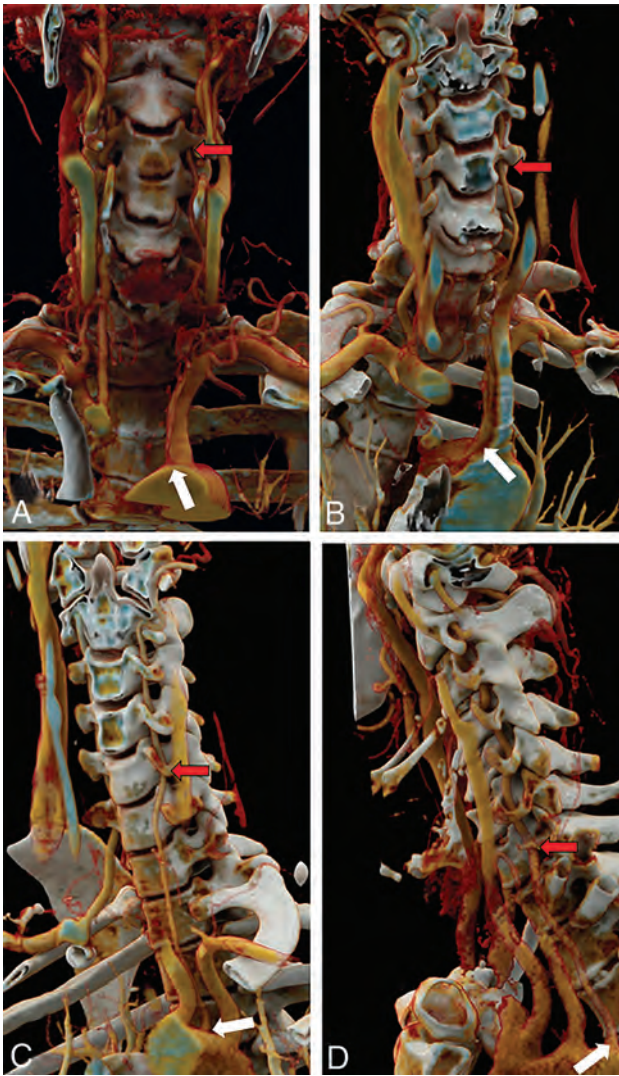


FIG 5. LVA variants. LVA origin directly from the aortic arch, between the LCCA and LSCA origins (white arrows) entering the FT (red arrows) at C3 (A), C4 (B), or C5 (C). D, The LVA originates as the fourth branch from the arch (white arrow) and enters the FT at C7 (red arrow).

with entry to the FT at C6 (Fig 1A, -C, and -D). We found that most (86%) of these typical arteries originated >2 cm from the origin of the RSCA. The most common pattern on the left was the origin from the left subclavian artery (LSCA) near the apex of its curve, with entry to the FT at C6 (Fig 1B–D).

Variants in right VA anatomy are illustrated in Fig 3. The most common variant encountered on the right was the artery originating within 2 cm of the right common carotid artery (30 cases, Fig 3C), with entry to the FT at C5. This was the only variant that demonstrated a statistically significant sex predilection, occurring more commonly in men than in women (21 versus 8, respectively, $P = .016$). Entry at C3 or C4 was also associated with proximal origin on the RSCA (Fig 3A, -B and Fig 4), and these vessels frequently originated even more proximally than those entering at C5. Entry at C7 was associated with origin either at the distal aortic arch or along the more distal RSCA (Fig 3D).

When the distances of the VA origins on the right were grouped by their FT entry level, there was some overlap, particularly between origins of vessels entering at C5 and C6 (Fig 4). However, there was good overall separation between these groups, and nearly no overlap between “typical” origins and those entering the FT at C3 or C4, which originated more proximally on the RSCA. The origin of arteries entering at C7 from the aortic arch (negative numbers in Fig 4) as well as at more distal locations along the RSCA contributed to a wide range of values for this subset of arteries.

Variants of LVA anatomy are illustrated in Fig 5. The most common variant on the left was direct origin from the aortic arch between the left common carotid artery (LCCA) and the LSCA (39 cases, Fig 5C), with entry to the FT at C5. The next most common variant was origin distal to the LSCA with entry at C7 (Fig 5D). The frequencies of different entries to the FT on both sides are summarized in Table 1.

In the cases with multiple origins (Fig 6), 9 (83%) were on the right, 2 (17%) were on the left, and one (8.3%) was bilateral (Table 2). No sex predilection was found in these cases (7 women and 5 men, $P > .05$). In the bilateral case, the left side had an accessory artery and the right side had 2 accessory arteries, such that the distal VA had a triple origin (Fig 6D). In all cases of accessory arteries, 1 moiety took origin from the SCA at the usual location for a normal VA, >2 cm from the RSCA origin, and entered the FT at C6. The other moiety took origin either from the RSCA within 2 cm of its origin or directly from the arch between the LCCA and LSCA, joining with the normal VA already in the FT. One aberrant branch on the right entered at C3 (Fig 6C), and one on the left entered at C5. In the remaining cases with accessory arteries, the aberrant moiety entered at C4. In the triplicated case, the C6 origin was close to the normal location along the SCA (17 mm from the RSCA origin), and the other moieties, entering the FT at C4 and C5, originated at 7 and 11 mm, respectively. No accessory moieties entered at C7 on either side.

When VA variants were mapped by their origins and coded for their level of entry to the FT, these patterns became clearer (Fig 7). While the VAs entering normally at the C6 FT originated from a relatively wide range of distances along the SCA on both sides, virtually all cases of “high-entry” at C3–C5 took origin from relatively narrow vascular segments. Overall, these high-entry vessels (entering FT at C5–C3) originated from a small segment of the RSCA, 93% originating within 2 cm of the RSCA origin. In addition, 2 cases with high-entry originated from the right common carotid artery itself. In contrast, only 14% of VAs entering the C6 FT originated within this range. On the left, these originated from the small segment between the LCCA and the LSCA, or from the proximal segment of the LSCA.

Most cases with “low-entry” at C7 originated from the aortic arch distal to the LSCA. A single right VA, originating even more distally from the thoracic aorta, entered the FT at C7 but coursed along the homologous costovertebral joint beginning at T4.

There were exceptions to the patterns we observed. For instance, in 4 cases, the LVA took origin from the aortic arch between the LCCA and LSCA and entered the FT normally at

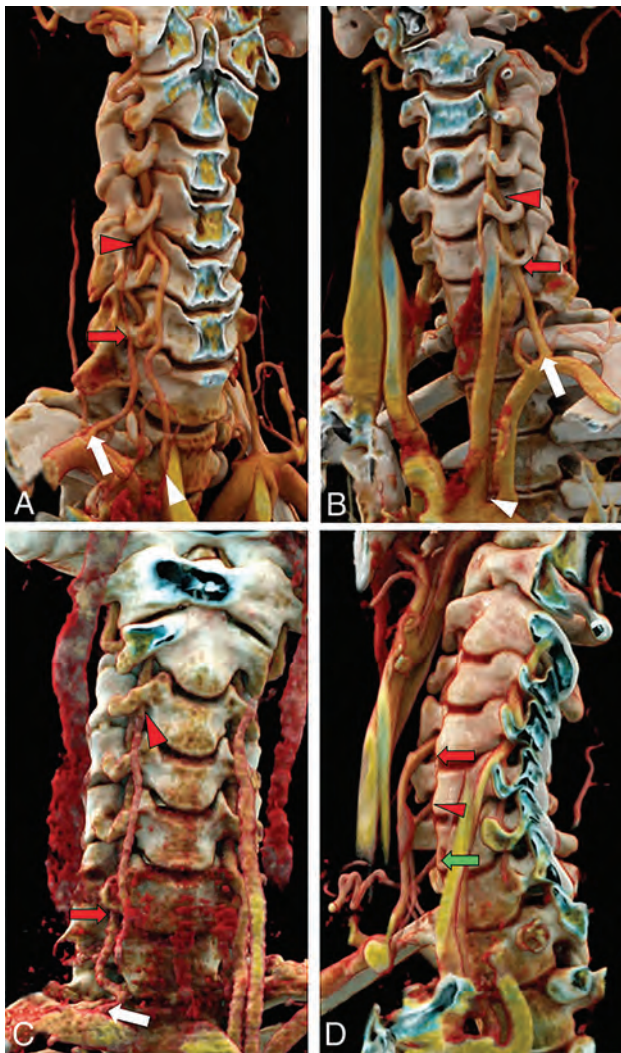


FIG 6. Multiple origins of the VAs. *A*, Two moieties originate proximally and distally along the LSCA. The moiety originating more distally (*white arrow*) at the expected VA origin enters the FT at C6 (*red arrow*), and the more proximal moiety (*white arrowhead*), originating within 2 cm of the RSCA, joins the first moiety at C4/C5 (*red arrowhead*), forming a fused artery that enters the FT at C4. This is the most common multiple-origin pattern. *B*, A similar pattern is noted on the left with the normal VA origin (*white arrow*), dominant in this case, entering the FT at C6 (*red arrow*) and the variant origin, originating from the arch between LCCA and LSCA (*white arrowhead*), joining at C4/C5 with a fused artery in the FT at C4 (*red arrowhead*). *C*, A rare subvariant, with 1 RVA moiety originating 8 mm from the right common carotid artery (not shown) and entering the FT at C3 (*red arrowhead*) and the other originating normally from the RSCA (*white arrow*) and entering at C6 (*red arrow*). *D*, An extremely rare variant, with the RVA having 3 origins, originating at 7, 11, and 14 mm along the RSCA and entering at C4 (*red arrow*), C5 (*red arrowhead*), and C6 (*green arrow*), respectively.

C6. In 5 cases, 2 on the right and 3 on the left, the VA took origin at a normal location on the SCA (defined here as >2 cm from the RSCA origin on the right, as described above) and entered the FT at C7. In 4 of these cases, there was a common origin of the VA and the costocervical trunk (CCT), and in the fifth case (on the left), the VA origin was within a few millimeters of the CCT.

Table 2: Distribution of variant VA entries to the FT in an enriched sample of all 125 cases with variant VAs^a

	RVA (%)	LVA (%)
Single origins		
C3	2 (3.6%)	1 (1.2%)
C4	14 (25.4%)	11 (13.6%)
C5	31 (56.4%)	47 (55.6%)
C7	7 (12.7%)	24 (28.9%)
Thoracic	1 (1.8%)	0 (0%)
Multiple origins		
C3, C6	1 (8.3%)	0 (0%)
C4, C6	7 (58.3%)	2 (16.7%)
C5, C6	1 (8.3%)	1 (8.3%)
C4, C5, C6	1 (8.3%)	0 (0%)

^a This sample includes the consecutive sample described earlier as well as an additional set of selected variants that were encountered outside of the sampling period.

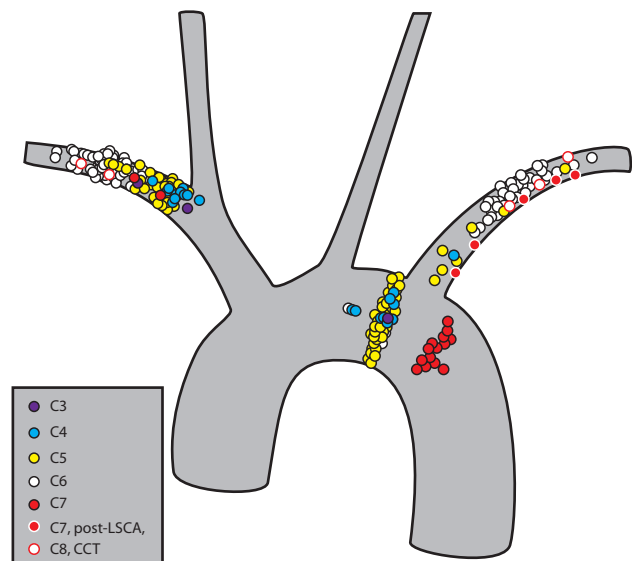


FIG 7. The origins of the VAs plotted against an idealized aortic arch. For this illustration, each VA origin was plotted in a 1D manner as a function of distance from the RSCA origin on the right or from the LSCA on the left. The position in any dimension other than that along the axis of the vessel is not based on anatomic data, and the distribution of vessel origins in the medial-lateral or craniocaudal dimension is used only to permit better visualization of the data points. Typical origins giving rise to VAs entering the FT at C6 are shown in white. Origins of vessels entering the FT at C3, C4, C5, and C7 are shown in purple, cyan, yellow, and red, respectively. Vessels originating along the posterior wall of the LSCA and entering at C7 are shown in red with a *white outline*. In addition, vessel origins entering at C7 whose vessel origin is shared with the CCT are shown in white with a *red outline*. Most of the high-entry vessels, which enter at C3–C5, originate in the proximal SCA on the right and directly from the arch or in the proximal subclavian artery on the left. Most of the low-entry vessels originate distal to or along the posterior wall of the LSCA in the region of the aortic isthmus.

DISCUSSION

The VAs form from longitudinal anastomotic vessels that bridge the cervical intersegmental arteries (ISAs) during development.²⁸ These ISAs supply the somites in the developing embryo. The SCAs derive wholly or in part from the seventh cervical ISAs, and the VAs derive from the anastomotic arteries of the first through sixth cervical ISAs, entering the FT of the sixth vertebral body.²⁹

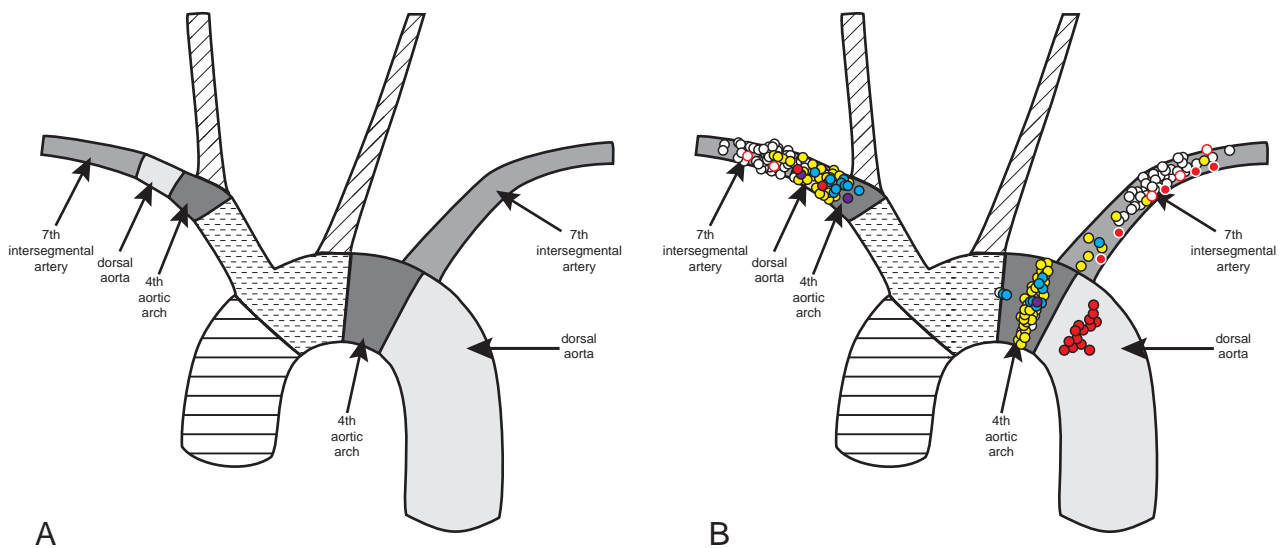


FIG 8. A, The embryologic origins of the aortic arch and proximal great vessels, adapted from Schoenwolf et al.³¹ B, VA origin map (from Fig 7) superimposed on the embryologic map. Note that while most VAs take origin from the seventh ISA segment of the SCA on both sides, the high-entry vessels take origin predominantly from the segments derived from the dorsal aorta and fourth aortic arch, and the low-entry vessels take origin predominantly from the distal aortic arch.

(For the purposes of this discussion, we use the generally accepted nomenclature, but we acknowledge the dissenting opinion of Padgett,³⁰ who considers the SCA as arising from the sixth cervical ISA.) This embryologic origin differs between the right and the left sides (Fig 8A). On the left, the entire SCA derives from the seventh ISA, but on the right, only the more distal portion of the SCA derives from the seventh ISA. However, the great vessels are also derived, in part, from the embryonic pharyngeal arch arteries and other embryonic aortic segments. In the more proximal RSCA, there is a segment derived from the fourth aortic arch and an additional segment derived from the embryonic dorsal aorta.³¹ The fourth arch segment is also represented on the left as part of the aortic arch between the LCCA and the origin of the LSCA.

Our data suggest that when the VA enters the FT at a higher-than-normal level, it takes origin from a segment distinct from the 7th ISA, most commonly the pharyngeal fourth aortic arch segment (Fig 8B). This origin explains the similarity in the FT entry point for right-sided vessels taking origin on the very proximal RSCA and for left-sided vessels with direct origin from the aortic arch between the LCCA and LSCA.

Low-entry VAs were a more heterogeneous group. Overall, when either VA entered the FT at a lower-than-normal level (nearly always at C7), it usually originated from the aortic arch segment derived from the left dorsal aorta in the region of the aortic isthmus (the segment between the LSCA origin and the ductus arteriosus; Fig 8B). An unexpected finding was that in 5 of 6 (83%) cases in which the VA had what appeared to be a normal origin on the SCA but entry to the FT at C7, there appeared to be a common origin of the VA and the CCT. In the remaining case (17%), the VA took origin within a few millimeters of the CCT. This feature may point toward yet another variant origin, distinct from the segments described above, and suggests a connection between the CCT and the C7 FT. Among the remaining VAs with origin from the LSCA itself and entering the FT at C7, all

had their origins along the posterior wall of the LSCA, which might be conceived of as a domain contiguous to and possibly embryologically inseparable from the typical C7 origin just distal to the LSCA.

Earlier studies have stated that variant origins of the RVA are relatively rare.^{1,11,32} We found their frequency to be nearly two-thirds that of left-sided variants. This discrepancy may be explained by the failure of most other studies to recognize that the proximal RSCA is fundamentally different from the more distal RSCA. Indeed, 1 earlier study did recognize the unique nature of the very proximal RSCA, and in that study, nearly the same number of right- and left-sided variants were noted.³ We build on these observations by quantitatively defining the atypical origin segment on the RSCA and linking these key findings with the distinct embryologic origin of this segment of the RSCA and its homolog on the left. We found that by using a cutoff of 2 cm from the origin of the RSCA, we captured 93% of high-entry VAs and misclassified only 14% of normal VAs, optimizing our sensitivity for detecting a variant entry. We also note that the variant configuration in which the RVA originates proximally on the RSCA and enters the FT at C5 was the only variant with a statistically significant sex predilection, occurring more commonly in men. We note this finding with some caution because these variants are rare, and the number of cases is small. Further study may bolster or negate this finding, though it does raise interesting questions of the interplay of sex and vascular development.

Although most cases with variant VAs occur on only 1 side, we observed a 3.9-fold increased frequency of bilaterally-variant VAs compared with the frequency that would be expected if the events were truly independent. This observation implies that a variant vessel on one side increases the likelihood of a variant vessel on the contralateral side and suggests that the factor or factors that give rise to these variants may not be restricted only to 1 side but may be influencing other developmental processes, with still undefined effects.

There were, of course, exceptions to the patterns we describe here, and some of these may point toward additional connections not recognized earlier. Among the 5 right VAs with what appears to be a variant origin but a normal entry at C6, the VA took origin between 13 and 19 mm from the RSCA origin. Conversely, in 3 left- and 1 right-sided VA, a normal origin gave rise to an artery entering at C5. Given the wide range of origin sites of normal VAs and the realities of vascular redundancy and tortuosity that are well-described, especially with aging,³³ this small number of outliers may reflect this range of values. Finally, on the left, 4 VAs took origin directly from the arch, between the LCCA and LSCA, and entered the FT at C6. We cannot explain these cases at present, but note that they are very uncommon, and future studies may help in understanding their development and significance.

CONCLUSIONS

The numerous variants of the anatomy of the cervical VAs, while relatively rare, are potentially clinically important, both in surgical and endovascular settings. Although they appear to be a diverse group of variants, they tend to follow fairly simple general rules, best understood by considering the embryologic basis of their origins. Overall, these findings suggest a systematic connection between the fourth arch and the higher FT and between the dorsal aorta or CCT and the lower FT. These simple organizing principles can help explain not only the range of variants seen but also parse the otherwise seemingly highly variable course of the RVA, demonstrating that both sides follow the same basic patterns as a function of their embryology.

ACKNOWLEDGMENT

The authors wish to thank Dr Patrick R. Hof for helpful comments and anatomical insights.

Disclosure forms provided by the authors are available with the full text and PDF of this article at www.ajnr.org.

REFERENCES

- Meila D, Tysiac M, Petersen M, et al. **Origin and course of the extracranial vertebral artery: CTA findings and embryologic considerations.** *Clin Neuroradiol* 2012;22:327–33 CrossRef Medline
- Budhiraja V, Rastogi R, Jain V, et al. **Anatomical variations in the branching pattern of human aortic arch: a cadaveric study from central India.** *ISRN Anat* 2013;2013:828969 CrossRef Medline
- Uchino A, Saito N, Takahashi M, et al. **Variations in the origin of the vertebral artery and its level of entry into the transverse foramen diagnosed by CT angiography.** *Neuroradiology* 2013;55:585–94 CrossRef Medline
- Woraputtaporn W, Ananteerakul T, Iamsaard S, et al. **Incidence of vertebral artery of aortic arch origin, its level of entry into transverse foramen, length, diameter and clinical significance.** *Anat Sci Int* 2019;94:275–79 CrossRef Medline
- Tasdemir R, Cihan OF. **Multidetector computed tomography evaluation of origin, V2 segment variations and morphology of vertebral artery.** *Folia Morphol (Warsz)* 2023;82:274–81 CrossRef Medline
- Li X, Guan L, Zilundu PL, et al. **The applied anatomy and clinical significance of the proximal, V1 segment of vertebral artery.** *Folia Morphol (Warsz)* 2019;78:710–19 CrossRef Medline
- Koenigsberg RA, Pereira L, Nair B, et al. **Unusual vertebral artery origins: examples and related pathology.** *Catheter Cardiovasc Interv* 2003;59:244–50 CrossRef Medline

- Vitošević F, Vitošević Z, Rasulić L. **The right vertebral artery arising from the right common carotid artery: report of a rare case.** *Surg Radiol Anat* 2020;42:1263–66 CrossRef Medline
- Yasin ALF, Shukri K, Aljaziri O, et al. **Aberrant origin of bilateral vertebral arteries associated with bovine aortic arch.** *Surg Radiol Anat* 2022;44:309–13 CrossRef Medline
- Siedlecki Z, Szostak M, Nowak K, et al. **Atypical course of vertebral artery outside the cervical spine: case report and review of the literature.** *World Neurosurg* 2021;145:405–08 CrossRef Medline
- Magklara EP, Pantelia ET, Solia E, et al. **Vertebral artery variations revised: origin, course, branches and embryonic development.** *Folia Morphol (Warsz)* 2021;80:1–12 CrossRef Medline
- Tsantili AR, Karampelias V, Samolis A, et al. **Anatomical variations of human vertebral and basilar arteries: a current review of the literature.** *Morphologie* 2023;107:169–75 CrossRef Medline
- Choi Y, Chung SB, Kim MS. **Prevalence and anatomy of anomalous left vertebral artery originated from aorta evaluated by computed tomographic angiography.** *Surg Radiol Anat* 2018;40:799–806 CrossRef Medline
- Omotoso BR, Harrichandparsad R, Moodley IG, et al. **An anatomical investigation of the proximal vertebral arteries (V1, V2) in a select South African population.** *Surg Radiol Anat* 2021;43:929–41 CrossRef Medline
- Yamaki KI, Saga T, Hirata T, et al. **Anatomical study of the vertebral artery in Japanese adults.** *Anat Sci Int* 2006;81:100–06 CrossRef Medline
- Vujmilović S, Spasojević G, Vujnović S, et al. **Variability of the vertebral artery origin and transverse foramen entrance level: CT angiographic study.** *Folia Morphol (Warsz)* 2018;77:687–92 CrossRef Medline
- Yaprak F, Ozer MA, Govsa F, et al. **Variations of the extracranial segment of vertebral artery as a bleeding risk factor.** *Surg Radiol Anat* 2021;43:1735–43 CrossRef Medline
- Yi X, Xie P, Zhang L, et al. **Entrance and origin of the extracranial vertebral artery found on computed tomography angiography.** *Sci Rep* 2022;12:15274 CrossRef Medline
- Kim MS. **Duplicated vertebral artery: literature review and clinical significance.** *J Korean Neurosurg Soc* 2018;61:28–34 CrossRef Medline
- Bordes SJ, Iwanaga J, Zarrintan S, et al. **Accessory vertebral artery: an embryological review with translation from Adachi.** *Cureus* 2021;13:e13448 CrossRef Medline
- Moran J, Kahan JB, Schneble CA, et al. **High-entry vertebral artery variant during anterior cervical discectomy and fusion.** *Case Rep Orthop* 2021;2021:8105298 CrossRef Medline
- Guan Q, Chen L, Long Y, et al. **Iatrogenic vertebral artery injury during anterior cervical spine surgery: a systematic review.** *World Neurosurg* 2017;106:715–22 CrossRef Medline
- Yu Z, Lyu S, Lang D, et al. **Vertebral artery course variation leading to an insufficient proximal anchoring area for thoracic endovascular aortic repair.** *Vascular* 2022 Nov 15. [Epub ahead of print] CrossRef Medline
- Gombert A. **Management of an isolated left vertebral artery on the arch during zone 2 landing thoracic endovascular aortic repair: a multicentre retrospective study - possible treatment options for a rare anatomical aortic variant or ne discere cessa.** *Eur J Vasc Endovasc Surg* 2023;65:338 CrossRef Medline
- Komiyama M, Morikawa T, Nakajima H, et al. **High incidence of arterial dissection associated with left vertebral artery of aortic origin.** *Neurol Med Chir (Tokyo)* 2001;41:8–11; discussion 11–12 CrossRef Medline
- Murray A, Meguid EA. **Anatomical variation in the branching pattern of the aortic arch: a literature review.** *Ir J Med Sci* 2022 Oct 22. [Epub ahead of print]. CrossRef Medline
- Açar G, Çiçekcibaş ı AE, Uysal E, et al. **Anatomical variations of the aortic arch branching pattern using CT angiography: a proposal for a different morphological classification with clinical relevance.** *Anat Sci Int* 2022;97:65–78 CrossRef Medline
- Padgett DH. **The development of the cranial arteries in the human embryo.** *Contrib Embryol* 1948;212:205–61

29. Anderson RH, Bamforth SD. **Morphogenesis of the mammalian aortic arch arteries.** *Front Cell Dev Biol* 2022;10:892900 CrossRef Medline
30. Padget DH. **Designation of the embryonic intersegmental arteries in reference to the vertebral artery and subclavian stem.** *Anat Rec* 1954;119:349–56 CrossRef Medline
31. Schoenwolf GC, Bleyl SB, Brauer PR, et al. **Development of the vasculature.** In: Schoenwolf GC, Bleyl SB, Brauer PR, et al *Larsen's Human Embryology*. Elsevier; 2020:298–334
32. Lazaridis N, Piagkou M, Loukas M, et al. **A systematic classification of the vertebral artery variable origin: clinical and surgical implications.** *Surg Radiol Anat* 2018;40:779–97 CrossRef Medline
33. Velez E, Boyer N, Acevedo-Bolton G, et al. **CT-reconstructed three-dimensional printed models of the right subclavian artery and aorta define age-related changes and facilitate benchtop catheter testing.** *J Invasive Cardiol* 2014;26:E141–44 Medline

Reliable Initial Trauma CT Findings of Supraclavicular Brachial Plexus Injury in Patients Sustaining Blunt Injuries

M.R. Povlow, J.R. Davis, A.M. Betts, S.M. Clayton, F.J. Cloran, J.K. Aden, and J.L. Ritter



ABSTRACT

BACKGROUND AND PURPOSE: Traumatic brachial plexus injuries are uncommon but can be debilitating. Early diagnosis is critical. Most patients undergo CT after trauma. We sought to identify correlative CT findings of supraclavicular brachial plexus injuries to discern who may require further evaluation with MR imaging and to measure multireviewer performance for their interpretations.

MATERIALS AND METHODS: We identified all MR imaging examinations of the brachial plexus from our institution from January 2010 to January 2021 and included those performed for trauma. We excluded patients with penetrating or infraclavicular injuries and without preceding CTA of the neck or CT of the cervical spine. The cohort of 36 cases and 50 controls remained for analysis and were assessed for 6 findings: scalene muscle edema/enlargement, interscalene fat pad effacement, first rib fracture, cervical spine lateral mass/transverse process fracture, extra-axial cervical spinal hemorrhage, and cervical spinal cord eccentricity, forming a reference key. A resident physician and 2 neuroradiologists (blinded to the MR imaging) independently reviewed each CT scan for these findings. We measured agreement (Cohen κ) between observers and against the reference key.

RESULTS: Interscalene fat pad effacement (sensitivity, specificity, 94.44%, 90.00%; OR = 130.33; $P < .001$) and scalene muscle edema/enlargement (sensitivity, specificity, 94.44%, 88.00%; OR = 153.00; $P < .001$) correlated significantly with brachial plexus injury. Agreement between observers and the key was almost perfect for those findings and fractures (pooled $\kappa \geq 0.84$; $P < .001$). Agreement between observers was variable ($\kappa = 0.48$ – 0.97 ; $P < .001$).

CONCLUSIONS: CT can accurately predict brachial plexus injuries, potentially enabling earlier definitive evaluation. High interobserver agreement suggests that findings are consistently learned and applied.

ABBREVIATION: BPI = brachial plexus injuries

The brachial plexus is a complex neurologic structure in the neck and upper extremity supporting many functions (Fig 1). Brachial plexus injuries (BPI) are uncommon injuries in patients affected by trauma, occurring in about 1%.¹ Common causative mechanisms include traction on the head and neck such as in vehicular collisions (particularly motorcycles and snowmobiles) and

penetrating trauma in cases of stabbings or shootings.¹ BPI may be classified by the varying degrees of damage to the nerves and nervous system supporting structures,² initially based on the work by Sunderland³ and Seddon,⁴ and these degrees of damage carry important prognostic information.⁵ The site of injury is clinically important because supraclavicular injuries, especially preganglionic rootlet avulsions, are the most grave.^{1,6} Other factors including diagnostic delay and delayed referral for surgical repair, both increasing the time from injury to repair, have also shown significant detriment to functional recovery.⁷

Diagnostic imaging, as a noninvasive complement to surgical exploration, has become critical in evaluating patients with suspected BPI. The evolution of optimal imaging assessment for BPI dramatically occurred across time, beginning with conventional radiographs and myelography, followed by CT myelography, and currently rests at MR imaging of the brachial plexus as the criterion standard in an attempt to accurately detect the location of injury.^{8–11} CT without myelography lacks the superior soft-tissue contrast resolution of MR imaging and historically has not been used to evaluate BPI.² It

Received July 24, 2022; accepted after revision May 31, 2023.

From the Department of Radiology (M.R.P., J.R.D., A.M.B., S.M.C., F.J.C., J.L.R.), and United States Army Graduate Medical Education (J.K.A.), Joint Base San Antonio–Fort Sam Houston, San Antonio, Texas.

The views expressed herein are those of the author(s) and do not necessarily reflect the official policy or position of the Defense Health Agency, Brooke Army Medical Center, the Department of Defense, nor any agencies under the U.S. Government.

Please address correspondence to Michael R. Povlow, MD, Department of Radiology, Brooke Army Medical Center, 3551 Roger Brooke Dr, Joint Base San Antonio–Fort Sam Houston, San Antonio, TX 78234; e-mail: michaelr.povlow.mil@health.mil

Indicates open access to non-subscribers at www.ajnr.org

Indicates article with online supplemental data.

<http://dx.doi.org/10.3174/ajnr.A7919>

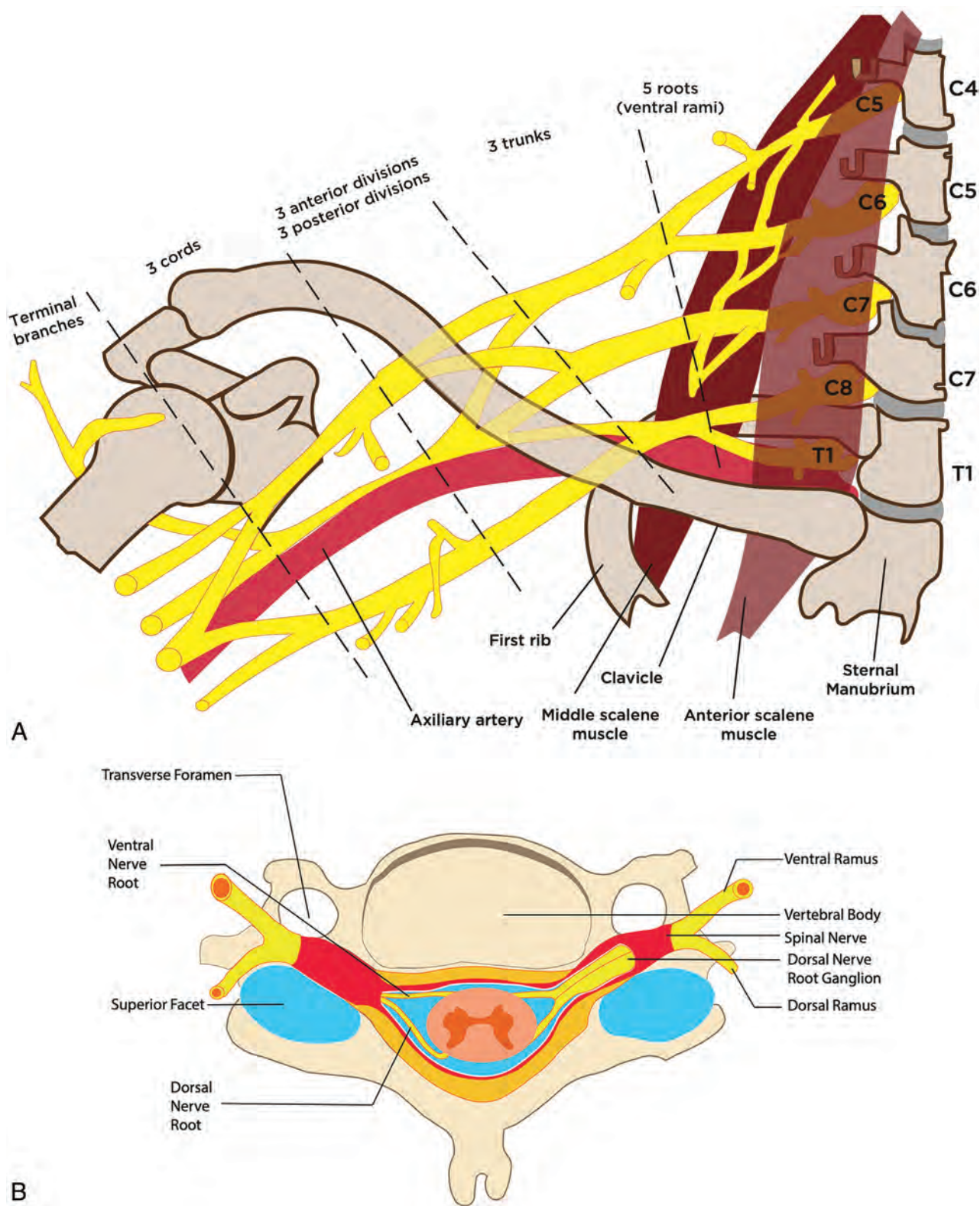


FIG 1. Anatomy of the brachial plexus. A frontal illustration (A) shows the anatomy of the brachial plexus as it arises from the neural foramina from the C4 to T1 levels, coursing between the anterior and middle scalene muscles and giving rise to many nerve branches. The cervical nerve roots of the brachial plexus are numbered 1 higher than the level where they originate (eg, the C5 nerve root arises from the C4 level, the C6 root from the C5 level, and so forth) because the C1 nerve root arises from above the C1 vertebral body at the skull base, and subsequently, there is a C8 nerve root but not a C8 vertebral body. The brachial plexus is divided into 5 roots, 3 trunks, 6 divisions, 3 cords, and terminal branches. A cross-sectional illustration (B) shows the anatomy of the proximal portions of the brachial plexus and nerve rootlets as they exit the spinal cord. Fibers from the dorsal rootlet complex with first-order sensory nerves in the dorsal root ganglion and fibers from both ventral and nerve rootlets blend before separating into ventral and dorsal nerve rami outside the neural foramina. The ventral rami go on to become the roots of the brachial plexus.

is, however, often performed for initial trauma evaluation and may detect the first signs of a traumatic lesion in this sensitive area.²

The objectives of this retrospective study are 2-fold. First, we aimed to establish the diagnostic utility of traumatic findings of BPI on CT by identifying injuries and injury patterns on the initial CT imaging in a cohort of patients with subsequent MR imaging performed for concern for BPI, thereby enabling radiologists to predict the presence of BPI on the basis of the initial trauma CT scan earlier in the hospital course. If successful, this process enables earlier definitive imaging and surgical treatment or, in the case of a nonsurgical injury, early physical therapy for prevention of long-term morbidity. Second, we aimed to evaluate

the interobserver agreement between a resident physician and 2 fellowship-trained neuroradiologists when evaluating these findings, with the end goal of extrapolating the validity and generalizability that might be expected in various practice environments.

MATERIALS AND METHODS

Given that this is a retrospective study, our local human research protections office declared the study to be human subjects research exempt from institutional research board and associated regulatory requirements. The Health Insurance Portability and Accountability Act (HIPAA) regulations applied, but given the retrospective analysis, a waiver of HIPAA authorization was approved. Data were kept in compliance with all HIPAA standards.

Our 2-part retrospective reader-based diagnostic performance study began with a retrospective search for all consecutive brachial plexus MR imaging examinations performed at our level 1 trauma center from January 2010 through January 2021 (Table 1), which was performed using our hospital's PACS. The inclusion criterion for our cohort was to have undergone MR imaging for brachial plexus evaluation. Following exclusion of MR imaging examinations performed for nontraumatic reasons, MR imaging examinations were then separated into groups by whether they were interpreted as positive or negative for BPI. Any examination initially interpreted as indeterminate was independently reviewed by a fellowship-trained neuroradiologist (J.L.R., with a 2-year neuro-radiology fellowship and 14 years of postfellowship experience), and a final determination was made. Examinations were excluded if they were not performed for the evaluation of trauma (Fig 2).

Any examination that included a penetrating or infraclavicular injury (ie, inferior to the clavicle) was excluded. We then reviewed the imaging performed before MR imaging, and patients who did not undergo an initial evaluation with either CT neck angiography or CT of the cervical spine without contrast for evaluation of traumatic injuries (within 48 hours of injury) were excluded. CT myelograms were not included in this study because they neither reflect the criterion standard nor are typically used in initial polytrauma imaging.

Imaging Parameters

The protocol and imaging parameters for the MR imaging of the brachial plexus, CT of the cervical spine, and the CT neck angiography varied during 11 years, but the most common protocol and ranges are the following:

1. MR imaging of the brachial plexus examination included a large-FOV coronal STIR of the bilateral brachial plexus as well as 3-plane spin-echo 2D oblique imaging along the

Table 1: Patient demographics and mechanisms of injury by case group

Characteristic	Cases (n = 36)	Controls (n = 50)
Age (range) (mean) (yr)	18–75 (38.7)	18–73 (41.5)
Sex		
Male	29	36
Female	7	14
Mechanism of injury		
Motor vehicle collision	26	25
Motorcycle collision	5	1
Fall from height ^a	3	8
All-terrain vehicle accident	2	0
Motor vehicle vs pedestrian	0	7
Assault	0	4
Fall from standing	0	3
Fall from horse	0	1
Bicycle accident	0	1

^aFall from height = (>10 ft, 3.048 m).

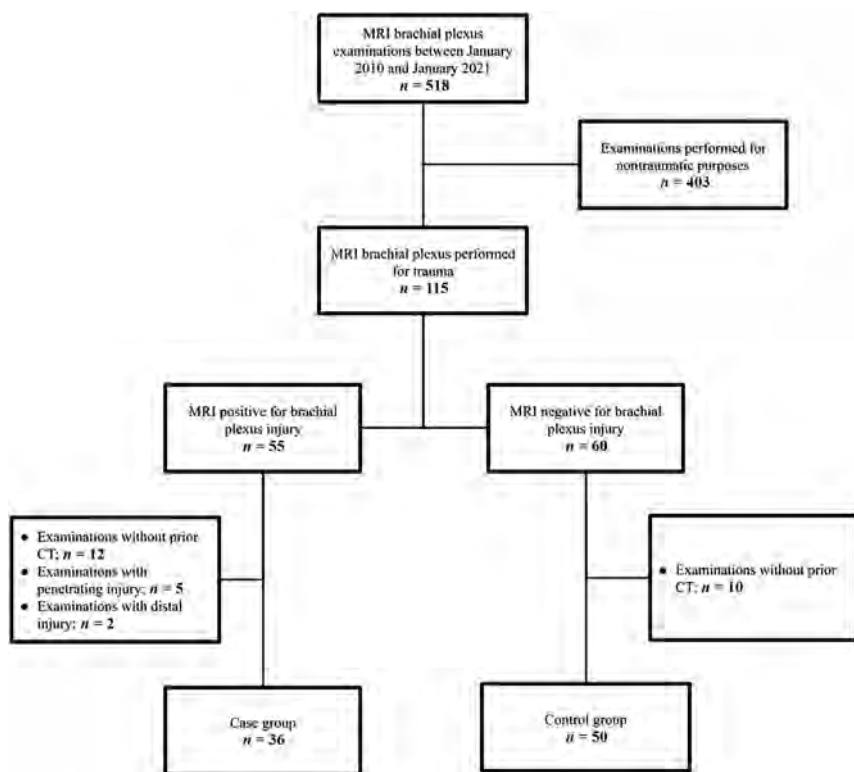


FIG 2. Inclusion and exclusion criteria. A flowchart delineates the inclusion and exclusion criteria used in this study, resulting in a case group of 36 and a control group of 50.

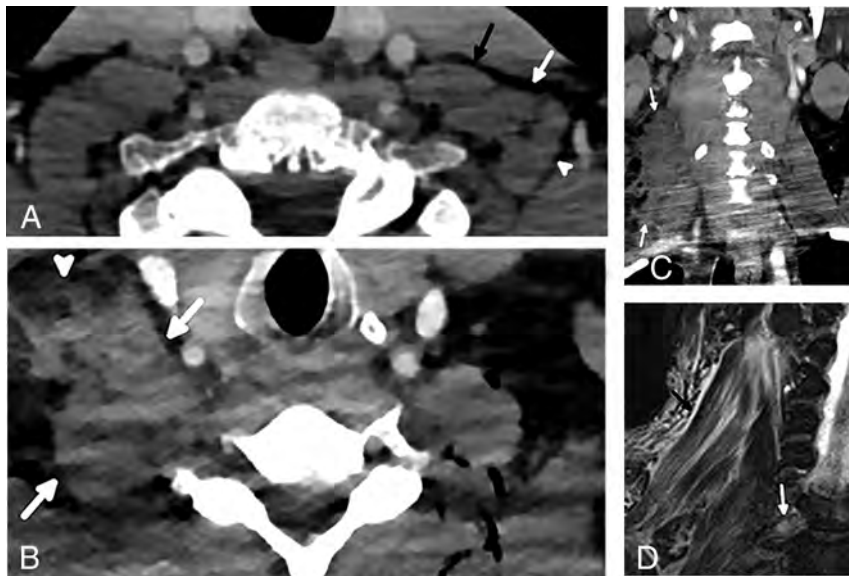


FIG 3. Normal and abnormal scalene muscles in different patients. An axial CT image in a 48-year-old man (A) without BPI shows normal anterior (black arrow), middle (white arrow), and posterior (arrowhead) scalene muscles without enlargement or edema. An axial CT image in a 52-year-old man (B) with BPI shows enlargement of the right scalene muscles (arrows) with extensive surrounding edema (arrowhead). A coronal CT image in the same patient (C) shows the extent of the asymmetric edema (arrows). A coronal T2 STIR MR imaging performed a day later in the 52-year-old patient (D) again shows scalene enlargement and edema (black arrow). Thickening and signal hyperintensity within the right C7 root (white arrow) are consistent with a stretch injury; similar findings were present at other levels.

course of the side of clinical concern in both T1 and STIR. The T1 images were acquired with a TR range of 566–700 ms and a TE range of 9–10 ms. The STIR images were acquired with a TR range of 2500–2600 ms and a TE range of 75–76 ms. Also performed were axial oblique 3D volumetric spoiled gradient-echo sequences with a TR of 15 ms, a TE of 5 ms, and a flip angle of 28°.

2. The CT cervical spine examination was performed at 120 kV (peak) using dose-modulation acquisition techniques. Slice thicknesses were 2 mm and acquired in the axial plane. Three-plane sharpened bone kernel images were provided as were axial and sagittal planes in a smooth soft-tissue kernel.
3. The CT neck angiography examinations were performed at 120 kVp and used dose-modulation acquisition techniques. Slice thickness was 1 mm and was acquired in the axial plane using a smooth soft-tissue kernel with coronal and sagittal reformats. Patients received 100 mL of iodine-based IV contrast of iodixanol, 320 mg/mL (Visipaque; GE Healthcare).

Reference Standard

For the first portion of our study, a resident physician (M.R.P., postgraduate year 4) and the senior author (J.L.R.) evaluated all CT examinations for the presence of 6 specific findings, which were predetermined on the basis of a prior, smaller-scale retrospective abstract:¹² scalene muscle edema/enlargement (Fig 3), interscalene fat pad effacement (Fig 4), first-rib fracture, cervical spine lateral mass or transverse process fracture, extra-axial cervical spinal hemorrhage (Fig 5), and cervical spinal cord eccentricity (Fig 6). Before determining the presence or absence of these

findings, the study orders were randomized and the demographic information was hidden. These results were tabulated and used as the reference key against which observers would be measured during the second portion of the study. We determined the sensitivity, specificity, and OR of these findings with 95% CIs when compared with the presence or absence of BPI on the MR imaging examination.

Agreement Compared with the Reference Key and between Observers

For the second portion of our study, a separate resident physician (J.R.D., postgraduate year 5) and 2 separate fellowship-trained neuroradiologists (A.M.B., 2-year neuroradiology fellowship and 7 years of postfellowship experience; S.M.C., 1-year neuroradiology fellowship and 3 years of postfellowship experience) underwent individual 15-minute training sessions led by the first author, which detailed positive and negative examples of CT findings from cases outside the study cohort. The examinations

were de-identified, and the readers then independently reviewed each CT examination, blinded to the results of the MR imaging or neurologically localizing information, and determined whether the 6 CT findings were present or absent on each examination, interpreted in a specific order sorted by examination date. The observers were able to use all images provided in the examination, including multiplanar reformats and reconstruction kernels (eg, bone, soft-tissue) if they were performed at the time of the initial imaging acquisition, and all standard tools available in the PACS (eg, window width and level adjustment, sharpening and softening filters). If the patient had undergone both a CT of the cervical spine and CT neck angiography, the observers were provided with the CT neck angiogram because the overall data provided (eg, a larger FOV, improved soft-tissue contrast resolution) were better on this examination. Interobserver agreement (Cohen κ) for each reviewer was compared against the reference key generated in the first portion of the study, as well as against the other reviewers. Pooled interobserver agreement (Cohen κ) was calculated from the individual reviewer's data by determining a two-thirds majority (ie, when ≥ 2 of the 3 reviewers determined a finding present or absent when evaluated independently), which was compared with the reference key for the presence or absence of each finding.

All statistical analyses were performed using JMP, Version 13.2 (SAS Institute) by a professional statistician (J.K.A.). Significance for statistical tests was set at $P < .05$. κ statistics were appraised as to their level of agreement on the basis of prior work by Landis and Koch:¹³ $\kappa < 0.00$, "poor"; $\kappa = 0.00$ –0.20, "slight"; $\kappa = 0.21$ –0.40, "fair"; $\kappa = 0.41$ –0.60, "moderate"; $\kappa = 0.61$ –0.80, "substantial"; $\kappa = 0.81$ –1.00, "almost perfect."

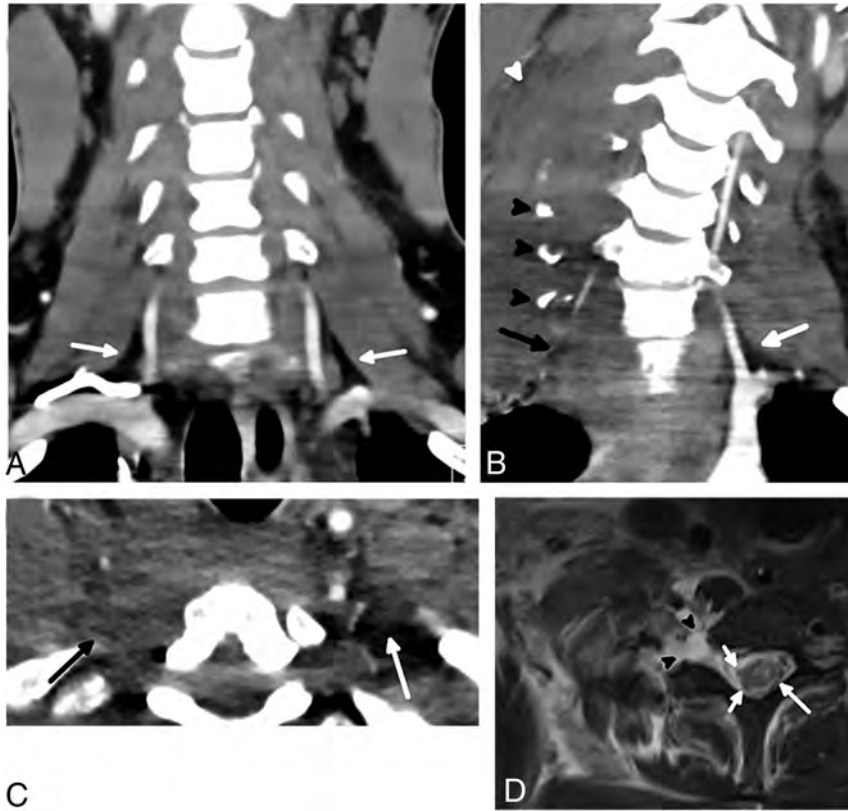


FIG 4. Normal and abnormal interscalene fat pads in different patients. A coronal CT scan in a 26-year-old man (A) without BPI demonstrates smoothly margined scalene muscles with normal interscalene fat pad (arrows). The coronal plane is a good place to assess the interscalene fat pad quickly by looking for this triangle of fat in the region of the proximal vertebral arteries, which should not have any stranding or hematoma. A coronal CT scan in a 25-year-old man (B) with BPI shows complete effacement of the right interscalene fat pad (black arrow) compared with the normal left interscalene fat pad (white arrow). Multiple displaced cervical transverse process fractures (black arrowheads) with scalene enlargement and edema (white arrowhead) are also present. An axial CT in the 25-year-old patient (C) shows the interscalene fat pad effacement (black arrow) in a different plane, compared with the normal left interscalene fat pad (white arrow). An axial T2-weighted MR imaging with fat saturation (D) performed a day later in the injured patient shows avulsion of the ventral and dorsal nerve rootlets (short white arrows), which was better appreciated when reviewing multiple sequential images. The spinal cord is slightly eccentric to the left and has abnormally increased signal (long white arrow), most pronounced within the gray matter. A large pseudomeningocele is present (arrowheads).

RESULTS

A total of 518 brachial plexus MR imaging examinations were reviewed (Fig 2), of which 403 were excluded because they were not performed for evaluating a traumatic injury. Of the 115 remaining examinations, 55 were positive for BPI and 60 were negative for BPI, constituting the cases and controls. There were 2 positive examinations that demonstrated infraclavicular BPI and 5 with penetrating trauma, so they were excluded from further analysis. Another 12 examinations were excluded from the case group and 10 from the control group because they did not have an initial CT of the cervical spine or CT neck angiography. A total of 36 cases and 50 controls remained for analysis. The spectrum of injuries found on the MR imaging examinations of the brachial plexus included nerve rootlet avulsion, nerve rupture, and neuropraxia, all occurring within the supraclavicular brachial plexus. The range of time between initial CT imaging and MR imaging of the brachial plexus spanned 24 hours to 9 months.

were highest for first-rib fractures, where they were almost perfect (0.84–0.93, $P < .001$). Agreement was also almost perfect between readers 1 and 2 for cervical lateral mass/transverse process fracture (0.86, $P < .001$). Spinal cord eccentricity had moderate agreement between all reader pairs (0.48–0.59, $P < .001$), and scalene muscle edema/enlargement had moderate agreement between readers 1 and 2 and 1 and 3 (0.49 and 0.59, $P < .001$). Agreement for the remaining findings was substantial for all reader pairs (0.64–0.74, $P < .001$).

DISCUSSION

Of the 6 CT findings, scalene muscle edema/enlargement and interscalene fat pad effacement were most strongly associated with BPI and demonstrated good sensitivity and specificity. This has a sound anatomic basis because the brachial plexus runs through the interscalene fat pad between the anterior and middle scalenes, and damage to one structure may risk damage to the

Reference Standard

Scalene muscle edema/enlargement and interscalene fat pad effacement were both 94.44% (95% CI, 81.86%–98.46%) sensitive for BPI with specificities of 88.00% (95% CI, 76.19%–94.38%) and 90.00% (95% CI, 78.64%–95.65%), respectively (Table 2). Of the remaining 4 findings, cervical lateral mass/transverse process fracture was most sensitive, 55.56% (95% CI, 39.58%–70.46%) and spinal cord eccentricity was least sensitive, 13.89% (95% CI, 6.08%–28.66%); however, all findings were specific in this cohort, ranging from 86.00% to 100.00%. Except for spinal cord eccentricity, each finding was significantly associated with BPI (OR = 3.91–153.00, $P \leq .01$).

Agreement Compared with the Reference Key and between Observers

Pooled κ statistics from all reviewers compared with the reference key were substantial or almost perfect for all findings (0.77–0.94, $P < .001$) and were highest for first-rib and cervical lateral mass/transverse process fractures (Online Supplemental Data). Except for spinal cord eccentricity, individual κ statistics compared with the reference key were also substantial or almost perfect (0.65–0.97, $P < .001$) and highest for fractures. For spinal cord eccentricity, the individual κ statistics were moderate for reviewers 1 and 2 (0.59 and 0.48, $P < .001$) and substantial for reviewer 3 (0.79, $P < .001$). Individual κ statistics between reviewers

other. Interobserver agreement for these findings was particularly strong between the neuroradiologists, despite the subjectivity that is inherent to the evaluation of the soft tissues on CT. While the brachial plexus itself is not as well-characterized in detail on CT as on MR imaging, evidence of damage to these intimately adjacent structures acts as a valid surrogate marker for BPI. In the

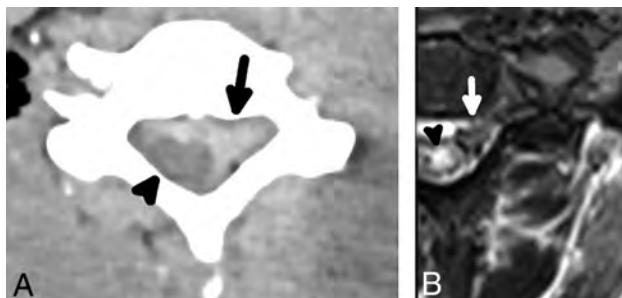


FIG 5. A 42-year-old man with preganglionic BPI and extra-axial hemorrhage. An axial CT image (A) shows a large extra-axial hematoma centered at the left of the spinal canal (arrow), which appears to compress the eccentric spinal cord (arrowhead). An axial T2 STIR MR imaging (B) in the same patient performed a day later shows an extra-axial hematoma (arrow); the hematoma and motion artifacts on the examination limit the diagnostic quality, but multilevel nerve rootlet avulsions are evident on sequential images. There is also severely abnormal signal hyperintensity (arrowhead) and a probable focus of hemorrhage (focal T2 hypointensity) in the spinal cord.

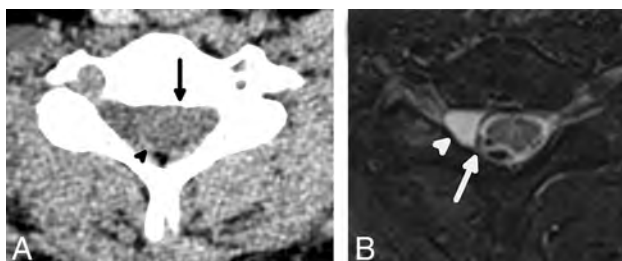


FIG 6. A 26-year-old man with preganglionic BPI and eccentricity of the spinal cord. An axial CT image (A) shows subtle eccentricity of the spinal cord and thecal sac (arrow) with an asymmetric amount of CSF in the right aspect of the spinal canal, which is indicative of a pseudomeningocele. There is also thin extra-axial hemorrhage (arrowhead) along the posterior aspect of the spinal cord. An axial T2 STIR MR imaging performed a day later in the same patient (B) shows complete avulsion of the ventral and dorsal nerve rootlets with eccentricity of the spinal cord (arrow), which is lateralized to the left of the spinal canal, compatible with preganglionic BPI. A small pseudomeningocele is confirmed on MR imaging (arrowhead) and is a finding highly associated with nerve rootlet avulsion.

case of interscalene fat pad effacement, this notion is concordant with previous assumptions that a hematoma in the interscalene fat pad is highly suspicious for BPI.² Scalene muscle edema and enlargement are evident when there is fat stranding adjacent to the scalenes or visible enlargement of the muscle bodies (Fig 3) and can be quickly assessed on axial and coronal images. Interscalene fat pad effacement also typically manifests with fat stranding or frank hematoma, and we found that this was most easily and quickly assessed by scrutinizing the fat adjacent to the proximal vertebral arteries on coronal images (Fig 4), though this region can and should also be assessed on other multiplanar images. Both findings are best assessed with a soft-tissue reconstruction kernel, possibly making its routine addition to a trauma CT cervical spine examination valuable.

First-rib and cervical lateral mass/transverse process fractures are injuries that indicate high-energy trauma with a vector that overlaps the brachial plexus. The scalene muscles, between which the brachial plexus courses, originate at the transverse processes of C2 through C7, and the anterior and middle scalenes insert on the first rib. Abrupt and forceful lateral flexion of the neck may cause traction and result in avulsion of the contralateral scalene muscles and has been postulated to be the primary cause of cervical transverse process fractures;¹⁴ this may also account for a proportion of first-rib fractures for the same reason. Such traction on the neck has also been associated with BPI,¹ and it has been reported that as many as 10% of patients with cervical transverse process fractures may have concomitant BPI.¹⁵ We found that both findings were specific in this cohort for and significantly associated with BPI. This finding is concordant with prior literature and also supports the assumption, based on the anatomy, that scalene muscle injury is closely associated with BPI. Fracture detection is already part of a standard trauma search pattern, and in keeping with this notion, we found interobserver agreement to be excellent and the highest of all CT findings. However, because fractures are a common finding in polytrauma, caution must be used when raising the suspicion for BPI if no other specific findings are present.

Extra-axial spinal canal hemorrhage manifests on CT as hyperattenuating products outside the spinal cord and can be identified when sought. While larger amounts of hemorrhage may be most readily identified, subtle cases with smaller hemorrhages can be challenging to visualize on CT compared with MR imaging, which is extremely sensitive to blood products. This issue is, in part, due to the lower contrast resolution of CT and the proximity to osseous structures, which can prevent selection of an optimal window width and level setting. Spinal cord eccentricity is also a subtle finding on CT, which can be difficult to

Table 2: Prevalence, sensitivities, specificities, and ORs of the CT findings

Finding	Cases (n = 36)	Controls (n = 50)	Sensitivity (95% CI)	Specificity (95% CI)	OR, P Value (95% CI)
Scalene muscle edema/enlargement	34	6	94.44 (81.86–98.46)	88.00 (76.19–94.38)	130.33; P < .001 (24.77–685.87)
Interscalene fat pad effacement	34	5	94.44 (81.86–98.46)	90.00 (78.64–95.65)	153.00; P < .001 (27.97–836.89)
First-rib fracture	14	7	38.89 (24.78–55.14)	86.00 (73.81–93.05)	3.91; P = .01 (1.38–11.09)
Cervical lateral mass or transverse process fracture	20	4	55.56 (39.58–70.46)	92.00 (81.16–96.85)	14.38; P < .001 (4.27–48.45)
Extra-axial spinal canal hemorrhage	10	0	27.78 (15.85–43.99)	100.00 (92.86–100)	40.02; P = .01 (2.26–709.90)
Spinal cord eccentricity	5	0	13.89 (6.08–28.66)	100.00 (92.86–100)	17.63; P = .05 (0.9425–329.97)

identify prospectively because differences in patient positioning and the close similarities in the attenuation of the spinal cord compared with the adjacent CSF are likely to result in lower precision. Coupled with the low prevalence of these findings in our cohort, we favor that these imaging subtleties were the reasons that sensitivity was low compared with the other findings. Spinal cord eccentricity was also the only finding that was not significantly associated with BPI in this cohort, possibly also relating to its low prevalence. On the other hand, extra-axial spinal canal hemorrhage and spinal cord eccentricity were 100% specific for BPI in this cohort, and we suggest that when present, they indicate severe injury that correlates more highly with nerve rootlet avulsion in the same manner as a pseudomeningocele, both of which may be better appreciated on MR imaging or a CT myelogram.^{2,6,8,16} Caution should be exercised in the use of extra-axial hemorrhage within the cervical spine as a predictor of brachial plexus injury because extra-axial intracranial hemorrhage as well as vertebral fractures may also lead to spinal canal hemorrhage.

With κ analysis of the CT findings, pooled and individual statistics showed that agreement was substantial or near-perfect with the exception of spinal cord eccentricity. This result may be, in part, because of the difficulty in identifying the contents of the spinal canal. In regard to interobserver κ statistics, the analysis showed that agreement was most consistently high between the 2 neuroradiologists for denoting the presence of scalene muscle edema/enlargement and interscalene fat pad effacement, likely due to similar levels of expertise and consistency.

There were limitations to our study design. There was selection bias because CT examinations were chosen for analysis only if the MR imaging had been performed later to assess for BPI. Doing so does not take into account all patients undergoing CT neck angiography or CT of the cervical spine for trauma; therefore, the authors could not determine whether the findings presented may be equally or more prevalent in situations in which there is no clinical concern for BPI. Clinical concern for BPI also increases the pretest probability of finding BPI and abnormal findings on CT. The readers, while blinded to the results of the MR imaging, still implicitly expected that there would be a higher-than-normal number of cases positive for BPI in the study cohort due to this increased pretest probability. Subsequently, it is possible that detection of the CT findings may have been subject to a degree of bias that would not be present for a radiologist interpreting unknown cases in his or her normal practice.

Finally, this was a single-institution study, which may limit its overall generalizability. However, given our diverse patient population, this is thought to be less of a concern, and experiences would likely be comparable at other level 1 trauma centers. A future prospective trial with a larger cohort would be warranted to determine whether these findings would be valid with inclusion of all patients with CT neck angiography and cervical spine CT after their traumatic episode and would mitigate selection bias.

There were also minor limitations in image quality and examination protocols due to varied examination practices during an 11-year period on multiple scanners. For example, given the

traditional CT neck angiography or cervical spine protocol at our institution, the complete extent of the first rib was not always seen, and while first-rib fracture was ultimately a finding of secondary importance, it could still limit performance and utility in some cases. Streak artifacts from contrast within the vascular system or from the upper extremities at times obscured visualization of the structures at the base of the neck. Finally, soft-tissue reconstructions were only variably present on cervical spine CT examinations, limiting evaluation of the most significant CT findings of BPI, namely scalene muscle edema/enlargement and interscalene fat pad effacement.

Despite these limitations and MR imaging is ubiquitous in major medical centers, identification of possible BPI at the time of initial CT trauma imaging has a potential impact in multiple scenarios. In the setting of a patient who is under general anesthesia or comatose at the time of initial imaging and cannot participate in a neurologic examination, concerning CT findings may prompt further imaging and specialist consultation. Also, small community hospitals, stand-alone emergency rooms, and urgent care clinics in the United States may have CT as their most advanced cross-sectional resource; identification of possible BPI may lead to more prompt disposition and transfer of the patient. Furthermore, in the situation of locales in underprivileged countries or hospitals established in austere environments overseas, BPI identification on CT may lead to prompt transfer to a higher level of care. Ultimately, identifying these potential high-yield findings on CT may advance radiologists' ability to care for patients in a broad spectrum of environments.

CONCLUSIONS

Assessment of initial CT neck angiography or cervical spine imaging performed for the work-up of traumatic injury can predict which patients are at risk of BPI and which patients may benefit from early MR imaging of the brachial plexus. In particular, scalene muscle edema/enlargement and interscalene fat pad effacement correlate highly and can be quickly incorporated into an existing trauma search pattern. However, because MR imaging remains the imaging criterion standard for detecting and describing BPI, negative or equivocal CT findings should not prevent further evaluation in patients with suspicious clinical findings or a high-risk mechanism of injury. We also found substantial or almost perfect interobserver agreement on all findings when comparing the reference key and the resident physician and neuroradiologist observers, despite the subjectivity and subtlety of some of the findings. While we found that interobserver agreement for single findings between readers was more variable, agreement was still good for key findings like scalene muscle edema/enlargement and interscalene fat pad effacement. This finding suggests that these results are relatively straightforward and accessible, allowing radiologists with varying levels of comfort with neurotrauma imaging to successfully apply this knowledge in standard practice. We suggest that knowledge of these high-value findings is important to any radiologist who routinely interprets trauma imaging and may potentially decrease costly delays in care for patients with BPI.

ACKNOWLEDGMENT

The authors would like to thank Mr Ernesto Menchaca for his diligent work and patience in providing our medical illustrations.

Disclosure forms provided by the authors are available with the full text and PDF of this article at www.ajnr.org.

REFERENCES

1. Midha R. **Epidemiology of brachial plexus injuries in a multitrauma population.** *Neurosurgery* 1997;40:1182–89 CrossRef Medline
2. Gilcrease-Garcia BM, Deshmukh SD, Parsons MS. **Anatomy, imaging, and pathologic conditions of the brachial plexus.** *Radiographics* 2020;40:1686–714 CrossRef Medline
3. Sunderland S. **A classification of peripheral nerve injuries producing loss of function.** *Brain* 1951;74:491–516 CrossRef Medline
4. Seddon HJ. **Three types of nerve injury.** *Brain* 1943;66:237–88 CrossRef
5. Singer AD, Meals C, Kesner V, et al. **The multidisciplinary approach to the diagnosis and management of nonobstetric traumatic brachial plexus injuries.** *AJR Am J Roentgenol* 2018;211:1319–31 CrossRef Medline
6. Wade RG, Takwoingi Y, Wormald JCR, et al. **MRI for detecting root avulsions in traumatic adult brachial plexus injuries: a systematic review and meta-analysis of diagnostic accuracy.** *Radiology* 2019;293:125–33 CrossRef Medline
7. Martin E, Senders JT, DiRisio AC, et al. **Timing of surgery in traumatic brachial plexus injury: a systematic review.** *J Neurosurg* 2019;130:1333–45 CrossRef
8. Doi K, Otsuka K, Okamoto Y, et al. **Cervical nerve root avulsion in brachial plexus injuries: magnetic resonance imaging classification and comparison with myelography and computerized tomography myelography.** *J Neurosurg* 2002;96:277–84 CrossRef Medline
9. Walker AT, Chaloupka JC, de Lotbiniere AC, et al. **Detection of nerve rootlet avulsion on CT myelography in patients with birth palsy and brachial plexus injury after trauma.** *AJR Am J Roentgenol* 1996;167:1283–87 CrossRef Medline
10. Gad DM, Hussein MT, Omar NN, et al. **Role of MRI in the diagnosis of adult traumatic and obstetric brachial plexus injury compared to intraoperative findings.** *Egypt Journal of Radiology and Nuclear Medicine* 2020;51:195 CrossRef
11. Takahara T, Hendrikse J, Yamashita T, et al. **Diffusion-weighted MR neurography of the brachial plexus: feasibility study.** *Radiology* 2008;249:653–60 CrossRef Medline
12. Tharin B, Kini J, York G, et al. **Traumatic Brachial Plexus Injuries: Retrospective Review of Findings on Presenting CT Evaluation.** Presented at: American Society of Emergency Radiology (ASER) 23rd Annual Meeting, September 14, 2011. Key Biscayne, Florida
13. Landis JR, Koch GG. **The measurement of observer agreement for categorical data.** *Biometrics* 1977;33:159–74 CrossRef Medline
14. Newell N, Pearce AP, Spurrier E, et al. **Analysis of isolated transverse process fractures sustained during blast-related events.** *J Trauma Acute Care Surg* 2018;85:S129–33 CrossRef Medline
15. Woodring JH, Lee C, Duncan V. **Transverse process fractures of the cervical vertebrae: are they insignificant?** *J Trauma* 1993;34:797–802 CrossRef Medline
16. Yoshikawa T, Hayashi N, Yamamoto S, et al. **Brachial plexus injury: clinical manifestations, conventional imaging findings, and the latest imaging techniques.** *Radiographics* 2006;26:S133–43 CrossRef Medline

Somatostatin Receptor–PET/CT/MRI of Head and Neck Neuroendocrine Tumors

J.N. Rini, G. Keir, C. Caravella, A. Goenka, and A.M. Franceschi



ABSTRACT

BACKGROUND AND PURPOSE: Due to its high sensitivity, somatostatin receptor–PET may detect smaller lesions and more extensive disease than contrast-enhanced MR imaging, while the superior spatial resolution of MR imaging enables lesions to be accurately localized. We compared results of somatostatin receptor–PET/MRI with those of MR imaging alone and assessed the added value of vertex-to-thigh imaging for head and neck neuroendocrine tumors.

MATERIALS AND METHODS: Somatostatin receptor–PET/CT was acquired as limited brain or head and neck imaging, with optional vertex-to-thigh imaging, following administration of $^{64}\text{Cu}/^{68}\text{Ga}$ DOTATATE. Somatostatin receptor–PET was fused with separately acquired contrast-enhanced MR imaging. DOTATATE activity was classified as comparable, more extensive, and/or showing additional lesions compared with MR imaging. Vertex-to-thigh findings were classified as positive or negative for metastatic disease or incidental.

RESULTS: Thirty patients (with 13 meningiomas, 11 paragangliomas, 1 metastatic papillary thyroid carcinoma, 1 middle ear neuroendocrine adenoma, 1 external auditory canal mass, 1 pituitary carcinoma, 1 olfactory neuroblastoma, 1 orbital mass) were imaged. Five had no evidence of somatostatin receptor–positive lesions and were excluded. In 11/25, somatostatin receptor–PET/MRI and MR imaging were comparable. In 7/25, somatostatin receptor–PET/MRI showed more extensive disease, while in 9/25, somatostatin receptor–PET/MRI identified additional lesions. On vertex-to-thigh imaging, 1 of 17 patients was positive for metastatic disease, 8 of 17 were negative, and 8 of 17 demonstrated incidental findings.

CONCLUSIONS: Somatostatin receptor–PET detected additional lesions and more extensive disease than contrast-enhanced MR imaging alone, while vertex-to-thigh imaging showed a low incidence of metastatic disease. Somatostatin receptor–PET/MRI enabled superior anatomic delineation of tumor burden, while any discrepancies were readily addressed. Somatostatin receptor–PET/MRI has the potential to play an important role in presurgical and radiation therapy planning of head and neck neuroendocrine tumors.

ABBREVIATIONS: FWHM = full width at half maximum; HNPGL = head and neck paraganglioma; max = maximum; NCCN = National Comprehensive Cancer Network; NET = neuroendocrine tumor; PitNET = pituitary neuroendocrine tumor; SSA = somatostatin analog; SSTR = somatostatin receptor; SUV = standard uptake value

Neuroendocrine tumors (NETs) are a heterogeneous group of neoplasms characterized by cell surface overexpression of somatostatin receptors (SSTRs). NETs occur throughout the body, most commonly in the gastrointestinal tract, pancreas, and lungs.¹ In the head and neck, the most common NETs are meningiomas and head and neck paragangliomas (HNPGLs).^{2–4}

Less common entities include olfactory neuroblastoma, middle ear neuroendocrine tumors, medullary thyroid carcinoma, and pituitary lesions.^{5–7}

SSTRs serve as the target for functional imaging of NETs using radiolabeled somatostatin analogues (SSAs). There are 5 main subtypes of SSTRs, with type 2 receptors most frequently overexpressed in NETs.⁸ Functional imaging of NETs was originally performed with planar and SPECT imaging using ^{111}In pentetate (OctreoScan; Mallinckrodt).^{9–11} Since 2016, beginning with the FDA approval of ^{68}Ga DOTATATE, the European Medicines Agency approval of ^{68}Ga DOTATOC, and the subsequent FDA approval of ^{64}Cu DOTATATE in 2020, functional imaging of NETs has transitioned to PET with SSAs,¹² a technique, collectively referred to as SSTR-PET. In 2017, the Society of Nuclear Medicine and Molecular Imaging recommended that SSTR-PET should replace ^{111}In pentetate scintigraphy.¹³

Received March 20, 2023; accepted after revision June 14.

From the Nuclear Medicine Division (J.N.R., G.K., C.C.), Department of Radiology, and Department of Radiation Oncology (A.G.), Donald and Barbara Zucker School of Medicine at Hofstra/Northwell, Manhasset, New York; and Neuroradiology Division (A.M.F.), Department of Radiology, Donald and Barbara Zucker School of Medicine at Hofstra/Northwell, Lenox Hill Hospital, New York, New York.

Please address correspondence to Ana M. Franceschi, MD, PhD, Department of Radiology, Lenox Hill Hospital, 100 East 77th St, 3rd Floor, New York, NY 10075; e-mail: afranceschi@northwell.edu; @AFranceschi_MDPhD

Indicates article with online supplemental data.

<http://dx.doi.org/10.3174/ajnr.A7934>

DOTATATE-PET/CT protocol parameters

Protocol	PET ^a		CT ^b	
	Bed Positions	Acquisition Time (Min/Bed)	mA	Pitch (mm/Rot)
Brain	1	10	95 Fixed mA	1.375
Head/neck	3	5	50–440 Auto mA Noise index 18.0	0.984
Vertex-to-thigh	7–8	5	30–440 Auto mA Noise index 28.5	0.984

Note:—Min indicates minute; Rot, rotation time.

^a All 3D PET data were reconstructed using VUE Point FX (GE Healthcare) TOF and Sharp IR; ⁶⁴Cu-DOTATATE: 256 matrix, 3 iterations, 8 subsets, “standard” z-axis filter, and a Gaussian postfilter of 7.0-mm FWHM; ⁶⁸Ga DOTATATE: 192 matrix, 2 iterations, 24 subsets, standard z-axis filter, and a Gaussian postfilter of 6.4-mm FWHM.

^b All helical CT configurations used 120 kV(peak), 3.75-mm section thickness, and a 0.8-second rotation.

Advantages of SSTR-PET, compared with scintigraphy, include improved sensitivity of lesion detection, lower radiation dose, and shorter and more convenient study duration.^{14,15}

SSTR-PET is most frequently used to evaluate NETs that arise from gastroenteropancreatic sites. The Society of Nuclear Medicine and Molecular Imaging Appropriate Use Criteria for SSTR-PET focus on its role in well-differentiated gastroenteropancreatic NETs.^{13–15} While the guidelines do not specifically address the role of SSTR-PET in head and neck tumors, they indicate that the technique will likely serve as a valuable tool for the assessment of many additional SSTR-positive diseases.¹³ In fact, the current National Comprehensive Cancer Network (NCCN) Guidelines for Central Nervous System Cancers state that meningiomas exhibit high SSTR density, which allows the use of SSTR imaging to help delineate the extent of disease and to pathologically define an extra-axial lesion, as well as for distinguishing residual tumor from postoperative scarring in subtotally resected/recurrent tumors.^{16,17} In addition, the NCCN guidelines suggest that SSTR-PET may also be indicated for medullary thyroid carcinoma, depending on the calcitonin/carcinoembryonic antigen doubling time.¹⁸

Due to its high sensitivity, SSTR-PET may detect smaller lesions and more extensive disease than contrast-enhanced MR imaging alone, while hybrid PET/MRI systems offer the added value of the superior spatial resolution of MR imaging, which enables a more accurate anatomic localization of lesions compared with PET or PET/CT.¹⁹ Combined SSTR-PET/MRI is superior to either technique alone for oncologic imaging;²⁰ however, the availability of dedicated PET/MRI scanners in clinical practice remains limited. In the absence of simultaneous PET/MRI systems, SSTR-PET is routinely performed in the clinical setting as PET/CT from the vertex-to-thigh. Because distant metastases are uncommon with meningiomas and HNPGLs,^{21,22} depending on the clinical indication, SSTR-PET imaging limited to the brain or head and neck may be sufficient for assessment of neuroendocrine tumors in the head and neck. The advantages of a limited SSTR-PET imaging include reduced imaging acquisition times, a shorter CT range, and a smaller display FOV, which is optimized for imaging of the brain and head and neck. Additionally, the anatomy included in both limited SSTR-PET

and separately acquired MR imaging is more successfully fused using neuroimaging postprocessing software compared with vertex-to-thigh PET, allowing SSTR-PET/MRI interpretation.

Therefore, we recently introduced a SSTR-PET/CT/MR imaging protocol for head and neck neuroendocrine tumor assessment. The protocol includes a limited SSTR-PET of the brain or head and neck, fusion with a separately acquired contrast-enhanced MR imaging using commercially available software, and an optional SSTR-PET/CT from vertex to thigh. The purpose of this study was to compare the results of limited SSTR-PET/MRI with those

of separately acquired MR imaging of the brain or head and neck and to assess the added value of vertex-to-thigh imaging.

MATERIALS AND METHODS

Beginning in May 2022, before scheduling patients with known or suspected SSTR-positive head and neck tumors for SSTR-PET/CT, clinical notes and structural MR imaging/CT head and neck imaging were reviewed, and the study was protocolled by a nuclear medicine physician as a limited brain or head and neck study, with or without vertex-to-thigh imaging, based on lesion location and the request of the referring physician.

SSTR-PET/CT was acquired 50–60 minutes following IV administration of 148-MBq (4-mCi) ⁶⁴Cu DOTATATE or 185-MBq (5-mCi) ⁶⁸Ga DOTATATE using a Discovery 710HD (GE Healthcare) or a Biograph mCT 64 (Siemens) scanner. Imaging times for brain, head and neck, and vertex-to-thigh protocols were approximately 10, 15, and 40 minutes, respectively. Reconstruction parameters specific for ⁶⁴Cu DOTATATE included a 256 matrix, 3 iterations, 8 subsets, and a postfilter cutoff of 7.0-mm full width at half maximum (FWHM). Reconstruction parameters for ⁶⁸Ga DOTATATE included a 192 matrix, 2 iterations, 24 subsets, and a postfilter cutoff of 6.4-mm FWHM (Table). Limited SSTR-PET was corrected for attenuation using CT and was fused with separately acquired contrast-enhanced MR imaging of the brain or neck using MIMneuro software (Version 7.2.7; MIM software). Dedicated contrast-enhanced MR imaging of the brain and neck were interpreted by fellowship-trained neuroradiologists as part of routine clinical care. A fellowship-trained neuroradiologist with 10 years of experience in PET/MRI interpreted brain and head and neck SSTR-PET/MRI, while a nuclear medicine physician with 20 years of experience interpreted concurrently obtained vertex-to-thigh images.

Following institutional review board approval, the neuroradiologist classified DOTATATE activity as comparable, locally more extensive, and/or showing additional lesions, compared with separately acquired contrast-enhanced MR imaging of the brain or head and neck. The nuclear medicine physician classified vertex-to-thigh images, excluding the head and neck, as positive or negative for metastatic disease or as showing incidental findings.

RESULTS

Thirty patients (25 females, 5 males; age range, 16–77 years; mean age, 55 years) with known or suspected SSTR-positive head and neck tumors were imaged with limited SSTR-PET/CT (limited brain [18/30, 60% patients], limited head and neck [12/30, 40% patients], and vertex-to-thigh [17/30, 57% patients]),

with either ^{64}Cu DOTATATE (29 patients) or ^{68}Ga DOTATATE (1 patient) (Online Supplemental Data). For 29/30 patients, limited SSTR-PET was fused with separately acquired contrast-enhanced MR imaging of the brain or MR imaging of the head and neck. For 1 patient with a cochlear implant, MR imaging was not performed.

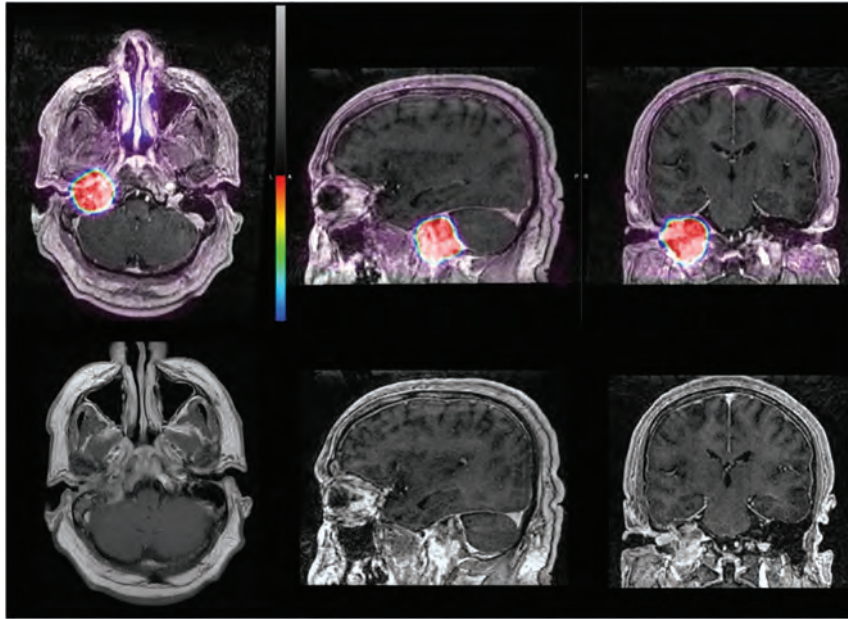


FIG 1. A 55-year-old man with a SSTR-avid mass centered in the right jugular fossa, which extends into the right middle ear cavity, measuring $3.7 \times 3.6 \times 3.5$ cm, consistent with glomus jugulotympanic paraganglioma. In this example, SSTR-PET/MRI findings are comparable with the extent of disease identified by contrast-enhanced MR imaging.

Twenty-five patients had SSTR-positive lesions (including 12 meningiomas, 10 HBPGLs [3 glomus jugulare tumors, 2 glomus tympanicum tumors, 3 glomus jugulotympanicum tumors, 1 glomus vagale, 1 multiple cervical paraganglioma]; 1 had a suspected cervical paraganglioma on MR imaging of the neck with subsequent biopsy positive for metastatic papillary thyroid carcinoma, 1 had a pituitary carcinoma, and 1 had an olfactory neuroblastoma).

In 11/25 (44%) subjects, findings of SSTR-PET/MRI and contrast-enhanced MR imaging were comparable (Figs 1 and 2). In 7/25 (28%) patients, SSTR-PET/MRI showed locally more extensive disease than contrast-enhanced MR imaging alone (Figs 3 and 4). Of these 7 patients, 6 patients had meningiomas, typically imaged in the postoperative setting, with SSTR-PET/MRI detecting additional transosseous involvement (2 patients), recurrence at the craniotomy site (3 patients), and/or disease at the skull base (1 patient with prominent

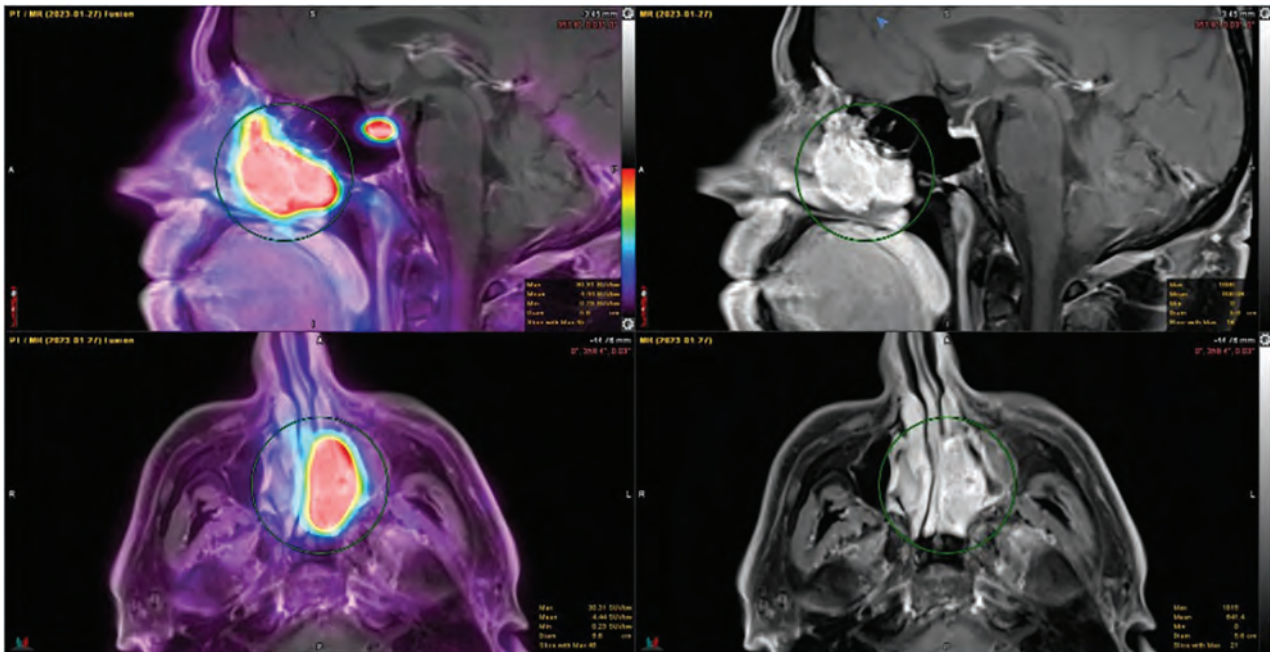


FIG 2. A 46-year-old man with a SSTR-avid homogeneously enhancing soft-tissue mass arising from the left nasal cavity, measuring $4.0 \times 1.9 \times 4.1$ cm in anterior-posterior by transverse by craniocaudal dimensions, consistent with biopsy-proved olfactory neuroblastoma (esthesioneuroblastoma). There was no evidence of intracranial tumor extension. In this example, SSTR-PET/MRI findings are comparable with the extent of disease identified by contrast-enhanced MR imaging.

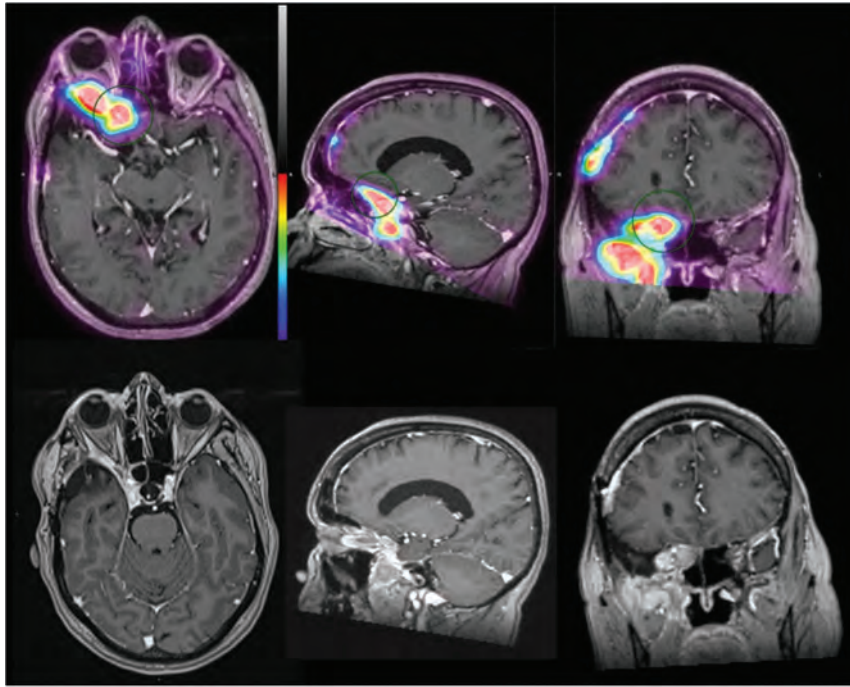


FIG 3. A 63-year-old woman post-right pterional craniotomy for meningioma resection with SSTR-avid recurrent meningioma arising from the right sphenoid wing and infiltrating the right orbital apex, right cavernous sinus, right sphenoid sinus, and right posterior ethmoid air cells and extending inferiorly along the right anterior temporal convexity and into the right masticator space. SSTR-positive recurrence is also noted at the right frontal craniotomy site. In this example, SSTR-PET/MRI findings were more extensive than on the basis of structural imaging because the extracranial tumor component was not identified on contrast-enhanced MR imaging.

extracranial tumor extension into the right masticator space), compared with contrast-enhanced MR imaging of the brain alone. One of the 7 patients had recurrent/residual pituitary carcinomas, which had progressed with the patient on somatostatin analog therapy. Meanwhile, in 9/25 (36%) subjects, SSTR-PET/MRI identified additional lesions (Fig 5). Most of these patients (5/9) had incidentally detected subcentimeter meningiomas, 1 patient had a parathyroid adenoma, and another had temporomandibular joint arthritis. Most interesting, in 2 patients, SSTR-PET/MRI detected additional glomus jugulare tumors, which were not identified by initial contrast-enhanced MR imaging. One of the patients presented with tongue weakness and fasciculations, with negative findings on MR imaging of the brain (retrospective review of the MR imaging revealed an enhancing lesion centered in the left jugular foramen and expanding the left hypoglossal canal). Given progressive symptoms, the patient underwent surgical exploration, but no lesion was identified. Subsequent SSTR-PET/MRI demonstrated a left glomus jugulare paraganglioma measuring $1.4 \times 2.2 \times 1.7$ cm (maximum standard uptake value [SUVmax], 148.65). The patient was treated by stereotactic radiosurgery with curative intent. The second patient had multiple known cervical paragangliomas, previously assessed by contrast-enhanced MR imaging of the neck. In this case, SSTR-PET/MRI showed an additional, previously undetected right glomus jugulare tumor measuring 0.5×0.5 cm (SUVmax, 29.63).

Five patients had no evidence of SSTR-positive lesions and were excluded from the final analysis. Three patients were imaged

with concern for tumor recurrence on contrast-enhanced MR imaging (meningioma, middle ear neuroendocrine adenoma, and carotid body tumor, respectively), but there was no evidence of SSTR-positive lesions to suggest residual or recurrent tumor. For 1 patient with an indeterminate mass in the left external auditory canal on MR imaging and CT of the temporal bones, SSTR-PET had negative findings, and findings favored cholesterol granuloma or cholesteatoma or, less likely, a low-grade non-SSTR-positive neoplasm. For 1 patient with an orbital mass concerning for optic nerve sheath meningioma versus orbital cavernous venous malformation (cavernous hemangioma), SSTR-PET was negative for the former, and findings favored orbital cavernous venous malformation (Fig 6).

For SSTR-PET/CT vertex-to-thigh imaging, 1 of 17 (6%) studies was positive for metastatic disease (an SSTR-positive lung nodule measuring 1.4 cm, SUVmax = 8.4, in a patient with biopsy confirmation of recurrent papillary thyroid carcinoma), and 8 of 17 (47%) studies were negative. On 8/17 (47%) SSTR-PET vertex-to-thigh studies, there

were indeterminate/incidental findings, including nonavid subcentimeter lung nodules (3 subjects), ground glass lung opacity, adrenal adenoma, indeterminate gallbladder focus, indeterminate adrenal gland focus, a benign breast lesion (SSTR-avid breast lesion, benign on subsequent biopsy), probable benign cervical and axillary lymph nodes, leiomyomatous uterus, enlarged prostate gland with indeterminate focus, and nonspecific cutaneous foci (2 patients).

DISCUSSION

Recent advances and the increased availability of hybrid PET/CT and PET/MRI systems are revolutionizing neuro-oncologic imaging. Specifically, the use of radiolabeled amino acid PET tracers, which bind to specific receptors on tumors, offers improved accuracy in defining the tumor versus background and guiding treatment strategies.²³ Furthermore, several $^{68}\text{Ga}/^{64}\text{Cu}$ -labeled SSAs have recently entered clinical practice, allowing the detection of cell-surface expression of SSTRs, each varying in their short-chain peptide hormone analog and DOTA chelator.^{2,12} DOTA-TATE is a radioconjugate that contains a SSA, TATE, radiolabeled with positron-emitting radionuclides, ^{68}Ga or ^{64}Cu , via a chelating agent, DOTA. SSTR-targeted PET imaging has several advantages over scintigraphy, including improved spatial resolution and accuracy, decreased radiation dose and cost, and increased patient convenience due to the relatively short radiopharmaceutical half-life.² Because SSTR-PET identifies more lesions than structural imaging alone,⁴ it should be considered an integral

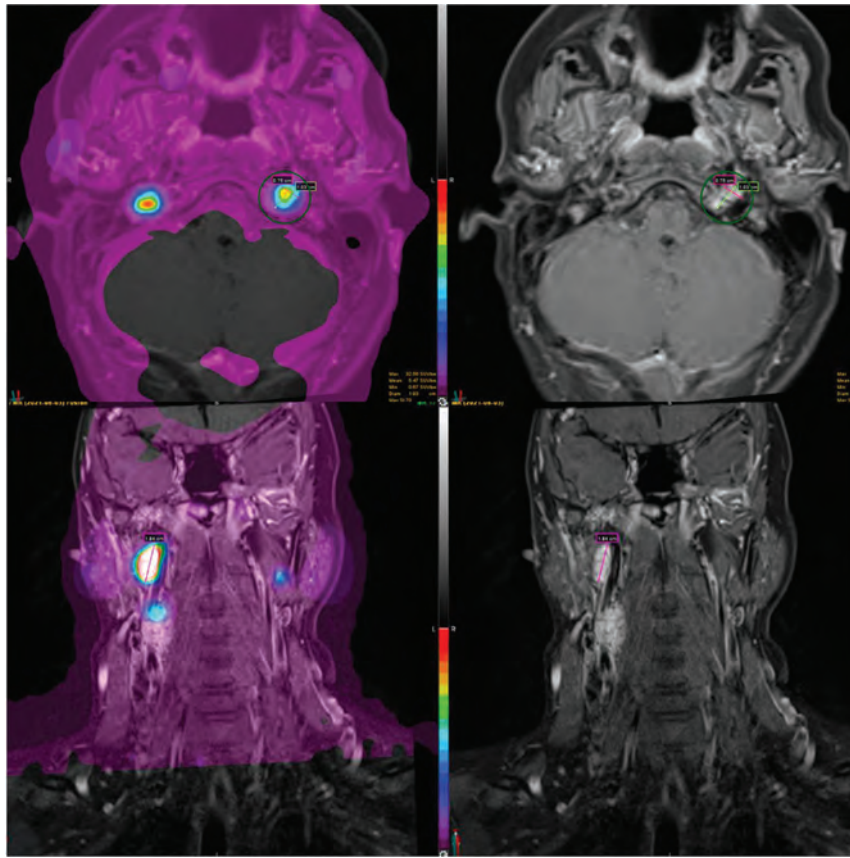


FIG 4. A 31-year-old woman with a vividly enhancing submandibular mass positive for neuroendocrine markers. The patient had SSTR-avid carotid body tumors, a glomus vagale tumor, and glomus jugulare tumors bilaterally. In this example, SSTR-PET/MRI findings were more extensive than on the basis of structural imaging because the right glomus jugulare tumor was not identified on contrast-enhanced MR imaging.

element of clinical management for suspected neuroendocrine tumors in the head and neck. Hybrid PET/MRI allows the systematic addition of high-resolution MR imaging to PET, thereby providing precise and consistent anatomic information, which helps to overcome difficulties in localization inherent to PET and may exclude or identify the presence of multiple pathologies.¹⁹ SSTRs are overexpressed in many tumors of the head and neck, including meningiomas, HNPGLs, middle ear NETs, olfactory neuroblastomas, medullary thyroid carcinoma, and pituitary lesions such as pituitary neuroendocrine tumors (PitNETs, formerly known as pituitary adenomas)²⁴ and pituitary carcinomas.³⁻⁷

Meningiomas are the most common primary intracranial tumors. Approximately 50% of patients may undergo a subtotal tumor resection, which is associated with lower overall survival and lower progression-free survival.²¹ Contrast-enhanced MR imaging of the brain is the current standard of care for the diagnosis and treatment planning of meningiomas; however, it can be limited in the setting of postsurgical or postradiation treatment changes. In addition, MR imaging may be limited if lesions are infiltrative, transosseous, or in the region of the skull base and cavernous sinus.³ SSTR-PET/MRI has demonstrated promise in the assessment of resected and irradiated meningiomas, with improved sensitivity and disease-extent evaluation, particularly in

cases in which MR imaging findings are equivocal.^{3,26} In our series, SSTR-PET/MRI identified additional meningiomas in 4 of 13 (31%) patients imaged for meningioma follow-up. Additionally, 2 new meningiomas were identified by SSTR-PET/MRI in a patient who was imaged for an unrelated head and neck lesion (glomus tympanicum). In 6 of 13 (46%) patients with meningiomas, a greater extent of disease was identified by SSTR-PET/MRI compared with contrast-enhanced MR imaging alone, with SSTR-PET/MRI typically detecting recurrent/transosseous involvement, recurrent/residual tumor at the craniotomy site, and disease at the skull base. In fact, in only 3 of the 13 patients with meningiomas (23%), findings were the same on SSTR-PET/MRI compared with structural imaging. The results of SSTR-PET/MRI helped guide the planning of stereotactic radiation therapy for patients with meningiomas at our institution, as has been described in the literature.²⁵⁻²⁹ In fact, when incorporating SSTR-PET/MRI into radiation treatment-planning of intermediate-risk meningiomas, Mahase et al²⁸ demonstrated a 50% reduction in the dose to several critical structures, with no local recurrences at 6 months. Kim et al²⁵ found a sensitivity as high as 86.1% and a specificity as high as 97.6% when

using different diagnostic SUV thresholds for meningioma diagnosis. An important caveat is that SSTR-negative meningiomas are known to occur; however, they are exceedingly rare.³⁰

The diagnosis of neuroendocrine tumors, including HNPGLs, is challenging because symptoms are highly variable and the tumors are often small. In fact, there is typically a delay of 5–7 years from the first symptoms to diagnosis in these patients.²² SSTR expression can be seen physiologically in a number of organs, including the spleen, adrenal glands, kidneys, pituitary gland, liver, thyroid, and salivary glands.³¹ Because HNPGLs occur in locations that typically do not demonstrate SSTRs, SSTR-PET is optimally positioned to help delineate known lesions and assess additional paragangliomas not identified by structural imaging.^{2,4,31} Janssen et al⁴ found that ⁶⁸Ga DOTATATE PET identified more paragangliomas than other imaging modalities, including [¹⁸F] FDOPA, [¹⁸F] FDG, and [¹⁸F] FDOPA PET/CT, and contrast-enhanced CT or MR imaging. The identification of multiple neuroendocrine tumors can have important implications for genetic testing and hereditary information that can impact not only the patient but also family members, who may undergo screening as a result. In patients with an *SDHx* mutation predisposed to multiple hereditary paragangliomas and pheochromocytomas, guidelines recommend head and neck MRA and SSTR

imaging, in addition to CT of the chest, abdomen, and pelvis.^{32,33} In our study, SSTR-PET/MRI found additional paragangliomas in 2 of 11 subjects with HNPGL (18%), which were not suspected by contrast-enhanced MR imaging of the brain or neck. One of these

patients presented with tongue weakness and fasciculations, with 2 MR imaging studies with negative findings and negative surgical exploration of the left skull base, while the other patient had multiple known cervical paragangliomas, with an additional glomus jugulare detected by SSTR-PET/MRI. Furthermore, in 2 patients imaged for HNPGL assessment, SSTR-PET/MRI identified additional lesions, including 2 meningiomas, a PitNET, and a parathyroid adenoma.

Olfactory neuroblastoma (esthesioneuroblastoma) is a rare sinonasal neuroendocrine tumor thought to originate from the stem cells of the olfactory epithelium.⁵ Although olfactory neuroblastomas have a relatively favorable prognosis, no standardized treatment guidelines have been established. One complicating factor has been their propensity for locoregional recurrence.³⁴ [¹⁸F] FDG-PET is frequently used for tumor staging in patients with advanced disease and evaluating treatment response.³⁵ However, olfactory neuroblastomas also demonstrate high SSTR expression, and the application of SSTR-targeted imaging with histologic correlation was initially demonstrated by Rostomily et al,³⁶ using ¹¹¹In-pentetreotide scintigraphy. Since then, molecular imaging of olfactory neuroblastomas has transitioned to

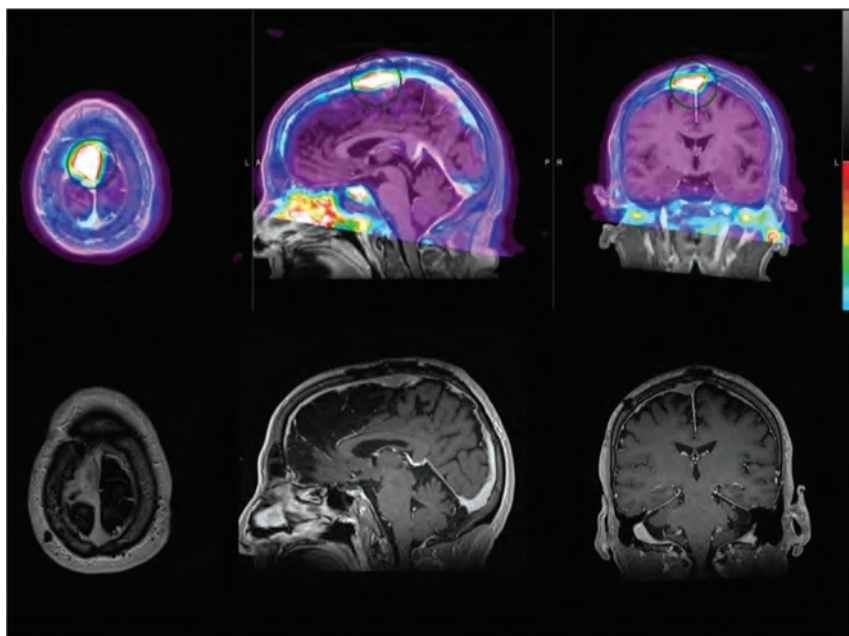


FIG 5. A 69-year-old woman with a SSTR-avid recurrent meningioma in the right frontal parasagittal region and associated invasion of the calvaria and superior sagittal sinus. Incidentally noted is SSTR-positivity in the left temporomandibular joint with prominent articular/periarticular enhancement, suggestive of inflammatory/infectious arthritis. In this example, SSTR-PET/MRI findings are more extensive than on the basis of structural imaging because calvarial invasion was not identified by contrast-enhanced MR imaging of the brain.

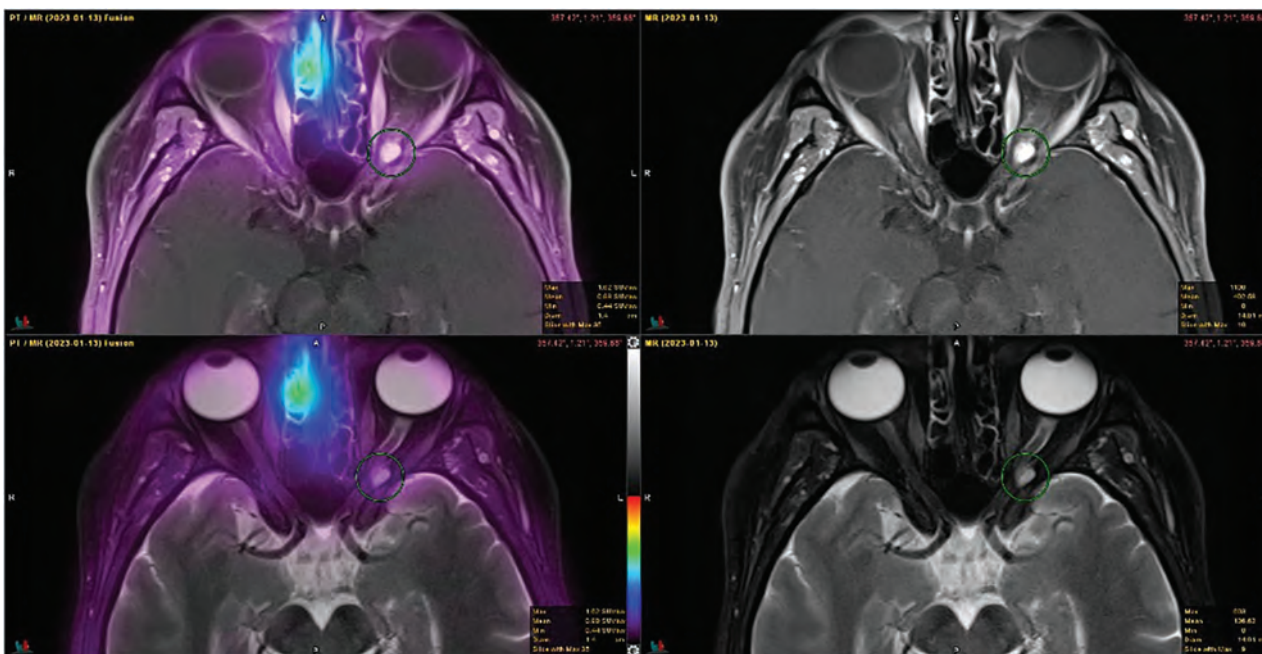


FIG 6. A 52-year-old woman presenting with a visual field disturbance and contrast-enhanced MR imaging demonstrating a left orbital mass concerning for orbital nerve sheath meningioma versus orbital cavernous venous malformation (cavernous hemangioma). Findings of SSTR-PET were negative and represent an orbital cavernous venous malformation. The patient was subsequently referred for surgical management.

PET with ^{68}Ga -/ ^{64}Cu -labeled SSAs. In 1 cohort, Roytman et al⁵ found that DOTATATE-PET/MRI demonstrated utility in evaluating treatment response, identifying metastases and soft-tissue metastatic burden, and distinguishing inflammatory from metastatic adenopathy. The distinction between inflammatory and metastatic adenopathy was particularly useful compared with metabolic [^{18}F] FDG-PET. An important caveat is that low-level SSTR expression may be seen with infection or inflammation, including in the resection cavity in the immediate postoperative setting. In our single case of olfactory neuroblastoma, SSTR-PET/MRI found the same extent of disease as contrast-enhanced MR imaging had; however, it helped to confirm the absence of locoregional metastases, which are found in 10%–44% of patients at the time of diagnosis.³³

Finally, PitNETs are the third most common intracranial neoplasm. Approximately 30% are nonfunctional adenomas, lacking early clinical and biochemical signs.³⁷ Thus, they often present due to symptoms of mass effect once they reach >1 cm (macroadenomas). These lesions are difficult to treat because surgical resection may be incomplete, especially when the cavernous sinus is involved, and adjuvant radiation therapy may be associated with hypopituitarism and neurocognitive impairment.³⁷ Immunohistochemical studies have demonstrated that SSTRs are expressed in a varying proportion of nonfunctional adenomas.^{38–40} In a study of 37 patients with nonfunctional adenomas diagnosed in the context of a clinical trial for lanreotide (SSA) therapy, 34/37 (92%) were positive by ^{68}Ga DOTATATE PET using an SUVmean of >2 cutoff, which may assist in predicting tumor response to SSTR type 2 preferential SSA therapy.⁶ Meanwhile, pituitary carcinomas are rare neoplasms and are associated with a poor prognosis. A case report by Xiao et al⁴¹ suggested that ^{68}Ga DOTATATE-PET was superior to [^{18}F] FDG-PET for lesion assessment, though the affinity of ^{68}Ga DOTATATE compared with [^{18}F] FDG varies depending on the aggressiveness of the tumor.⁷ In addition, ^{68}Ga DOTATATE-PET has demonstrated promise in identifying patients with pituitary carcinomas who are candidates for ^{177}Lu DOTATATE (LUTATHERA; Advanced Accelerator Applications) peptide receptor radionuclide therapy and monitoring treatment response.⁴² In our case of pituitary carcinoma, the patient was treated with a SSA (lanreotide) following resection and prior radiation and systemic chemotherapy. SSTR-PET/MRI identified a greater extent of disease and confirmed progression of disease while the patient was on lanreotide, compared with contrast-enhanced MR imaging alone.

CONCLUSIONS

In our series of head and neck neuroendocrine tumors, SSTR-PET/MRI detected additional lesions and more extensive disease compared with contrast-enhanced MR imaging. While SSTR-PET/MRI is superior to either technique alone,¹⁹ the availability of simultaneous PET/MRI scanners in clinical practice remains limited. In the absence of a dedicated hybrid PET/MRI system, limited SSTR-PET may be fused with separately acquired contrast-enhanced MR imaging of the brain or head and neck using commercially available software, as presented here, thereby enabling PET/MRI assessment in a real-world clinic setting. In addition, vertex-to-thigh imaging showed a low incidence of

metastatic disease, raising the possibility that limited imaging of the head and neck may be sufficient in this patient population. However, in patients with syndromes and/or genetic disorders, a limited head and neck protocol may miss other occult lesions throughout the body. Therefore, the choice of SSTR-PET imaging protocol ultimately depends on a discussion with the referring clinician and careful review of clinical history on a case-by-case basis. In conclusion, SSTR-PET/MRI has the potential to play an important role in presurgical and radiation therapy planning of head and neck neuroendocrine tumors, as well as for monitoring treatment response and evaluating tumor recurrence in these patients.

Disclosure forms provided by the authors are available with the full text and PDF of this article at www.ajnr.org.

REFERENCES

1. Schimmack S, Svejda B, Lawrence B, et al. **The diversity and commonalities of gastroenteropancreatic neuroendocrine tumors.** *Langenbecks Arch Surg* 2011;396:273–98 CrossRef Medline
2. Ivanidze J, Roytman M, Sasson A, et al. **Molecular imaging and therapy of somatostatin receptor positive tumors.** *Clin Imaging* 2019;56:146–54 CrossRef Medline
3. Ivanidze J, Roytman M, Lin E, et al. **Gallium-68 DOTATATE PET in the evaluation of intracranial meningiomas.** *J Neuroimaging* 2019;29:650–56 CrossRef Medline
4. Janssen I, Chen CC, Taieb D, et al. **^{68}Ga -DOTATATE PET/CT in the localization of head and neck paragangliomas compared with other functional imaging modalities and CT/MRI.** *J Nucl Med* 2016;57:186–91 CrossRef Medline
5. Roytman M, Tassler AB, Kacker A, et al. **[^{68}Ga]-DOTATATE PET/CT and PET/MRI in the diagnosis and management of esthesioneuroblastoma: illustrative cases.** *J Neurosurg Case Lessons* 2021;1:CASE2058 CrossRef Medline
6. Boertien TM, Booi J, Majoie CB, et al. **^{68}Ga -DOTATATE PET imaging in clinically non-functioning pituitary macroadenomas.** *Eur J Hybrid Imaging* 2020;4:4 CrossRef Medline
7. Garmes HM, Carvalheira JB, Reis F, et al. **Pituitary carcinoma: a case report and discussion of potential value of combined use of ^{68}Ga -DOTATATE and F-18 FDG PET/CT scan to better choose therapy.** *Surg Neurol Int* 2017;8:162 CrossRef Medline
8. John M, Meyerhof W, Richter D, et al. **Positive somatostatin receptor scintigraphy correlates with the presence of somatostatin receptor subtype 2.** *Gut* 1996;38:33–39 CrossRef Medline
9. Krenning EP, Kwekkeboom DJ, Bakker WH, et al. **Somatostatin receptor scintigraphy with [^{111}In -DTPA-D-Phe1]- and [^{123}I -Tyr3]-octreotide: the Rotterdam experience with more than 1000 patients.** *Eur J Nucl Med* 1993;20:716–31 CrossRef Medline
10. Bombardieri E, Ambrosini V, Aktolun C, et al; Oncology Committee of the EANM. **^{111}In -pentetreotide scintigraphy: procedure guidelines for tumour imaging.** *Eur J Nucl Med Mol Imaging* 2010;37:1441–48 CrossRef Medline
11. Lamberts SW, Bakker WH, Reubi JC, et al. **Somatostatin-receptor imaging in the localization of endocrine tumors.** *N Engl J Med* 1990;323:1246–49 CrossRef Medline
12. Johnbeck CB, Knigge U, Loft A, et al. **Head-to-head comparison of ^{64}Cu -DOTATATE and ^{68}Ga -DOTATOC PET/CT: a prospective study of 59 patients with neuroendocrine tumors.** *J Nucl Med* 2017;58:451–57 CrossRef Medline
13. Hope TA, Bergsland EK, Bozkurt MF, et al. **Appropriate use criteria for somatostatin receptor PET imaging in neuroendocrine tumors.** *J Nucl Med* 2018;59:66–74 CrossRef Medline
14. Hope TA. **Updates to the appropriate-use criteria for somatostatin receptor PET.** *J Nucl Med* 2020;61:1764 CrossRef Medline

15. Hope TA, Allen-Auerbach M, Bodei L, et al. **SNMMI procedure standard/EANM practice guideline for SSTR-PET: imaging neuroendocrine tumors.** *J Nucl Med* 2023;64:204–10 CrossRef Medline
16. Horbinski C, Nabors LB, Portnow J, et al. **NCCN Guidelines Insights: Central Nervous System Cancers, Version 2.2022.** *Natl Compr Canc Netw* 2023;21:12–20 CrossRef Medline
17. Nabors LB, Portnow J, Ahluwalia M, et al. **Central Nervous System Cancers, Version 3.2020, NCCN Clinical Practice Guidelines in Oncology.** *J Natl Compr Canc Netw* 2020;18:1537–70 CrossRef Medline
18. Haddad RI, Bischoff L, Ball D, et al. **Thyroid Carcinoma, Version 2.2022, NCCN Clinical Practice Guidelines in Oncology.** *J Natl Compr Canc Netw* 2022;20:925–51 CrossRef Medline
19. Catana C. **Principles of simultaneous PET/MR imaging.** *Magn Reson Imaging Clin N Am* 2017;25:231–43 CrossRef Medline
20. Mayerhoefer ME, Prosch H, Beer L, et al. **PET/MRI versus PET/CT in oncology: a prospective single-center study of 330 examinations focusing on implications for patient management and cost considerations.** *Eur J Nucl Med Mol Imaging* 2020;47:51–60 CrossRef Medline
21. Rogers L, Barani I, Chamberlain M, et al. **Meningiomas: knowledge base, treatment outcomes, and uncertainties: a RANO review.** *J Neurosurg* 2015;122:4–23 CrossRef Medline
22. Yao JC, Hassan M, Phan A, et al. **One hundred years after “carcinoid”: epidemiology of and prognostic factors for neuroendocrine tumors in 35,825 cases in the United States.** *J Clin Oncol* 2008;26:3063–72 CrossRef Medline
23. Pimlott SL, Sutherland A. **Molecular tracers for the PET and SPECT imaging of disease.** *Chem Soc Rev* 2011;40:149–62 CrossRef Medline
24. Trouillas J, Jaffrain-Rea ML, Vasiljevic A, et al. **How to classify the pituitary neuroendocrine tumors (PitNET)s in 2020.** *Cancers (Basel)* 2020;12:514 CrossRef Medline
25. Kim SH, Roytman M, Madera G, et al. **Evaluating diagnostic accuracy and determining optimal diagnostic thresholds of different approaches to [68Ga]-DOTATATE PET/MRI analysis in patients with meningioma.** *Sci Rep* 2022;12:9256 CrossRef Medline
26. Nyuyki F, Plotkin M, Graf R, et al. **Potential impact of 68Ga-DOTATOC PET/CT on stereotactic radiotherapy planning of meningiomas.** *Eur J Nucl Med Mol Imaging* 2010;37:310–18 CrossRef Medline
27. Prasad RN, Perlow HK, Bovi J, et al. **⁶⁸Ga-DOTATATE PET: the future of meningioma treatment.** *Int J Radiat Oncol Biol Phys* 2022;113:868–71 CrossRef Medline
28. Mahase SS, Roth O'Brien DA, No D, et al. **[⁶⁸Ga]-DOTATATE PET/MRI as an adjunct imaging modality for radiation treatment planning of meningiomas.** *Neurooncol Adv* 2021;3:vdab012 CrossRef Medline
29. Hintz EB, Park DJ, Ma D, et al. **Using 68Ga-DOTATATE PET for postoperative radiosurgery and radiotherapy planning in patients with meningioma: a case series.** *Neurosurgery* 2023;93:95–101 CrossRef Medline
30. Roytman M, Pisapia DJ, Liechty B, et al. **Somatostatin receptor-2 negative meningioma: pathologic correlation and imaging implications.** *Clin Imaging* 2020;66:18–22 CrossRef Medline
31. Shastry M, Kayani I, Wild D, et al. **Distribution pattern of 68Ga-DOTATATE in disease-free patients.** *Nucl Med Commun* 2010;31:1025–32 CrossRef Medline
32. Gimenez-Roqueplo AP, Caumont-Prim A, Houzard C, et al. **Imaging work-up for screening of paraganglioma and pheochromocytoma in SDHx mutation carriers: a multicenter prospective study from the PGL EVA Investigators.** *J Clin Endocrinol Metab* 2013;98:E162–73 CrossRef Medline
33. Ikram A, Paraganglioma RA. **StatPearls.** StatPearls Publishing, 2022. <https://www.ncbi.nlm.nih.gov/books/NBK549834/>. Accessed May 22, 2023
34. Zollinger LV, Wiggins RH, Cornelius RS, et al. **Retropharyngeal lymph node metastasis from esthesioneuroblastoma: a review of the therapeutic and prognostic implications.** *AJNR Am J Neuroradiol* 2008;29:1561–63 CrossRef Medline
35. Dublin AB, Bobinski M. **Imaging characteristics of olfactory neuroblastoma (esthesioneuroblastoma).** *J Neurol Surg B Skull Base* 2016;77:1–5 CrossRef Medline
36. Rostomily RC, Elias M, Deng M, et al. **Clinical utility of somatostatin receptor scintigraphic imaging (octreoscan) in esthesioneuroblastoma: a case study and survey of somatostatin receptor subtype expression.** *Head Neck* 2006;28:305–12 CrossRef Medline
37. Even-Zohar N, Greenman Y. **Management of NFAs: medical treatment.** *Pituitary* 2018;21:168–75 CrossRef Medline
38. Fusco A, Giampietro A, Bianchi A, et al. **Treatment with octreotide LAR in clinically non-functioning pituitary adenoma: results from a case-control study.** *Pituitary* 2012;15:571–78 CrossRef Medline
39. Gabalec F, Drastikova M, Cesak T, et al. **Dopamine 2 and somatostatin 1-5 receptors coexpression in clinically non-functioning pituitary adenomas.** *Physiol Res* 2015;64:369–77 CrossRef Medline
40. Ramirez C, Cheng S, Vargas G, et al. **Expression of Ki-67, PTTG1, FGFR4, and SSTR 2, 3, and 5 in nonfunctioning pituitary adenomas: a high throughput TMA, immunohistochemical study.** *J Clin Endocrinol Metab* 2012;97:1745–51 CrossRef Medline
41. Xiao J, Zhu Z, Zhong D, et al. **Improvement in diagnosis of metastatic pituitary carcinoma by ⁶⁸Ga DOTATATE PET/CT.** *Clin Nucl Med* 2015;40:129–31 CrossRef Medline
42. Novruzov F, Aliyev JA, Jaunmuktane Z, et al. **The use of 68Ga DOTATATE PET/CT for diagnostic assessment and monitoring of 177Lu DOTATATE therapy in pituitary carcinoma.** *Clin Nucl Med* 2015;40:47–49 CrossRef Medline

Glutaric Aciduria Type 1: Comparison between Diffusional Kurtosis Imaging and Conventional MR Imaging

B. Bian, Z. Liu, D. Feng, W. Li, L. Wang, Y. Li, and D. Li



ABSTRACT

BACKGROUND AND PURPOSE: Routine MR imaging has limited use in evaluating the severity of glutaric aciduria type 1. To better understand the mechanisms of brain injury in glutaric aciduria type 1, we explored the value of diffusional kurtosis imaging in detecting microstructural injury of the gray and white matter.

MATERIALS AND METHODS: This study included 17 patients with glutaric aciduria type 1 and 17 healthy controls who underwent conventional MR imaging and diffusional kurtosis imaging. The diffusional kurtosis imaging metrics of the gray and white matter were measured. Then, the MR imaging scores and diffusional kurtosis imaging metrics of all ROIs were further correlated with the morbidity scores and Barry-Albright dystonia scores.

RESULTS: The MR imaging scores showed no significant relation to the morbidity and Barry-Albright dystonia scores. Compared with healthy controls, patients with glutaric aciduria type 1 showed higher kurtosis values in the basal ganglia, corona radiata, centrum semiovale, and temporal lobe ($P < .05$). The DTI metrics of the basal ganglia were higher than those of healthy controls ($P < .05$). The fractional anisotropy value of the temporal lobe and the mean diffusivity values of basal ganglia in glutaric aciduria type 1 were lower than those in the control group ($P < .05$). The diffusional kurtosis imaging metrics of the temporal lobe and basal ganglia were significantly correlated with the Barry-Albright dystonia scores. The mean kurtosis values of the anterior and posterior putamen and Barry-Albright dystonia scores were most relevant ($r = 0.721, 0.730$, respectively). The mean kurtosis values of the basal ganglia had the best diagnostic efficiency with area under the curve values of 0.837 for the temporal lobe, and the mean diffusivity values of the basal ganglia in glutaric aciduria type 1 were lower than those in the control group ($P < .05$). The diffusional kurtosis imaging metrics of the temporal lobe and basal ganglia were significantly correlated with the Barry-Albright dystonia scores. The mean kurtosis values of the anterior and posterior putamen and Barry-Albright dystonia scores were most relevant ($r = 0.721, 0.730$, respectively). The mean kurtosis values of the basal ganglia had the best diagnostic efficiency with area under the curve values of 0.837.

CONCLUSIONS: Diffusional kurtosis imaging provides more comprehensive quantitative information regarding the gray and white matter micropathologic damage in glutaric aciduria type 1 than routine MR imaging scores.

ABBREVIATIONS: AD = axial diffusivity; AK = axial kurtosis; AP = anterior putamen; AUC = under the curve; BAD = Barry-Albright dystonia; CBH = cerebellar hemisphere; CH = caudate head; CR = corona radiata; CS = centrum semiovale; DKI = diffusional kurtosis imaging; DN = bilateral dentate nucleus; FA = fractional anisotropy; FL = frontal lobes; GA-1 = glutaric aciduria type 1; GCDH = glutaryl-CoA dehydrogenase; GP = globus pallidus; HC = healthy control; MD = mean diffusivity; MK = mean kurtosis; P = pons; PL = parietal lobes; PP = posterior putamen; RD = radial diffusivity; RK = radial kurtosis; ROC = receiver operating characteristic curve; SN = substantia nigra; Th = thalamus; TL = temporal lobes

Glutaric aciduria type-1 (GA-1) is a rare autosomal recessive disorder characterized by a deficiency of glutaryl-CoA dehydrogenase (GCDH) activity, often involving the CNS.¹⁻³ Mutations

in the *GCDH* gene encoding the mitochondrial matrix protein GCDH have been found. They result in defective or missing GCDH and lead to abnormal accumulation of organic acids, such as glutaric acid, 3-hydroxy-glutaric acid, and glutarylcarnitine in the blood,

Received March 21, 2023; accepted after revision June 7.

From the Departments of Radiology (B.B., Z.L., D.L.), and Outpatient Pediatrics (D.F.), and Gene Therapy Laboratory (Y.L.), The First Hospital of Jilin University, Changchun, Jilin, China; and State Key Laboratory of Stem Cell and Reproductive Biology (W.L., L.W.), Chinese Academy of Sciences and University, Beijing, China.

This work was supported by the Natural Science Foundation of Jilin Province, YDZJ202101ZYTS019, YDZJ202101ZYTS084 and National Key Research and Development Program, 2019YFA0110800.

Please address correspondence to Dan Li, MD, Department of Radiology, The First Hospital of Jilin University, Changchun, Jilin, China; e-mail: li_d@jlu.edu.cn

Indicates open access to non-subscribers at www.ajnr.org

Indicates article with online supplemental data.

<http://dx.doi.org/10.3174/ajnr.A7928>

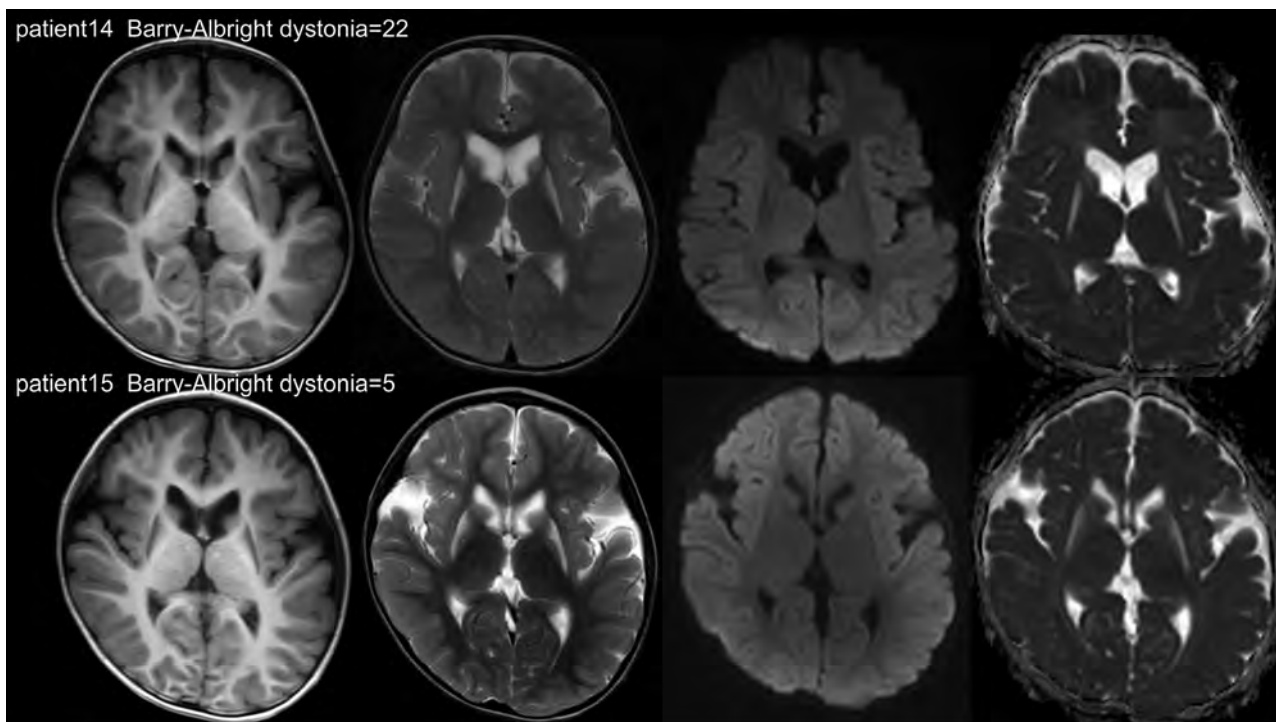


FIG 1. Clinoradiologic contradiction. Both patients showed T2WI prolongation and no diffusion restriction in the putamen, but the BAD scores were very different.

urine, CSF, and brain tissue. Bilateral striatal necrosis was previously pathologically and clinically found in patients with GA-1, resulting in a severe dystonic movement disorder.⁴⁻⁶ The clinical manifestations of patients with GA-1 include an acute encephalopathic crisis precipitated by intercurrent febrile illness, macrocephalus, hypotonia, and choreoathetosis and seizures, and patients usually end with permanent motor and mental disability.

MR imaging findings are an important tool for the diagnosis of GA-1, which include characteristic cyst-like bilateral enlargement of the Sylvian fissures, signal abnormalities, and atrophy of the supratentorial WM and the deep GM structures.⁷⁻⁹ However, we found a clinoradiologic contradiction in conventional brain MR imaging results. Specifically, we established that patients with GA-1 may have outcomes of dystonia deterioration that are quite different, even if similar abnormal signals of the striatum have been obtained (Fig 1). In addition, Mohammad et al,⁸ Sadek et al,⁹ and Garbade et al¹⁰ came to different conclusions judging by routine MR imaging–detected abnormalities, revealing the association between clinical and imaging features. Therefore, conventional imaging examinations are insufficient to accurately assess brain damage in patients with GA-1.

On the basis of a Gaussian distribution model, DTI is used to quantitatively assess the damage to brain tissue. This approach can be widely applied to detect CNS metabolic disease changes, such as those of leukoencephalopathy with brainstem and spinal cord involvement and high lactate, metachromatic leukodystrophy, phenylketonuria, and Krabbe disease.¹¹⁻¹⁴ However, the displacement of water molecules is restricted by barriers, including cell membranes and organelles—that is, the movement of water molecules in the human body does not follow the Gaussian distribution. Hence, studies on biologic structures by DTI may be

inappropriate.¹⁵ Diffusional kurtosis imaging (DKI) quantifies non-Gaussian diffusion of water in biologic systems and has been suggested to be advantageous over DTI; it better characterizes both normal and pathologic brain tissue and is particularly valuable for the assessment of GM.¹⁵ The kurtosis reveals the degree of water diffusion restriction and brain tissue microstructural complexity.

To date, no studies have used DKI for the assessment of patients with GA-1. In this investigation, we used DKI to detect GM and WM microstructural changes in 17 patients with GA-1. We aimed to elucidate whether DKI parameters could be sufficiently sensitive to detect micropathologic changes in similar abnormal signal areas and whether they could be of value for severity evaluation.

MATERIALS AND METHODS

Subjects

This prospective study was performed in accordance with the Declaration of Helsinki for studies involving humans and after approval of the First Hospital of Jilin University internal review board (20K060-001) and the parents of the patients. The diagnosis of GA-1 was established by brain MR imaging and biochemical (urine organic acids and plasma acylcarnitines) and *GCDH* gene mutation analyses.¹⁶ A group of 17 healthy controls (HCs) of similar age and sex were enrolled by community recruitment. All healthy subjects had no history of neurologic or psychiatric disorders and had normal MR imaging findings. The patients with GA-1 and HCs did not differ in either age or sex ($P > .9$ in both instances) (Table). Written informed consent was obtained from parents or authorized legal representatives of all children who participated in the study. After diagnosis, metabolic

Demographic characteristics of patients with GA-1 and healthy controls

Variable	GA-1 (n = 17)		HCs (n = 17)	
	Mean	Range	Mean	Range
Age (mo)	38 (SD, 17)	11–84	38 (SD, 17)	11–84
Sex (M/F)	6/11	–	6/11	–
BAD scores	14 (SD, 5)	4–22	0	0
Morbidity scores	2 (SD, 0.5)	1–3	0	0
Urinary glutaric acid ($\mu\text{mol}/\text{mol}$) ^a	617 (SD, 725)	16.2–2937.62	–	–
Blood C5DC ($\mu\text{mol}/\text{mol}$)	4 (SD, 8)	0.19–38.07	–	–

Note:—C5DC indicates glutarylcarnitine; BAD, barry-albright dystonia; en dash, not applicable.

^aClassified as high (urinary glutaric acid >100 mmol/mol) or low (<100 mmol/mol).

treatment was started in all patients with GA-1, including a lysine-free, low-lysine diet; a tryptophan-reduced amino acid formula; and other therapies for treating neurologic manifestations according to relevant guidelines.¹⁶

MR Imaging

All patients were scanned using a 3T MR imaging system with a 32-channel head coil (Ingenia Elition X; Philips Healthcare). The sequences and parameters were as follows:

- 3D-T1WI: TR/TE = 6.6/3.0 ms, FOV = 240 × 240 × 170 mm, matrix = 240 × 240, in-plane resolution = 1 × 1 mm, section thickness = 1 mm, imaging time = 8 minutes 21 seconds.
- T2WI: TR/TE = 3600/1200 ms, FOV = 230 × 230 × 134 mm, matrix = 288 × 288, section thickness = 5 mm, imaging time = 1 minute 12 seconds.
- FLAIR: TR/TE = 9000/143 ms, FOV = 230 × 230 × 125 mm, matrix = 256 × 256, section thickness = 5 mm, imaging time = 2 minutes 42 seconds.
- DWI: single-shot echo-planar sequence. TR/TE = 2084/72 ms, FOV = 230 × 230 × 125 mm, matrix = 152 × 126, section thickness = 2.5 mm, imaging time = 0 minutes 25 seconds. A b-value of 1000 s/mm² was chosen.
- DKI: echo-planar imaging diffusion sequence with a total number of 55 diffusion-encoding directions. TR/TE = 4128/80 ms, FOV = 220 × 220 × 130 mm, matrix = 88 × 86, section thickness = 2.5 mm with a 1-mm gap, imaging time = 4 minutes 37 seconds. There were 3 b-values of 0, 1000, and 2000 s/mm².

Clinical and Neurologic Outcome and Neuroimaging Evaluation

Patients underwent a thorough history-taking, clinical examination, and neurologic-outcome assessment, management, and treatment. All patients with GA-1 and HCs were evaluated using the morbidity scores and Barry-Albright dystonia (BAD) scores.^{9,10,17} Morbidity score items included loss of mobility, feeding problems, respiratory problems, and seizures necessitating treatment. A point was given for the presence of each item, with a total morbidity score ranging from 0 (asymptomatic) to 4 (severe morbidity). Dystonia severity was quantified using the BAD score, which is a 5-point, criterion-based, ordinal scale designed to assess dystonia in 8 body regions: eyes, mouth, neck, trunk, and the 4 extremities. Raters scored dystonia as none (0), slight (1), mild (2), moderate (3), and severe (4).

Conventional MR Imaging Scores

In the study, MR imaging scores were analyzed on the basis of a previously described pattern-recognition approach of assessing GA-1.⁸⁻¹⁰ All routine MR images of patients with GA-1 were independently reviewed and scored by authors B.B. and D.L., who have 10 and 21 years of experience with neuroimaging, respectively. In addition, 2 reviewers were blinded to the clinical and biochemical examinations of patients. The cortex was scored as follows: 0 = unaffected, 1 = temporal atrophy, and 2 = frontotemporal atrophy. Each putamen, caudate, globus pallidus, thalamus, dentate, hippocampus, and cerebellum was rated as follows: 0 = unaffected, 1 = T2 hyperintensity, and 2 = atrophy. Each of the ventricles and external CSF spaces was rated as follows: 0 = unaffected, 1 = mildly/moderately dilated, and 2 = markedly dilated. Other scored abnormalities were of the WM (0 = unaffected, 1 = localized T2 hyperintensity, 2 = generalized/diffuse hyperintensity) and the subdural hematoma/hygroma (0 = none, 1 = unilateral, 2 = bilateral).

DKI Analysis

DKI data of all patients were exported from the workstation and converted to the NifTI data format by MRICron (<https://www.nitrc.org/projects/mricron/>). The NifTI data were imported into the free software Diffusional Kurtosis Estimator (<http://www.nitrc.org/projects/dke>) for spatial smoothing, median filtering, linear trend removal, and denoise processing.¹⁸

Seven DKI metrics were extracted (Fig 2): mean kurtosis (MK), radial kurtosis (RK), axial kurtosis (AK), fractional anisotropy (FA), axial diffusivity (AD), radial diffusivity (RD), and mean diffusivity (MD). The metrics values were measured in the brain regions: bilateral dentate nucleus (DN), cerebellar hemisphere (CBH), pons (P), substantia nigra (SN), globus pallidus (GP), anterior putamen (AP), posterior putamen (PP), caudate head (CH), thalamus (Th), corona radiata (CR), centrum semiovale (CS), frontal lobes (FL), parietal lobes (PL), and temporal lobes (TL). The ROI (32 mm²: cerebellar hemisphere, pons, thalamus, and 16 mm²: other brain regions) method was applied in all subjects by a radiologist who had 10 years of experience in neuroimaging. All brain regions were measured 3 times bilaterally, and an average size was calculated to minimize the error value.

Statistical Analysis

All statistical tests were performed using SPSS 22.0 statistical software (IBM). For DKI parameters in the ROIs, quantitative results are expressed as mean (SD). All data were tested for normality and variance homogeneity before analyses. A comparison between the patients with GA-1 and the control group of the same brain region was performed by *t* test for 2 independent samples to evaluate the

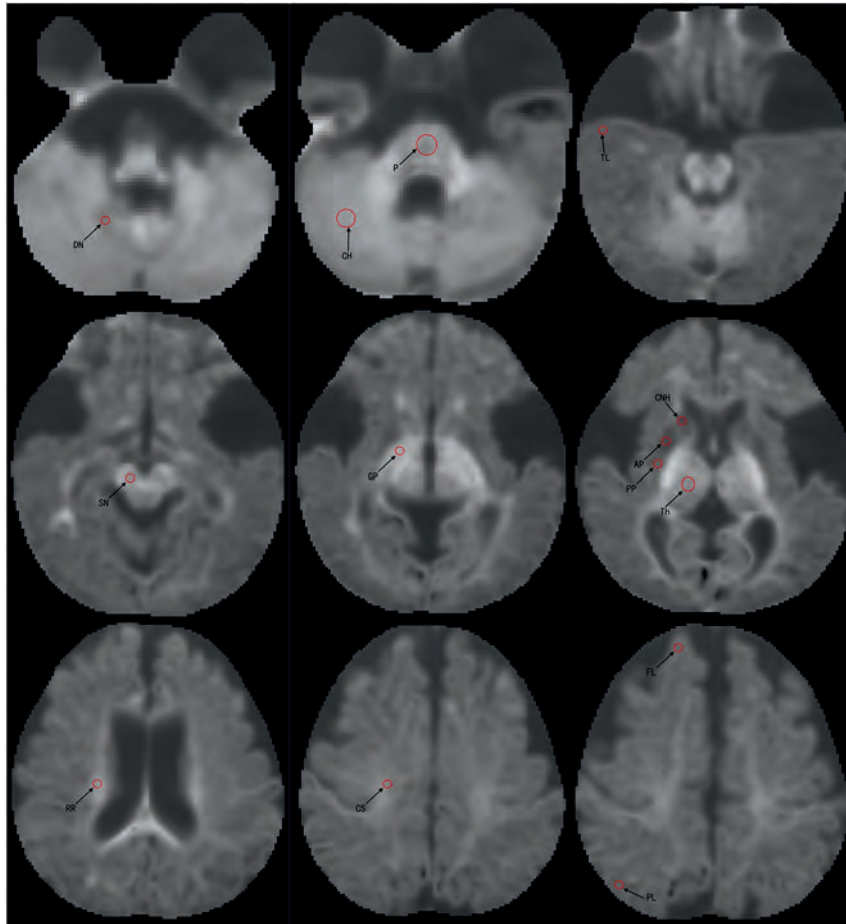


FIG 2. Example of the selection of ROIs (red circle) from the DN, CBH, P, SN, GP, AP, PP, CH, Th, CR, CS, FL, PL, and TL of patients with GA-1. Radiologists manually drew the ROIs (16 mm² and 32 mm²) on the gray level of the MK map.

DKI parameters. A P value $< .05$ was considered to indicate a statistically significant difference. Qualitative data were expressed as frequency and percentage. A dichotomized design was applied for routine MR imaging findings, with interobserver reliability expressed as a Fleiss κ . The correlations between MR imaging and morbidity scores or BAD scores were tested statistically using the Mann-Whitney U statistic or the Kruskal-Wallis test.^{9,10} The Pearson or Spearman correlation analysis was used to test the relationships between DKI parameters and morbidity scores or BAD scores. Receiver operating characteristic curve (ROC) analysis was used to evaluate the diagnostic performance of different brain region parameters with the strongest correlations. An area under the curve (AUC) of >0.5 indicated a significant diagnostic value, and an AUC value closer to 1 was indicative of a better diagnostic value.

RESULTS

Study Population

We included 17 patients (11 female, 6 male) with confirmed GA-1 and complete information, including MR imaging findings and neurologic outcomes. A summary of demographic, clinical, and laboratory features, and MR imaging scores of patients with GA-1 is presented in the Online Supplemental Data. The mean age at MR imaging was 38.4 (SD, 17) months; median, 35 months; range,

11–84 months for all patients. Four (23.5%) patients with GA-1 had insidious onset, and 9 (52.9%) manifested acute onset, whereas 4 (23.5%) were asymptomatic. All patients had hypokinesia and dystonia, and one (5.8%) had a seizure during the MR imaging.

Conventional MR Imaging Abnormalities and Association of MR Imaging Scores with the Morbidity and Barry-Albright Dystonia Scores

The MR imaging abnormalities of 17 patients with GA-1 are given in the Online Supplemental Data. 100% of the patients with GA-1 had expansion of the CSF anterior to the temporal lobes and widening of the Sylvian fissures, though the degrees of expansion were not always symmetric. Ventricle dilation was present in 94% of the examined patients ($n = 16$). None of the patients had subdural hematoma/hygroma. WM changes were present in 88% of the patients ($n = 15$). In the GM, the striatum had a high signal or atrophy on T2WI. The most frequently occurring abnormalities (100%) were of the putamen and the globus pallidus. The abnormalities of the caudate head, thalamus, dentate, hippocampus, and cerebellum were 59%, 18%, 47%, 23%, and 0, respectively. Six patients (35%) had hyperintensities in the corpus callosum. The central tegmental tract had restricted diffusion and low ADC in 4 patients (23%). The values of the

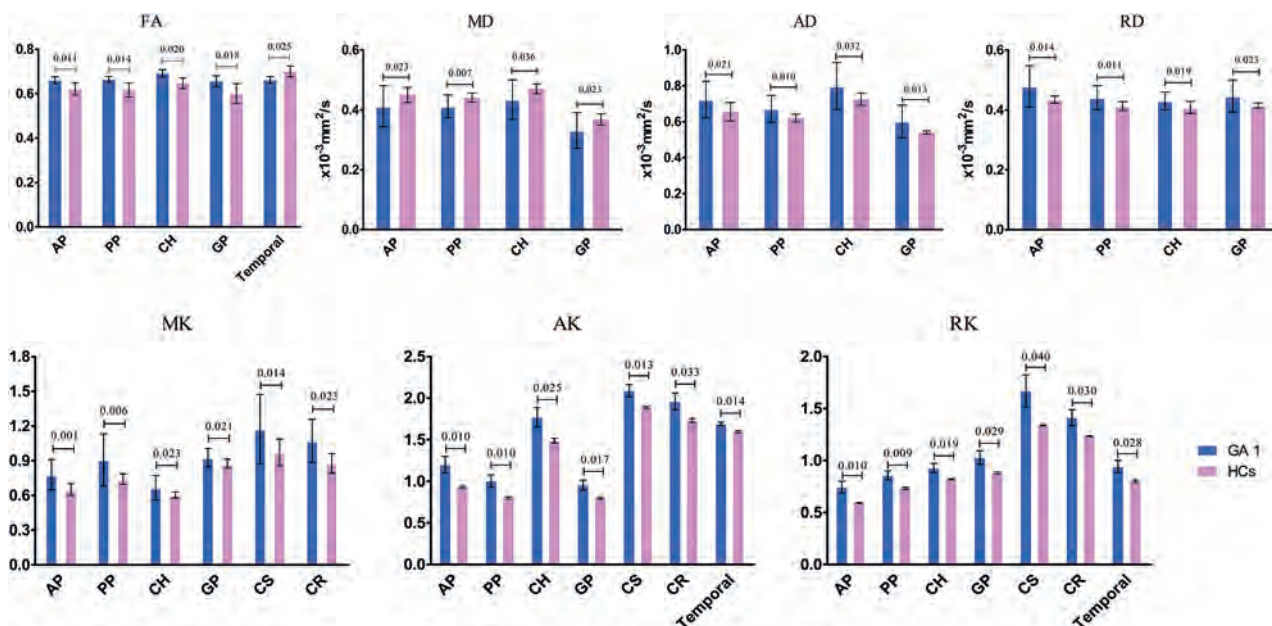


FIG 3. DKI values of ROI bar graphs in predefined ROIs with differences ($P < .05$) in the patients with GA-1 and healthy groups.

associations of the MR imaging scores with the morbidity and BAD scores are given in the Online Supplemental Data. All brain regions showed no relation to the morbidity and BAD scores.

Comparison of the Brain Region DKI Metrics in Patients with GA-1 and Healthy Subjects

The kurtosis metrics (MK, AK, and RK values) and FA, AD, and RD values of the AP, PP, CH, and GP of the GA-1 group were significantly higher than those of the corresponding brain region in the control group ($P < .05$). The MD values of the AP, PP, CH, and GP in the GA-1 group were significantly lower than those in the control group ($P < .05$). The MK, AK, and RK values of the CS and the CR in the GA-1 group were significantly higher than those in the control group ($P < .05$). The RD, AD, AK, and RK values of the TL in the GA-1 group were higher, whereas the FA values were lower than those in the control group ($P < .05$) (Fig 3). No significant difference was observed in the DKI parameters of other ROI between the 2 groups.

Correlation between DKI Metrics and BAD Scores and Morbidity Scores

The data of the association of the DKI parameters of different ROIs with the BAD scores and morbidity scores are provided in the Online Supplemental Data. The results (Fig 4) show a negative correlation in the FA of the TL, MK, AK, and RK of the AP and PP; MK and AK of the GP; and MK of the CH, with significant differences (all, $P < .05$). In addition, there was a significant positive association of the AD values of the TL ($r = 0.596$, $P = .012$) and the MD values of the PP ($r = 0.548$, $P = .023$) with the BAD scores.

ROC Analyses for Diagnostic Performances

The values of MK in the AP, PP, CH and GP, as well as RK in the AP distinguished the patients with GA-1 ($AUC > 0.5$, $P < .05$),

among which the MK of the AP had the highest AUC (0.837), whereas the MK of the GP had the lowest AUC (0.723) (Fig 5).

DISCUSSION

In patients with GA-1, acute striatal necrosis during infancy is the principal cause of morbidity and mortality, which leads to chronic oromotor, skeletal, and respiratory complications of dystonia.⁵ A previous study revealed that routine MR imaging abnormalities may regress, be stable for years, or progress.⁸ In our investigation, 17 patients with GA-1 manifested characteristic and region-specific brain MR imaging abnormalities (Online Supplemental Data), but no brain structure abnormality appeared to correlate with the morbidity and BAD scores (Table, all $P > .05$), a finding inconsistent with the results of a previous study in which striatal necrosis was identified by routine MR imaging as the most reliable predictor of a movement disorder,⁸ which may be related to the small sample size used in our research. In addition, Strauss et al found that older GA-1 patients with significant T2 or FLAIR hypersignal and intact basal ganglia could have normal motor function and neurocognitive performance, which also indicates that conventional MR has disadvantages in precisely assessing GA-1 patients' motor impairment.¹⁹

To better understand the mechanisms of gray/white matter damage, we first prospectively investigated the changes of the DKI parameters in 17 patients with GA-1. In many CNS diseases,²⁰⁻²² such as multiple sclerosis and Parkinson disease, DKI metrics have become an important biomarker for the detection of anisotropic and isotropic diffusion.²³ DKI provides not only the diffusion tensor metrics (FA, MD, AD, and RD) but also the kurtosis metrics (AK, RK, and MK).^{15,23} Furthermore, kurtosis reveals the degree of diffusion restriction and tissue microstructural complexity. A change in the MK value depends on the structural complexity of the ROIs, and an increase of the MK value is due to increased cell-packing density and microstructural complexity.^{18,22} AK and RK are of value for providing additional

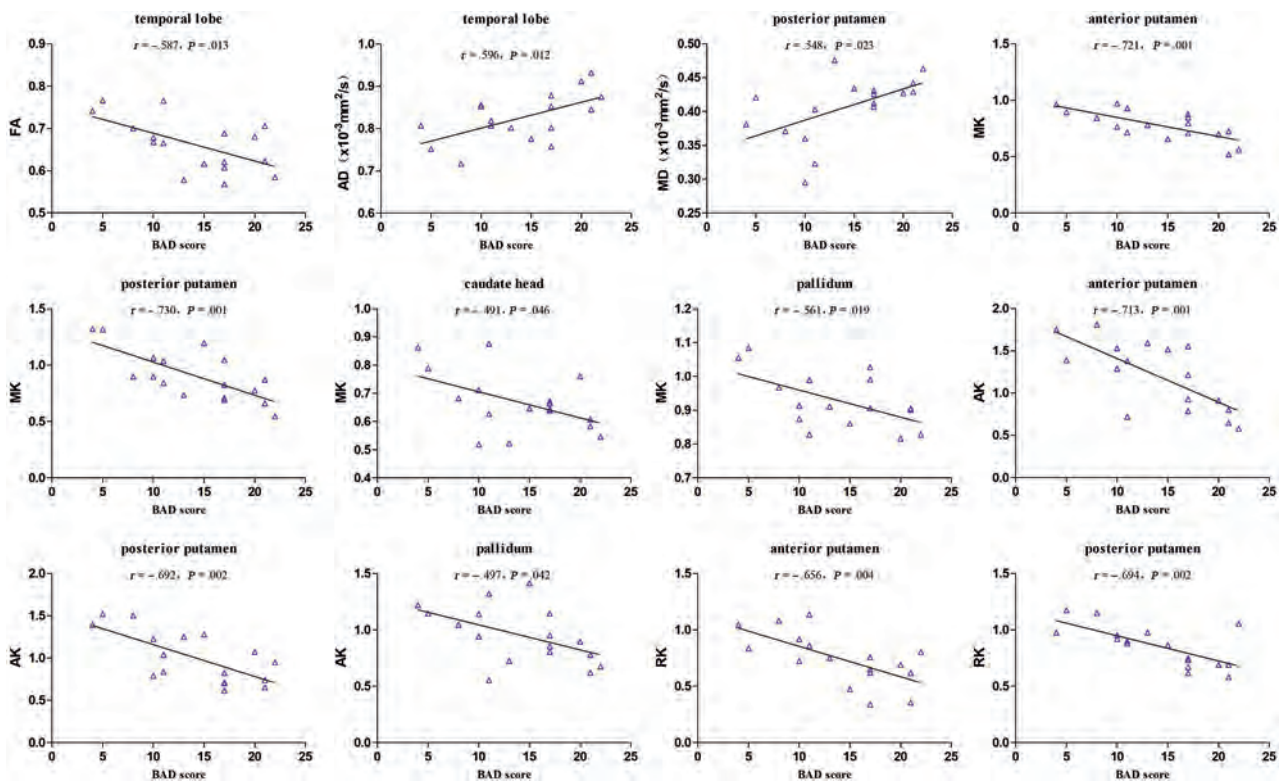


FIG 4. The association analyses with maximal correlation coefficients between the DKI metrics (FA, MD, MK, AK, and RK values) and the BAD scores.

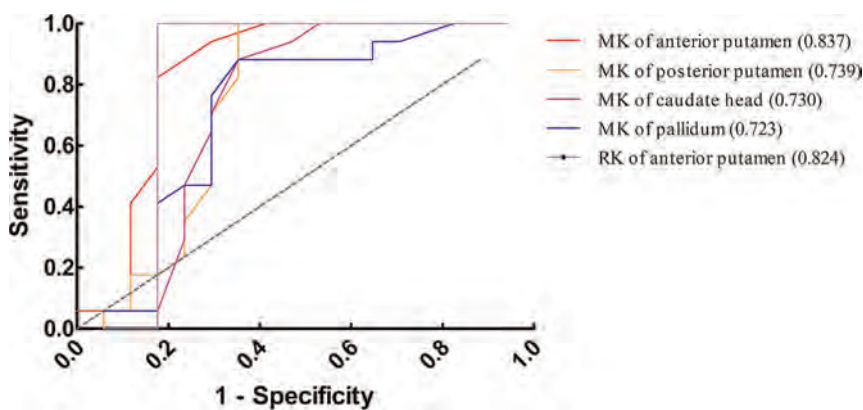


FIG 5. ROC curve analyses (AP, PP, CH and GP) were performed for the diagnosis of GA-1 to assess the diagnostic performance in the brain structures of the DKI parameters with the strongest correlation. The AUCs of different parameters were compared.

information of the axonal and myelin integrity of the WM bundles. The decrease in RK is associated with demyelination, whereas a change in AK reflects axonal degeneration. Additionally, increases in RD and AD are linked to myelin degeneration and axonal degeneration, respectively.²⁴

GA-1 animal model studies show that the pathologic mechanism of brain injury is realized via cytotoxic edema, bilateral striatal neurodegeneration, neuronal swelling, and vacuole formation leading to cerebral capillary occlusion.^{5,25} Thus, the extracellular tortuosity, decreased membrane permeability, and cell swelling during cytotoxic edema in specific brain regions of patients with GA-1 are

reflected by an increase in kurtosis metrics and FA. We found that the increase in MK, AK, and RK of the putamen, caudate head, and pallidum (Fig 3) could be related to cell swelling, ischemic state, and an increase in the volume fraction of limited water diffusion. The cytotoxic edema reduced the extracellular volume and restriction in water motion, which gave rise to a decrease in the MD value. In addition, the changes in MK, AK, and RK of the centrum semiovale and corona radiata revealed that water diffusion may be limited in the fiber structure and may be affected by the cytotoxic effect of glutaric acid, which may indicate that in patients with GA-1, kurtosis metrics are more sensitive to the damage of the WM bundles than DTI metrics (FA, MD, AD, and RD). The kurtosis value is able to reflect the changes in microstructure in both WM and GM.²⁶ Temporal lobe atrophy is a common MR imaging manifestation, but the mechanism of its neuron damage is not fully understood.⁷ In this study, RD, AD, AK, and RK of the temporal lobe were higher than those in the control group, indicating that the changes might be associated with the alterations of the glutaric acid level.

In our study, the significant correlation between the BAD score and DKI metrics, including the MK, AK, and RK in the putamen, caudate head, and pallidum, supported the hypothesis that striatum microstructural changes may contribute to a permanent motor

decline and dystonia (Fig 4). The anterior putamen MK values had the strongest correlations with the BAD scores compared with the FA, MD, AD, AK, and RK values. Thus, kurtosis metrics can serve as a sensitive imaging biomarker in detecting striatum pathology in patients with GA-1. Our results indicate that DKI enables the timely detection of changes in the brain tissue microstructure of patients with GA-1, which is more beneficial for the assessment of the disease severity compared with routine brain MR imaging scores. By comparing the diagnostic efficiency of DKI parameters, we found that the MK and RK of the anterior putamen (AUC = 0.837 and 0.824, respectively) in patients with GA-1 had a higher sensitivity for dystonia assessment than other parameters.

Our study has some limitations. First, the small sample size may have influenced the results. Second, the DKI metrics were measured on the basis of ROIs manually placed in various regions, which might have yielded imperfect reference values and thus bias. In addition, the ROI-based approach was focused on a limited number of spatially-defined regions within the brain, such as in the large WM tracts (eg, the corpus callosum). Third, more time points and longer time spans are required to better investigate the changes of the gray/white matter across time. Fourth, this was not a multicenter study; thus, its results may not be generalizable.

CONCLUSIONS

To our knowledge, this is the first DKI study of GA-1. Using DKI, we compared the magnitude and direction of diffusion in patients with GA-1 with abnormalities in different brain areas to gain insight into the microstructure of the affected brain tissue. The kurtosis values could serve as a surrogate biomarker for assessment of putaminal damage and reflect dyskinesia, which is correlated with prognosis. In the future, longitudinal studies with larger samples and a greater age span are needed to understand the MR imaging markers of GA-1.

Disclosure forms provided by the authors are available with the full text and PDF of this article at www.ajnr.org.

REFERENCES

- Hedlund GL, Longo N, Pasquali M. **Glutaric acidemia type 1.** *Am J Med Genet C Semin Med Genet* 2006;142C:86–94 CrossRef Medline
- Fu Z, Wang M, Paschke R, et al. **Crystal structures of human glutaryl-CoA dehydrogenase with and without an alternate substrate: structural bases of dehydrogenation and decarboxylation reactions.** *Biochemistry* 2004;43:9674–84 CrossRef Medline
- Schmiesing J, Lohmoller B, Schweizer M, et al. **Disease-causing mutations affecting surface residues of mitochondrial glutaryl-CoA dehydrogenase impair stability, heteromeric complex formation and mitochondria architecture.** *Hum Mol Genet* 2017;26:538–51 CrossRef Medline
- Funk CB, Prasad AN, Frosk P, et al. **Neuropathological, biochemical and molecular findings in a glutaric acidemia type 1 cohort.** *Brain* 2005;128:711–22 CrossRef Medline
- Zinnanti WJ, Lazovic J, Housman C, et al. **Mechanism of metabolic stroke and spontaneous cerebral hemorrhage in glutaric aciduria type I.** *Acta Neuropathol Commun* 2014;2:13 CrossRef Medline
- Boy N, Garbade SF, Heringer J, et al. **Patterns, evolution, and severity of striatal injury in insidious- vs acute-onset glutaric aciduria type I.** *J Inher Metab Dis* 2019;42:117–27 CrossRef Medline
- Ntorkou AA, Daire J, Renaldo F, et al. **Enlargement of the optic chiasm: a novel imaging finding in glutaric aciduria type I.** *AJNR Am J Neuroradiol* 2021;42:1722–26 CrossRef Medline

- Mohammad SA, Abdelkhalik HS, Ahmed KA, et al. **Glutaric aciduria type 1: neuroimaging features with clinical correlation.** *Pediatr Radiol* 2015;45:1696–705 CrossRef Medline
- Sadek AA, Aladawy MA, Magdy RM, et al. **Clinico-radiological correlation in 26 Egyptian children with glutaric acidemia type 1.** *Neuropediatrics* 2021;52:431–40 CrossRef Medline
- Garbade SF, Greenberg CR, Demirkol M, et al. **Unravelling the complex MRI pattern in glutaric aciduria type I using statistical models—a cohort study in 180 patients.** *J Inher Metab Dis* 2014;37:763–73 CrossRef Medline
- Steenweg ME, Pouwels PJ, Wolf NI, et al. **Leucoencephalopathy with brainstem and spinal cord involvement and high lactate: quantitative magnetic resonance imaging.** *Brain* 2011;134:3333–41 CrossRef Medline
- van Rappard DF, Konigs M, Steenweg ME, et al. **Diffusion tensor imaging in metachromatic leukodystrophy.** *J Neurol* 2018;265:659–68 CrossRef Medline
- Clocksins HE, Hawks ZW, White DA, et al. **Inter- and intra-tract analysis of white matter abnormalities in individuals with early-treated phenylketonuria (PKU).** *Mol Genet Metab* 2021;132:11–18 CrossRef Medline
- Guo AC, Petrella JR, Kurtzberg J, et al. **Evaluation of white matter anisotropy in Krabbe disease with diffusion tensor MR imaging: initial experience.** *Radiology* 2001;218:809–15 CrossRef Medline
- Jensen JH, Helpert JA. **MRI quantification of non-Gaussian water diffusion by kurtosis analysis.** *NMR Biomed* 2010;23:698–710 CrossRef Medline
- Boy N, Muhlhausen C, Maier EM, et al. **Additional individual contributors. Proposed recommendations for diagnosing and managing individuals with glutaric aciduria type I: second revision.** *J Inher Metab Dis* 2017;40:75–101 CrossRef Medline
- Barry MJ, VanSwearingen JM, Albright AL. **Reliability and responsiveness of the Barry-Albright Dystonia Scale.** *Dev Med Child Neurol* 1999;41:404–11 CrossRef Medline
- Qiao PG, Cheng X, Li GJ, et al. **MR diffusional kurtosis imaging-based assessment of brain microstructural changes in patients with Moyamoya disease before and after revascularization.** *AJNR Am J Neuroradiol* 2020;41:246–54 CrossRef Medline
- Strauss KA, Lazovic J, Wintermark M, et al. **Multimodal imaging of striatal degeneration in Amish patients with glutaryl-CoA dehydrogenase deficiency.** *Brain* 2007;130:1905–20 CrossRef Medline
- Guglielmetti C, Veraart J, Roelant E, et al. **Diffusion kurtosis imaging probes cortical alterations and white matter pathology following cuprizone induced demyelination and spontaneous remyelination.** *Neuroimage* 2016;125:363–77 CrossRef Medline
- Tan S, Hartono S, Welton T, et al. **Utility of quantitative susceptibility mapping and diffusion kurtosis imaging in the diagnosis of early Parkinson's disease.** *Neuroimage Clin* 2021;32:102831 CrossRef Medline
- Spampinato MV, Chan C, Jensen JH, et al. **Diffusional kurtosis imaging and motor outcome in acute ischemic stroke.** *AJNR Am J Neuroradiol* 2017;38:1328–34 CrossRef Medline
- Marralle M, Collura G, Brai M, et al. **Physics, techniques and review of neuroradiological applications of diffusion kurtosis imaging (DKI).** *Clin Neuroradiol* 2016;26:391–403 CrossRef Medline
- Helpert JA, Adisetiyo V, Falangola MF, et al. **Preliminary evidence of altered gray and white matter microstructural development in the frontal lobe of adolescents with attention-deficit hyperactivity disorder: a diffusional kurtosis imaging study.** *J Magn Reson Imaging* 2011;33:17–23 CrossRef Medline
- Isasi E, Korte N, Abudara V, et al. **Glutaric acid affects pericyte contractility and migration: possible implications for GA-I pathogenesis.** *Mol Neurobiol* 2019;56:7694–707 CrossRef Medline
- Hori M, Fukunaga I, Masutani Y, et al. **Visualizing non-Gaussian diffusion: clinical application of q-space imaging and diffusional kurtosis imaging of the brain and spine.** *Magn Reson Med* 2012;11:221–33 CrossRef Medline

Epileptogenic Tubers Are Associated with Increased Kurtosis of Susceptibility Values: A Combined Quantitative Susceptibility Mapping and Stereoelectroencephalography Pilot Study

A. Chari, J. Sedlacik, K. Seunarine, R.J. Piper, P. Hales, K. Shmueli, K. Mankad, U. Löbel, C. Eltze, F. Moeller, R.C. Scott, M.M. Tisdall, J.H. Cross, and D.W. Carmichael



ABSTRACT

BACKGROUND AND PURPOSE: Prior studies have found an association between calcification and the epileptogenicity of tubers in tuberous sclerosis complex. Quantitative susceptibility mapping is a novel tool sensitive to magnetic susceptibility alterations due to tissue calcification. We assessed the utility of quantitative susceptibility mapping in identifying putative epileptogenic tubers in tuberous sclerosis complex using stereoelectroencephalography data as ground truth.

MATERIALS AND METHODS: We studied patients with tuberous sclerosis complex undergoing stereoelectroencephalography at a single center who had multiecho gradient-echo sequences available. Quantitative susceptibility mapping and $R2^*$ values were extracted for all tubers on the basis of manually drawn 3D ROIs using T1- and T2-FLAIR sequences. Characteristics of quantitative susceptibility mapping and $R2^*$ distributions from implanted tubers were compared using binary logistic generalized estimating equation models designed to identify ictal (involved in seizure onset) and interictal (persistent interictal epileptiform activity) tubers. These models were then applied to the unimplanted tubers to identify potential ictal and interictal tubers that were not sampled by stereoelectroencephalography.

RESULTS: A total of 146 tubers were identified in 10 patients, 76 of which were sampled using stereoelectroencephalography. Increased kurtosis of the tuber quantitative susceptibility mapping values was associated with epileptogenicity ($P = .04$ for the ictal group and $P = .005$ for the interictal group) by the generalized estimating equation model. Both groups had poor sensitivity (35.0% and 44.1%, respectively) but high specificity (94.6% and 78.6%, respectively).

CONCLUSIONS: Our finding of increased kurtosis of quantitative susceptibility mapping values (heavy-tailed distribution) was highly specific, suggesting that it may be a useful biomarker to identify putative epileptogenic tubers in tuberous sclerosis complex. This finding motivates the investigation of underlying tuber mineralization and other properties driving kurtosis changes in quantitative susceptibility mapping values.

ABBREVIATIONS: DRE = drug-resistant epilepsy; GEE = generalized estimating equation; QSM = quantitative susceptibility mapping; SEEG = stereoelectroencephalography; TSC = tuberous sclerosis complex

Tuberous sclerosis complex (TSC) is a genetic disorder often associated with difficult-to-treat drug-resistant epilepsy

(DRE).¹ While some studies report favorable outcomes following resective epilepsy surgery to treat TSC-associated DRE, others report that only about 50% become seizure-free following resective surgery, especially in complex cases with no clear dominant tuber.²⁻⁶ There is an increasing practice of using stereoelectroencephalography (SEEG) to guide surgery in these patients, with a recognition that the best outcomes are achieved in patients with a clear “dominant” tuber and a focal putative seizure onset zone.⁷

Received December 11, 2022; accepted after revision June 7, 2023.

From Developmental Neurosciences (A.C., K. Seunarine, R.J.P., M.M.T., J.H.C.), Great Ormond Street Institute of Child Health and Department of Medical Physics and Bioengineering (K. Shmueli), University College London, London, UK; Departments of Neurosurgery (A.C., K. Seunarine, R.J.P., M.M.T.), Neuroradiology (J.S., P.H., K.M., U.L.), Neurology (C.E., R.C.S., J.H.C.), and Neurophysiology (F.M.), Great Ormond Street Hospital, London, UK; Department of Pediatric Neurology (R.C.S.), Nemours Children's Hospital, Wilmington, Delaware; and Engineering and Physical Sciences Research Council/Wellcome Centre for Medical Engineering and Department of Biomedical Engineering (D.W.C.), School of Biomedical Engineering and Imaging Sciences, King's College London, London, UK.

A. Chari is supported by a Great Ormond Street Hospital Children's Charity Surgeon Scientist Fellowship. This work has been supported by the Great Ormond Street Hospital-National Institute of Health Research Biomedical Research Center and, in part, by the Henry Smith Charity and Action Medical Research (GN2214). D.W.C. was supported by the King's College London Wellcome/Engineering and Physical Sciences Research Council Center for Medical Engineering (WT 203148/Z/16/Z).

Please address correspondence to Aswin Chari, MD, Developmental Neurosciences, Great Ormond Street Institute of Child Health, University College London, 30 Guilford St, London, WC1N 1EH UK; e-mail: Aswin.chari.18@ucl.ac.uk; @aswinchari

Indicates open access to non-subscribers at www.ajnr.org

Indicates article with online supplemental data.

<http://dx.doi.org/10.3174/ajnr.A7929>

However, targeting tubers as part of an SEEG implantation plan in these patients can be difficult because there is often a high tuber burden, semiology can be difficult to interpret, and video-electroencephalography lateralization and localization are often poor. The interpretation of neuroimaging is further complicated by heterogeneity in the appearance of tubers, with some imaging features more associated with epilepsy than others. One study identified 3 radiologically different tuber types based on T1-, T2-, and T2-FLAIR characteristics; the dominant type of tuber in a patient was associated with the likelihood of autism spectrum disorder, infantile spasms, and seizures, though no insights were drawn about the epileptogenicity of specific tubers.⁸ Another study used this classification to quantitatively assess the epileptogenicity of tubers and the surrounding cortex during SEEG. It concluded that resection of the dominant tuber associated with a T2-FLAIR hypointense center, a higher epileptogenicity index compared with other tubers and the perituberal cortex, continuous interictal epileptiform discharges, and stimulation-induced seizures were associated with 80% seizure freedom. Outcomes were less favorable when there was a more complex organization of the epileptogenic zone.⁹

Studies have identified calcification as an indicator of DRE and epileptic foci in TSC, though these studies have predominantly used CT scans to assess whether there was calcification as a binary variable.^{10,11} In the past few years, quantitative susceptibility mapping (QSM) has become more prevalent as a MR imaging technique, with the ability to detect intracranial calcification with high levels of sensitivity and specificity.¹² QSM is an advancement of SWI in which postprocessing techniques are applied to quantify the magnetic susceptibility of tissue. Its advantage is that it removes the blooming artifacts in SWI that are a factor of tissue geometry and orientation, leading to precise local quantification of magnetic susceptibility.¹³ Magnetic susceptibility is increased by paramagnetic materials (hemorrhage, iron, gadolinium contrast) and decreased by diamagnetic materials (eg, calcification), and levels of these minerals have previously been shown to be altered in focal cortical dysplasia.¹⁴ As part of the QSM processing, an R2* map is also generated, which is a measure of the amount of dephasing caused by B₀ field inhomogeneities either from macroscopic field perturbations or those due to local susceptibility effects.¹³ In contrast to QSM, local field perturbations due to paramagnetic or diamagnetic materials have a similar effect.

In this exploratory pilot study, we sought to assess whether the QSM signal in tubers was able to identify putative epileptogenic tubers in a cohort of children with TSC undergoing SEEG as part of their presurgical evaluation for DRE. To explore the characteristics of the QSM distribution within each tuber, we assessed summary statistics of the histograms in each tuber (median, upper quartile, lower quartile, skewness, and kurtosis). We hypothesized that QSM and the associated R2* values would differ between epileptogenic and nonepileptogenic tubers, with epileptogenic tubers having lower QSM and higher R2* values as a result of increased calcium content and that this difference may affect both the median values and skewness of the distributions.

MATERIALS AND METHODS

This was a single-center retrospective cohort study reported according to the STrengthening the Reporting of OBServational

studies in Epidemiology (STROBE) guidelines. Because it used routinely collected clinical data, ethics approval and the need for individual patient informed consent was waived by the research and development department at Great Ormond Street Hospital, and this study was registered as a clinical audit with the clinical audit department at Great Ormond Street Hospital.

We studied a series of consecutive patients with TSC undergoing SEEG evaluation between January 2016 and December 2020 and who also had multiecho gradient-echo imaging suitable for QSM as part of their routine clinical MR imaging before SEEG was available for study inclusion. The decision to perform SEEG, the interpretation of the SEEG results, and offers of resective surgery were collected by the epilepsy surgery multidisciplinary team without reference to the QSM data.

Image Acquisition

Images were acquired using a 3T MR imaging scanner (Magnetom Prisma; Siemens) with a 20-channel head and neck receive coil. The image-acquisition parameters for the anatomic T1-weighted 3D-MPRAGE scan were the following: TI = 900 ms, TR = 2300 ms, TE = 2.74 ms, flip angle = 8°, readout bandwidth = 200 Hz/pixel, 1-mm³ isotropic voxel size, acquisition matrix = 256 × 256 × 240, parallel acquisition acceleration factor = 2, coronal orientation, total scan time = 5 minutes 19 seconds.

The image acquisition parameters for the 3D T2-FLAIR were the following: TI = 1800 ms, TR = 5000 ms, TE = 395 ms, echo-train length = 233 with variable flip angle optimized for T2-weighting, readout bandwidth = 650 Hz/pixel, acquisition matrix = 384 × 291 × 240 reconstructed to 0.65 × 0.65 × 1 mm³ voxel size, parallel acquisition acceleration factor = 2, coronal orientation, total scan time = 6 minutes 10 seconds.

The image acquisition parameters for the R2*/QSM 3D multiecho gradient-echo sequence were the following: TEs = 3, 7, 11, 15, 19, 23, and 27 ms, TR = 38 ms, flip angle = 15°, readout bandwidth = 360 Hz/pixel, acquisition matrix = 192 × 156 × 144 reconstructed to 0.6-mm³ isotropic voxel size, 6/8 partial Fourier factor in phase and section-encoding directions, parallel acquisition acceleration factor = 2 in a phase-encoding direction, transverse orientation, total scan time = 5 minutes 41 seconds.

QSM Processing

Single-channel image data were combined for each TE by the sum of squares of all single-channel magnitude images. The combined phase image φ was calculated for each TE by the sum of conjugate complex multiplication between the previous and current TEs. The conjugate complex multiplication eliminates the incongruous spatial phase sensitivities of each coil element, allowing the phase correct summation of the complex image data. The combined phase image of the first TE was set to zero.

$$\phi_{TE_n} = \arg \left(\sum_{n=1}^N z_{TE_{n-1}} \cdot \bar{z}_{TE_n} \right) \forall n > 1$$

A brain mask was computed on the first echo magnitude image using the FSL Brain Extraction Tool (<http://fsl.fmrib.ox.ac.uk/fsl/fslwiki/BET>).¹⁵ The R2* map was calculated on the logarithmic

magnitude images using the Moore-Penrose pseudoinverse implementation. The frequency shift was calculated from the combined phase images of all TEs using the `Fit_ppm_complex.m` function in the MEDI toolbox (https://github.com/huawu02/MEDI_toolbox/blob/main/UPDATES.m).¹⁶ The local frequency shift was calculated using the projection onto dipole fields method with an eroded brain mask (85% of the original size of the FSL BET brain mask) to minimize nonlocal phase contributions.¹⁷ The QSM map was then calculated from the local frequency shift using the iterative Tikhonov dipole inversion method.¹⁸

Image Processing

Manual segmentation of all visible tubers was performed using coregistered volumetric T1- and T2-FLAIR MR imaging using ITK-SNAP (www.itksnap.org).¹⁹ This was performed by the first author (A.C.), who is a neurosurgical resident with experience in pediatric epilepsy, under the supervision of a neuroradiologist with a special interest in pediatric epilepsy (K.M.). To reduce QSM artifacts from the pial surface vessels, we limited the manual segmentations to 1–2 mm away from the pial surface (Fig 1A). Manual visual checks were performed to ensure that all implanted tubers were segmented.

Imaging from the SEEG (including the electrode locations), the QSM and R2* maps, and postoperative scans were coregistered to the original volumetric T1 and validated visually (Fig 1A). Using these coregistered maps and the report from the SEEG procedure, we classified each segmented tuber as being implanted or not and, if implanted, whether it was labeled as having ictal epileptiform activity (ie, part of the seizure onset zone, “ictal”) or interictal epileptiform activity (“interictal”). This classification was based on the SEEG report, which was completed by the clinical team including a consultant neurophysiologist, consultant neurologist, and consultant neurosurgeon with experience in SEEG. The definition of “ictal” was that there was electrophysiologic change in the tuber at seizure onset, and the tuber was identified as one that should be resected as part of any surgery were it to be offered. The definition of “interictal” was persistent interictal epileptiform discharges in the tuber. In addition, note was made of whether the tuber was resected from the postoperative imaging.

Statistical Analysis

QSM and R2* values from each tuber were extracted on the basis of the coregistered QSM and R2* maps. To characterize the distribution of quantitative data from each tuber, we extracted the size of the tuber (number of voxels) and the median, upper quartile, lower quartile, skewness, and kurtosis of the QSM and R2* maps for each tuber (Fig 1B).

Using the values above (11 variables in total), 2 generalized estimating equation (GEE) binary logistic regression models were constructed using only the implanted tubers to assess whether there were factors that were predictive of whether the tuber was ictal or interictal. GEE models accommodate for repeated measures, which, in this case, are the potential intrasubject correlation between many tubers in the same patient. Following evaluation of model specificity and sensitivity, these model parameters were

then applied to the unimplanted tubers to predict ictal and interictal tubers from the unimplanted tubers and assess whether the predicted unresected ictal and interictal tuber burden correlated with the outcome following SEEG-guided resective epilepsy surgery.

Software, Data, and Code Availability Statement

All image processing was performed using the tools described above and in-house scripts in Matlab, Release 2020b (MathWorks) for QSM processing and data extraction and SPSS (IBM) for GEE modeling. Code is available at www.github.com/aswinchari/QSM. The GitHub repository contains the tuber information used to construct the GEE models. Coregistered imaging data are available from the corresponding authors on reasonable request.

RESULTS

Clinical Results

During the 5-year period, 14 children with TSC underwent SEEG. One child had previously undergone tuber resection, while another had undergone resective surgery for a subependymal giant cell astrocytoma. In 12 children (85.7%), a seizure-onset zone was identified following SEEG, and resective surgery was offered. All except 1 child had undergone resective surgery, including resection of single tuber and multiple tubers \pm mesial temporal structures.

At a median follow-up of 2.0 years (range, 1.0–4.3 years), 2 patients (18.2%) had an Engel Class I outcome, 3 (27.3%) had an Engel Class II outcome, 5 (45.4%) had an Engel Class III outcome, and 1 (9.1%) had an Engel Class IV outcome.

QSM and R2* Results

Of the 14 patients, 11 had undergone QSM as part of their preoperative scans, but 1 patient had to be excluded due to artifacts from dental braces. Therefore, the scans of 10 patients were included in the subsequent analyses (Online Supplemental Data). From these patients, a total of 146 tubers were masked (range, 6–23 tubers per patient), of which 76 were sampled by SEEG electrodes (range, 4–13 tubers per patient) and 70 were not. Of the sampled tubers, 20 were labeled as ictal, and 34, as interictal.

By means of the 76 tubers sampled by SEEG electrodes, 2 binary logistic GEE models were constructed to predict whether tubers were involved in ictal onset (ictal model) or interictal activity (interictal model). For both models, the only factor independently associated with ictal or interictal status was the kurtosis of the QSM histogram ($P = .04$ for the ictal model and $P = .005$ for the interictal model) (Online Supplemental Data). The predictions of the models were used to assess whether they correctly categorized the implanted tubers; both models had poor sensitivity (35.0% and 44.1%, respectively) but high specificity (94.6% and 78.6%, respectively) (Fig 2A).

The developed model parameters were subsequently applied to the test data set of unimplanted tubers. They identified 10 tubers as ictal and 27 as interictal, of which 7 were overlapping. These were spread across most of the subjects with a range of 0–4 additional ictal tubers and 0–6 additional interictal tubers identified that were not sampled by SEEG (Online Supplemental Data).

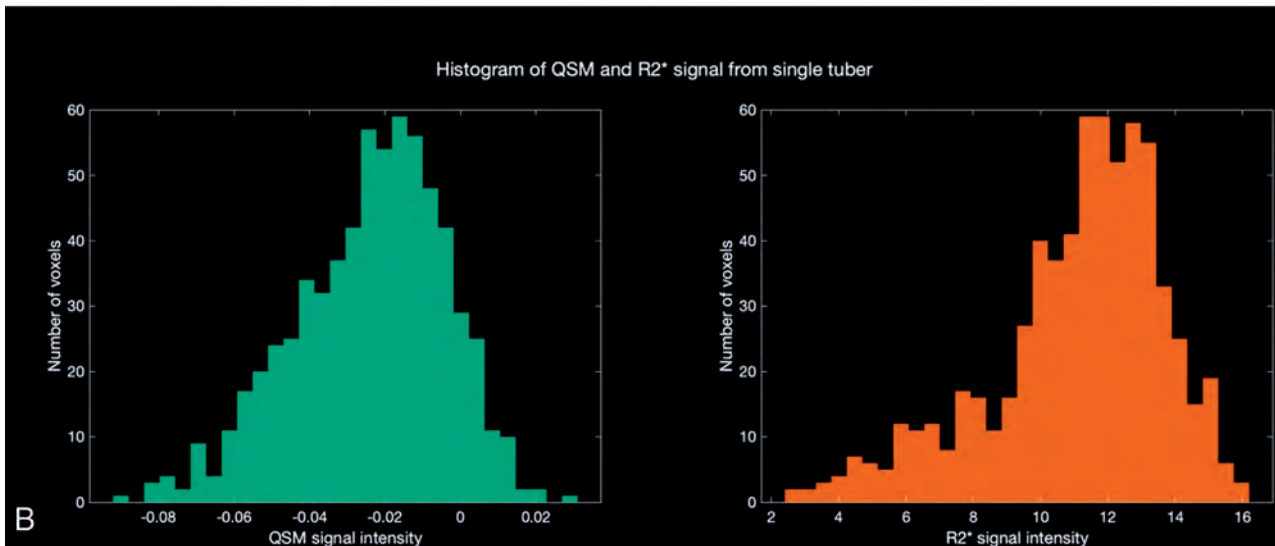
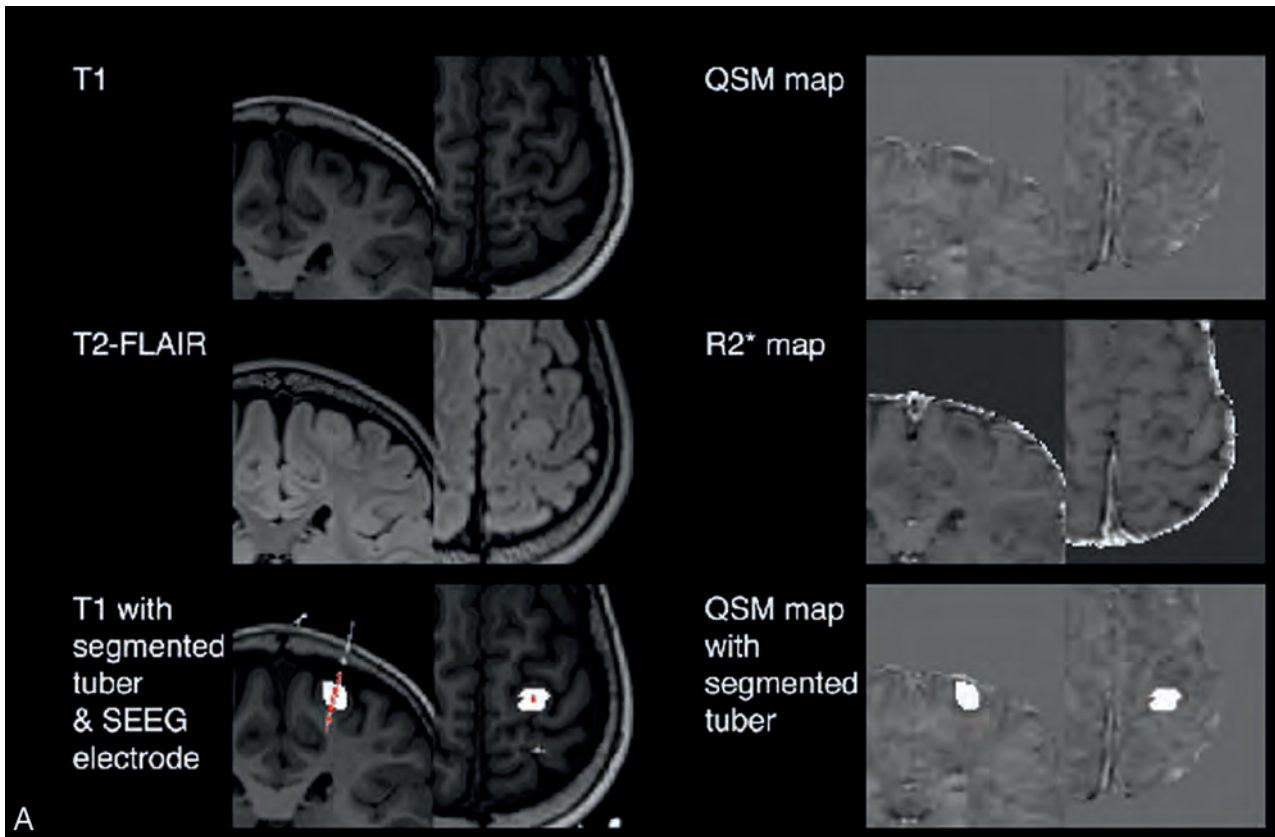


FIG 1. Methods summary. *A*, Illustrative images of T1-, T2-FLAIR, segmented tubers and overlying electrodes, QSM, and R2* maps used in this study. *B*, Histograms show distributions of QSM and R2* values for the left motor strip tuber identified in *A*.

Figure 2*B* shows the distribution of QSM kurtosis values across all tubers that were implanted and from the model predictions. This shows the association between higher kurtosis (heavier tails of QSM values) and ictal and interictal tubers. Similar trends were not seen when plotting the median QSM values across all tubers (Fig 2*C*).

Last, the predictions of the models were used to assess whether there was a linear association between the Engel outcome and the total number of unresected predicted ictal and

interictal tubers (Fig 3). Although there was a modest positive relationship for the ictal model, the regression coefficients were not statistically significant for either model (ictal regression coefficient = 0.42, $R^2 = 0.23$, $P = .16$; interictal regression coefficient = 0.10, $R^2 = 0.003$, $P = .88$).

Illustrative Example

As an example, we present the case of a 10-year-old child diagnosed with TSC at 11 months of age with 4 different seizure types,

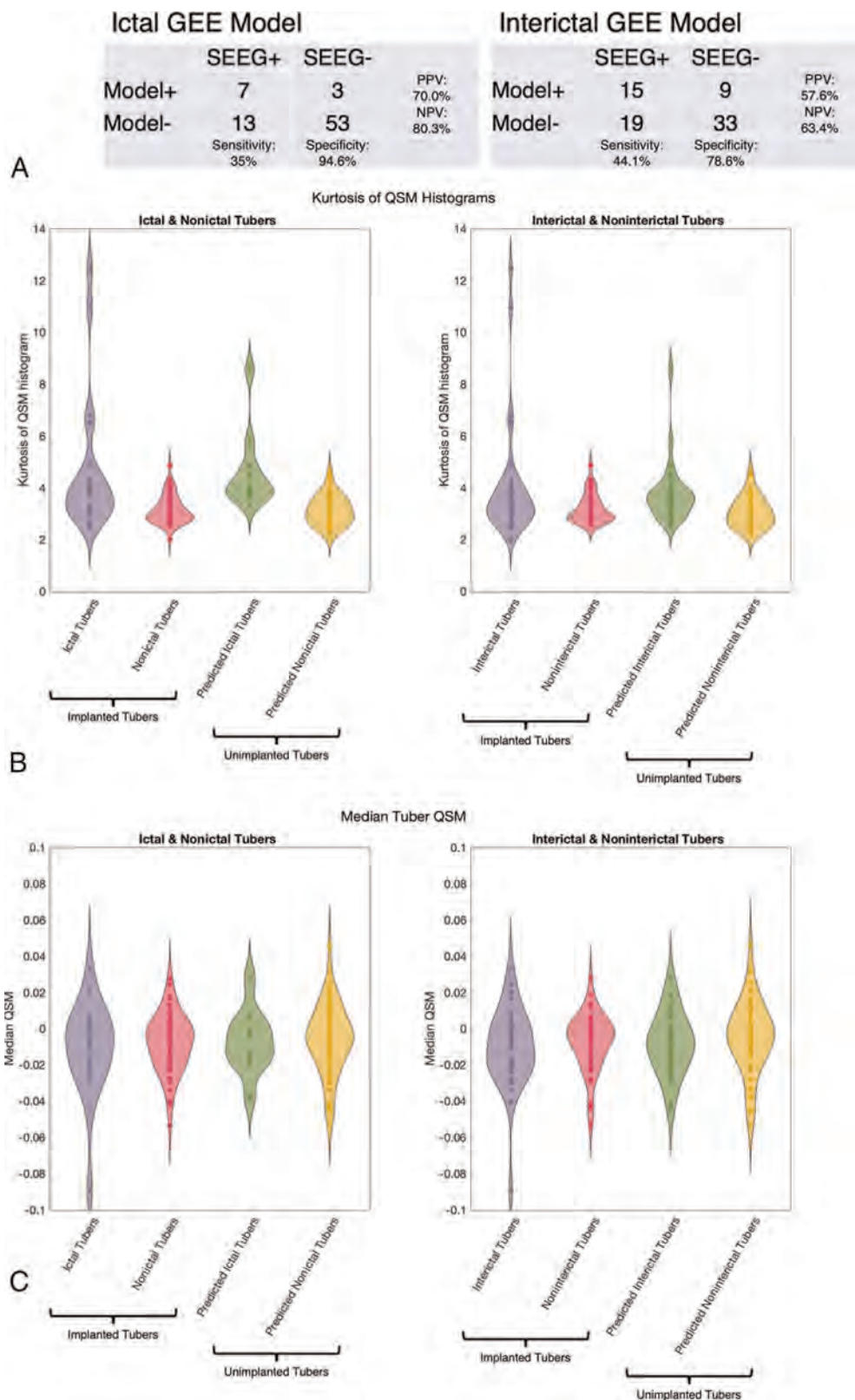


FIG 2. Output of GEE models. A, The 2×2 tables illustrate the sensitivity and specificity of the developed models to identify ictal and interictal tubers in the implanted tubers B, Violin plots of the kurtosis of the QSM histograms across implanted and nonimplanted tubers show higher kurtosis in the SEEG-identified and model-predicted ictal and interictal tubers, albeit with a degree of overlap. C, Violin plots of the median QSM values across implanted and nonimplanted tubers show higher kurtosis in the SEEG-identified and model-predicted ictal and interictal tubers, showing no difference between groups.

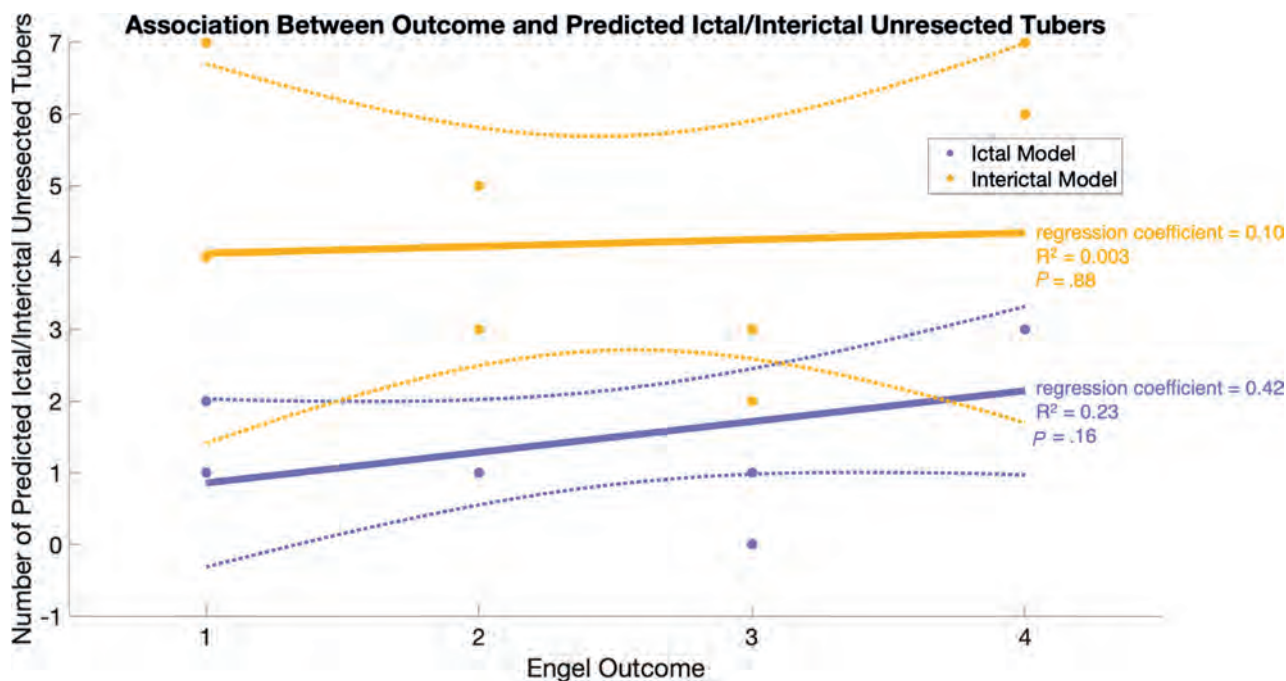


FIG 3. Association between model-predicted unresected tubers and postoperative Engel outcomes. There was no significant correlation between outcome and the total number of unresected ictal and interictal tubers predicted by the model (ictal regression coefficient = 0.42, $R^2 = 0.23$, $P = .16$; interictal regression coefficient = 0.10, $R^2 = 0.003$, $P = .88$). Note that for this analysis, 2 patients who did not undergo subsequent surgical intervention were classified as Engel class IV, and the Engel class was considered a linear variable.

including, most commonly, asymmetric spasms with more right-body involvement than left. Ictal video telemetry recordings for 3 seizure types lateralized to the left hemisphere, while one lateralized to the right. Interictal EEG showed bilateral epileptiform activity, but this was more pronounced on the left. MR imaging showed evidence of bilateral tubers with no clear dominant tuber. An interictal magnetoencephalogram was performed, showing interictal activity in the left prefrontal and temporoparietal regions. On the basis of the findings above, a bilateral SEEG implantation was planned with more left-sided than right-sided electrodes (Fig 4A). This identified 2 tubers involved in seizure onset (Fig 4B, red tubers). These tubers were subsequently resected, and 2 years after the operation, the patients had an Engel Class III outcome with significant reduction in seizure frequency and duration and associated improvement in cognition and attention.

The ictal GEE model using the QSM data identified an additional potential epileptogenic tuber in the right occipital region (Fig 4B, green tuber), which was not sampled by the SEEG electrodes. The normalized QSM histograms of all 3 tubers are shown, illustrating a narrower width and, therefore, increased kurtosis compared with all the other 15 tubers in the same patient (Fig 4C).

DISCUSSION

To our knowledge, this is only the second study to use QSM in TSC and the first to quantitatively analyze the QSM characteristics. The previous study showed that QSM was feasible in the context of identifying calcifications in both tubers and subependymal nodules.

On the basis of the ground truth of SEEG interpretation, we found that a model containing QSM and $R2^*$ signal characteristics may be helpful in identifying putative epileptogenic tubers in TSC with a high level of specificity but low sensitivity (Fig 2A). This finding suggests that preoperative QSM may be a useful adjunct for the selection of tubers for SEEG exploration because ictal lesions nearly always had high kurtosis in our sample. These results warrant prospective assessment. Specifically, epilepsy in TSC can be associated with complex networks; therefore, tubers distant from the regions identified by semiology and video-electroencephalography may be involved in seizure generation and warrant sampling.⁷ Most interesting, most patients in this cohort (8/10) had additional unimplanted tubers identified as potentially epileptogenic by the model, which, combined with the evidence that only 2 patients had an Engel Class I outcome, provides preliminary evidence that these additional tubers may have been worthwhile to sample as part of the SEEG exploration. The poor correlation of unresected predicted ictal tubers with outcome (Fig 3) is explained by the poor sensitivity of the model, and further prospective work might identify additional features to improve the sensitivity, such as other modalities of MR imaging incorporated into the model or data such as electrical source modeling.²⁰ However, the high specificity suggests that the models may be useful in the prospective identification of putative epileptogenic tubers that could then be targeted for confirmation through SEEG recordings. Indeed, there is a precedent for using radiologic biomarkers to identify additional areas to explore during SEEG.²¹

In our GEE models, we identified the kurtosis of the QSM signal histogram being significantly associated with both ictal

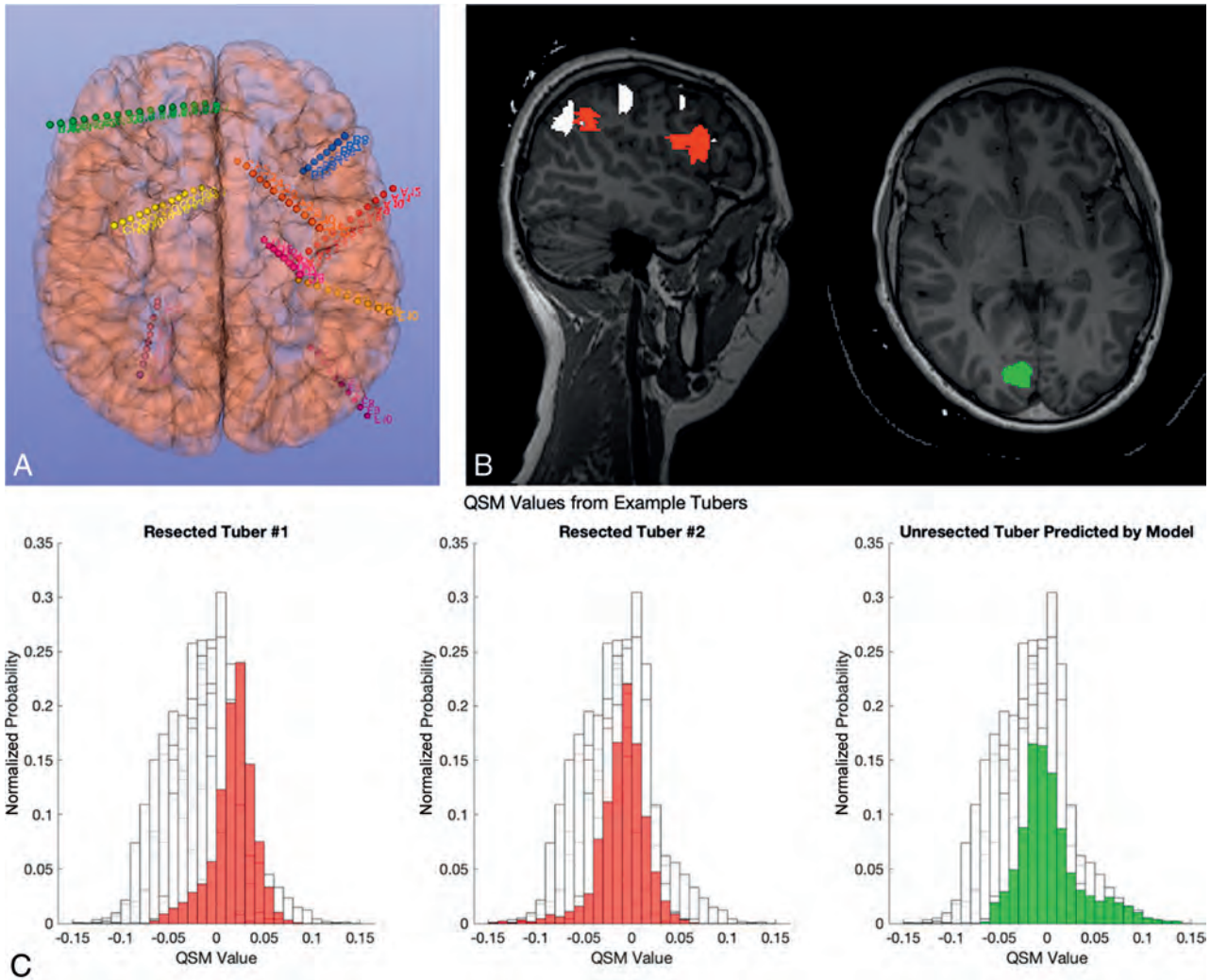


FIG 4. Illustrative case example. *A*, Illustration of bilateral SEEG implantation with a more left-sided electrode. *B*, Sagittal and axial T1 images with overlying tuber segmentation. The 2 identified epileptogenic tubers that were subsequently resected are shown in red, while a third tuber in green was not sampled but identified as potentially epileptogenic by the GEE model. *C*, Histograms of the QSM values of the 3 tubers shown in *B* overlaid on the histograms of 15 other tubers from the same patient (in white). Note that they all seem to have a higher kurtosis.

($P = .04$) and interictal ($P = .005$) tubers, with increased kurtosis in epileptogenic tubers without significant changes in the median QSM values. This finding suggests that although there may not necessarily be an average increase in the calcium content within epileptogenic tubers, the distribution of QSM values had thicker tails. Increased kurtosis of QSM values being associated with epileptogenicity is a novel finding and requires both a biologic explanation and external validation, especially because it does not fully agree with previous studies that indicate calcification as a marker of epileptogenicity.^{10,11} For example, Lorio et al¹⁴ found decreased QSM values, corresponding to increased calcium and zinc in focal epileptogenic lesions such as in focal cortical dysplasia type IIb. The high kurtosis in this study could be explained by the thicker tails on both sides of the distribution, indicating areas of low susceptibility (eg, from high calcium) and high susceptibility (eg, from areas of increased blood flow or iron deposition) compared with nonepileptogenic tubers.

Indeed, alterations of iron deposition have also been described in radiologically classified tubers of focal cortical dysplasia; these

require electrophysiologic and histopathologic correlation, which may give insight into why certain radiologic characteristics (for example, high QSM kurtosis or low T2-FLAIR intensity) are associated with epileptogenicity. This knowledge may aid the targeting of putative epileptogenic tubers in future SEEG implantations. In addition, our model does not account for the dynamics of epileptogenicity within a tuber, where the core, periphery, and perituberal tissue may contribute differently to seizure onset; again, this issue would require further study.⁹ QSM signal distributions have also been linked to a chronic inflammatory response and glial activation in MS lesions,²² and it would, therefore, be interesting to correlate longitudinal imaging findings with markers of epileptogenicity and, ultimately, histology to understand the potential role of inflammation in tubers and how they contribute to epileptogenesis.

The study has a number of limitations. First, it is a small single-center retrospective series that requires internal prospective and external validation. The cohort was small, and only 18% of subjects were seizure-free at last follow-up, indicating a complex

cohort. QSM is also inherently associated with artifacts, such as from the cortical surface, which may have affected the results; despite our attempts to reduce such artifacts, novel postprocessing pipelines may help reduce them further.²³ The utility of the model would also be improved by understanding the biologic basis for increased kurtosis leading to epileptogenicity, such as postoperative analysis of tissue mineral content. The tubers were segmented using only the T1- and T2-FLAIR sequences. It is conceivable that incorporating the QSM maps into the interpretation of tuber characteristics may aid radiologic interpretation of the nature and extent of tubers.

We were unable to include quantitative analyses of T1- and T2-FLAIR signal characteristics, CT scan densities, and the SEEG signals in this study, but these may be useful constructs for future studies for quantitatively assessing associations between CT/MR imaging signal characteristics and quantitative markers of SEEG epileptogenicity. Existing SEEG markers of epileptogenicity include cortico-cortical evoked potentials, neuronal spiking activity and fast ripples, and more in-depth analyses could relate QSM characteristics to these.²⁴⁻²⁶ In addition, there may be a more nuanced interpretation of SEEG in TSC that we have not considered; the ethos at our institution is to consider tubers as individual entities being either involved or not involved in the seizure onset, but we acknowledge that other schools may consider parts of tubers or perituberal tissue to be epileptogenic; therefore, future studies may seek to assess QSM signal characteristic distributions within and around tubers as markers of epileptogenic tissue. There is also a possibility of dynamic changes in QSM signals, which were not captured in this study because the postoperative imaging protocols did not include QSM in our institution.

CONCLUSIONS

Despite these limitations, this study provides important proof of principle that quantification and assessment of tuber mineral content through QSM may be a useful biomarker in the identification of the putative epileptogenic tubers in TSC. Most important, our results, that high kurtosis is associated with epileptogenicity with a high specificity and low sensitivity, did not support our hypothesis that epileptogenicity would be associated with increased calcium and, therefore, a greater prevalence of lower QSM values. This result does not refute the hypothesis that calcification is an important marker in tuber epileptogenicity but may indicate a more complex process. Increased QSM kurtosis could involve changes in mineral content (eg, calcium and iron) and perhaps inflammation and blood flow changes, all of which may relate to epileptogenicity. Larger cohorts, external validation, and correlation with histologic and tissue mineral analysis are required to further this work.

Disclosure forms provided by the authors are available with the full text and PDF of this article at www.ajnr.org.

REFERENCES

- Nabbout R, Belousova E, Benedik MP, et al. **Historical patterns of diagnosis, treatments, and outcome of epilepsy associated with tuberous sclerosis complex: results from TOSCA Registry.** *Front Neurol* 2021;12:697467 CrossRef Medline
- Arya R, Tenney JR, Horn PS, et al. **Long-term outcomes of resective epilepsy surgery after invasive presurgical evaluation in children with tuberous sclerosis complex and bilateral multiple lesions.** *J Neurosurg Pediatr* 2015;15:26–33 CrossRef Medline
- Fallah A, Guyatt GH, Snead OC, et al. **Predictors of seizure outcomes in children with tuberous sclerosis complex and intractable epilepsy undergoing resective epilepsy surgery: an individual participant data meta-analysis.** *PLoS One* 2013;8:e53565 CrossRef Medline
- Fallah A, Rodgers SD, Weil AG, et al. **Resective epilepsy surgery for tuberous sclerosis in children: determining predictors of seizure outcomes in a multicenter retrospective cohort study.** *Neurosurgery* 2015;77:517–24; discussion 524 CrossRef Medline
- Liu S, Yu T, Guan Y, et al. **Resective epilepsy surgery in tuberous sclerosis complex: a nationwide multicentre retrospective study from China.** *Brain* 2020;143:570–81 CrossRef Medline
- Specchio N, Pepi C, de Palma L, et al. **Surgery for drug-resistant tuberous sclerosis complex-associated epilepsy: who, when, and what.** *Epileptic Disord* 2021;23:53–73 CrossRef Medline
- Park JT, Vaca GF. **Stereo-EEG in tuberous sclerosis complex.** *Pediatr Neurol Briefs* 2020;34:6 CrossRef Medline
- Gallagher A, Grant EP, Madan N, et al. **MRI findings reveal three different types of tubers in patients with tuberous sclerosis complex.** *J Neurol* 2010;257:1373–81 CrossRef Medline
- Neal A, Ostrowsky-Coste K, Jung J, et al. **Epileptogenicity in tuberous sclerosis complex: a stereoelectroencephalographic study.** *Epilepsia* 2020;61:81–95 CrossRef Medline
- Altman NR, Purser RK, Post MJ. **Tuberous sclerosis: characteristics at CT and MR imaging.** *Radiology* 1988;167:527–32 CrossRef Medline
- Zhang MN, Zou LP, Wang YY, et al. **Calcification in cerebral parenchyma affects pharmacoresistant epilepsy in tuberous sclerosis.** *Seizure* 2018;60:86–90 CrossRef Medline
- Chen W, Zhu W, Kovanlikaya I, et al. **Intracranial calcifications and hemorrhages: characterization with quantitative susceptibility mapping.** *Radiology* 2014;270:496–505 CrossRef Medline
- Ruetten PP, Gillard JH, Graves MJ. **Introduction to quantitative susceptibility mapping and susceptibility weighted imaging.** *Br J Radiol* 2019;92:20181016 CrossRef Medline
- Lorio S, Sedlacik J, So PW, et al. **Quantitative MRI susceptibility mapping reveals cortical signatures of changes in iron, calcium and zinc in malformations of cortical development in children with drug-resistant epilepsy.** *Neuroimage* 2021;238:118102 CrossRef Medline
- Jenkinson M. **BET: MR-Based Estimation of Brain, Skull and Scalp Surfaces.** In: *Proceedings of the Annual Meeting of the Organization for Human Brain Mapping*, Toronto, Ontario, Canada. June 12–16, 2005
- Liu T, Wisnieff C, Lou M, et al. **Nonlinear formulation of the magnetic field to source relationship for robust quantitative susceptibility mapping.** *Magn Reson Med* 2013;69:467–76 CrossRef Medline
- Liu T, Khalidov I, de Rochefort L, et al. **A novel background field removal method for MRI using projection onto dipole fields (PDF).** *NMR Biomed* 2011;24:1129–36 CrossRef Medline
- Karsa A, Punwani S, Shmueli K. **An optimized and highly repeatable MRI acquisition and processing pipeline for quantitative susceptibility mapping in the head-and-neck region.** *Magn Reson Med* 2020;84:3206–22 CrossRef Medline
- Yushkevich PA, Piven J, Hazlett HC, et al. **User-guided 3D active contour segmentation of anatomical structures: significantly improved efficiency and reliability.** *Neuroimage* 2006;31:1116–28 CrossRef Medline
- Centeno M, Tierney TM, Perani S, et al. **Combined electroencephalography-functional magnetic resonance imaging and electrical source imaging improves localization of pediatric focal epilepsy.** *Ann Neurol* 2017;82:278–87 CrossRef Medline

21. Chari A, Adler S, Wagstyl K, et al. **IDEAL approach to the evaluation of machine learning technology in epilepsy surgery: protocol for the MAST trial.** *BMJ Surg Interv Health Technol* 2022;4:e000109 CrossRef Medline
22. Gillen KM, Mubarak M, Park C, et al. **QSM is an imaging biomarker for chronic glial activation in multiple sclerosis lesions.** *Ann Clin Transl Neurol* 2021;8:877–86 CrossRef Medline
23. Yaghmaie N, Syeda WT, Wu C, et al. **QSMART: quantitative susceptibility mapping artifact reduction technique.** *Neuroimage* 2021;231:117701 CrossRef Medline
24. Wang Y, Yuan L, Zhang S, et al. **Fast ripples as a biomarker of epileptogenic tuber in tuberous sclerosis complex patients using stereo-electroencephalograph.** *Front Hum Neurosci* 2021;15:680295 CrossRef Medline
25. Yu X, Ding P, Yuan L, et al. **Cortico-cortical evoked potentials in children with tuberous sclerosis complex using stereo-electroencephalography.** *Front Neurol* 2019;10:1093 CrossRef Medline
26. Despouy E, Curot J, Denuelle M, et al. **Neuronal spiking activity highlights a gradient of epileptogenicity in human tuberous sclerosis lesions.** *Clin Neurophysiol* 2019;130:537–47 CrossRef Medline

Posterior Fossa Horns in Hurler Syndrome: Prevalence and Regression

S. Huang, D. Hall, and D. Nascene

ABSTRACT

SUMMARY: Posterior fossa “horns” caused by internal hypertrophy of the occipitomastoid sutures are one of the more recently defined cranial abnormalities described in mucopolysaccharidoses, especially in Hurler Syndrome. However, details of this finding, including the development and natural history, are not well-understood. Two hundred eighty-six brain MR imaging studies of 61 patients with mucopolysaccharidosis I-Hurler syndrome treated at single institution between 1996 and 2015 were studied. Posterior fossa horn height was measured as the perpendicular distance from the tip of the horn to the expected curvature of the occipital inner table. Fifty-seven of the 61 patients (93.4%) had evidence of posterior fossa horns on at least one occasion. The initial average height of the right horn was 4.5 mm, and the left horn, 4.7 mm. Most of the posterior horns regressed before transplantation in our cohort, though the exact age was variable among the patients. Nearly all patients in our cohort had posterior fossa horns, and these horns regressed with age. The regression of the horns frequently started before transplantation. This trend has not been previously described, and it may suggest unknown effects of mucopolysaccharidosis on skull development.

ABBREVIATIONS: GAG = glycosaminoglycan; MPS IH = mucopolysaccharidosis I-Hurler syndrome

Mucopolysaccharidosis type I-Hurler syndrome (MPS IH) is characterized by α -L-iduronidase deficiency, leading to dermatan sulfate and heparan sulfate accumulation, which are types of glycosaminoglycans (GAGs). MPS IH is the most severe form of lysosomal storage disease with GAG deposits in all tissues, causing organ damage, neurocognitive delay, and musculoskeletal abnormalities.^{1,2} Although enzyme replacement therapy and hematopoietic stem cell transplantation have a positive impact on neurocognitive development and mortality, these treatments do not seem to halt or reverse damage in other tissues.³⁻⁶

Many intracranial and skull radiographic findings of MPS IH have been described. For instance, dilated perivascular spaces, cerebral atrophy, abnormal white matter, and ventriculomegaly are common findings.^{7,8} Dysostosis multiplex, the constellation of skeletal manifestations due to altered endochondral and membranous bone growth, includes a J-shaped sella turcica, thickened cortical bone, poor maxillary sinus pneumatization, sphenoid wing remodeling, and abnormally shaped vertebral bodies.⁸⁻¹⁰ Recently, posterior fossa “horns”

were described as a new common feature in patients with mucopolysaccharidosis and were most common in patients with MPS IH.⁹ These horns result from internal hypertrophy of the occipitomastoid sutures, which the authors believed to be caused by GAG deposits and early suture closure.^{9,11} Posterior fossa horns could impact the development of the posterior cranial fossa and/or hydrocephalus, but no study has fully examined the prevalence and progression in patients with MPS IH.

In this study, we describe the prevalence of posterior fossa horns in patients with MPS IH, and their evolution with age.

MATERIALS AND METHODS

All patients with MPS IH treated at our institution between 1996 and 2015 were retrospectively reviewed. Each brain MR imaging of all patients during this period was reviewed. Axial reconstructions from 0.9-mm MPRAGE T1-weighted or axial 4-mm T2-weighted TSE images were used for measurement. When present, both the left and right posterior fossa horns were measured as the perpendicular distance from the tip of the horn to the expected curvature of the inner table of the occipital bone (Fig 1A). Consensus reviews were achieved among a medical student, a radiology resident, and a staff neuroradiologist. Basic linear regression was used to detect relationships between the changes of posterior fossa horns and age. Summary statistics and the Student *t* test were used to describe the averages of the posterior fossa horns.

Received March 3, 2023; accepted after revision June 7.

From the Departments of Neurosurgery (S.H.) and Radiology (D.H., D.N.), University of Minnesota, Minneapolis, Minnesota.

Please address correspondence to Shiwei Huang, MD, Department of Neurosurgery, University of Minnesota, 420 Delaware St SE MMC 96, Room D429, Mayo Building, Minneapolis, MN 55455; e-mail: huan2256@umn.edu

<http://dx.doi.org/10.3174/ajnr.A7931>

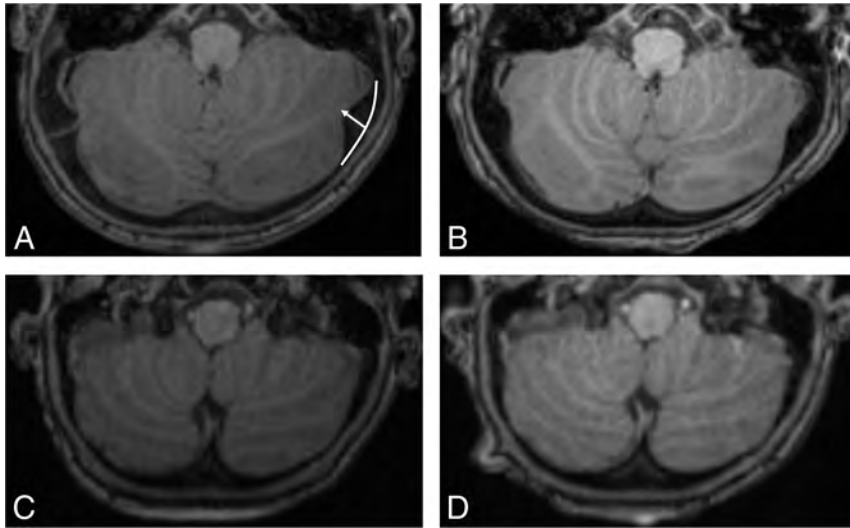


FIG 1. A, T1-weighted axial images demonstrate a progressive decrease in the size of the posterior fossa horns in a patient who underwent hematopoietic stem cell transplantation at 1 year of age. The height of the posterior fossa horn is measured from the expected curvature of the inner table (curved white line) to the tip of the horn (A, white arrow). The posterior horns measure 6.3 mm R/5.4 mm L at 0.9 years (A). They are 4.1 mm R/3.2 mm L at 1.8 years (B) and 2.0 mm R/1.0 mm L at 4.1 years (C). D, They are 0 mm R/0 mm L at 5.9 years (D).

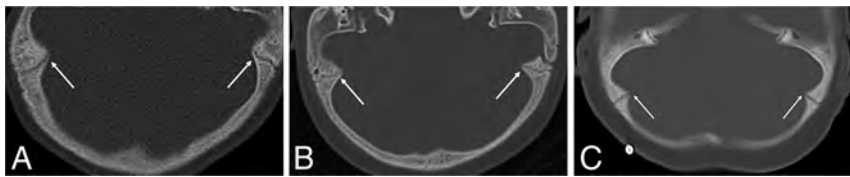


FIG 2. CT images show bilateral internal hypertrophy yet open occipital mastoid sutures (white arrows) in 3 different patients with MPS IH. A, This is the first patient with CT at the head bone window obtained at 1 year of age. B, This is the second patient with CT at the head bone window obtained at 1.6 years of age. C, This is the third patient with CT at the head bone window obtained at 1 year of age.

RESULTS

Two hundred eighty-six brain MR imaging studies in 61 patients from 1996 to 2015 were reviewed. Fifty-seven of the 61 (93.4%) patients reviewed were found to have varying degrees of posterior fossa horns at some time point during this period. Ages ranged from 1 month to 20 years, with a mean age of 4.7 years and median age of 3.4 years. Among patients who had posterior fossa horns, the average age at their first scan was 1.6 years, and among patients who did not have posterior fossa horns during this period, the average age at their first scan was 11.2 years. There was no statistical difference between the left and right posterior fossa horns ($P > .01$). Three patients had CT scans showing coexisting open occipitomastoid sutures and posterior fossa horns at an early age (Fig 2). The average left and right posterior fossa horns were largest before 1 year of age, 5.8 mm and 6.7 mm, respectively, and the sizes progressively decreased as the patients aged (Table and Fig 3). There is a significant negative correlation ($R^2 = 0.23$, $P < .01$, and $R^2 = 0.32$, $P < .01$) between the size of both left and right posterior fossa horns and age. The longitudinal regression of the posterior fossa horns is illustrated in 29 patients who each had ≥ 5 scans and received a hematopoietic stem cell

transplant, which shows that the decrease in size of the posterior fossa horns started before transplantation (Fig 4).

DISCUSSION

Hematopoietic stem cell transplant and enzyme replacement therapy have drastically improved the life span of patients with MPS IH, but such treatments have had limited effects on musculoskeletal abnormalities.^{2,6} Many studies have examined the brain MR imaging findings of MPS IH, and most recently Damar et al⁹ described the findings of posterior fossa horns due to internal hypertrophy of the occipitomastoid sutures in an MPS IH population and reported an incidence of 54% (6 of 11). However, to our knowledge, no literature has tracked the prevalence and regression of these posterior fossa horns among patients with MPS IH.⁹⁻¹¹

We found that posterior fossa horn prevalence was much higher at 93.4% (57/61) in our cohort of patients with MPS IH. The largest posterior fossa horns were found in the youngest patients (Table and Fig 3). A possible explanation for the different prevalence between the study of Damar et al⁹ and our study could be that our larger study had longitudinal follow-up across a broad range of ages, which included several young patients. The study of Damar et al reported a mean age of 8 in all types of mucopolysaccharidosis studied, but it

did not report the mean age of the MPS IH cohort. We found that 7 of 61 (11.5%) patients developed posterior fossa horns or had a transient increase in the size of posterior fossa horns before the 2 years of age, but in these patients, the posterior fossa horns quickly regressed like the rest of the cohort. We theorize that a study with older children could potentially miss the transient appearance of posterior fossa horns in young childhood because we demonstrated that the small proportion of our cohort of patients who did not have posterior fossa horns during the study period was much older than the patients who did (11.2 versus 1.6 years).

In this study, we report a decrease in the severity and prevalence in posterior fossa horns in MPS IH patients with age. These findings have not been reported in this population before. In 29 patients who had >5 measurements and transplantation, it is evident that even before the transplantation, the posterior fossa horns started to regress, suggesting that this phenomenon may be a natural consequence of growth and development in MPS IH rather than a response to hematopoietic stem cell treatment (Fig 4).

Skull sutures serve as sites of intramembranous bone growth, and their timed expansion allows brain growth.¹² The fusion patterns vary depending on the suture, and particularly, the

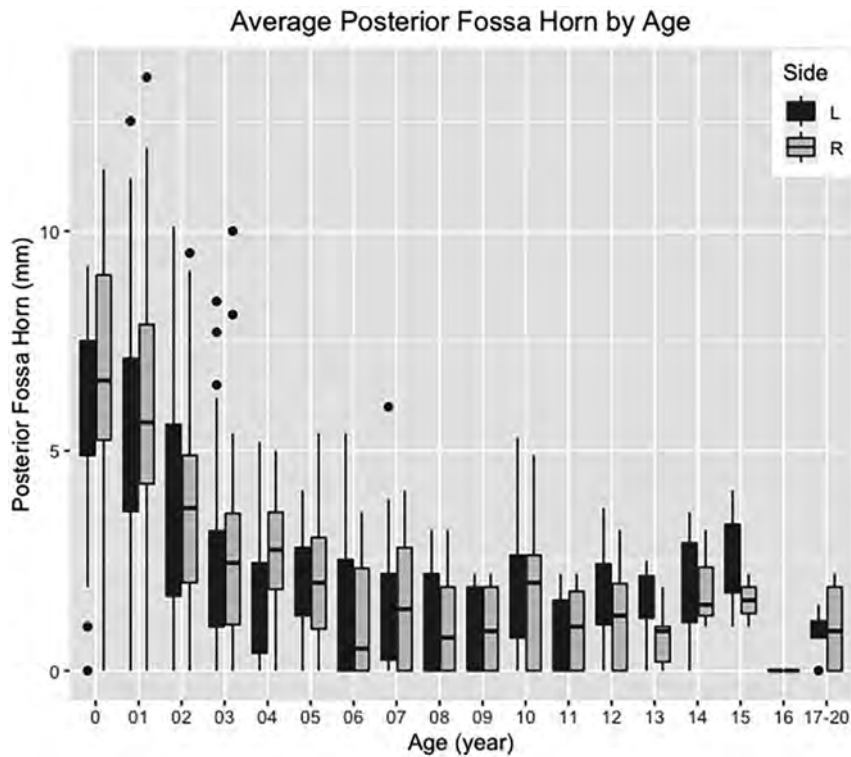


FIG 3. Average left and right posterior fossa horns by age. R indicates right; L, left.

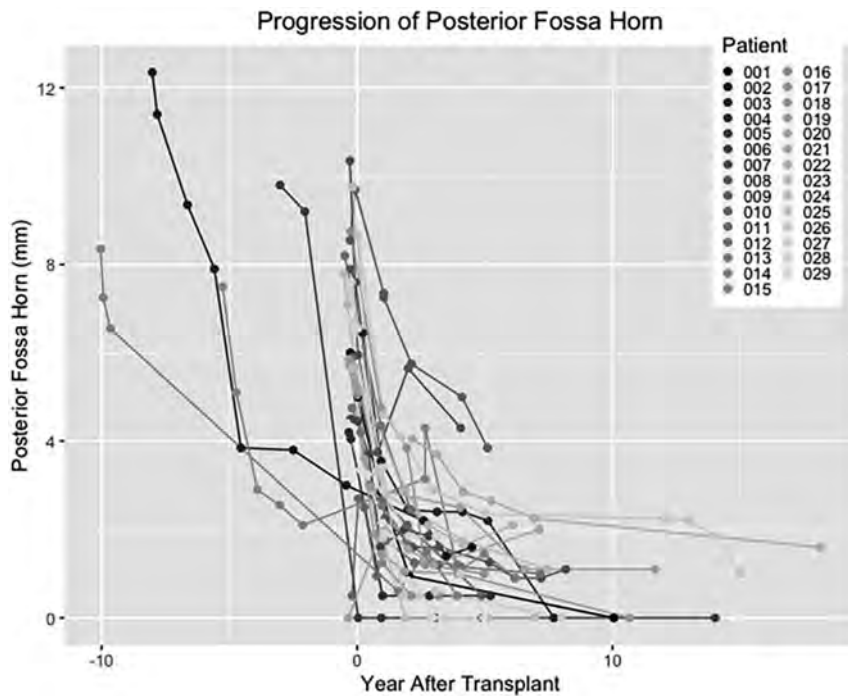


FIG 4. Progression of posterior fossa horns as patients age in 29 patients who had ≥ 5 measurements. Year 0 denotes the year of transplantation.

occipitomastoid suture only partially closes in $< 30\%$ of healthy individuals and can stay open even in the ninth decade.^{13,14} Oussoren et al¹¹ examined the incidence of early closure of major sutures in patients with mucopolysaccharidosis and showed that as many as 11 of 14 patients with MPS IH (71%) had early major

suture closure resulting in craniosynostosis. However, to our knowledge, there is no study examining the minor sutures in patients with MPS IH. While CT scans were not commonly performed in our cohort, we found 3 separate cases with large posterior fossa horns and open occipitomastoid sutures, suggesting that the prominence of the posterior horn was not due to early suture closure as postulated in the early study involving major sutures but rather likely due to the effects of MPS IH (Fig 2).

Damar et al⁹ also observed posterior fossa horns in 4 of 14 patients with mucopolysaccharidosis II (Hunter syndrome) and 2 of 14 patients with mucopolysaccharidosis VI (Maroteau-Lamy syndrome). Again, it is unclear whether the actual prevalence of posterior fossa horns in other forms of mucopolysaccharidosis is higher due to the effect of age as we described. It is also unclear whether this finding is present in patients with other forms of lysosomal storage disease or even in the healthy cohort because this finding has only been recently described. A longitudinal study with a large patient cohort is needed to further address this question.

One study limitation is that the age at the first scan was variable and the follow-up interval was also different, but the data still illustrated the overall decrease of posterior fossa horns bilaterally with time. Also, we had relatively few patients in the neonate period, and the timing of posterior fossa horn development has not yet been determined. Additional studies could further elucidate the growth of posterior fossa horns, such as whether posterior fossa horns are present in utero, perhaps with fetal MR imaging. Also, future studies could determine whether posterior fossa horns result in any consequences, such as vascular compression, that may lead to transient intracranial venous hypertension or perhaps contribute to the development of hydrocephalus.

CONCLUSIONS

Posterior fossa horns are very common in younger patients with MPS IH. In our cohort, these posterior fossa horns decreased in size in all patients, beginning before transplantation, a feature not previously reported. Posterior fossa horns are present despite open occipitomastoid sutures, contrary to the previous postulation that early fusion of

Average right and left posterior fossa horn breakdown by age

Age Range (yr)	No.	Average L Posterior Fossa Horn (mm)	Average R Posterior Fossa Horn (mm)
0–1	35	5.8 (SD, 2.2)	6.7 (SD, 2.7)
1–2	58	5.5 (SD, 2.8)	6.0 (SD, 2.7)
2–3	43	3.5 (SD, 2.5)	3.9 (SD, 2.4)
3–4	30	2.5 (SD, 2.2)	2.7 (SD, 2.3)
4–5	22	2.0 (SD, 1.7)	2.6 (SD, 1.4)
5–6	18	1.8 (SD, 1.3)	2.1 (SD, 1.6)
6–7	14	1.6 (SD, 1.7)	1.2 (SD, 1.3)
7–8	14	1.8 (SD, 1.7)	1.5 (SD, 1.6)
8–9	8	1.2 (SD, 1.4)	1.1 (SD, 1.3)
9–10	4	1.0 (SD, 1.2)	1.0 (SD, 1.2)
10–11	8	1.9 (SD, 1.9)	1.8 (SD, 1.7)
11–12	5	1.0 (SD, 1.0)	1.0 (SD, 1.0)
12–13	10	1.8 (SD, 1.3)	1.2 (SD, 1.2)
13–14	6	1.6 (SD, 0.9)	0.8 (SD, 0.7)
14–15	3	1.9 (SD, 1.8)	1.9 (SD, 1.2)
15–16	2	2.6 (SD, 2.2)	1.6 (SD, 0.8)
16–17	2	0.0	0.0
>17	4	0.9 (SD, 0.6)	1.0 (SD, 1.2)

Note:—L indicates left; R, right.









sutures could be the cause of the posterior fossa horns. These findings suggest other effects of MPS IH on the developing skeletal system that are not fully understood.

Disclosure forms provided by the authors are available with the full text and PDF of this article at www.ajnr.org.

REFERENCES

- Muenzer J. Overview of the mucopolysaccharidoses. *Rheumatology (Oxford)* 2011;50(Suppl 5):v4–v12 CrossRef Medline
- Muenzer J, Wraith JE, Clarke LA; International Consensus Panel on Management and Treatment of Mucopolysaccharidosis I. Mucopolysaccharidosis I: management and treatment guidelines. *Pediatrics* 2009;123:19–29 CrossRef Medline
- Dusing SC. Developmental outcomes in children with Hurler syndrome after stem cell transplantation. *Dev Med Child Neurol* 2007;49:646 CrossRef Medline
- Eisengart JB, Rudser KD, Tolar J, et al. Enzyme replacement is associated with better cognitive outcomes after transplant in Hurler syndrome. *J Pediatr* 2013;162:375–80.e1 CrossRef Medline
- Hampe CS, Wesley J, Lund TC, et al. Mucopolysaccharidosis type I: current treatments, limitations, and prospects for improvement. *Biomolecules* 2021;11:189 CrossRef Medline
- Eisengart JB, Rudser KD, Xue Y, et al. Long-term outcomes of systemic therapies for Hurler syndrome: an international multicenter comparison. *Genet Med* 2018;20:1423–29 CrossRef Medline
- Matheus MG, Castillo M, Smith JK, et al. Brain MRI findings in patients with mucopolysaccharidosis types I and II and mild clinical presentation. *Neuroradiology* 2004;46:666–72 CrossRef Medline
- Palmucci S, Attinà G, Lanza ML, et al. Imaging findings of mucopolysaccharidoses: a pictorial review. *Insights Imaging* 2013;4:443–59 CrossRef Medline
- Damar Ç, Derinkuyu BE, Kiliçkaya MA, et al. Posterior fossa horns; a new calvarial finding of mucopolysaccharidoses with well-known cranial MRI features. *Turk J Med Sci* 2020;50:1048–61 CrossRef Medline
- White KK, Sousa T. Mucopolysaccharide disorders in orthopaedic surgery. *J Am Acad Orthop Surg* 2013;21:12–22 CrossRef Medline
- Oussoren E, Mathijssen IM, Wagenmakers M, et al. Craniosynostosis affects the majority of mucopolysaccharidosis patients and can contribute to increased intracranial pressure. *J Inherit Metab Dis* 2018;41:1247–58 CrossRef Medline
- Opperman LA. Cranial sutures as intramembranous bone growth sites. *Dev Dyn* 2000;219:472–85 CrossRef Medline
- Vu GH, Xu W, Go BC, et al. Physiologic timeline of cranial-base suture and synchondrosis closure. *Plast Reconstr Surg* 2021;148:973E–82E CrossRef Medline
- Rodriguez JJ, McLaughlin AC, Thompson JT. Analysis of cranial base suture fusion patterns. *J Craniofac Surg* 2021;32:1679–82 CrossRef Medline

Deep Learning–Generated Synthetic MR Imaging STIR Spine Images Are Superior in Image Quality and Diagnostically Equivalent to Conventional STIR: A Multicenter, Multireader Trial

 L.N. Tanenbaum,  S.C. Bash,  G. Zaharchuk,  A. Shankaranarayanan,  R. Chamberlain,  M. Wintermark,  C. Beaulieu, M. Novick, and  L. Wang



ABSTRACT

BACKGROUND AND PURPOSE: Deep learning image reconstruction allows faster MR imaging acquisitions while matching or exceeding the standard of care and can create synthetic images from existing data sets. This multicenter, multireader spine study evaluated the performance of synthetically created STIR compared with acquired STIR.

MATERIALS AND METHODS: From a multicenter, multiscanner data base of 328 clinical cases, a nonreader neuroradiologist randomly selected 110 spine MR imaging studies in 93 patients (sagittal T1, T2, and STIR) and classified them into 5 categories of disease and healthy. A DICOM-based deep learning application generated a synthetically created STIR series from the sagittal T1 and T2 images. Five radiologists (3 neuroradiologists, 1 musculoskeletal radiologist, and 1 general radiologist) rated the STIR quality and classified disease pathology (study 1, $n = 80$). They then assessed the presence or absence of findings typically evaluated with STIR in patients with trauma (study 2, $n = 30$). The readers evaluated studies with either acquired STIR or synthetically created STIR in a blinded and randomized fashion with a 1-month washout period. The interchangeability of acquired STIR and synthetically created STIR was assessed using a noninferiority threshold of 10%.

RESULTS: For classification, there was a decrease in interreader agreement expected by randomly introducing synthetically created STIR of 3.23%. For trauma, there was an overall increase in interreader agreement by +1.9%. The lower bound of confidence for both exceeded the noninferiority threshold, indicating interchangeability of synthetically created STIR with acquired STIR. Both the Wilcoxon signed-rank and t tests showed higher image-quality scores for synthetically created STIR over acquired STIR ($P < .0001$).

CONCLUSIONS: Synthetically created STIR spine MR images were diagnostically interchangeable with acquired STIR, while providing significantly higher image quality, suggesting routine clinical practice potential.

ABBREVIATIONS: Acq-STIR = acquired STIR; CNN = convolutional neural network; DL = deep learning; IQ = image quality; RMSE = root mean square error; RMSPE = root mean square percentage error; Syn-STIR = synthetically created STIR

Typical clinical protocol for spine MR imaging uses T1WI, T2WI, and STIR scans to depict anatomy and provide adequate sensitivity to a variety of pathologic conditions.

STIR offers a combination of T1 and T2 contrast-weighting and nulled fat signal to highlight pathologic changes in tissues. The fat suppression offered by STIR is more uniform and resistant to magnetic field inhomogeneities than other fat-saturation methods such as spectral “fat-sat,” especially near metallic foreign

bodies, tissue interfaces with high susceptibility differences (like the skull base/sinuses), and across large body parts like the spine. On lower-field permanent magnets with lower homogeneity, STIR may be the only fat-suppression method available. STIR images have inherently lower SNR than T1WI and T2WI. Despite approaches that use larger voxel sizes to mitigate this challenge, scan times are still long, more susceptible to motion, and harder for patients to tolerate.


Deep learning (DL)-based reconstruction techniques mitigate this challenge by enabling faster acquisitions while matching or even exceeding standard-of-care image quality (IQ).^{1–4} Recent work has led to DL methods that can generate entirely synthetic image contrasts, potentially shortening overall study times by removing the need to acquire certain series.

Synthesizing new contrast information from available images has been an active area of research in the MR imaging domain. Convolutional neural network (CNN)-based approaches have

Received March 20, 2023; accepted after revision June 1.

From RadNet (L.N.T., S.C.B.), New York, New York; Stanford University Medical Center (G.Z., C.B.), Stanford, California; Subtle Medical (A.S., R.C., L.W.), Menlo Park, California; MD Anderson Cancer Center (M.W.), University of Texas, Houston, Texas; and All-American Teleradiology (M.N.), Bay Village, Ohio.

Please address correspondence to Lawrence Tanenbaum, MD, RadNet, 5 Columbus Circle, 9th Floor, New York, NY 10019; e-mail: nuromri@gmail.com; @nuromri

 Indicates article with online supplemental data.

<http://dx.doi.org/10.3174/ajnr.A7920>

demonstrated state-of-the-art performance for MR imaging contrast synthesis.⁵⁻⁸ While most of the literature has focused on one-to-one synthesis, several studies considered the many-to-one synthesis problem, in which the algorithm takes multiple contrasts as input and generates 1 missing contrast.^{5,7,9} Previous work has demonstrated the potential to synthesize STIR images from T1WI and T2WI.¹⁰ This study goes further by using examinations from multiple scanner manufacturers and a wider variety of magnetic field strengths, including a more comprehensive set of pathologies, and by performing voxelwise analysis of the synthetically created STIR (Syn-STIR) images. Furthermore, the technical methods used in this work integrate multiple maps (including an anatomy-aware segmentation map and a pathology saliency map) in the reconstruction network, so the syn-STIR images maintain high consistency with the acquired STIR (Acq-STIR) images. Our methods also avoid the use of generative adversarial networks, which are prone to introducing structures in synthesized images that are not present in the source images.

This multicenter, multireader study evaluated the diagnostic interchangeability and qualitative image quality of a DL-generated Syn-STIR against a clinical standard-of-care Acq-STIR. There are established methods to assess the interchangeability of the 2 image-acquisition methods, which determine whether the images are diagnostically equivalent.¹¹ Two images are interchangeable or diagnostically equivalent if a given patient would receive the same diagnosis regardless of which of the 2 images was used. Diagnostic equivalence is tested by comparing an interreader agreement using the baseline imaging method with an interreader agreement using the method being tested versus the baseline while accounting for variability across cases and readers. In addition, multiple quantitative methods were also used to compare the Syn-STIR images with the Acq-STIR images.

MATERIALS AND METHODS

Overview

A DL model was applied to synthesize a sagittal Syn-STIR series from the sagittal T1 and sagittal T2 of clinical spine MR imaging studies. The model contains 3 phases, an anatomy-aware map, a pathology-aware map, and a reconstruction map. For the anatomy-aware map, the segmentation map was obtained for each anatomy, making the anatomy-based operation feasible. The pathology-aware map is a saliency map used to guide the network to maintain pathologic consistency. During the training process, the 2 inputs (sagittal T1 and sagittal T2) were fed into the reconstruction network under separate branches and later concatenated to avoid potential blurriness due to misregistration. We implemented the DL model in TensorFlow (<https://www.tensorflow.org/>), trained on an NVIDIA V100 GPU (<https://www.nvidia.com/en-us/data-center/v100/>) with an ADAM optimizer (<https://machinelearningjourney.com/index.php/2021/01/09/adam-optimizer/>),¹² and applied image registration between the 2 inputs to reduce potential misalignment. The network was trained by comparing the output Syn-STIR image with the Acq-STIR image through multiple loss functions (Online Supplemental Data).

Participants and Distribution of Pathologies

With institutional review board approval, a nonreader senior neuroradiologist identified the dominant pathology (as described below) in a multicenter, multiscanner data base of 328 approximately equal numbers of cervical, thoracic, and lumbar spine MR imaging cases referred for a variety of conditions. From this group, 93 unique patients were evaluated in 2 separate studies. First, 80 patients (40 females, 36 males, 4 not available; age range, 16–89 years) were selected randomly from among 5 categories of disease (defined as the most dominant pathology) based on the findings on the complete study (study 1). The categories were cord lesion ($n = 8$), noncord lesion ($n = 15$), degenerative disease ($n = 20$), infection ($n = 10$), trauma ($n = 17$), and healthy ($n = 10$). The readers were given instructions outlining which clinical entities should fall into each category and to help with classification when multiple pathologies were present. More details can be found in the Online Supplemental Data. In addition, a second study evaluating the ability of readers to identify important features in the setting of trauma was performed (study 2). Patients (13 men, 17 women; age range, 18–89 years) for study 2 included 10 with no imaging evidence of trauma (separate from the patients in study 1) and 20 with imaging evidence of trauma (17 of the patients with trauma in study 1 supplemented by 3 additional patients). These cases were evaluated for the following findings: prevertebral fluid collections (class I), bone edema related to fracture (class II), and posterior soft-tissue/ligamentous injury (class III). The case distribution was class I/II ($n = 3$), class I/II/III ($n = 7$), class I/III ($n = 5$), class II ($n = 1$), class II/III ($n = 1$), class III ($n = 4$), and class none ($n = 9$).

Image Acquisition

The images were acquired on a variety of scanners, including 3T Discovery 750 and 750w, 3T Signa Premier, and 1.5T HDxt (GE Healthcare); 3T Magnetom Skyra, 3T Magnetom Verio (Siemens); 1.5T Intera (Philips Healthcare); 1.5T Vantage Titan (Canon); 0.6T (Fonar Upright) and 0.3T AIRIS Elite (Hitachi/Fujifilm). The case distribution by field strength for study 1 was 0.6T ($n = 1$), 1T ($n = 1$), 1.5T ($n = 43$), and 3T ($n = 35$), and for study 2, it was 1T ($n = 2$), 1.5T ($n = 16$), and 3T ($n = 12$). The image acquisitions consisted of sagittal T1, T2, and STIR series using the individual institution's routine clinical protocol. Section thickness ranged from 3 to 5 mm. FOV varied from 18 to 24 cm cervical; 27 to 30 cm lumbar; and 30 to 38 cm thoracic; and the acquisition matrix varied from 192×192 to 800×380 .

Image Processing

The Syn-STIR images were created off-line from existing DICOM images using a vendor-neutral, CNN software application (SubtleSYNTH; Subtle Medical). The CNN was trained to generate synthetic sagittal STIR images using the sagittal T1 and T2 images as input. Because the application was DICOM-based, processing did not require proprietary raw k -space input; thus, it was capable of processing images from any MR imaging platform. The training set included hundreds of thousands of MR images from a variety of vendors, scanner models, field strengths, and clinical sites, as well as a variety of disease states/clinical

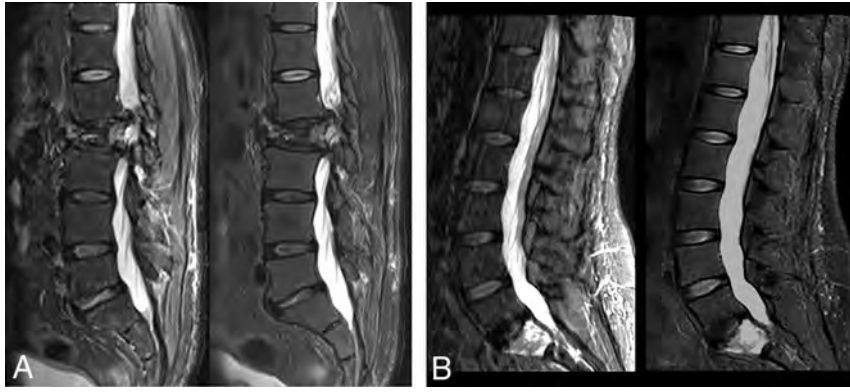


FIG 1. A, L2 body fracture. Conventional acquired STIR (*left*) and DL synthesized STIR (*right*). Note the Syn-STIR manifests fewer motion artifacts, improved sharpness, and greater apparent SNR. B, Sacral metastasis. Conventional Acq-STIR (*left*) and DL Syn-STIR (*right*). Note the striking reduction in motion artifacts as well as superior overall quality of the Syn-STIR.

indications, thus experiencing a range of tissue contrasts, acquisition parameters, patient anatomies, and image quality.

Image Assessment

Five radiologists (3 neuroradiologists, 1 musculoskeletal radiologist, 1 general radiologist experienced in spine MR imaging) evaluated 160 cases. Each case consisted of 3 sagittal image series: either T1, T2, and Acq-STIR ($n = 80$) or T1, T2, and Syn-STIR ($n = 80$). The image sets were presented in a blinded and randomized fashion on a commercial DICOM viewer, with a 1-month washout period between reading sessions (study 1). To assess diagnostic equivalence, each reader individually classified the pathologies present. Readers also rated the Acq-STIR and Syn-STIR image quality on a 5-point Likert scale (1 = unacceptable, 2 = poor, 3 = adequate, 4 = good, 5 = excellent), which served as a collective summary assessment of individual image-quality metrics, such as perceived SNR, contrast-to-noise ratio, image sharpness, and artifacts. The same readers also evaluated the trauma-specific study ($n = 30$ subjects, $n = 60$ studies) in the same blinded and randomized fashion with the same 1-month washout period (study 2). They were asked to individually classify the findings for the presence/absence of the following: 1) prevertebral fluid collections, 2) fracture-related bone edema, and 3) posterior soft-tissue/ligamentous injury. In addition, 2 neuroradiologists, including one not involved with studies 1 or 2, performed a blinded side-by-side, qualitative evaluation of the study 1 Acq-STIR and Syn-STIR images, rating the extent of disease and diagnostic confidence on a 5-point Likert scale, as well as noting evidence or absence of image aberrations.

RESULTS

Diagnostic-Equivalence Analysis

The 2 imaging methods were assessed for interchangeability or diagnostic equivalence by comparing the interreader agreement within Acq-STIR images with the interreader agreement between Syn-STIR and Acq-STIR images. Interreader agreement for Acq-STIR images was calculated as the percentage of comparisons between 2 different readers for the same case in which the readers' classifications agreed. Interreader agreement for Acq-STIR

versus Syn-STIR images was calculated as the percentage of comparisons between 2 different readers for the same case that the readers' classification when 1 reader was using the Acq-STIR image and the other reader was using the Syn-STIR image agreed with each other. The agreement probability was calculated by mean of a logistic regression model with random effects using the "glmer" function from the "lme4" package in R statistical and computing software (<http://www.r-project.org/>) following methods described in the literature.^{11,13} A noninferiority analysis was performed with a preset hypothesis that the difference in diagnostic classification for interreader agreement for Acq-STIR and Syn-STIR was not

>10% lower than the interreader agreement between Syn-STIR and Acq-STIR.

Image-Quality Statistical Analysis

Wilcoxon rank-sum tests were performed to assess the equivalence or superiority of the image quality for each feature. Statistically significant superiority for a feature was determined by $P < .05$. Adjustment for significance tests for multiple comparisons was made using a Bonferroni correction.

Voxel-Intensity Analysis

To evaluate the voxelwise correlation between the Syn-STIR image and the conventional STIR image, we drew 4 ROIs on each target tissue (vertebral bone, disc, CSF, spinal cord, and fat) and calculated the mean of the 4 ROIs per series. Note that areas without any pathologies were selected. For example, in patients with degenerative disease, ROIs were drawn only on the healthy disc. Similar rules applied to other tissues as well. Bland-Altman analysis^{14,15} was then applied, followed by the Shapiro-Wilk results on the difference.¹⁶ Additionally, root mean square error (RMSE) and root mean square percentage error (RMSPE) were calculated. A Passing-Bablok regression analysis was performed to evaluate agreement between the 2 images.¹⁷

Sample image pairs are shown in Fig 1, demonstrating similar fat-saturated T2-weighted image contrast of the Syn-STIR as the Acq-STIR. Lower noise levels are seen in the Syn-STIR images.

Diagnostic Interchangeability

The estimate of interchangeability (diagnostic equivalence) when accounting for readers and cases as random effects was -3.23% (95% CI, -6.61% – 0.19%), evaluated over 1000 bootstrapped samples (Fig 2). The decrease in interreader agreement expected when interchanging Acq-STIR images with Syn-STIR images was 3.23%. Based on the results, the estimate of interchangeability was not significantly worse than the noninferiority limit of 10% ($P = .001$). On the basis of the prespecified noninferiority criteria of 10%, we concluded that interchanging the Acq-STIR images with Syn-STIR images would not lead to a significant decrease in

interreader agreement; thus, the Syn-STIR was deemed diagnostically equivalent to the Acq-STIR.

For the trauma subset, the 3 structure-based classifications (prevertebral fluid collections, fracture-related bone edema, and posterior soft-tissue/ligamentous injury) were analyzed separately as different classes (Fig 3). The estimate of interchangeability (diagnostic equivalence) when accounting for readers and cases as random effects for the 3 classes was +0.85% (95% CI, -4.13%–5.48%), +2.3% (95% CI, -2.8%–7.1%), and +2.2% (95% CI, -2.2%–6.4%),

respectively; each class evaluated >1000 bootstrapped samples. In other words, the interreader agreement can be expected to improve by 0.85%, 2.3%, and 2.2% when interchanging traditional STIR images with Syn-STIR images. Based on the results, the estimate of interchangeability was not significantly worse than the noninferiority limit of 10% ($P = .001$). Given all 3 classes, a final analysis was performed in which the results described above from the 3 classes were combined, and “class” was included as a fixed effect in the statistical model. The interchangeability estimate was +1.9% (95% CI, -1.1%–5.0%), indicating that there was an improvement in the interreader agreement found when interchanging Acq-STIR images with Syn-STIR images. We, therefore, conclude that for the trauma study Syn-STIR was interchangeable with Acq-STIR.

Image-Quality Analysis

Acq-STIR images had an average IQ score of 3.21 (SD, 1.08), and Syn-STIR images scored an average of 3.71 (SD, 1.14). A Wilcoxon signed-rank test showed a significantly higher median IQ score for Syn-STIR images than Acq-STIR images (median = 0.4, $P < .0001$). A t test on the paired difference in IQ scores across artificial intelligence-generated and Acq-STIR images showed a significantly higher average

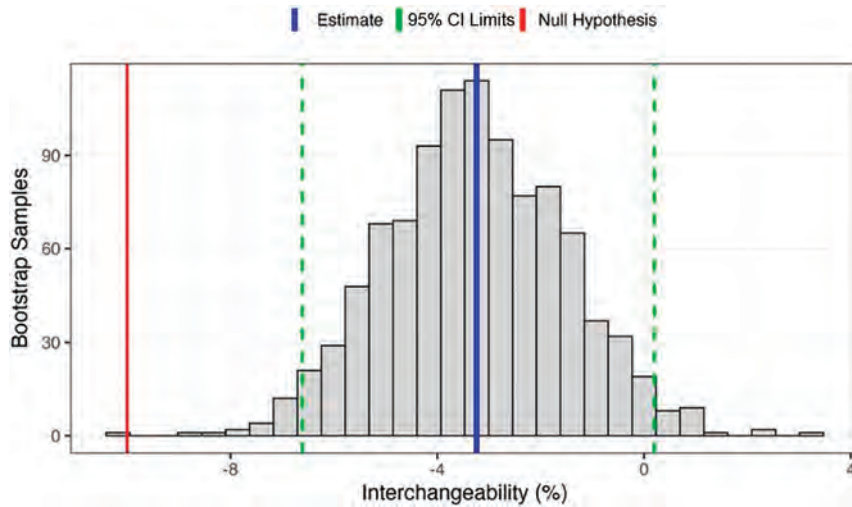


FIG 2. Interchangeability when accounting for readers and cases as random effects under the whole-cohort estimated >1000 bootstrapped samples.

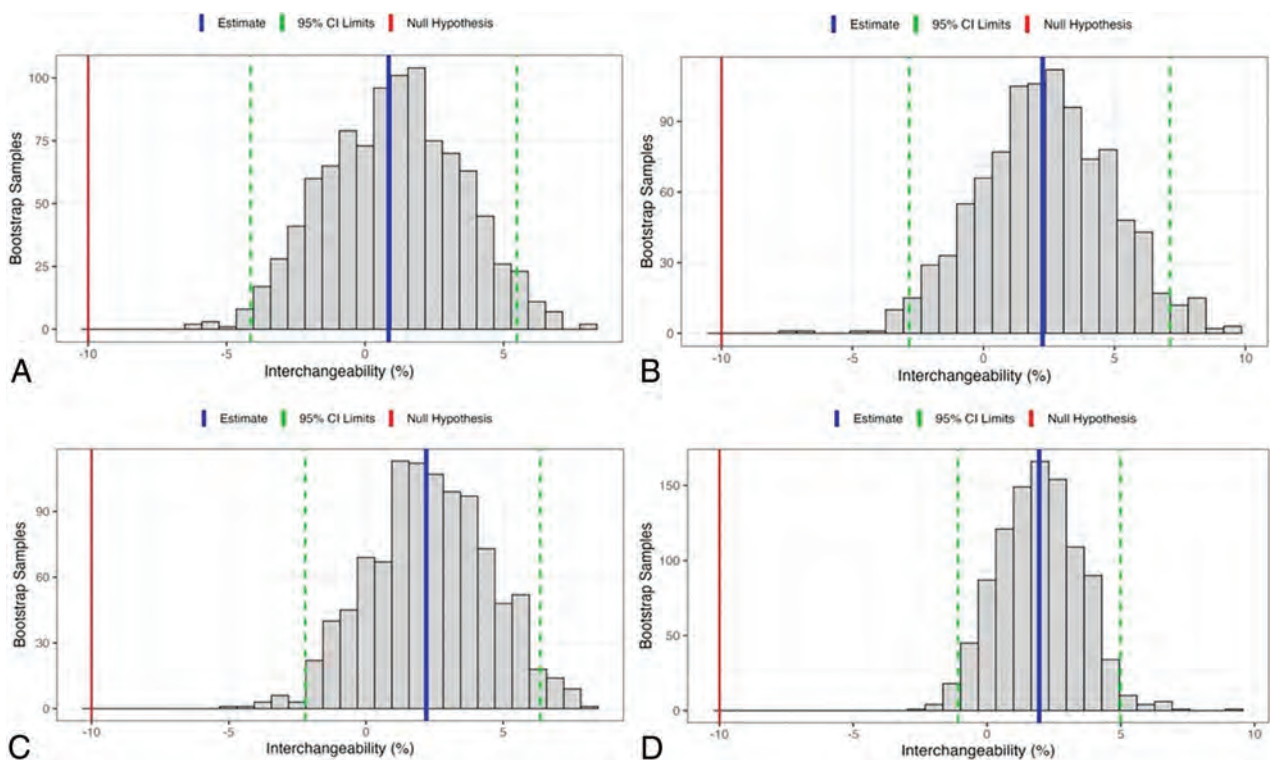


FIG 3. Interchangeability when accounting for readers and cases as random effects under the trauma cohort estimated >1000 bootstrapped samples. The x-axis represents the estimated interchangeabilities in the unit of percentage, and the y-axis represents the count of bootstrapped samples. A, Trauma class I. B, Trauma class II. C, Trauma class III. D, Mixed effect for all 3 classes.

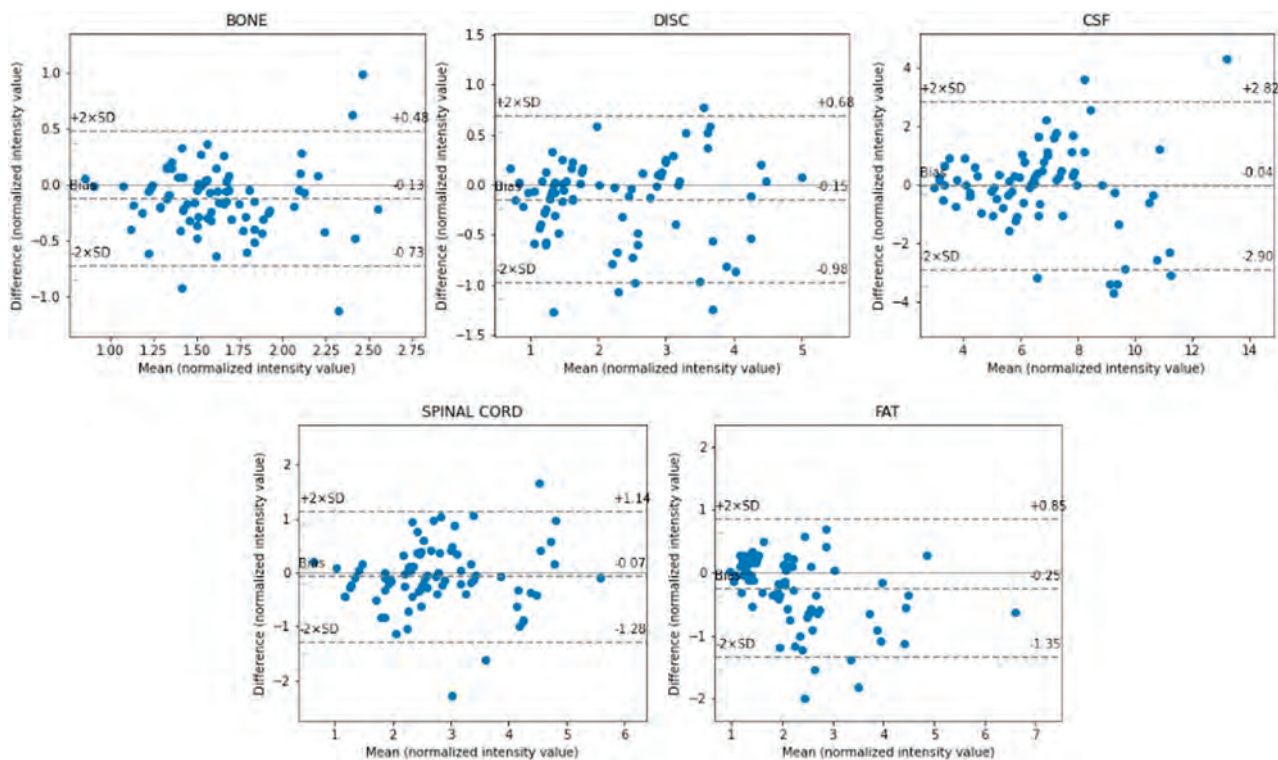


FIG 4. Bland-Altman plots for each tissue from 80 clinical cases. The x-axis represents the mean of the normalized intensity value from Syn-STIR and its nearest neighbor from Acq-STIR, and the y-axis represents the difference between the normalized intensity value from Syn-STIR and its nearest neighbor from the Acq-STIR.

IQ score for Syn-STIR images compared with Acq-STIR images (mean paired difference = 0.50; 95% CI, 0.33–0.67; $P < .0001$).

Side-by-Side Comparison

In the blinded, side-by-side evaluation of the cases in study one, 94.9% of Syn-STIR sets demonstrated equal or a better extent of disease compared with Acq-STIR for the first reader and 97.5% for the second reader; 88.6% of cases provided equal or higher diagnostic confidence with Syn-STIR for the first reader and 87.3% for the second reader. In addition, no unexpected differences were found between the 2 STIR types, indicating that the Syn-STIR method did not create unique artifacts.

Voxel Consistency

The Bland-Altman plots for voxel consistency are shown in Fig 4. For each tissue, the bias (the mean of the difference between the Acq-STIR and Syn-STIR) was close to zero. The smallest average bias was from the CSF, which was -0.04 normalized intensity units, and the largest average bias was from fat, which was around -0.25 normalized intensity units. The Shapiro-Wilk results showed that all P values were $> .05$, implying that the difference between the Acq-STIR and the Syn-STIR is normally distributed.

In addition, the RMSE and RMSPE between the Acq-STIR and Syn-STIR images for each patient were 0.45 and 17.88 normalized intensity units, respectively. For all 80 cases, the median of the RMSE value was 0.45 normalized intensity units, and the median of the RMSPE percentage was 17.9%. After confirming that the 5 tissues passed the Shapiro-Wilk test for normality, the Passing-Bablok regression was applied to estimate the regression

line and intercept (Fig 5). The slopes of the disc, CSF, and spinal cord were 1.06, 1.05, and 1.07, which indicate a high correlation between the 2 results. The slope of bone and fat was 0.85 and 0.78, respectively. The results indicate excellent voxelwise consistency between the Acq-STIR and the Syn-STIR images.

DISCUSSION

STIR is quite powerful in depicting spine pathology and thus is part of almost all routine spine imaging protocols; however, conventional reconstruction scan times are long. Also, because of the fat inversion pulse, the SNR of the images is lower than that of other sequences. A synthetically generated STIR could result in approximately 3–5 minutes of scan time avoided or up to 25% overall time-savings per examination, increasing imaging enterprise efficiency. Because up to 30% of patients report significant anxiety, largely from claustrophobia, during an MR imaging study, scan-time reductions inherently improve the patient's experience.¹⁸ The authors' internal multicenter surveys have shown that even minor reductions in examination length result in a significantly higher level of patient satisfaction.¹⁹

MR imaging examinations are susceptible to image degradation from motion, particularly during lengthy scans. Motion is a significant challenge in MR imaging, occurring in 29% of inpatient/emergency department examinations and 7% of outpatient studies²⁰ and can lead to the need to repeat sequences or entire studies. Andre et al²¹ found that 19.8% of all MR imaging sequences needed to be repeated due to motion artifacts, correlating with US \$592 revenue loss per hour and an annual loss of US \$115,000 per scanner.

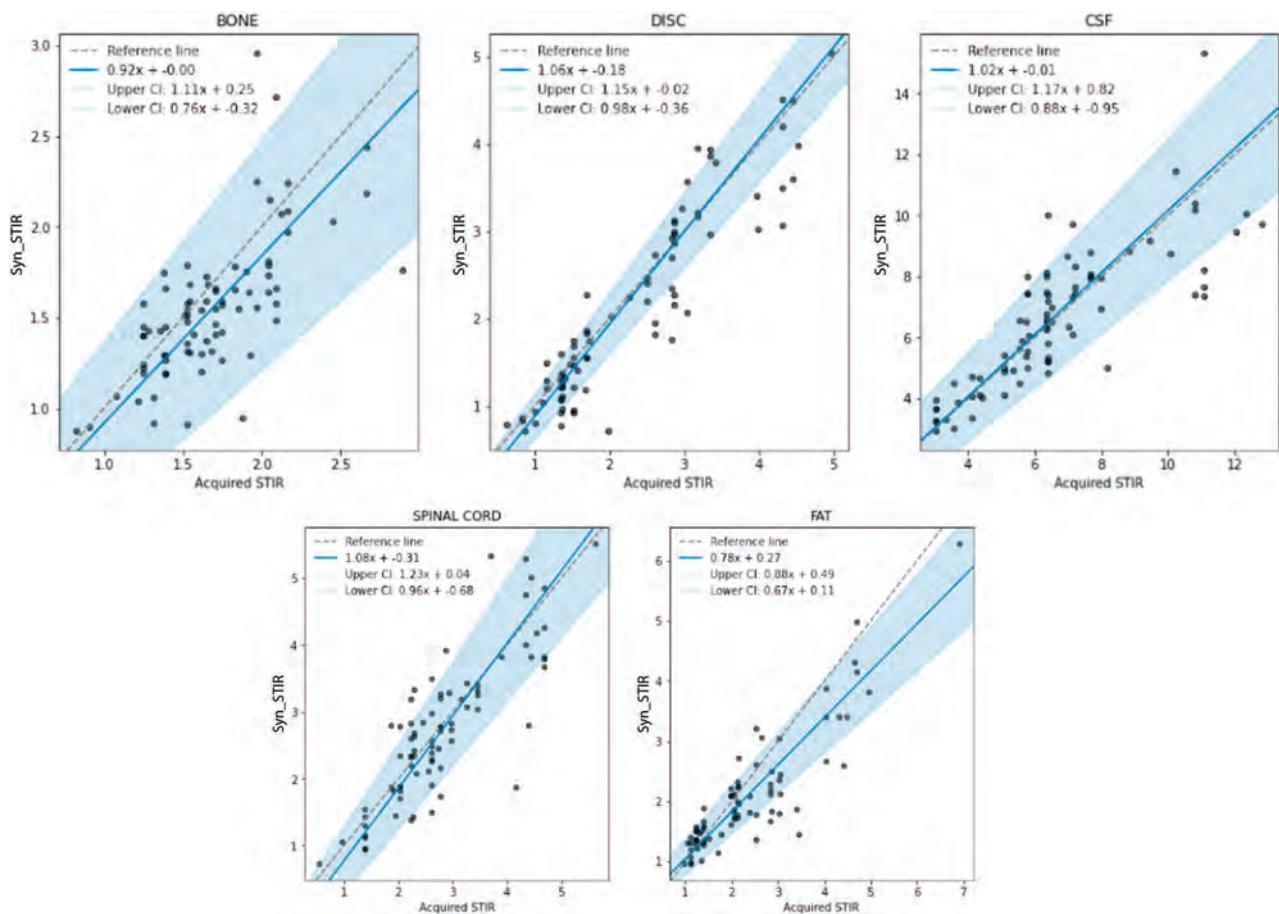


FIG 5. Passing-Bablok regression applied to estimate the regression line and intercept. The slope of the disc, CSF, and spinal cord is 1.06, 1.05, and 1.07, which indicates a high correlation between the 2 results. The slope of bone and fat is 0.85 and 0.78, respectively. The results indicate excellent voxelwise consistency between the Acq-STIR and Syn-STIR images.

The generally inverse relationship between MR image quality and scan duration is well-established.^{1,2} Traditionally reconstructed, high-resolution, high-SNR images require acquisition times that can be quite long. DL-based image reconstruction is increasingly used in practice to reduce the time required to provide high-quality images by up to 50%.^{1,2} DL image synthesis offers effective 100% series acceleration. In addition, because the synthesized images in our study receive the SNR and spatial resolution of the acquired T1WI and T2WI scans, Syn-STIR can be expected to offer better image quality than is practical with an Acq-STIR.

Previous work on MR imaging sequence-to-sequence translation has been performed⁴⁻¹⁰ but generally in subjects without pathology. This study demonstrated excellent performance in a patient cohort with a diverse set of typical spinal pathologies and evaluated key imaging findings commonly assessed with STIR imaging.

Absolute quality ratings could potentially obscure subtle failures and artifacts in the synthetically reconstructed image. Thus, a blinded, side-by-side evaluation was performed to compare the extent of disease and diagnostic confidence as well as to interrogate for evidence of image aberrations. We found that 96% of Syn-STIR sets manifested equal or better extent of disease compared with Acq-STIR, and 88% of cases provided equal or higher

diagnostic confidence with Syn-STIR. Most important, no unexpected image appearances (“hallucinations”) or information losses were detected. Although our study had no cases in which the network failed to generate an acceptable Syn-STIR image, the quality of the Syn-STIR image depends on the quality of the input T1 and T2 images. Therefore, if the input images were to have gross artifacts or high noise levels, these could manifest on the Syn-STIR series.

Our study patients were imaged on scanners of differing vendors and field strengths, drawn from a variety of geographically diverse facilities, and encompassed a variety of disease entities, but we acknowledge a risk of inadvertent patient-selection bias or disease-representation bias during the initial gathering of the larger patient cohort.

In this randomized, blinded trial, Syn-STIR demonstrated superior image quality with respect to Acq-STIR. A potential limitation is that the overall qualitative image-quality assessment was a collective summary of perceived metrics against typical expectations and is thus biased by subjective preferences. However, quantitative measures, such as statistical analysis of voxel consistency across STIR data sets, were robust. Future exploration could apply synthetic image generation to additional body parts and other scanning techniques.

CONCLUSIONS

DL-based Syn-STIR MR images, derived from acquired T1WI and T2WI DICOM data sets from multiple centers, scanners, and field strengths, proved statistically interchangeable in diagnostic performance with traditionally acquired STIR and provided superior perceived image quality. Quantitative measures demonstrated consistent results, validating both the high accuracy of the Syn-STIR images and the generalizability of the DL method. This Syn-STIR method offers a promising clinical solution for faster and more comfortable spine MR imaging examinations.

Disclosure forms provided by the authors are available with the full text and PDF of this article at www.ajnr.org.

REFERENCES

1. Bash S, Johnson B, Gibbs W, et al. **Deep learning image processing enables 40% faster spinal MR scans which match or exceed quality of standard of care.** *Clin Neuroradiol* 2022;32:197–203 CrossRef Medline
2. Bash S, Wang L, Airriess C, et al. **Deep learning enables 60% accelerated volumetric brain MRI while preserving quantitative performance: a prospective, multicenter, multireader trial.** *AJNR Am J Neuroradiol* 2021;42:2130–37 CrossRef Medline
3. Zaharchuk G, Gong E, Wintermark M, et al. **Deep learning in neuro-radiology.** *AJNR Am J Neuroradiol* 2018;39:1776–84 CrossRef Medline
4. Liu J, Pasumarthi S, Duffy B, et al. **One model to synthesize them all: multi-contrast multi-scale transformer for missing data imputation.** *IEEE Trans Med Imaging* 2023 Mar 4 [Epub ahead of print] CrossRef Medline
5. Li H, Paetzold JC, Sekuboyina A, et al. **DiamondGAN: unified multi-modal generative adversarial networks for MRI sequences synthesis.** In: Shen E, Liu T, Peters, TM, et al. *Medical Image Computing and Computer Assisted Intervention–MICCAI*. Springer International Publishing; 2019:795–803
6. Denck J, Guehring J, Maier A, et al. **Enhanced magnetic resonance image synthesis with contrast-aware generative adversarial networks.** *J Imaging* 2021;7:133 CrossRef Medline
7. Yurt M, Dar SU, Erdem A, et al. **mustGAN: multi-stream Generative Adversarial Networks for MR image synthesis.** *Med Image Anal* 2021;70:101944 CrossRef Medline
8. Dar SU, Yurt M, Karacan L, et al. **Image synthesis in multi-contrast MRI with conditional generative adversarial networks.** *IEEE Trans Med Imaging* 2019;38:2375–88 CrossRef Medline
9. Lee D, Kim J, Moon WJ, et al. **CollaGAN: Collaborative GAN for Missing Image Data Imputation.** In: *2019 IEEE/CVF Conference on Computer Vision and Pattern Recognition (CVPR)*. IEEE, Long Beach, California. June 15–20, 2019:2487–96 CrossRef
10. Haubold J, Demircioglu A, Theysohn JM, et al. **Generating virtual short tau inversion recovery (STIR) images from T1- and T2-weighted images using a conditional generative adversarial network in spine imaging.** *Diagnostics (Basel)* 2021;11:1542 CrossRef Medline
11. Obuchowski NA, Subhas N, Schoenhagen P. **Testing for interchangeability of imaging tests.** *Acad Radiol* 2014;21:1483–89 CrossRef Medline
12. Kingma DP, Ba J. **Adam: A Method for Stochastic Optimization.** *arXiv*. December 22, 2014. <http://arxiv.org/abs/1412.6980>. Accessed January 15, 2023
13. Khatri G, Pedrosa I, Ananthakrishnan L, et al. **Abbreviated-protocol screening MRI vs. complete-protocol diagnostic MRI for detection of hepatocellular carcinoma in patients with cirrhosis: an equivalence study using LI-RADS v2018.** *J Magn Reson Imaging* 2020;51:415–25 CrossRef Medline
14. Giavarina D. **Understanding Bland Altman analysis.** *Biochem Med (Zagreb)* 2015;25:141–51 CrossRef Medline
15. Altman DG, Bland JM. **Measurement in medicine: the analysis of method comparison studies.** *The Statistician* 1983;32:307–17
16. Henderson AR. **Testing experimental data for univariate normality.** *Clin Chim Acta* 2006;366:112–29 CrossRef Medline
17. Sotgia S, Zinellu A, Pinna GA, et al. **A new general regression-based approach for method comparison studies.** *Clin Chem Lab Med* 2008;46:1046–49 CrossRef Medline
18. Tanenbaum L. **Quality, efficiency, and survival with patient centric imaging.** In: *Proceedings of 7th Annual Snowmass 2023: Hot Topics in Radiology: Advanced Imaging and Artificial Intelligence*. Snowmass Village, Colorado. February 5–10, 2019
19. Meléndez JC, McCrank E. **Anxiety-related reactions associated with magnetic resonance imaging examinations.** *JAMA* 1993;270:745–47 CrossRef Medline
20. Zaitsev M, Maclaren J, Herbst M. **Motion artifacts in MRI: a complex problem with many partial solutions.** *J Magn Reson Imaging* 2015;42:887–901 CrossRef Medline
21. Andre JB, Bresnahan BW, Mossa-Basha M, et al. **Toward quantifying the prevalence, severity, and cost associated with patient motion during clinical MR examinations.** *J Am Coll Radiol* 2015;12:689–95 CrossRef Medline

Resisted Inspiration Improves Visualization of CSF-Venous Fistulas in Spontaneous Intracranial Hypotension

P.G. Kranz, M.D. Malinzak, L. Gray, J. Willhite, and T.J. Amrhein



ABSTRACT

BACKGROUND AND PURPOSE: CSF-venous fistulas are an important cause of spontaneous intracranial hypotension but are challenging to detect. A newly described technique known as resisted inspiration has been found to augment the CSF-venous pressure gradient and was hypothesized to be of potential use in CSF-venous fistula detection but has not yet been investigated in patients with spontaneous intracranial hypotension. The purpose of this investigation was to determine whether resisted inspiration results in improved visibility of CSF-venous fistulas on CT myelography in patients with spontaneous intracranial hypotension.

MATERIALS AND METHODS: A retrospective cohort of patients underwent CT myelography from November 2022 to January 2023. Patients with an observed or suspected CSF-venous fistula identified during CT myelography using standard maximum suspended inspiration were immediately rescanned using resisted inspiration and the Valsalva maneuver. The visibility of the CSF-venous fistula among these 3 respiratory phases was compared, and changes in venous drainage patterns between phases were assessed.

RESULTS: Eight patients with confirmed CSF-venous fistulas who underwent CT myelography using the 3-phase respiratory protocol were included. Visibility of the CSF-venous fistula was greatest during resisted inspiration in 5/8 (63%) of cases. Visibility was optimal with the Valsalva maneuver and maximum suspended inspiration in 1 case each, and it was equivalent in all respiratory phases in 1 case. In 2/8 (25%) cases, the pattern of venous drainage shifted between respiratory phases.

CONCLUSIONS: In patients with spontaneous intracranial hypotension, resisted inspiration improved visualization of CSF-venous fistulas in most, but not all, cases. Further investigation is needed to determine the impact of this technique on the overall diagnostic yield of myelography in this condition.

ABBREVIATIONS: CTF = CT fluoroscopy; CTM = CT myelography; CVF = CSF-venous fistula; DSM = digital subtraction myelogram; SIH = spontaneous intracranial hypotension

CSF-venous fistula (CVF) has been recognized during the past several years as the causative lesion in an increasing proportion of cases of spontaneous intracranial hypotension (SIH).¹ Multiple new interventions have been developed to treat CVFs, with relatively high reported success rates.²⁻⁵ Use of these techniques depends on accurate anatomic localization of the CVF, which remains challenging in many cases.

A variety of technical innovations have been described to enhance the visibility of CVFs on imaging, to improve detection.⁶⁻⁹ One report found that the appearance of CVFs varied with the respiratory phase, with augmented visibility of CVFs during inspiration compared with expiration or the Valsalva maneuver.⁸ More

recently, Mark et al¹⁰ found that a technique of resisted inspiration resulted in decreased pressure within the superior vena cava and increased CSF pressure compared with normal inspiration. Although the investigation did not directly explore the effect of this technique on CVF visualization, the authors hypothesized that it could potentially aid in CVF detection by augmenting the pressure gradient between the CSF and the venous system, thereby promoting transit of contrast through the fistula.

The purpose of this investigation was to determine whether a resisted inspiratory technique resulted in improved subjective visualization of CVFs in patients with SIH compared with other respiratory phases, including maximum suspended inspiration and the Valsalva maneuver, using serial image acquisition of CT myelography (CTM) during 3 separate phases of respiration.

MATERIALS AND METHODS

Subjects

This retrospective cohort included patients with SIH who underwent CTM at our institution between November 2022 and January

Received March 3, 2023; accepted after revision June 7.

From the Department of Radiology, Duke University Medical Center, Durham, North Carolina.

Please address correspondence to Peter G. Kranz, MD, Department of Radiology, Box 3808, Duke University Medical Center, Durham, NC 27710; e-mail: peter.kranz@duke.edu; @PeterGKranz

<http://dx.doi.org/10.3174/ajnr.A7927>

2023. The procedure schedule in the institutional electronic medical record was reviewed to identify patients who had undergone postmyelogram CT to evaluate a CSF leak. Patients were included if they satisfied the International Classification of Headache Disorders, 3rd ed, criteria for SIH,¹¹ had a suspected CVF identified on CTM at the time of scan acquisition, and subsequently were imaged with the 3-phase respiratory protocol described below. Patients without an imaging-verified CVF after the work-up was complete were excluded. The investigation was approved by the local institutional review board and is compliant with Health Insurance Portability and Accountability Act.

Myelographic Technique

CTM was performed using an intrathecal injection of 10 mL of iopamidol containing 300 mg/mL of iodine (Isovue-M 300; Bracco) with the patient in lateral decubitus position to increase the density of intrathecal contrast over the nerve roots in the thoracic spine, a technique previously shown to augment detection of CVFs.⁶

Imaging was performed on a 64-detector row CT scanner (Discovery 750HD; GE Healthcare) or on a photon-counting detector CT scanner (NAEOTOM alpha; Siemens). Intrathecal contrast was injected using either CT fluoroscopy (CTF) or conventional fluoroscopic guidance. In cases in which CTF was used, diagnostic CTM was performed immediately after contrast injection. In cases in which conventional fluoroscopy was used for the intrathecal injection, the patient was transferred to the CT scanner for subsequent diagnostic CTM, and care was taken to maintain the lateral decubitus position during transport to avoid mixing of contrast.

Resisted Inspiration Technique

The initial CTM scan was performed with the patient instructed to breathe in deeply and hold his or her breath (ie, maximum suspended inspiration). This process is equivalent to the “normal inspiration” phase reported by Mark et al.¹⁰ Images were reviewed on the CT scanner console by the performing radiologist in real-time to assess a hyperdense paraspinal vein indicating the presence of a CVF.¹² If no CVF was seen on the initial scan, the patient was turned to the contralateral decubitus position and repeat scanning of the thoracic spine was performed with maximum suspended inspiration.

In cases in which a CVF was observed or suspected to be present due to the presence of a hyperdense paraspinal vein on immediate review of either decubitus scan by the radiologist, repeat scanning limited to the level of interest was performed using a resisted inspiration technique, followed by a third scan acquired during the Valsalva maneuver. For resisted inspiratory scans, the patient was provided with a 5-mL syringe (Luer-Lock syringe; Becton-Dickinson) with the plunger removed to hold between his or her lips and instructed to breathe in continuously through the syringe beginning immediately before and then continuously throughout image acquisition, similar to the resisted inspiration technique previously reported.¹⁰ The syringe was then removed from the patient’s lips, and the limited area of interest was scanned a third time with the patient performing a Valsalva maneuver.

Image Analysis

Cases were retrospectively and independently reviewed by 2 neuroradiologists with 11 and 14 years of experience in treating SIH. Cases were reviewed on the PACS using the thinnest available section thickness (0.625 mm for scans performed on the 64-detector row CT and 0.2 mm on the photon-counting detector CT). Each radiologist assessed which respiratory phase optimally showed the CVF. Disagreement on the initial classification between readers was resolved by consensus.

Images from all 3 phases of respiration were coregistered and reviewed in a 3-plane MPR reformat. Cases were categorized into one of the following groups on the basis of the reader’s subjective analysis: One of the respiratory phases was superior to the other 2 in showing the CVF (pattern A), 2 of the respiratory phases were equally superior to the third (pattern B), or all respiratory phases were equivalent in depicting the CVF (pattern C).

Additionally, cases were categorized as either showing the same distribution of draining veins on all respiratory phases or showing drainage patterns that differed with the respiratory phase. Differing drainage was defined as new drainage into 1 of the following 3 regions of the venous plexus not seen on other respiratory phases: the internal epidural venous plexus, external epidural venous plexus, or basivertebral venous plexus.¹

The time of intrathecal contrast injection and of each of the 3 respiratory phase scans was determined from the timestamp of the images stored in the PACS. Time intervals between contrast injection and each of the subsequent 3 scan acquisitions were calculated on the basis of these timestamps. Differences in the time interval from contrast injection to the first CTM scan were compared in subjects for whom CTF was used for intrathecal injection versus those for whom conventional fluoroscopy was used by means of unpaired *t* tests. *P* values < .05 were considered statistically significant.

RESULTS

Ninety-one patients who underwent postmyelogram CT were reviewed for eligibility. Of these, 8 subjects were scanned using the 3-phase respiratory protocol and met the inclusion and exclusion criteria. The mean subject age was 56.6 (SD, 9.9) years (range, 44–73 years). Five of 8 (63%) subjects were women. Seven patients reported orthostatic headache as their primary symptom, and 1 patient reported impaired hearing as the primary symptom. In all cases, brain MR imaging with contrast was performed before CTM and showed changes compatible with SIH (at least 1 of the following signs: dural enhancement, venous distension, or brain sagging). In 6/8 cases, the CVF was identified on the first lateral decubitus scan, ipsilateral to the side positioned down during intrathecal contrast injection (left side in 5 cases, right side in 1 case). In the other 2 cases, no CVF was seen on the first scan but was identified after the subject had been rolled onto the contralateral decubitus position (right side in both cases). Spinal levels and laterality of identified CVFs are shown in the Table.

The mean time interval from intrathecal contrast injection to scan acquisition for the first respiratory phase (ie, maximum suspended inspiration) was 20.5 minutes (range, 7.7–55.9 minutes). The mean time interval between the acquisition of the first respiratory phase and the second phase (ie, resisted inspiration) was

Patient characteristics, CVF location, and behavior of CVF drainage investigated with 3-phase respiratory technique

Case No.	Age (yr)	Sex	CVF Level	CVF Side	Visibility Pattern ^a	Drainage Pattern Varies with Phase ^b	Best Phase for CVF Visualization
1	55	F	T12	R	A	N	RI
2	49	F	T3	L	A	N	MI
3	67	M	T3	L	A	N	V
4	60	F	L1	R	A	N	RI
5	48	F	T9	R	A	N	RI
6	57	M	T5	L	A	Y	RI
7	73	M	T7	L	C	Y	—
8	44	F	T7	L	A	N	RI

Note:—The en dash indicates that no single phase was superior; RI, resisted inspiration; MI, maximum suspended inspiration; V, Valsalva maneuver; M, male; F, female; R, right; L, left; N, no; Y, yes.

^aThe visibility pattern is classified as follows: One respiratory phase is superior to the others (A), 2 phases are equally superior to the third (B), or all respiratory phases are equivalent in depicting the CVF (C).

^bY indicates that the drainage pattern shifted to other portions of the epidural venous plexus with different respiratory phases; N indicates no shift.

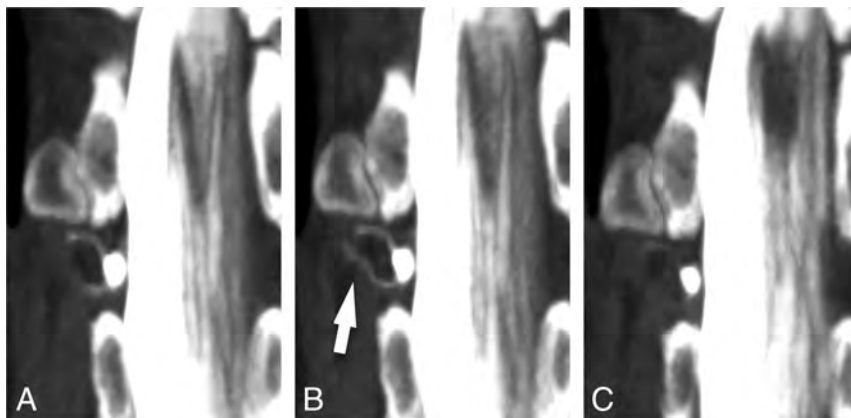


FIG 1. A right T12 CVF best visualized during resisted inspiration. Coronal MIP images from CTM performed in a patient with SIH are shown during maximum suspended inspiration (A), resisted inspiration (B), and the Valsalva maneuver (C). Although the CVF (arrow) is visible to varying degrees on all phases, visualization is best during resisted inspiration.

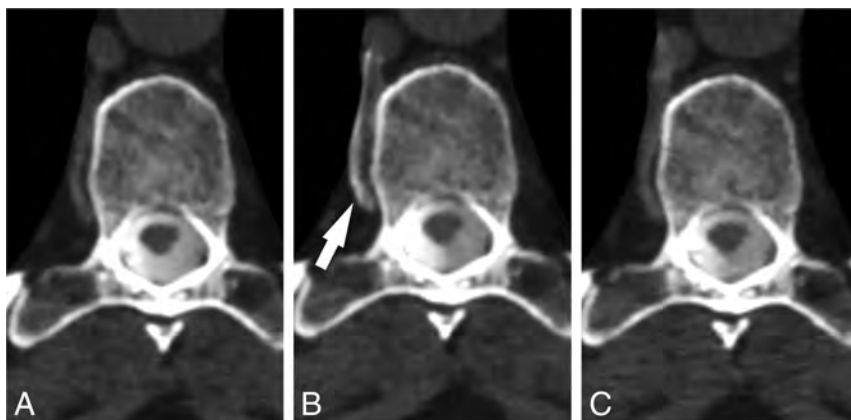


FIG 2. A right T9 CVF best visualized during resisted inspiration. Axial MIP images from CTM performed on a patient with SIH are shown during maximum suspended inspiration (A), resisted inspiration (B), and the Valsalva maneuver (C). Drainage of the CVF into a segmental vein (arrow) is best seen during resisted inspiration.

4.5 minutes (range, 2.3–6.5 minutes). The mean time interval between the acquisition of the second respiratory phase and the third phase (ie, the Valsalva maneuver) was 3.5 minutes (range, 1.4–6.2 minutes). In 2 cases (subjects 3 and 4), intrathecal

contrast injection was performed using conventional fluoroscopy before the patient was moved to the CT scanner; in one of these cases, dynamic myelography was performed under conventional fluoroscopy before CTM, and in the other case, injection was performed before CTM on the photon-counting detector CT because that scanner was not equipped with a CTF package. The remaining 6 injections were performed using CTF. The time interval between the contrast injection and the first scan was significantly longer for those cases in which conventional fluoroscopy was used for intrathecal contrast injection compared with those cases in which CTF was used (mean time to imaging, 42.3 versus 11.7 minutes; $P = .01$).

A single respiratory phase was found to best depict the CVF in 7/8 (88%) cases (pattern A) (Figs 1 and 2). Of these 7 cases, the resisted inspiration phase was assessed as the superior phase of respiration in 5 instances. The Valsalva maneuver (Fig 3) and maximum suspended inspiration best depicted the CVF in 1 instance each; both of these CVFs were located on the left at the T3 level. In 1/8 (12%) cases, all respiratory phases resulted in equivalent visualization of the CVF, which was located on the left at T7 (pattern C). There were no cases in which 2 phases were equally superior to the third in visualizing the CVF

(pattern B). Thus overall, resisted inspiration best depicted the CVF in 5/8 (63%) total cases in our study.

A change in the venous drainage pattern was observed between the different respiratory phases in 2/8 (25%) cases. In 1

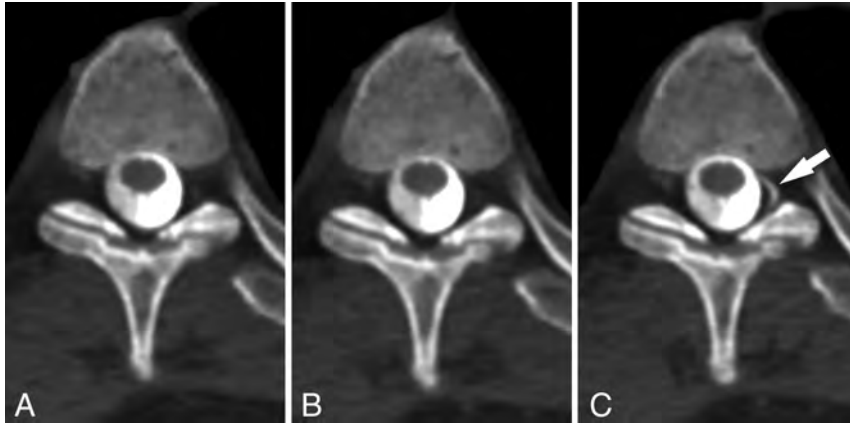


FIG 3. A left T3 CVF best visualized during the Valsalva maneuver. Axial MIP images from CTM performed on a patient with SIH are shown during maximum suspended inspiration (A), resisted inspiration (B), and the Valsalva maneuver (C). The CVF originating at the T3 level on the left (arrow) is best visualized during the Valsalva maneuver. The presence of a CVF was suspected on the basis of faint hyperdensity in the same location on the initial maximum suspended inspiration image.

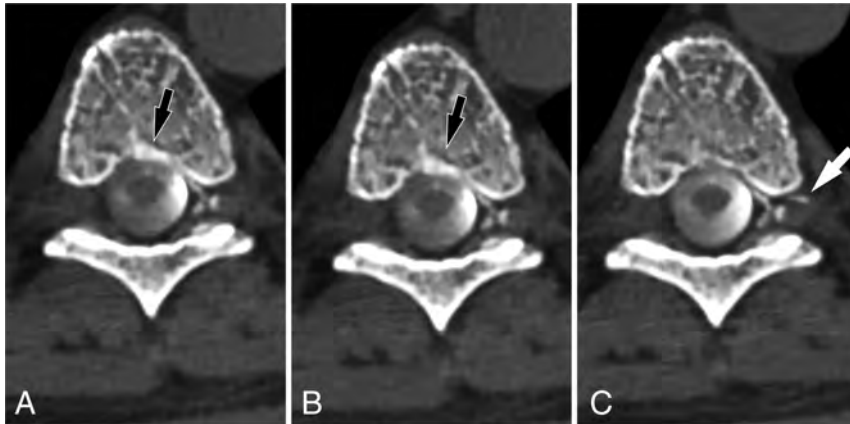


FIG 4. A left T7 CVF drainage pattern shifts with varying respiratory phases. Axial images from CTM performed on a patient with SIH are shown during maximum suspended inspiration (A), resisted inspiration (B), and the Valsalva maneuver (C). The primary drainage of the CVF is into the internal epidural venous plexus, but during inspiratory phases, a component of drainage is also seen into the basivertebral venous plexus (black arrows). This drainage decreases during the Valsalva maneuver, with new drainage visible into the external epidural venous plexus via an intervertebral vein (white arrow).

case (the aforementioned left T7 CVF), drainage was seen into the basivertebral venous plexus on both inspiratory phases, but it partially shifted away from the basivertebral plexus and into the external epidural venous plexus during the Valsalva maneuver (Fig 4). In another case, resisted inspiration resulted in the best visualization of the CVF in the internal epidural venous plexus but also shifted some drainage of the CVF into the external epidural venous plexus.

DISCUSSION

Our investigation found that in 5/8 (63%) cases, resisted inspiration resulted in superior visualization of the CVF compared with maximum suspended inspiration or the Valsalva maneuver. A recent investigation hypothesized that resisted inspiration might

prove superior to maximum suspended inspiration on the basis of venous manometry data obtained during various phases of respiration, but it did not directly test the effect on patients with actual CVFs.¹⁰ Our investigation conducted in cases of patients with SIH supports the hypothesis posited by Mark et al¹⁰ that resisted inspiration can be useful in enhancing the visibility of a CVF.

Resisted inspiration did not result in improved visibility of CVFs in all cases, however. In 2 cases, the CVF was best visualized on a different phase of inspiration (maximum suspended inspiration and the Valsalva maneuver, respectively). Both of these CVFs were located at T3 on the left. While it is possible that this association is coincidental, venous drainage of the upper left thoracic spine differs from that in the remainder of the thoracic spine. Specifically, the second through fourth thoracic vertebral levels on the left usually drain into the superior intercostal vein, while the rest of the thoracic spine drains into the azygous system.¹³ It is possible that resisted inspiration may affect augmentation of venous drainage differently in the upper left thoracic spine on the basis of this anatomic difference, though more experience with this technique will be needed to determine if this observation is reproducible.

We also observed that in some cases, the pattern of venous drainage may change on the basis of the respiratory phase. Variations in intrathoracic pressure and the resultant changes in venous pressures during different phases of respiration may influence the route of venous drainage for a single fistula. This

possibility could be consequential because some patterns of venous drainage may be more difficult to detect than others. For instance, drainage into the internal epidural venous plexus or basivertebral venous plexus could lie behind the overlying intrathecal contrast column and, therefore, be obscured on planar imaging such as digital subtraction myelography. Similarly, on CTM, drainage into the basivertebral venous plexus could potentially be less conspicuous than drainage into other routes because of the surrounding bone of the vertebral body. With greater experience, it may be possible to predict which phase of respiration is most likely to augment CVF visualization. It is also possible that multiple phases of respiration may be needed during an examination, depending on the vertebral level being imaged.

Some institutions use decubitus Trendelenburg patient positioning coupled with multiple phases of scanning within seconds

after intrathecal contrast bolus injection, sometimes referred to as “dynamic CTM,” to visualize CVFs.^{9,14} We did not use this technique for the CTMs in our study because we have found in our experience that maintaining a dense pool of contrast over the nerve roots is more important than temporal resolution when investigating possible CVFs with CTM, which can be accomplished without a dynamic contrast bolus. Moreover, a dynamic decubitus CTM technique would have made comparison of respiratory phases impossible because the migration of the contrast bolus would not provide adequate time for investigation of multiple respiratory phases. Although we make an effort to scan as quickly as possible after intrathecal contrast injection, our study does show that some delay in scanning does not preclude detection of CVFs as long as dense contrast can be maintained over the spinal nerve roots.

Our study has several limitations. First, this investigation included only CVFs seen or suspected during the initial imaging in maximum suspended inspiration. Although this study design has the potential to bias the results in favor of this particular inspiratory phase, we, nevertheless, found resisted inspiration to be superior to maximum suspended inspiration in most cases. However, because of this study design, the study cannot directly determine whether resisted inspiration will result in greater detection of fistulas in cases in which no fistula is seen at all on maximum suspended inspiration. Although it seems plausible that it might be helpful, the use of resisted inspiration as the sole respiratory phase used during an examination may be difficult to implement in practice in some cases, for several reasons: First, the length of time a patient can maintain inspiration against resistance may be insufficient to allow scanning of all vertebral levels of interest during CTM. When examinations are performed using DSM, resisted inspiration may be difficult to implement because the progressive expansion of the thorax may result in misregistration during image subtraction. Furthermore, resisted inspiration also depends on active cooperation and would not, therefore, be possible if examinations were performed with the patient under general anesthesia, which is used by some practitioners when performing DSM.

A second limitation of the study is that all variables that affect CVF visibility are not currently known; thus, factors unrelated to the respiratory phase (such as changes in contrast density in the thecal sac, differences in the cardiac cycle, or other unknown factors) may serve as confounders. Individual patients being scanned in the same session at very close time intervals may mitigate these effects, but this scenario does not completely exclude such influences. Finally, our study design relied on subjective assessments of CVF visibility by experienced, unblinded readers. Future investigations may consider whether more explicitly structured assessments by readers with varying levels of experience may better reflect the diagnostic performance of this technique across varied clinical practice environments.

CONCLUSIONS

Our investigation found that resisted inspiration resulted in improved visualization of CVFs among actual patients with SIH in most cases. Further work is needed to determine whether this technique can be implemented clinically on a routine basis and whether it increases the overall diagnostic yield of myelography in patients with SIH.

Disclosure forms provided by the authors are available with the full text and PDF of this article at www.ajnr.org.

REFERENCES

1. Kranz PG, Gray L, Malinzak MD, et al. **CSF-venous fistulas: anatomy and diagnostic imaging.** *AJR Am J Roentgenol* 2021;217:1418–29 CrossRef Medline
2. Schievink WI, Maya M, Prasad RS, et al. **Spinal CSF-venous fistulas in morbidly and super obese patients with spontaneous intracranial hypotension.** *AJNR Am J Neuroradiol* 2021;42:397–401 CrossRef Medline
3. Wang TY, Karikari IO, Amrhein TJ, et al. **Clinical outcomes following surgical ligation of cerebrospinal fluid-venous fistula in patients with spontaneous intracranial hypotension: a prospective case series.** *Oper Neurosurg (Hagerstown)* 2020;18:239–45 CrossRef Medline
4. Brinjikji W, Savastano LE, Atkinson JLD, et al. **A novel endovascular therapy for CSF hypotension secondary to CSF-venous fistulas.** *AJNR Am J Neuroradiol* 2021;42:882–87 CrossRef Medline
5. Mamlouk MD, Shen PY, Sedrak MF, et al. **CT-guided fibrin glue occlusion of cerebrospinal fluid-venous fistulas.** *Radiology* 2021;299:409–18 CrossRef Medline
6. Kranz PG, Gray L, Amrhein TJ. **Decubitus CT myelography for detecting subtle CSF leaks in spontaneous intracranial hypotension.** *AJNR Am J Neuroradiol* 2019;40:754–56 CrossRef Medline
7. Schievink WI, Maya MM, Moser FG, et al. **Lateral decubitus digital subtraction myelography to identify spinal CSF-venous fistulas in spontaneous intracranial hypotension.** *J Neurosurg Spine* 2019 Sept 13 [Epub ahead of print] CrossRef Medline
8. Amrhein TJ, Gray L, Malinzak MD, et al. **Respiratory phase affects the conspicuity of CSF-venous fistulas in spontaneous intracranial hypotension.** *AJNR Am J Neuroradiol* 2020;41:1754–56 CrossRef Medline
9. Mamlouk MD, Ochi RP, Jun P, et al. **Decubitus CT myelography for CSF-venous fistulas: a procedural approach.** *AJNR Am J Neuroradiol* 2021;42:32–36 CrossRef Medline
10. Mark IT, Amans MR, Shah VN, et al. **Resisted inspiration: a new technique to aid in the detection of CSF-venous fistulas.** *AJNR Am J Neuroradiol* 2022;43:1544–47 CrossRef Medline
11. **Headache Classification Committee of the International Headache Society (IHS): the International Classification of Headache Disorders, 3rd edition.** *Cephalalgia* 2018;38:1–211 CrossRef Medline
12. Kranz PG, Amrhein TJ, Schievink WI, et al. **The “hyperdense paraspinous vein” sign: a marker of CSF-venous fistula.** *AJNR Am J Neuroradiol* 2016;37:1379–81 CrossRef Medline
13. Borg N, Cutsforth-Gregory J, Oushy S, et al. **Anatomy of spinal venous drainage for the neurointerventionalist: from puncture site to intervertebral foramen.** *AJNR Am J Neuroradiol* 2022;43:517–25 CrossRef Medline
14. Madhavan AA, Benson JC, Cutsforth-Gregory JK, et al. **Co-existing fast CSF leaks and CSF-venous fistulas on dynamic CT myelography.** *Radiol Case Rep* 2022;17:2968–71 CrossRef Medline

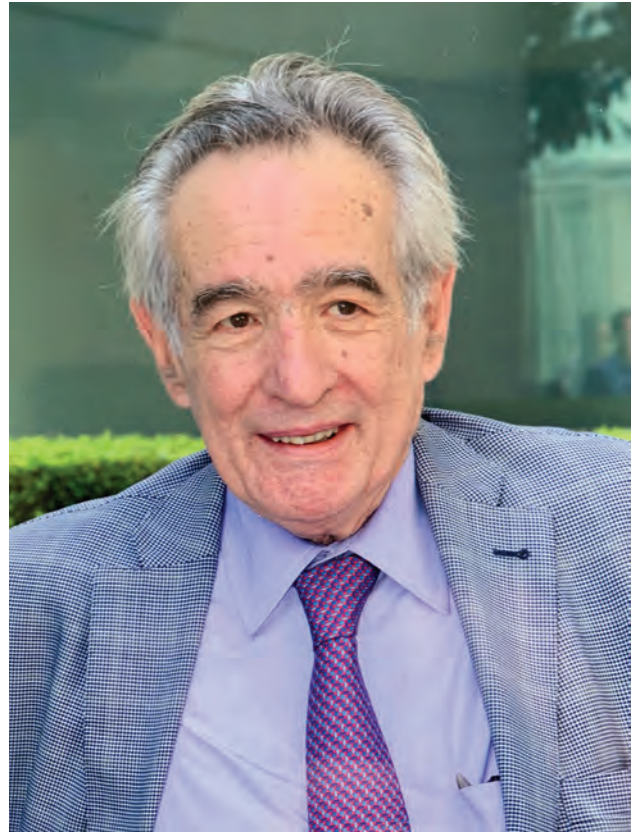
Professor Antonios Valavanis

On behalf of the Swiss Society of Neuroradiology (SSNR), its central committee, and our membership, we are sad to announce the death of one of its prominent members, Professor Antonios Valavanis, after a long period of illness that he would fight bravely. He would remain active until the end. Indeed, Professor Antonios Valavanis was one of the original founding members, Past President, and honorary member. Besides being instrumental in the foundation of the Society in 1988, he was President of our Society for 2 periods for a total of 15 years, from 1993 to 1999 and from 2001 to 2010. Together with Dr Huber from Bern, he was the leader of one of the two Historic branches of Swiss neuroradiology, the Zurich branch.

Born on January 20, 1952, in Athens, Greece, he would study medicine in Zurich from 1970 to 1977 and graduate from the University of Zurich (UZH) medical school in 1977. He would then start his training in radiology and neuroradiology at the University Hospital of Zurich (USZ), where he became the first assistant professor in 1984 and then full professor in 1994. In 1994, he was also appointed chairman of the Clinic of Neuroradiology at USZ. This was an important event; thereafter, neuroradiologic divisions would develop across Switzerland, both in university hospitals and regional centers. He would remain chairman of the Institute for Neuroradiology at the USZ until his retirement in 2017. He became a neuroradiologist at a time of dramatic methodologic changes in both diagnostic and interventional radiology as a whole but especially in neuroradiology, when more invasive methods such as pneumoencephalography were being replaced by CT and MR imaging and catheter techniques were beginning to allow selective angiography and treatment of cerebrovascular diseases.

Under his leadership, neuroradiology in Switzerland became a full specialty with 2 branches, diagnostic and interventional; currently in Switzerland, there are now 2 consecutive subdivisions in neuroradiology: diagnostic and interventional (or “invasive” as he would call it to encompass advanced imaging). While he would make his main academic and clinical impact in interventional neuroradiology, he still considered diagnostic neuroradiology a central part of both the subspecialty and the practical clinical work-up of patients with diseases of the CNS. His scientific output has been extensive, and he has published 200 articles covering the whole field of neuroradiology. Initially in his career, he published extensively with his colleagues W. Wichmann, J. Hayek, and O. Schubiger on diagnostic approaches to patients with diseases of the brain, leading him to publish the book *Clinical Imaging of the Cerebello-Pontine Angle* with O. Schubiger and T.P. Naidich, who would remain close colleagues. His main focus would remain the study of complex cerebrovascular diseases such as arteriovenous malformations; he made an immense contribution to the understanding of these entities. He later published the book *Interventional Neuroradiology* on this topic.

Following the impetus created among other clinical leaders in Zurich such as Hugo Krayenbuhl and Hess Walter Rudolf and along with world-renowned specialists such as Professors G.



Yasargil and U. Fisch, he established Zurich as one of the world's leading centers for interventional neuroradiology. In the early 1980s, he was among the first in the world to introduce the use of modern interventional techniques for lesions of the CNS. This introduction helped to establish neuroradiology as a fully clinical-based specialty in Switzerland.

Due to his many achievements, he was the recipient of many national and international honors. In 1983, he won the Science Prize of the European Society of Neuroradiology and was President of the 17th Congress of the European Society of Neuroradiology in Zurich in 1991. He also established the long-running Zurich Course on Interventional Neuroradiology attended by neuroradiologists from all over the world, which comprised a world-wide faculty. In 2018, he was appointed an honorary member of the SSNR. He served on the editorial board of the journal *Neuroradiology* from 1988 to 2004 and served on multiple committees. He went on to found the Clinical Neurocenter in Zurich and was instrumental in founding the Swiss Federation of Clinical Neurosciences, over which he would preside. He also founded its journal, *Clinical and Translational Neuroscience*.

The SSNR established the Antonios Valavanis Medal in his honor, with the first 2 recipients being Professors Luc Picard and Georges Rodesch (both from France), both highly ranked neuroradiologists who participated in the European movement of clinically-oriented neuroradiology. The newly opened diagnostic and

interventional angiography suite at the USZ was also named in his honor in October 2021. In 1992, he was appointed international consultant to the editor by the *American Journal of Neuroradiology*, and he was the editor-in-chief of *Neuroradiologia Helvetica*, the journal of the SSNR.

He has been a leader and a pioneer in making neuroradiology a central part of clinical neurosciences. His legacy in Switzerland

has been immense, and he will be missed by all his direct and indirect pupils. We, therefore, wholeheartedly extend our condolences to his friends and family.

 **I. Wanke**
 **K.O. Lövblad**
 **L. Remonda**

<http://dx.doi.org/10.3174/ajnr.A7939>

Appreciation and Concerns Regarding the Published Study “CURES”

We have read with great interest the recently published article entitled, “A Pragmatic Randomized Trial Comparing Surgical Clipping and Endovascular Treatment of Unruptured Intracranial Aneurysms” in the *American Journal of Neuroradiology*.¹ The results of the study, which randomized patients with unruptured cerebral aneurysms to endovascular or surgical treatment, have captured our attention, and we find the extracted data highly useful.

The researchers should be commended for their effort in conducting such a comprehensive study. However, I would like to address an important concern related to the challenges encountered during patient recruitment for randomized trials in a complex condition like this. Consequently, the analyzed group may represent a small subgroup of patients we encounter in our clinical practice.

In this regard, I would like to draw attention to another study conducted by the same authors, the CAM study, which we believe could be more valuable in terms of providing clinically relevant results. The CAM study not only randomized patients into treatment groups compared with a conservative group, but it also included a registry of nonrandomized patients. This approach may offer a more realistic perspective and enhance the applicability of the findings to real-world clinical practice.

While we appreciate the significance of the CURES study,¹ we would encourage further investigation and analysis within a larger patient population to address the limitations associated with patient selection. By doing so, we believe that the conclusions

drawn from future studies such as the CAM study would provide a more comprehensive understanding of the treatment options for unruptured cerebral aneurysms.²

Once again, I would like to express our gratitude to the authors for their dedication to advancing scientific knowledge and improving patient care through their research. We remain eagerly engaged in the ongoing dialogue surrounding this topic and look forward to the publication of subsequent studies that address the concerns outlined above.

Disclosure forms provided by the authors are available with the full text and PDF of this article at www.ajnr.org.

REFERENCES

1. Darsaut TE, Findlay JM, Bojanowski MW, et al. **A pragmatic randomized trial comparing surgical clipping and endovascular treatment of unruptured intracranial aneurysms.** *AJNR Am J Neuroradiol* 2023;44:634–40 CrossRef Medline
2. Iancu D, Collins J, Farzin B, et al. **Recruitment in a pragmatic randomized trial on the management of unruptured intracranial aneurysms.** *World Neurosurg* 2021;149:e521–34 CrossRef Medline

© I. Arrese

© R. Sarabia

Unit of Vascular Neurosurgery
Hospital Universitario Río Hortega
Valladolid, Spain

<http://dx.doi.org/10.3174/ajnr.A7925>

REPLY:

We thank Drs Arrese and Sarabia for their interest in our study.¹ While they “find the extracted data highly useful,” they are concerned that “the analyzed group may represent a small subgroup of the patients we encounter in our clinical practice.”² Moreover, they “would encourage further investigation and analysis within a larger patient population to address the limitations associated with patient selection.”² In other words, the crucial question they ask and that any clinician confronted with new trial results is entitled to ask is, Should I change my practice in the light of this new evidence? The authors of the letter are concerned that patients might have been selected to participate in the study and that this selection may have affected the generalizability of results. The answer to the question (Should I change my practice?) depends, partly, on the type of practice and whether that practice is dogmatic or open to uncertainty. However, the authors are right that the answer also strongly depends on the type of patients who participated in the trial, and the concern that trial results may not be applicable to all or most patients encountered in practice is legitimate, highly pertinent, and generalizable to most, if not all, clinical trials.³

To address this concern, one must first examine the trial eligibility criteria (the criteria that defined who could be included in the trial). In that regard, CURES was pragmatic: Trial eligibility criteria were wide. However, we did not specify treatment eligibility criteria, criteria that would define who should be treated (by any method, surgical or endovascular) rather than observed. That problem remains unanswered to this day.⁴

Second, regarding generalizability, one must examine Table 1, which compares patient and aneurysm characteristics.¹ We believe not only that the CURES groups were comparable but also that trial patients were typical, if not representative of, clinical series of treated patients. They are actually similar to patients recruited in a current ongoing trial.⁵ One may note that there were few patients in CURES with large (> 15mm) or posterior circulation aneurysms.¹ Thus, we cannot claim, for example, that the trial provides a general answer for these patients.

Third, to assess generalizability, one must examine the registry of patients screened for participation. For practical reasons, screening logs were not required according to the CURES protocol. However, we do have a gross estimate of the proportion of patients with Unruptured intracranial aneurysms (UIAs) recruited in CURES by examining the flow chart of patients recruited in the Comprehensive Aneurysm Management (CAM) study in 1 center that also participated in CURES. CAM is a care trial that includes both treatment and observation registries and 2 randomized trials, one of which is similar to CURES. Approximately 50% of patients ($n = 205/403$) were observed and 10% ($n = 39/403$) were treated without question, but 20 of these 39 patients were included in the trial comparing endovascular with surgical treatment (51%). One hundred fifty-nine of 403 patients (40%) were proposed for the trial comparing treatment with conservative management, and of those, 98 (62%) were randomly allocated to surgical or endovascular treatment. We believe that the design of the CAM study encouraged trial participation so that our estimates

are upper boundaries, but from this single-center experience, we estimate that CURES results apply to, at most, 50% of patients with UIAs considered for treatment and to <25% of all patients with UIAs. We nevertheless believe that CURES results are the best available data to inform the care of most patients with UIAs considered eligible for surgical or endovascular treatment.

This last statement does not mean that CURES results should be integrated into a computer program comparing CURES treatment results with rupture risks in untreated patients (in observational studies of patients ineligible for treatment or for a trial) to supply a providential answer to the clinical uncertainty that concerns particular patients.^{6,7}

Finally, a classic motto of clinical trial methodology is that the design should be such that trial results impact medical practice. We believe that this motto is inadequate: The clinical uncertainty transparently revealed by the existence of the trial question should rather impact practice immediately, long before trial results become available.⁸ Surgical or endovascular treatment is appropriately recommended only once it has been shown beneficial to patients. In the meantime, promising (but potentially harmful) treatments should be offered in the form of a care trial designed to optimize care in the presence of uncertainty for each individual patient.⁹ The preventive treatment of patients with UIAs by surgical or endovascular means has yet to be shown clinically beneficial. In that context, optimal care is a care trial. The reason CURES cannot provide a final answer regarding the best treatment is that the primary outcome was a surrogate end point, an angiographic finding at 1 year. The price to pay for this better outcome was a higher immediate risk of transient morbidity. We have yet to show whether angiographic findings translate into better outcomes for patients in the future reality of everyday life.

Back to the crucial question of should I change my practice? We believe that for many readers of this reply the answer is yes.

For clinicians who believe that observation is best for most patients, CURES showed that treatment can be performed with low morbidity (2% at 1 year). They should, at the very least, mention to their patients that treatment might improve their expectation of a good outcome in the future.

For clinicians who believe that most UIAs should be treated by clipping, CURES showed that while angiographic results may be better at 1 year with clipping, this finding has yet to be proven clinically beneficial to patients. In the meantime, clipping was convincingly shown to be associated with added transient initial morbidity.

For clinicians who believe that most patients should undergo endovascular treatment, CURES showed that angiographic results (and thus the future potential morbidity associated with rupture risks or retreatments) may negate the lesser initial treatment risks.

Both surgical and endovascular advocates should recognize that their treatments have never been shown beneficial for patients. Given the current uncertainty, we all should question our practice; we should learn to teach and practice within the context of pragmatic care trials.

REFERENCES

1. Darsaut TE, Findlay JM, Bojanowski MW, et al. **A pragmatic randomized trial comparing surgical clipping and endovascular treatment**

- of unruptured intracranial aneurysms. *AJNR Am J Neuroradiol* 2023;44:634–40 CrossRef Medline
2. Arrese I, Sarabia R. **Appreciation and concerns regarding the published study “CURES”.** *AJNR Am J Neuroradiol* 2023;44 (In press)
 3. Rothwell PM. **Subgroup analysis in randomised controlled trials: importance, indications, and interpretation.** *Lancet* 2005;365:176–86 CrossRef Medline
 4. Raymond J, Darsaut TE, Molyneux AJ. **A trial on unruptured intracranial aneurysms (the TEAM trial): results, lessons from a failure and the necessity for clinical care trials.** *Trials* 2011;12:64 CrossRef Medline
 5. Iancu D, Collins J, Farzin B, et al. **Recruitment in a pragmatic randomized trial on the management of unruptured intracranial aneurysms.** *World Neurosurg* 2022;163:e413–19 CrossRef Medline
 6. Darsaut TE, Fahed R, Raymond J. **PHASES and the natural history of unruptured aneurysms: science or pseudoscience?** *J Neurointerv Surg* 2017;9:527–28 CrossRef Medline
 7. Fahed R, Darsaut TE. **The Delphi Oracle and the management of aneurysms.** *J Neurointerv Surg* 2017;9:e1–e2 CrossRef Medline
 8. Darsaut TE, Raymond J. **Ethical care requires pragmatic care research to guide medical practice under uncertainty.** *Trials* 2021;22:143 CrossRef Medline
 9. Raymond J, Darsaut TE, Altman DG. **Pragmatic trials can be designed as optimal medical care: principles and methods of care trials.** *J Clin Epidemiol* 2014;67:1150–56 CrossRef Medline

 **J. Raymond**

Department of Radiology
Centre Hospitalier de l'Université de Montréal
Montréal, Québec, Canada

 **T.E. Darsaut**

University of Alberta Hospital
Edmonton, Alberta, Canada

The Benefits of Ocular Ultrasound in Emergency Settings for the Evaluation of Orbital Compartment Syndrome

We read with great interest the recent article on the imaging features of orbital compartment syndrome (OCS) published in your esteemed journal.¹ The authors have provided valuable insight into the importance of CT in evaluating OCS. However, we would like to emphasize the potential benefits of favoring ocular ultrasound (US) over CT, especially in emergency settings, because OCS is an emergent, traumatic complication that requires rapid detection and intervention.

Ocular US is a noninvasive, real-time imaging technique that has distinct advantages over CT in emergency settings. First, it poses no risk of radiation exposure, making it safer for patients, particularly in cases in which multiple imaging studies may be needed. Second, its portability allows bedside assessment in emergency departments, facilitating rapid diagnosis and management of OCS without having to transport the patient to a radiology suite.² This can be crucial in time-sensitive situations such as OCS, in which delays in diagnosis and treatment can result in permanent vision loss. B-scan US can effectively evaluate the globe, extraocular muscles, optic nerve, and other soft-tissue structures within the orbit.² It can detect key findings related to OCS, such as retrobulbar hemorrhage, a leading cause of OCS, and subperiosteal hematomas, which may contribute to the condition.

Ocular US serves as an essential diagnostic tool in detecting critical signs associated with OCS. The guitar pick sign, a notable finding in OCS cases, corresponds to globe tenting observed in CT scans.² Globe tenting occurs when the shape of the eye becomes distorted due to increased intraorbital pressure, causing it to resemble the triangular form of a guitar pick. This eponymous sign when detected on ocular US indicates elevated pressure within the orbit and the potential presence of OCS. Swift identification of the “guitar pick” sign is vital for timely intervention and the prevention of possible vision loss. In addition to identifying the “guitar pick” sign, ocular US can also effectively diagnose other OCS-related findings. For instance, it can determine the presence of proptosis and a smaller superior ophthalmic vein in the affected orbit,³ which may be a sign of altered blood flow due to increased intraorbital pressure. Furthermore, retinal ischemia, a serious consequence of OCS, can be diagnosed with color flow Doppler and pulsed wave Doppler.² These diagnostic

capabilities make ocular US an indispensable instrument in the evaluation and management of OCS. During emergency situations, patients with local orbital trauma can opt for US due to its faster assessment process in comparison with CT scans, which involve multiple steps like image acquisition and consulting a radiologist, among others. However, CT scans are still the preferred method for evaluating patients with multiple injuries, given their superior capability to assess fractures, intracranial hemorrhages, and other conditions.

Another limitation of ocular US is its use in cases of globe rupture. In some situations, globe rupture can be easily identified clinically, while in others, it may be more difficult to diagnose and may necessitate CT or US for verification. Although ocular US is typically seen as a relative contraindication because of globe rupture, it can still be valuable. By minimizing changes in intraocular pressure (IOP) and using a plastic shield, the risk of increased IOP can be further reduced. A clinical review of 8 globe rupture cases showed that US had a 100% sensitivity and 99% specificity in detecting the condition.⁴

Despite these limitations, US offers valuable diagnostic insight into ocular conditions beyond trauma evaluation. US not only serves as a diagnostic tool for OCS-related findings but also proves useful following orbital decompression procedures. By assessing the postdecompression status of the eye, ocular US can help identify other potential conditions, such as retinal detachment, vitreous detachment, or vitreous hemorrhage.² This additional utility ensures that clinicians can provide comprehensive care for patients, effectively addressing any complications that may arise after orbital decompression surgery.

In conclusion, US might demonstrate imaging characteristics comparable with those of CT scans in diagnosing OCS. To facilitate faster and more accurate diagnoses in emergency departments, further research and clinical studies could help establish the role of US in diagnosing and monitoring patients with OCS.

Disclosure forms provided by the authors are available with the full text and PDF of this article at www.ajnr.org.

REFERENCES

1. Maier C, Thieme N, Beck-Broichsitter B, et al. **Imaging the tight orbit: radiologic manifestations of orbital compartment syndrome.** *AJNR Am J Neuroradiol* 2023;44:589–94 CrossRef Medline

<http://dx.doi.org/10.3174/ajnr.A7904>

2. Murali S, Davis C, McCrea MJ, et al. **Orbital compartment syndrome: pearls and pitfalls for the emergency physician.** *J Am Coll Emerg Physicians Open* 2021;2:e12372 CrossRef Medline
3. Shah SS, Khanam S. **Orbital Color Doppler Imaging.** In: Abai B, ed. *StatPearls*. StatPearls Publishing; 2022
4. Propst SL, Kirschner JM, Strachan CC, et al. **Ocular point-of-care ultrasonography to diagnose posterior chamber abnormalities: a systematic review and meta-analysis.** *JAMA Netw Open* 2020;3:e1921460 CrossRef Medline

 **I. Mese**

Department of Radiology
Health Sciences University
Erenkoy Mental Health and Neurology Training and Research Hospital
Istanbul, Turkey

 **C. Altıntas Taslicay**

Department of Radiology
MD Anderson Cancer Center
Houston, Texas

REPLY:

We thank Drs Mese and Altintas Taslicay for their interest in our work on imaging signs of orbital compartment syndrome (OCS).¹ First and foremost, we would like to stress again that OCS is primarily a clinical syndrome. If OCS has already been diagnosed on the basis of the physical examination, emergency decompression must not be delayed by any imaging study or by other diagnostic tests. Imaging can play a role when the clinical examination is limited (eg, by profuse periorbital hematoma), but any time delay inherent to performing imaging must be carefully weighed against the relatively small risks associated with the decompression procedure. Apart from that, radiologists should be aware of the typical imaging signs (proptosis, optic nerve stretching, and, in some cases, posterior globe tenting) so that they can alert the clinical team to the possible presence of OCS in cases in which this vision-threatening condition was not primarily suspected.

Our study investigated imaging findings of OCS before treatment and focused on CT imaging because this is the primary imaging technique for maxillofacial/orbital trauma. Furthermore, the ability to retrospectively reformat CT data sets proved useful for precisely comparing the affected orbit with the contralateral (control) orbit in a systematic manner.

The published literature on sonography in the context of OCS is very limited. However, it can be expected that the imaging phenotype that has been established on the basis of CT is generally

transferrable to sonography, provided that the pertinent anatomy can be visualized. One should be cautioned that intraorbital emphysema or practical difficulties in the context of open injuries will limit the acoustic window in some cases. As is always the case, the choice of imaging technique must be informed by the respective strengths and weaknesses of each technique and will also be influenced by institutional factors such as availability and local expertise. Using sonography for the serial follow-up of OCS after treatment is an interesting proposition that would require dedicated investigation.

REFERENCE

1. Maier C, Thieme N, Beck-Broichsitter B, et al. **Imaging the tight orbit: radiologic manifestations of orbital compartment syndrome.** *AJNR Am J Neuroradiol* 2023;44:589–94 CrossRef Medline

 **C. Maier**

Department of Radiology
Charité, Universitätsmedizin Berlin
Berlin, Germany

Department of Radiology
New York University School of Medicine
New York, New York

 **J.O. Voss**

Department of Oral and Maxillofacial Surgery
Charité, Universitätsmedizin Berlin
Berlin, Germany

Berlin Institute of Health
Berlin, Germany

<http://dx.doi.org/10.3174/ajnr.A7957>